

403 690

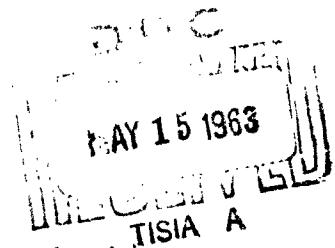
Final Report

STUDY OF FAILURE MECHANISMS

TECHNICAL DOCUMENTARY REPORT NO. RADC-TDR-63-30

December 1962

Rome Air Development Center  
Research and Technology Division  
Air Force Systems Command  
United States Air Force  
Griffiss Air Force Base, New York



(Prepared under Contract No. AF30(602)2558  
by S. M. Skinner and J. W. Dzimianski,  
Westinghouse Electric Corporation, Air Arm  
Division, Baltimore, Maryland)

CATALOGED BY  
AS AD NO. — 403690

**Best  
Available  
Copy**

Qualified requesters may obtain copies of this report from the Armed Services Technical Information Agency (ASTIA). Department of Defense contractors must be established for ASTIA services, or have their "need-to-know" certified by the military agency cognizant of their contract.

This report has been released to the Office of Technical Services, Department of Commerce, Washington 25, D.C., for sale to the general public.

When Government drawings, specifications, or other data are used for any purpose other than in connection with a definitely related Government procurement operation, the United States Government thereby incurs no responsibility nor any obligation whatsoever; and the fact that the Government may have formulated, furnished, or in any way supplied the said drawings specifications, or other data, is not to be regarded by implication or otherwise as in any manner licensing the holder or any other person or corporation, or conveying any rights or permission to manufacture, use, or sell any patented invention that may in any way be related thereto.

**Final Report**

**STUDY OF FAILURE MECHANISMS**

**TECHNICAL DOCUMENTARY REPORT NO. RADC-TDR-63-30**

**December 1962**

**Rome Air Development Center  
Research and Technology Division  
Air Force Systems Command  
United States Air Force  
Griffiss Air Force Base, New York**

**Project No. 5519, Task No. 45155**

**(Prepared under Contract No. AF30(602)2558  
by S. M. Skinner and J. W. Dzimianski,  
Westinghouse Electric Corporation, Air Arm  
Division, Baltimore, Maryland)**



## PREFACE

In order to achieve the levels of reliability required for future military systems, it becomes apparent that conventional statistical methods for determining reliability will have to be supplemented by a more fundamental philosophy, aimed at replacing the present lack of understanding of the causative mechanisms leading to failure by the fundamental principles governing these processes. The work reported here is one of several efforts supported by the Rome Air Development Center under a broad program conceived to achieve this purpose.

Specifically, this effort was intended to survey mechanisms leading to failure in electronic components and materials, in order to accumulate understanding of their modes of operation and to develop an experimental methodology designed to measure some of the more subtle quantities contributing to failure in electronics. The actual program consists of a number of individual tasks which vary from relatively abstract investigations, such as the stick-slip surface measurements, to those of almost immediate benefit to device reliability, such as the determination of the influence on transistor characteristics of surface charging. Some of the more pertinent tasks are discussed below.

### a. Causes of Failure During Manufacture and Tests of Military Systems

Two complex military data processing systems are analyzed in detail for types and causes of failure of electrical components. Based on the observed similarity of failure rate ratios, an attempt is made to formulate an approach to reliability determination based on device complexity with regard to the number of leads, junctions, etc, constituting the device. For the system analyzed, the values of failure factors and weightings are reasonable, and

the mathematical treatment leads to no absurdities. The failure classification study furnished the initial clue to the identification of the failure mechanism of surface charging in transistors, described below. However, it is not directly an experimental search for failure mechanisms, and its potential for identification of additional failure mechanisms was judged to be small, so that it was discontinued. The available data have been brought to the attention of others at RADC whose area of responsibility and interest is primarily in investigations of this sort.

#### b. Surface Studies - Electrical-Frictional Probe

The electrical-frictional probe technique has been demonstrated to be sensitive to changes in chemical composition, structure, and imperfections in semiconductor materials. In this respect, it may be a useful nondestructive test. Because of its importance to the principal investigator's theories of semiconductor action, an attempt was made to extend the utility of the electrical frictional probe measurements by including an analysis of stick-slip cycle measurements. The complete solution referred to in this report was not finished and is not yet available, because of the complexity involved in reducing the results of the computer program.

#### c. Surface Studies - Repetitive Surface Contacting

From this task, evidence is presented that semiconductor surfaces age nonuniformly. It appears that aging commences independently at a number of separate points on the surface and, to some extent, progresses outward from them. The implication here is that if several devices are fabricated on the same wafer, their performance parameters will differ depending on their radial location on the wafer. It is also shown that surface characteristics are influenced by the chemical composition and exposure conditions used with various etchants. Also, since it could be expected that pressure effects caused by impurity regions, temperature changes, acceleration, etc, might result in changes in surface characteristics, an experiment is described demonstrating that photo-EMF changes approximately linearly with pressure applied perpendicular to the surface of the sample.

While the various measurements under this task describe only gross effects and no attempt is made to resolve the complexity of the situation, the general implication from the experiments is that the altered electrical performance resulting from the described stresses and environments constitutes failure mechanisms which must be further considered. The immediate implication is that these altered performances may constitute failure when regarded against the objectives desired for system performance.

d. Volume Studies - The Flexure-Charge Experiments

This is a study of a potential failure mechanism induced by mechanical stress. Although the voltage responses occurring at continuous flexure times of less than one hour could not be correlated with readily observable gross mechanical damage, experimental evidence was obtained that these responses may result from the formation of surface fractures similar to the reversible cracks observed in flexurally stressed glasses; that is, they have the ability to heal almost completely upon removal of the tensile portion of the stress cycle. Also, it is shown that the mechanical damage tended to concentrate at alloy junctions and other sites of discontinuity, and is hastened by elevated temperature.

The implications of these experiments are that by stressing silicon (and probably other semiconductor materials), including stresses such as may be encountered in the fabrication of semiconductor devices, deterioration in performance of the device may result.

It appears that this phenomenon may occupy a significant position with regard to fundamental mechanisms of failure in electronics.

e. Transistor Failure Caused by Surface Charging

Work on this task assumed additional significance in view of the recent publicity concerning Telstar recovery procedures. Although unrelated to the Telstar project, this task identified the fact that surface charging could cause transistor failure and that the transistor could recover when the charge leaked off or was removed. As a result of this work, several recommendations are made regarding precautions which may be observed to reduce charge

accumulation during fabricating and processing of devices sensitive to this failure mechanism.

#### f. High Energy Radiation Induced Failures

A portion of the over-all effort devoted itself to the study of failure in magnetic devices, specifically, degradation mechanisms in ferrites under the influence of high energy radiation. Although ferrites have never posed a serious problem in reliability (and these experiments confirm this), it was decided to investigate these materials because they were accessible to measurements by a new technique, Mössbauer spectrum analysis, which permits sensitive observation of the internal magnetic fields of the material. Since there were no systematic changes in the Mössbauer spectra after irradiation, it is concluded that these materials are not sensitive to these radiations and, if some degradation does occur, it is not through the mechanism of chemical structure changes.

Another radiation-related study investigated the degradation mechanism of silicon radiation detector diodes. Of particular concern here was the apparent disagreement with existing junction theory of the variation of junction capacitance with radiation dosage.

Much data have been accumulated on several types of diodes. These data indicate the presence of certain low-lying defect energy levels which may be related to the anomalous capacitance effect. However, additional study and analysis of the data will be necessary for exact elucidation of the mechanisms.

The investigations conducted under this contract are considered to have successfully achieved the objective of performing a general survey of possible mechanisms leading to the failure of electronic materials and devices. The range of complexity involved in a physical approach to reliability has been demonstrated, and it has been shown that the use of new approaches and unique measurement techniques may be desirable for the understanding and elucidation of the fundamental processes occurring in device failure. This report is considered to represent a worthwhile contribution to the Physics of Failure program.

## FOREWORD

This report was prepared by the Westinghouse Electric Corporation, Air Arm Division, Baltimore, Maryland, on Air Force Contract No. AF30(602)2558 under Task No. 45155 of Project No. 5519, "Study of Failure Mechanisms," and summarizes the research for the period 1 July 1961 to 30 September 1962. The work was accomplished under the direction of Dr. S. M. Skinner and Dr. J. W. Dzimianski. Secondary report No. 384A1 has been assigned.

## ABSTRACT

Results from the work of the fourth quarter are presented, together with a summarization of earlier results, to exhibit the overall program.

Various approaches to the study of properties of semiconductor surfaces are taken up, in particular, the very sensitive electrical-frictional probe which is applied to the study of defects and processing technology under various conditions. The way in which this apparatus can be used to locate defective regions and junctions and to improve solid state processing technology, and the use of the frictional drag and stick-slip response to complement the electrical data, are described.

The distribution of failures in the manufacturing and testing phase of two military systems are compared, and the factors described which caused failure ratios in the one to be one-seventh those in the other. The failure factor method of failure analysis is described, and the values of the failure factors and weights of each in the two systems are computed. Utilization of the failure factor technique in accelerated testing design and analysis, and in the determination of reliability, is discussed.

By various studies, it has been determined that the aging of a semiconductor surface does not take place uniformly, but occurs differently at different regions on the surface. The effect of different types of etching and processing solutions on the photovoltaic response of the surface at individual points is used to investigate the nature of the aging and chemical changes on the surface. Dependence of the photovoltaic response and, therefore, of electrical characteristics of a semiconductor surface upon applied pressure is demonstrated, and its practical consequences are discussed. Various other surface phenomena and the effect of temperature on junction behaviors were studied.

By the electrical response to the repetitive flexure of samples of semiconducting material, particularly silicon dendrites, the existence of subvisible cracks in material subjected to

mechanical stresses was demonstrated. These are self-healing in the early stages; at higher temperatures, they occur more easily, and annealing apparently does not occur.

The new mechanisms of transistor failure found in the earlier stages of this work have been studied further. Characteristic changes in transistor performance have been demonstrated from the charging of passivating layers by electrons or ions, from the frictional effects of loose desiccant under vibration, from ultraviolet light, and from steep transients in the non-overload range. In all cases, recovery occurs by a relaxation mechanism, which, if translated to the manufacturers' carefully planned ambient environment, involves time constants often of days or months.

A number of failures are demonstrated which result from inadequate design or poor processing techniques in commercial transistors.

A multiple parameter study of the effects of short-period overload on various commercial transistors in the military specification quality range is described. Conservative build-up of stress was used, and discernible degradation appeared on several transistor types near the end of the testing period, indicating the likelihood of further degradation with extended testing.

The failure in thin films in memory devices at bends or steps in the substrate appears to be due to poor adhesion, as well as to any stresses involved at the bend in a perfectly adhering film.

A theoretical study of the transient effects in semiconductor materials because of combined conduction and diffusion, including the effect of temperature, and the heat dissipation to be expected as a function of time, frequency, and geometrical location in the material is described; this should be useful in respect to geometrical design to avoid maximum heat loss regions for given frequency ranges.

A study of the effects of high energy radiation of ferrites by use of the Mössbauer effect is described in full; the lattice structure is characterized, and the fact that no gross chemical or structural changes take place in the material, up to a dose of  $10^{11}$  rads, is confirmed.

Another study of the effects of high energy radiation is also reported; that is, the effect of electron irradiation upon capacitance and particle detection ability of silicon diodes. The

nature of the dependence of capacitance on radiation dose, and the probable existence of a new energy level in the forbidden region are shown.

#### PUBLICATION REVIEW

This report has been reviewed and is approved.

APPROVED:

for:

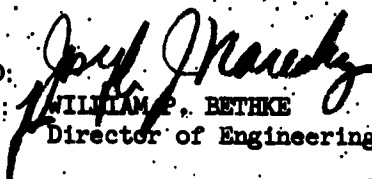


DAVID F. BARBER

Chief, Applied Research Laboratory  
Directorate of Engineering

APPROVED:

for:



WILLIAM P. BETHKE

Director of Engineering

FOR THE COMMANDER:



IRVING J. GABELMAN

Director of Advanced Studies



## TABLE OF CONTENTS

### 1. INTRODUCTION

Paragraph	Page
Introduction . . . . .	1

### 2. CONCLUSIONS

Conclusions . . . . .	7
-----------------------	---

### 3. RECOMMENDATIONS

Recommendations . . . . .	13
---------------------------	----

### 4. DATA AND DISCUSSION

4.1 Causes of Failure During Manufacture and Tests of Military Systems . . . . .	15
4.1.1 Systems Analyzed . . . . .	15
4.1.2 Reliability Controls . . . . .	15
4.1.3 Distribution of Modes of Failure . . . . .	16
4.1.4 Failure Rate Ratios . . . . .	18
4.1.5 A New Approach to Reliability . . . . .	18
4.1.6 Experimental and Conceptual Bases to the Approach . . . . .	19
4.1.7 Accelerated Testing . . . . .	21
4.2 Failure Factor Model for Analysis and Prediction of Component Reliability. . . . .	31
4.2.1 Basic Formulation of Failure Factor Approach. . . . .	33
4.2.2 Cautions . . . . .	34
4.2.3 Present Formulation: Four Failure Factors . . . . .	35
4.2.4 Computation of Failure Rates and Weightings of Failure Factors . . . . .	37
4.2.5 Summary and Discussion . . . . .	44

Paragraph	Page
4.3 Surface Studies: Electronic Material and Processing Characterization by the Electrical-Frictional Probe. . . . .	45
4.3.1 Apparatus and Early Results . . . . .	45
4.3.2 Surface and Volume Properties Measured by the Electrical-Frictional Probe . . . . .	45
4.3.3 Surface Investigation With Voltage Applied on Probe . . . . .	46
4.3.4 Use of the Electrical-Frictional Probe Electrical Trace in Examining Fabrication Techniques, Effects of Water Spot. . . . .	48
4.3.5 The Possibility of Precise Depth Measurement. . . . .	50
4.3.6 The Electrical-Frictional Probe Is a Nondestructive Test for Defects. . . . .	53
4.4 Surface Studies: Supplementation of Electrical Frictional Probe Information by Stick-Slip Measurements . . . . .	55
4.4.1 The Stick-Slip Relaxation Cycle . . . . .	55
4.4.2 IBM 7090 Computer Analysis of the Stick-Slip Relaxation Cycle - Initial Results . . . . .	56
4.4.3 Use of the Stick-Slip Cycle Measurements to Supplement the Surface Information Yielded by the Electrical Frictional Probe . . . . .	70
4.5 Surface Studies: The Nonuniformity and Aging of a Semiconductor Surface, Studied by Photovoltaic Response . . . . .	70
4.5.1 Apparatus. . . . .	70
4.5.2 Variation of Photovoltaic Response With Radius on Wafer. . . . .	72
4.5.3 Response to Chopped Light - Fresh Surface . . . . .	73
4.5.4 Response to Chopped Light - Aged Surface. . . . .	74
4.6 Surface Studies: Use of the Photovoltaic Effect for Study of Chemical Processes on Precise Locations of Semiconductor Surfaces . . . . .	75
4.6.1 Decrease of Initial Photovoltaic Response as a Function of Aging . . . . .	75
4.6.2 Effect of Chemical Treatments - Initial Results . . . . .	77
4.7 Chemical Study of Etching Processes by Use of the Photovoltaic Response . . . . .	79
4.7.1 Initial Sample Preparation . . . . .	79

Paragraph	Page
4.7.2 Design and Carrying Out of Experiment. . . . .	82
4.7.3 Procedures in Photoresponse Measurement. . . . .	86
4.7.4 Responses From Lapped Surfaces . . . . .	89
4.7.5 Responses From CP-4 Etched Surfaces - Effect of Etch Time. . . . .	91
4.7.6 Responses From HF-HNO <sub>3</sub> Etched Samples . . . . .	93
4.7.7 Responses From Superoxol Treated Surfaces . . . . .	97
4.7.8 Responses From CP-3 Etched Surfaces. . . . .	99
4.7.9 Analysis of Equivalent Circuit. . . . .	103
4.8 Dependence of Photovoltaic Response Upon Pressure . . . . .	107
4.8.1 Pressure Effects on Electronic Components . . . . .	107
4.8.2 Apparatus and Experimental Method. . . . .	107
4.8.3 Effect of Contact Pressure on Photoresponse of P-Germanium. . . . .	107
4.8.4 Effect of Contact Pressure on Steady State Photo-EMF . . . . .	107
4.8.5 Effect of Temperature Change on the Pressure Variation of the Photo-EMF . . . . .	112
4.8.6 Implication. . . . .	113
4.9 Surface Studies: Low Energy Electron Beam Scanning of Transistor Surfaces . . . . .	115
4.10 Surface Studies: Attempt to Map Charge Distributions on Semiconductor Surfaces . . . . .	117
4.10.1 Nature and Effects of Charge Distributions. . . . .	117
4.10.2 Techniques . . . . .	117
4.10.3 Use of Dispersions. . . . .	118
4.10.4 Use of Charged Powders . . . . .	118
4.11 Volume Studies: The Incidence of Cracks, Visible or Sub-visible, in Semiconductor Materials . . . . .	123
4.11.1 Apparatus Modifications . . . . .	123
4.11.2 Sample Displacement Cycle . . . . .	123
4.11.3 Sample Characteristics and Preparation . . . . .	125
4.11.4 P-N Junction Experiments. . . . .	129

Paragraph	Page
4.11.5 Ohmic Junction Experiments . . . . .	129
4.11.6 Variation of Position of Center Lead . . . . .	129
• 4.11.7 Fatigue Experiments . . . . .	130
4.11.8 Elevated Temperature Experiments . . . . .	132
4.11.9 Visible and Subvisible Cracks in Semiconductor Materials . . . . .	132
4.11.10 Elevated Temperature Results . . . . .	137
4.11.11 Conclusions . . . . .	139
4.12 Volume Studies: Utilization of the Electrical-Frictional Probe for Volume Studies of Semiconductor Materials . . . . .	141
4.13 Transistor Failure Caused by Surface Charging . . . . .	141
4.13.1 Failure From Charging by Application of Ions to the Transistor Surface . . . . .	144
4.13.2 Charging by Ultraviolet Light . . . . .	145
4.13.3 Failure Resulting From Transistor Vibration or Accelera- tion: Charging by Frictional Contact With Loose Desiccant Particles . . . . .	147
4.13.4 Failure Resulting From Nonoverload Steep Voltage Pulse . . . . .	147
4.14 Specific Failure Modes Related to Fabrication and Process- ing Techniques: Liaison and Correlation With Product Reliability Group . . . . .	149
4.15 The Effect of Carrier Diffusion in Semiconductor Materials . . . . .	155
4.15.1 Introduction . . . . .	155
4.15.2 General Formulation . . . . .	156
4.15.3 The Transients Resulting From the Diffusion Component of the Current . . . . .	165
4.15.4 Effect on Charge Carrier Distribution . . . . .	168
4.15.5 Equivalent Circuit . . . . .	169
4.16 Failure in Solid State Devices From Internal Heat Generation . . . . .	171
4.16.1 Introduction . . . . .	171
4.16.2 Dielectric Loss From Conduction and Diffusion . . . . .	171
4.16.3 Frequency Regions of Loss . . . . .	176

Paragraph	Page
4.16.4 Average Power . . . . .	176
4.17 Failure in Thin Films at Bends or Steps in Substrate . . . . .	179
4.17.1 Experimental Procedures . . . . .	180
4.17.2 Observations and Conclusions . . . . .	184
4.18 Multiple-Parameter Transistor Transient Overload Study . . . . .	185
4.18.1 Transistors Used and Experiment Design. . . . .	185
4.18.2 Types of Overload and Test Measurements. . . . .	186
4.18.3 Test Results . . . . .	190
4.18.4 Analysis of Results . . . . .	191
4.19 High-Energy Radiation Induced Failure in the Solid State - Study of Ferrites Using Mossbauer Effect . . . . .	195
4.19.1 Introduction . . . . .	195
4.19.2 Experimental Work . . . . .	208
4.19.3 Discussion of Results . . . . .	225
4.19.4 Significance . . . . .	235
4.20 High-Energy Radiation Induced Failure in the Solid State: Electron Damage to Capacitance and Particle Detection Capability of Si Diodes . . . . .	237
4.20.1 Purpose and Significance . . . . .	237
4.20.2 Scientific Background to the Measurements . . . . .	239
4.20.3 Irradiation and Measurement . . . . .	243
4.20.4 Results . . . . .	253
4.20.5 Summary of Radiation Mechanism Investigation and Significance . . . . .	265

## 5. REFERENCES

References . . . . .	267
----------------------	-----

## DISTRIBUTION LIST

Distribution List. . . . .	283
----------------------------	-----

## LIST OF APPENDIXES

Appendix	Page
I     Equations of Motion for the Flexure Test Apparatus . . . . .	271
II    Estimation of Error in Capacitance Measurements . . . . .	277

# LIST OF ILLUSTRATIONS

Figure		Page
1	Device Response to Increasing Stress . . . . .	23
2	Weighting Factors for System A . . . . .	42
3	Weighting Factors for System B . . . . .	43
4a	Bull's-Eye Wafer Cut in Half . . . . .	47
4b	Typical Response to Changes of Material Composition . . . . .	47
5	Circuit Arrangement Used in Surface Investigation . . . . .	48
6	Wafer With Water Drop Flaw and Slip-Stick Response Across It . . . . .	51
7	Magnified View of Stained Surface Flaw . . . . .	51
8a	Successive Traces From Defective Region of Figure 6. Upper Traces in Each Picture Are Mechanical Drag; Lower Traces Are Electrical. No Applied Voltage . . . . .	52
8b	Trace Over Same Region as in Figure 7a. With Voltage Applied to Probe. Note Smaller Amount of Detail on Electrical Trace . . . . .	52
9	Schematic Diagram of Samples on Temperature Gradient Region of Furnace . . . . .	53
10	Similarity Between Repetitive Traces . . . . .	53
11	$\phi$ the Normalized Force at Breakfree vs the Duration of the Stick-Slip Cycle Where $\lambda$ Is Greater Than 1 . . . . .	58
12a	Composite of $\phi$ vs $\theta$ Pairs That Yield a Stick-Slip Relaxation Cycle . . . . .	59
12b	Stick Observed as a Restoring Force Builds Up Nonlinearly . . . . .	59
13	Existence Regions and Forbidden Regions of Stick-Slip Solution . . . . .	60
14	Repetitive Contacting Apparatus . . . . .	71
15	Response of Contact With Different Points on Surface . . . . .	73
16	Photo-EMF Response Decay Rate for Extrinsic Germanium. . . . .	76
17	Germanium Wafer Sectioning Scheme. . . . .	80
18	Sketch Showing Potting of Samples. . . . .	81
19	Sketch of Finished Potted Sample . . . . .	82
20	Sample Measurement Areas . . . . .	87

Figure		Page
21	Photoresponse Waveform From Lapped Surface. . . . .	89
22	Photoresponse Waveform From CP-4 Etched Surfaces . . . . .	91
23	Photoresponse Waveform From CP-4 Etched Surfaces After 30-Second Etch . . . . .	92
24	Photoresponse Waveform From HF-HNO <sub>3</sub> -1 Etched Surface After 20-Second Etch (70-Hour Desiccation Interval) . . . . .	94
25	Photoresponse Waveform From HF-HNO <sub>3</sub> -1 Etched Surface After 190-Second Etch. . . . .	95
26	Photoresponse Waveform From HF-HNO <sub>3</sub> -1 Etched Surface After 190-Second Etch Showing Inversion After Long Time Interval . . . . .	96
27	Photoresponse Waveform From Superoxol Treated Surface . . . . .	98
28	Photoresponse Waveform From Superoxol Treated Surfaces . . . . .	99
29a	Photoresponse Waveform From CP-3 Etched Surface. . . . .	100
29b	Photoresponse Waveform From CP-3 Treated Surface . . . . .	101
30	Photoresponse Waveform From CP-3 Etched Surfaces . . . . .	102
31	Photoresponse of Waveforms From Lapped Surfaces . . . . .	104
32	Equivalent Circuit of Experimental Setup . . . . .	105
33	Equivalent Circuit, Including the CRO . . . . .	106
34	Effect of Repetitive Pressure on Photoresponse of 40 Ohm-CM P-Germanium . . . . .	108
35	Change in Photo-EMF With Repetitive Contact. . . . .	109
36	Effect of Repetitive Contact Accompanied by Coordinated Chopped Incandescent Light . . . . .	110
37	Response With Coordinated Chopped Incandescent Light and No Actual Contact. . . . .	111
38	Beginning and End Results of Tests on Thermal EMF From Ohmic Junctions. . . . .	112
39	Voltage Response Caused by Dynamic Stress (by Repetitive Contact Applied Perpendicularly) to Ohmic Contact on Surface of N-Silicon . . . . .	113



Figure		Page
40	Voltage Response of Combined Dynamic Stress and Incandescent Light Upon Ohmic Contact on Surface of N-Silicon . . .	114
41	Apparatus for Charged Powder Technique . . . . .	119
42	Results of Cycle of Flexure-Charge Apparatus . . . . .	124
43	N-Silicon Dendrite Web Sample Schematic Diagram and Equivalent Circuit . . . . .	126
44	N-Silicon Dendrite Web Electrical Representation . . . . .	127
45	Sample Mount . . . . .	128
46	Illuminated P-N Center Junction Sample . . . . .	129
47	Ohmic Center Junction Sample . . . . .	130
48	Typical Electrical Responses of Samples Subjected to Fatigue . . . . .	131
49	Typical Electrical Responses of Samples Subjected to Fatigue . . . . .	133
50	Pictorial Summary of Fatigue Experiment Results . . . . .	134
51	Typical Junction Area Damage Resulting From Repetitive Stressing . . . . .	135
52	Pictorial Summary of Elevated Temperature Experiments . . .	138
53a	Ions and Air on Surface of a Transistor . . . . .	142
53b	Separate Charging of Emitter and Collector . . . . .	143
54	Longwave UV on Surface of Alloyed Junction Transistor . . . . .	146
55	Effect of Loose Desiccant Under Vibration . . . . .	148
56	Circuitry for Pulse Charging . . . . .	149
57	Microscopic View of Opened Diode . . . . .	151
58	View of Diodes Failed During High Ambient Heat . . . . .	152
59	Electric Fields in Vicinity of Sample . . . . .	157
60	Model for Transient Conduction-Diffusion of Carriers . . . . .	159
61	Equivalent Circuit for Conduction-Diffusion in a Semiconducting Material . . . . .	169

Figure		Page
62	Dependence of Dielectric Constant on Relative Importance of Diffusion and Conduction . . . . .	174a
63	Dependence of Maximum $\epsilon''$ and $\delta$ on $r$ . . . . .	174b
64	Important Frequency Regions of Loss, $r = 10^4$ . . . . .	176a
65	Important Frequency Regions of Loss, $r = 1$ . . . . .	176a
66	Important Frequency Regions of Loss, $r = 10^{-3}$ . . . . .	176b
67	Design of Magnetic Film Memory Plane . . . . .	181
68	Stress Test Circuits . . . . .	187
69	Block Diagram of Mössbauer Velocity Spectrometer . . . . .	202
70	Energy Level Diagram for $\text{Fe}^{57}$ Nucleus Showing Zeeman Splittings (A, B) Quadrupole Interaction ( $\epsilon$ ) and Center Shift . . . . .	211
71	Spectrum of $\text{K}_4\text{Fe}^{57}(\text{CN})_6$ With Cr Source. . . . .	216
72	Plot of Mössbauer Spectra, Run 439, BV13 . . . . .	217
73	Plot of Mössbauer Spectra, Run 447, Indox V Oriented . . . . .	218
74	Plot of Mössbauer Spectra, Run 523, BV13 After $10^{11}$ Rad. . . . .	219
75	Plot of Mössbauer Spectra, Run 498, BV25 Oriented and Magnetized. . . . .	220
76	Plot of Mössbauer Spectra, Run 529, BV25 Oriented and Magnetized, After $10^{11}$ Rad . . . . .	221
77	Plot of Mössbauer Spectra, Run 509 . . . . .	222
78	Plot of Mössbauer Spectra, Run 515 . . . . .	222
79	Plot of Mössbauer Spectra, Run 518 . . . . .	223
80	Variation of Hf With Temperature, Westinghouse Hexagonal Ferrite . . . . .	229
81	Variation of Saturation Magnetization With Temperature . . . . .	230
82	View of Target Box Following Irradiation, Showing Swollen Surface Barrier Detectors . . . . .	244
83	Simplified Sketch of Measurement Circuitry. DC Blocking Capacitors, Calibration Inputs, and Switching Details Are Omitted. . . . .	246
84	Measurement Circuitry Included in Target Chamber (Dashed Outline) . . . . .	247

Figure		Page
85	Capacitance vs Bias of Abrupt Junction Si Diode, by Two Methods (Break in Plotted Line Corresponds to the Substitution of One Voltmeter for Another). . . . .	251
86	Dependence of Capacitance on Applied Bias at Several Dosages for Detector 2A. The Dots Indicate Pulse Division Measurements; the Open Circles Represent $\alpha$ -Particle Data. Each Successive Curve Is Shown Displaced Upward by a Factor of 2. . . . .	255

#### LIST OF TABLES

Table		Page
1	Transistors: Comparison of Verified Failures . . . . .	17
2	Tests With Exposure to Light . . . . .	49
3	Computed Parameters . . . . .	61
4	Germanium Etch Formulations . . . . .	85
5	Photoresponse Measurements . . . . .	88
6	Time vs Photoresponse . . . . .	97
7	Experimental Charge Mapping Materials . . . . .	121
8	Transistor Overload Tests, Initial Measurements . . . . .	186a
9	Transistor Overload Test, Parameter Changes From Overload. . . . .	186c
10	Mössbauer Spectra Obtained in This Program . . . . .	205
11	Magnetization of Small Ferrite Rods for Electron Irradiation. . . . .	215
12	Configuration and Spin Direction of Iron Ions in the Magneto-plumbite Structure . . . . .	227
13	Change in Capacitance Versus Bias Voltage Relationship of 10,000 Ohm-CM Detectors With Electron Dosage. B and m Are Constants of the Equation $C = B(V + 0.55)^{-m}$ , Where V Is the Applied Bias in Volts. (Values Given in Parenthesis Are Less Reliable.) . . . . .	256
14	Change in Capacitance Versus Bias Voltage Relationship of 1000 Ohm-CM Detectors With Electron Dosage. B and m Are Constants of the Equation $C = B(V + 0.55)^{-m}$ , Where V Is the Applied Bias in Volts. (Values Given in Parenthesis Are Less Reliable.) . . . . .	257

Table	Page
15 Change in Capacitance Versus Bias Voltage Relationship of 100 Ohm-CM Detectors With Electron Dosage. B and m Are Constants of the Equation $C = B(V + 0.55)^{-m}$ , Where V Is the Applied Bias in Volts. . . . .	258
16 Change in Some Counting Characteristics With Electron Dosage . . . . .	261

## 1. INTRODUCTION

Under the sponsorship of the Rome Air Development Center, Westinghouse Electric Corporation, Air Arm Division, is conducting a study to identify the particular mechanisms involved in the failure of electronic materials and electronic parts, and to accumulate an understanding of their modes of operation. This report presents the work of the fourth quarter and summarizes the work of the other three quarters of the study of failure mechanisms in electronic materials and components, and the manner in which the results may be used to improve the reliability of military systems.

The work was directed toward finding causes or mechanisms of failure, and utilizing this knowledge of the physical processes and behaviors to decrease component failures; it was not directed toward finding modes of failure such as broken leads, dielectric breakdown, or punchthrough, since these have been studied extensively by others.

During the four quarters of the study, there have been identified three mechanisms of transistor failure previously unrecognized or insufficiently understood, and their manner of affecting component performance has been shown together with recommendations for avoiding such deleterious effects. These are: transistor failure because of surface charging of the passivating layer, because of nonoverload steep pulse gradients during use, and because of loose desiccant in the transistor during vibration or acceleration of the system containing the transistor. A number of other possible mechanisms have been investigated.

To obtain clues as to previously unsuspected mechanisms of failure, a study was made of each of two military data processing systems throughout a full year of the manufacturing, assembly, and test phases. Systems reliability in this phase of the total cycle has not previously been investigated.

The systems were medium and highly complex respectively, and involved different physical processes and manners of data handling. Components in them included samples from each of the major manufacturers of components of quality suitable for military systems, and therefore the study is representative of similar results to be anticipated on other systems. Types and distributions of failures for each component were obtained for each system. The percentage distribution of responsibility for failure, and indicated by types and modes of failure, was derived as among: manufacturing, design, test, supplier, and miscellaneous.

Distributions of failure of various component types implied the operation of certain identical failure-producing processes or combinations of mechanisms, including those which were related to personnel error. A "failure factor" analysis for the study of reliability in military systems was developed as an addition to standard statistical analysis, permitting rapid conclusion on procedures favoring reliability. It also aids the prediction of component life under various environments, or the identifying of types of components, processing techniques, or system designs which will increase systems reliability.

Some transistors which had been tested after removal because of systems malfunctioning, and shown to have failed, were now found to have recovered and to exhibit the specified performance. In a number of others, minor treatment such as light surface etching would restore the performance. Such spontaneous, or induced, restoration of nearly original characteristics shows that a fuller knowledge of the physical behavior of failure mechanisms from the original raw materials to the final delivered military system can pay immediate dividends in increased reliability.

Three new types of apparatus were developed for studying surfaces of electronic components, based on the interaction between chemical, mechanical, and electrical parameters of materials. Each furnishes new information, and one should be of considerable value both to the study of mechanisms

of failure, and to the improvement of fabrication processes to enhance reliability. Examples of the sensitivity and use of this apparatus are given. It is a nondestructive test for defects in solid state devices which promote failure.

To obtain additional information about surfaces from this apparatus, the interaction between the surface and the sliding probe has been analyzed theoretically. The type of information which can be obtained from the time-dependent drag of the probe was described in Quarterly Report 3. The solution for the stick-slip behavior of the probe has been obtained and a mass of computer calculations partially analyzed.

The nature of the aging process of a semiconductor surface has been examined by a technique that enables identification of the aging at individual points on the surface. The conclusion follows that aging occurs differently at contiguous locations; maximum reliability may therefore be obtained in solid state devices through particular changes of fabricational processes. An unsuspected variation of the electrical properties of semiconductor surfaces near wafer edges was discovered; this calls for modification of dimensional design in microcircuitry in the vicinity of the edges. Experiments performed throw light on the nature of the chemical processes responsible for aging of the surface, and their relation to the chemical treatments given to material during its preparation.

Electrical characteristics of semiconducting materials have been found to vary noticeably under pressure. This discovery has implications in the use of components under acceleration or pressure. The effect occurs only during applied pressure. Present component design avoids harmful effects from this cause, but changed fabrication or design could cause it to appear.

It was discovered that the stressing of semiconductor materials which may occur during scribing, grinding, or polishing can produce subvisible cracks which alter the electrical performance of the solid state device. The sum total electrical effect of a series of junctions and connections, ohmic or otherwise, made according to present fabricational techniques can introduce

unbalanced thermal sensitivity so that during temperature change the device performance is modified by transients which persist until final thermal equilibrium is attained. This also would not normally be detected during routine tests.

The effects of internally generated heat on device performance and the way in which this factor can be utilized to locate regions of probable failure were described in Quarterly Report 3. Various types of behavior contribute to the generation of heat, and a number of them were considered; an example is given. It follows that thermal measurements, either by direct conduction or by infrared mapping of surfaces as a function of time, will be valuable in the detection of likely failures. However, it is both known and has been shown here, that not all failure mechanisms are related to the production of heat, and therefore other methods of investigation must be used as well.

The failure of thin films at bends or steps in a substrate and a number of other types of failure have been investigated individually, up to the point at which their maximum benefit to the study of mechanisms of failure has been attained. A limited but detailed multiple-parameter study of transient overload mechanisms of failure and overload during on-off condition of commercial transistors is reported.

A major amount of time has been spent in investigating the effects of high energy radiation, within the energy range of nuclear radiation, upon solid state devices. This was done primarily by two methods: the sensitive Mössbauer effect was used to look for failure mechanisms in ferrites, and the anomalous behavior of the effect of high energy radiation upon the capacitance of a silicon diode was investigated in considerable detail.

Of the results from the work described, those most important at the present time to reliability are probably: the new types of failure discovered which undoubtedly are occurring in present military systems, the new information obtainable from the surface of materials by methods developed under the contract and its relation to failure, the information with respect to aging



of semiconducting surfaces, and the effects of chemical processing techniques, the failure factor method of analysis, and the ways in which component fabrication and production can be improved. The other work described should be of considerable value later, but it is still in the developmental stage and to bring out its ultimate value requires some additional experimentation.

## 2. CONCLUSIONS

The following conclusions may be drawn from the results in the text of this and the three earlier reports:

a. Transistors may fail in use through various mechanisms, a number of which are not presently provided against: electrostatic charging of the passivating layer during manufacture or use, the effects of steep pulses of a magnitude less than overload, frictional effects of loose desiccant or other material within the case, major pressure changes resulting from environmental change or acceleration.

b. In a number of cases, "failed" transistors will recover over a period of time, or the cause of failure is sufficiently slight so that they can be restored by a slight etch or other treatment of the surface.

c. Transistors of all fabrication types, from five major manufacturers of transistors of the high quality necessary for military systems use, upon being tested by short period overloads of various types, showed excellent performance, for the main part being unaffected permanently or transiently by the overload stresses. Voltage stressing and power stressing produce roughly the same results, the major effect being noticeable in low or high frequency  $h_{fe}$ . Only continuous operation in the reverse breakdown region (which would be expected to cause damage) appears to give major characteristic changes in parameter values. High voltage turn-on pulsing, excessive power dissipation in the collector breakdown region, and continuous operation in the reverse breakdown region of the emitter-base junction appear to be the most severe stresses.

d. Analysis of the electronic component failures during a year's assembly and test of each of two military data processing systems supports

the view that similar groups of mechanisms are involved in the failures. By grouping these into failure factor categories, it becomes possible from the analysis of reliability experiments to identify particular portions of individual components whose design and processing should be looked at, in order to increase the reliability of the components, and therefore the system. The failure factor approach here developed appears to be an aid to the present statistical analysis of failure.

e. During this assembly and testing phase, it was shown that:

(1) The failure rates in system A were one-seventh or less those in system B because in system A special attention was paid to the removal of causes for failure, and primarily because of the incorporation of design reviews and the steps which they initiated.

(2) The distribution of responsibility for failures observed showed that the primary responsibility categories by components were: transistors - supplier and manufacturing; diodes - system design and supplier; capacitors - manufacturing and testing; resistors - testing.

f. Semiconducting materials, at various stages in the processing of solid state devices, cannot be regarded as either uniform or constant in electrical or chemical state. Even with careful processing, contiguous regions may be covered by quite different chemical compounds or be in quite different energy states. Except immediately (or a considerable time) after a particular etch or other chemical processing (and therefore particularly during the period in which further processing is likely to take place), portions of the surface are separately in transient states between that resulting from the last processing, and the final aged state.

g. The result of etching a semiconductor surface with different materials is a radically different surface chemically. The surface cannot be regarded as just a surface "from which the oxide has been removed." The difference in the chemical nature of surface regions, and of adsorbed substances from different types and techniques of etching, has both materials and electrical significance.

h. Routine and accepted processing techniques such as scribing, grinding, or bimetallic connection welding or attachment can create stresses sufficient to cause cracks which alter the electrical behavior of a semiconductor material. These cracks range in size from visible to subvisible; the latter show self-healing when stress is removed, but may be demonstrated by the application of stress. Since the cracks can be demonstrated, it is likely that such processing techniques also create commonly described defects in materials, such as dislocations. Elevated temperature increased the rate of formation of the cracks during periodic applied stresses, rather than promoting annealing.

i. The effects of errors in processing procedures, and the presence of either chemical or structural defects in the material or device can be pictured precisely by the "electrical-frictional probe" apparatus developed under this contract. A detailed description of the surface can be obtained through the study of the individual traces - electrical, frictional drag, load, and the stick-slip behavior. The chemical nature of the surface is indicated by the first, the geometrical and structural nature by the other two, and the rate of adhesion buildup by the stick-slip.

j. The "electrical-frictional probe" can furnish information either about the surface, or about the volume of the material directly below the surface, depending upon circuit parameters and environmental parameters used. By means of this apparatus, it is possible to follow with precision the changing nature of the material as the probe travels over a variety of p- and n-type surfaces; there is an indication that it measures the degree of heterogeneity of the surface remaining after a supposedly uniform diffusion or oxidation.

k. The nature of the chemical compounds developing at specific isolated points on the surface can be investigated by the techniques used in the present work.

l. The properties of semiconducting materials depend upon the curvature or geometry of the interface between their edge and air, and upon the pressure of contact with other materials. Unsuitable design can cause failures in solid state devices as pressure accumulates with changing environmental conditions, mechanical, thermal, or other.

m. Surface studies by means of repetitive contacting yield characteristic waveforms whose detailed shape is dependent upon the materials of the probe and of the surface. The waveform and contact phenomena, particularly the charging curve, can be of value in surface studies.

n. Thin films passing over sharp edges of steps were, in the present experiments, found to crack and separate primarily because of lack of adhesion, and secondarily because of any stresses maximizing at the edge of the step. Reliability of the device is therefore promoted by increasing the adhesion.

o. Lead connections and internal interconnections in ohmic or junction type solid state devices, show performance variability with changing temperature, and the sum of all these variations results in a drift or performance change of the device which varies with time until temperature equilibrium is again established. To overcome this, it is necessary to chemically (metallurgically) and electrically design internal connections as carefully as device junctions or circuit components are designed.

p. The nature of heat losses in materials can be used for obtaining information as to the processes and regions connected with failure. The well developed methods by which loss factor and dielectric constant can be measured can be utilized directly in this work. Certain identified types of losses can be directly sought, and other types can be inferred from the measurements.

q. The loss due to each of these measurable loss factors is of importance primarily in a particular frequency region. These frequency regions can be identified and systems design can be so planned as to avoid excessive

losses, and therefore avoid heat production and reduce the number of mechanisms conducive to failure in the military use of the system.

r. One example of a new type of loss connected with the solid state behavior of the semiconducting material is developed theoretically and the dependence of the frequency regions at which excessive heat production would be expected is indicated.

s. The result from the Mössbauer studies of high energy electron irradiation of ferrites confirms magnetic measurements that the total irradiation used (up to  $10^{11}$  rads) produces little measurable change in the composition or chemical structure of the materials studied. Any changes which may be observed in the electrical properties of the ferrite types studied, as a result of electron irradiation, must be caused by other than gross structural changes.

t. The capacitance of silicon diodes increases significantly with the increase of high energy irradiation, for high resistivity base material, and remains approximately constant for low resistivity base material. Leakage current increases, high frequency noise levels increase, and little annealing appears to take place. Indications were obtained that a defect energy level existed or was activated in the forbidden region.

### 3. RECOMMENDATIONS

It is recommended that:

a. The large amount of information which can be furnished by the "electrical-frictional probe" apparatus with respect to solid state devices, materials, and surfaces be more fully applied to the elucidation of new mechanisms of failure, and the detailed study of the behavior of known ones. Also that it be utilized in improving fabrication techniques to promote reliability of the completed electronic component.

b. That accelerated testing procedures be examined for the degree to which the reliability and failure results from them agree with the results from normal operation.

c. A number of specific processes used in solid state and microcircuit technology, particularly those in which success is a matter of state of the art, cause quite different results when techniques, concentrations, or methods of performance are varied by reasonable amounts. Such processes and techniques should be examined more fully to bring out the nature of their dependence upon the parametric variables connected with device processing.

d. In the manufacture of transistors, diodes, and microcircuit devices, there should be included, in addition to the present design and reliability considerations, provision that passivating layers will not become charged or will lose such charge rapidly, that no possibility exists of material breaking or becoming loose and rubbing over other surfaces, and design to minimize any harmful effects of steep pulses upon the performance of the device.

e. Systems design include the consideration of transient effects occurring in operation and at turn-off and turn-on, with special reference to

stresses imposed on components and the resulting degradation of performance.

f. Systems requirements upon devices involve more than is included in present specifications, since different components meeting specifications equally well can exhibit quite different reliability and performance. The nature of the additional requirements which should be incorporated into specifications to ensure best performance should be examined, and additional requirements included in the specifications.

g. Study be undertaken of the way in which instrumentation developed under the current contract can contribute to increased reliability of systems using components subjected to nondestructive tests.

h. In any further work on semiconductor materials under this program, the chief emphasis be placed upon the "electrical-frictional probe" and periodic contacting apparatuses. The flexure apparatus should be used primarily with more insulating materials.

i. Additional studies be undertaken on the development of reliability analysis methods which will permit rapid and accurate prediction of anticipated life, and of types of failure to be expected, and will identify where precautions should first be added in order to improve reliability most rapidly. As a first contribution to this end, a study of failures in the fabrication and packaging environment, and in field use, should be undertaken.

j. In order to further check the value of the "failure factor" approach to predicting reliability of components, and to implement and extend the advantages which can be gained from this technique, a program be set up to fabricate specific parts of devices (especially microelectronic devices) to give more meaningful values of the weighting factors under different environments and with different types of components, and to extend the range of its applicability, so that numerical calculations can be made of predicted reliability and phases of component structure requiring improvement.



## 4. DATA AND DISCUSSION

### 4.1 CAUSES OF FAILURE DURING MANUFACTURE AND TESTS OF MILITARY SYSTEMS

#### 4.1.1 Systems Analyzed

Two complex military data processing systems were analyzed in detail for the types and causes of failure of electrical components during 1 year's manufacture and test of each, before ultimate deliveries to the user. System A is more complex and sophisticated than is system B, containing over nine times as many transistors and capacitors, and over seven times as many resistors as does system A. The circuits are more sophisticated, and every attempt has been made to make the system as reliable as possible by upgrading the reliability of components (using HI RI components wherever possible, and a number of CPV08 and CPV09 capacitors), and in other ways.

#### 4.1.2 Reliability Controls

All systems failures on the manufacturing floor are detected at any one of five levels of testing by Quality Control testers. Engineering analysis usually verifies whether the component actually was faulty, by tests on it after removal from the system. Stringent controls are exercised so that no substitution of a component can be made without turning in the faulty component and initiating a series of quality control tests.

The components used are not only chosen initially from the best available, but a complex procedure for ensuring compliance with military specifications and reliability is incorporated into the procurement and use of the components:

- (1) An independent set of components engineers qualifies each component with respect to its design drawing before it can be used;
- (2) each part is also qualified as a part of its subassembly through exhaustive tests;
- (3) full specifications are drawn up and agreement is obtained from the manufacturer that his product will meet these rigorous (rather than the

usual production) specifications; (4) 33-percent additional parts of each type are purchased and the extras are tested to destruction; and (5) if the failure rate is too high, the part must be requalified by a complicated procedure which usually involves conferences with the vendor's upper management, and improvements initiated by them in their own factories.

Although the data on component failure obtained from these systems are much more detailed than would usually be possible, they list the failure mode rather than the mechanism causing the failure; the discrepancy report lists the external symptoms of what went wrong with the part.

#### 4.1.3 Distribution of Modes of Failure

These modes of failure have been analyzed to determine the relative frequency of types of failure, and therefore what malfunctioning should receive the greatest corrective attention. Also, a number of the failed components have received detailed autopsy in the laboratory to determine the mechanisms involved in the failure. From these data, and the experiments which followed, several mechanisms have been identified, certain of them apparently not previously suspected.

For each of four types of components, there was obtained the distribution of modes of failure in each of the two systems. Table 1 shows the distribution of types of failures in transistors.\*

From the table it may be seen that the majority of transistors failed because of shorted junctions. In system B, C-E shorts were predominant, while in system A, B-E shorts were predominant. Since many of the transistors used in both systems were of similar types, these percentage figures must represent the different stress levels the transistors were subjected to in the two systems. To obtain more data on the variation of transistor failures with B-E stress and C-E stress, the study described on paragraph 4.18 below was undertaken.

---

\* Much additional data is given in Quarterly Reports 2 and 3.

**TABLE 1**  
**TRANSISTORS**  
**COMPARISON OF VERIFIED FAILURES**

Type of Part Failure	System B		System A	
	No.	Percentage	No.	Percentage
Shorted	4	4.7	5	4.2
Shorted C-E	24	27.9	12	10.2
Shorted B-E	2	2.3	28	23.7
Shorted C-B	4	4.7	12	10.2
Shorted All Elements	4	4.7	6	5.1
Shorted B <sub>1</sub> - B <sub>2</sub> (Unijunction)	0	0.0	6	5.1
Shorted C-E, Open Base	<u>4</u>	<u>4.7</u>	<u>2</u>	<u>1.7</u>
Subtotals	42	49.0	71	60.2
Open	5	5.8	1	0.8
Open C-E	2	2.3	5	4.2
Open B-E	1	1.1	4	3.4
Open B	1	1.1	7	5.9
Open E	2	2.3	2	1.7
Open C	<u>2</u>	<u>2.3</u>	<u>0</u>	<u>0.0</u>
Subtotals	13	14.9	19	16.0
Low Gain	4	4.7	12	10.2
Low Beta Voltage	3	3.5	4	3.4
Degraded Electrically	14	16.3	4	3.4
Failed (more details not known)	6	7.0	0	0.0
Broken	2	2.3	3	2.5
Part OK, but source of system failure	<u>2</u>	<u>2.3</u>	<u>5</u>	<u>4.2</u>
TOTALS	86	100.0	118	99.9

#### 4.1.4 Failure Rate Ratios

Besides absolute failure rates for each component in each system, the failure rate ratios between components were computed. The ratio of the failure rate of transistors to that of diodes was close to 0.7 in both systems and similar ratios (though less significant statistically) emerged for the ratios with other components. Both absolute failure rates and failure rate ratios are given in Quarterly Reports 2 and 3.

#### 4.1.5 A New Approach to Reliability

The similarity in failure rate ratios implies that the complex mass of failure data is characterized by certain regularities which persist from system to system, at least in the same environment, such as manufacturing and test, or such as field use. This concept has led to the formulation of a new approach to reliability considerations; it regards certain identifiable design or construction characteristics of a component as categories or degrees of freedom to which are related the many mechanisms which may cause failure in the component. For example, the number of leads emerging from a component will affect the number of failures which may be expected from: lead breakage, open circuits because of improper lead attachment or joining, errors in attaching leads to voltage supply sources with subsequent burnout of the component, damage to other components from accidental short of one component by a lead from another component during assembly, the susceptibility to deterioration at point of joining by chemical or other processes such as "purple plague," etc. The categories are here called "failure factors." Some analysis of the failure factors was included in Quarterly Report 3. An extended treatment is given in paragraph 4.2.

The relative values or importances of failure factors in particular components are derived from the experimental data; also there is indicated the method of determining the relative weighting which should be assigned to a particular failure factor. Since a major difference in the two military systems analyzed was the type and reliability of capacitors which were employed in each, a narrow range of failure factor weightings has been derived for capacitors.

#### 4.1.6 Experimental and Conceptual Bases to the Approach

##### 4.1.6.1 Error and Mean Values

In Quarterly Report 2, it was noted that transistors, diodes, capacitors, and resistors each exhibit their own distinct failure rates. These failure rates were shown to be significantly different from each other. The question arises as to the magnitude of errors involved, and the significance of the results. The failure rates represent a mean, and not necessarily the exact value, because of the following:

a. All parts were tested under a wide range of stress conditions.

Stresses employed are not outside the workable ratings of the devices; however, system design considerations, especially in system B, may make full use of the allowable range of stresses.

b. Devices were classified only into major device classifications; each classification contains an unclassifiable distribution between processing variables and types of that component. Failure rates for the device are therefore average rates.

c. The calculation of device failures has included a small number of failures derived from the assumption that those devices which were not tested after being removed from the system would have a proportionate number of failed devices the same as those which were tested. While this assumption is true on the average, it may be somewhat in error in a particular case.

The rates obtained were those in factory assembly and testing, and therefore are more nearly but not exactly in the range of infant mortality rather than the catastrophic failures occasioned by typical useful life tests.

Because of the large numbers of each type of device, over ten thousand of each, the average stress of an average device treated here is a close estimate of the mean of a well-defined distribution of stresses and devices. Comparison of the means is therefore a legitimate procedure, and the conclusion may be made that each of the four group types of devices has a distinct failure rate characteristic of the device.

#### 4.1.6.2 Time Dependence

The consistent use of the constant failure rate to explain device failure is justified mainly on the basis that it is a clearly definable and simple way to set up classifiable equations. In actual practice, failure rates increase with time, which is the reason that a definite time has been chosen in paragraph 4.2 below. The times of failure due to some failure factors (or subfactors) will exhibit a bell-shaped probability distribution. Here, the Weibull distribution\* might more accurately describe the failure factor contributions to device failure. However, the existence of two parameters in the elementary

---

\*The Weibull distribution is described as  $F_r(t) = 1 - e^{-\frac{t^\beta}{a}}$ ;  $R_r(t) = e^{-\frac{t^\beta}{a}}$

The probability density function is  $f_r(t) = \frac{\beta}{a} t^{\beta-1} e^{-\frac{t^\beta}{a}}$ . The failure rate, which for the negative exponential distribution is constant with time, is, for the Weibull distribution,  $\frac{\beta}{a} t^{\beta-1}$  which is an increasing function for all  $\beta > 1$ ,  $a > 0$ . In the case when  $\beta = 1$ , the Weibull reduces to the negative exponential.

Just as the negative exponential is used in paragraph 4.2, the Weibull may be used,  $R_{\text{DEVICE}} = \prod_{r=1}^N \exp \left[ -\frac{t^\beta_r}{a_r} \right] = \exp \left[ -\frac{t^\beta_1}{a_1} - \frac{t^\beta_2}{a_2} - \frac{t^\beta_N}{a_N} \right]$  and equations set up to predict the failure rate of junctions, leads, etc. The new equations would be based not on failure rates and their summation but on a summation of integrals of failure rates:

$$\int_0^t \frac{\beta}{a} t^{\beta-1} dt = \frac{t^\beta}{a}, \text{ i. e., total failures.}$$

failure rate expression shows that much more data would be necessary to obtain the final solution. The incorporation of mechanisms of failure into the equations also promises to be much more complex than in the simple exponential expression.\*

#### 4.1.7 Accelerated Testing

##### 4.1.7.1 Traditional versus Accelerated Testing of Devices for Military Systems

Testing of electronic components individually by specification is insufficient for purposes of use in military systems. Suitable reliability information requires that the components be systems tested, subject to the various stresses encountered when in the system.

Greater complexity is involved in analyzing the reliability data from a systems test than if the items were individually placed on a rack and operated on a preset test schedule. The failure factor method can yield decreased complexity, at least in the use of the data for predictions and reliability evaluation.

Under present day technological progress, the rate of improvement of military systems by design review, by incorporation of new concepts and functions, and by altered military requirements, and the rate of advances in solid state technology are so rapid that when the results are obtained for

---

\*Many papers have been written on the mathematical and empirical aspects of the Weibull distribution. It is difficult, however, to incorporate the Weibull distributions of many different devices into the distribution of the failure time of a system. Of particular importance is when that system no longer has a straight series configuration. For convenience in this report, it has been assumed that all devices exhibit the series configuration with respect to the failure factors; this implies that device operation is contingent on all failure factors. This is not necessarily true. If actual failure of the device requires several failures among the failure factors, failure rates are no longer additive. Such considerations require more complex equations. Stochastic processes can make such equations available, and computers can solve them, if the additional complexity is justified. The use of decision theory and Bayesian techniques can be of considerable help in predicting failure rates on the basis of a short-term life test. This technique may be of importance in precisely determining the effect of failure mechanisms.

a device tested traditionally, both the system and the device may be obsolete. Nevertheless, reliability data are necessary to guide systems design. The answer would seem to be accelerated testing. This, however, introduces some difficulties; the failure factor approach may help overcome the difficulties, and improve the accuracy of reliability predictions.

#### 4.1.7.2 The Failure Factor Analysis as an Aid to Accelerated Testing

Accelerated testing procedures, whether weatherometer tests on paint samples or electrical tests on electronic devices, yield distributions of failures which rarely agree with the results from normal life test, either by distribution among modes or in time. The reasons, among others, include: (1) nonlinearities in the effect of different mechanisms of failure, (2) interdependence of mechanisms of failure so that an increase of one parameter increases the failure due to others, and (3) additional stresses or omitted stresses which accompany any increases in the stresses used.

In solid state materials, and in components and microcircuits made from them, metallurgical, chemical, structural, thermal, mechanical, and electrical effects are combined, and the effects of various types of radiation, including visual and IR ranges, may modify these. Other mechanisms not fully understood undoubtedly also influence component life; as more mechanisms of failure are identified and studied, consideration of their effects can be included in test planning and analysis to improve accelerated testing. However, even before this knowledge is accumulated, the failure factor approach can improve the quality of the information from accelerated testing.

The failure rate of devices from various mechanisms of failure can be expressed by some statistical distribution. For convenience, the exponential distribution is used here, but similar considerations follow for other techniques. From equation 4, page 33, the reliability with respect to a particular failure factor under a given stress environment is

$$R_{\text{DEVICE}} = \exp - (K_r \lambda_r) t.$$



For a given identifiable portion of the device such as lead or surface, the failure factor,  $\lambda_r$ , is corrected to  $K_r \lambda_r$  for the nature of the actual stresses as compared to a normal stress environment. The  $\lambda_r$  is a generalized failure factor under standard stress environment; if  $\lambda_r$  is  $\lambda_L$ , the  $\lambda_L$  is representative of the general overall universe of types of leads for devices incorporated in the system. Depending upon the number and particular leads used in the devices of the system examined, a weighting factor is assigned which is characteristic of that particular system. From the mathematical analysis, there emerges a value for each  $K\lambda$  and one for the weighting factor. The weighting factor is characteristic of the system, the  $K\lambda$ , of the failures due to leads for the particular device under the given stresses. If similar analyses of the system under a number of different stress environments are made, a set of  $K_{jr} \lambda_r$ 's is obtained. Presumably in all these, the  $\lambda_r$  is the same, but the  $K$ 's are different. To illustrate, consider an analysis of a system such as that of system A or system B in paragraph 4.2.4, but depending upon only two failure factors. Under normal stress conditions, which here are assumed to be essentially zero stress,  $K_1 \lambda_1 = 1.6$ ,  $K_2 \lambda_2 = 0.5$ , for the unit of time chosen. An accelerated test is performed on this system. To obtain more rapid failures, the stresses are increased. For present purposes, one stress only (say mechanical vibration or mechanical impact), designated as  $s$ , is considered. The  $K$ 's are therefore functions of  $s$ , and may be written  $K(s)$ . Assume that an analysis equivalent to that for system A or system B has been undertaken for failures in each of two types of components (transistors and diodes), for each stress level, and the values of the  $K \lambda$ 's and weighting factors which result are:

Weighting factors: for  $K_1 \lambda_1 = 0.25$ , for  $K_2 \lambda_2 = 1.1$  : diodes  
for  $K_1 \lambda_1 = 0.80$ , for  $K_2 \lambda_2 = 0.070$  : transistors

Stress, $s =$	0	1	3	5	10
$K_1 (s) \lambda_1$	1.6	3.6	7.7	11.4	21.6
$K_2 (s) \lambda_2$	0.5	0.5	0.6	0.5	0.5

Allowing for experimental error, the second failure factor is unaffected by the increased stress, and the first increases linearly with it.

$$K_1 \lambda_1 = 1.6 + 2s$$

$$K_2 \lambda_2 = 0.5$$

Since the  $\lambda$ 's have been defined to be independent of stresses, the increase in measured failure factors is attributable to the  $K$ 's only; if the nonstress condition is taken as a base reference, for which  $K_j = 1$ ,

$$\lambda_1 = 1.6, \lambda_2 = 0.5, K_1 = (1.6 + 2s)/1.6, K_2 = 1.0$$

The prediction can be made that the reliability of each device at a stress value of seven units will be

$$\begin{aligned} R_{di} &= \exp \left\{ - \left[ 0.25(15.6)(1.0) + 1.1(1.0)(0.5) \right] t \right\} \\ &= \exp (-4.45 t) \end{aligned}$$

$$\begin{aligned} R_{tr} &= \exp \left\{ - \left[ 0.80(15.6)(1.0) + 0.70(1.0)(0.5) \right] t \right\} \\ &= \exp (-12.83 t). \end{aligned}$$

Under normal stress, the reliability would have been:

$$\begin{aligned} R_{di} &= \exp \left\{ - \left[ (0.25)(1.6)(1.0) + 1.1(1.0)(0.5) \right] t \right\} \\ &= \exp (-0.95 t) \end{aligned}$$

$$\begin{aligned} R_{tr} &= \exp \left\{ - \left[ 0.80(1.6)(1.0) + 0.70(1.0)(0.5) \right] t \right\} \\ &= \exp (-1.63 t). \end{aligned}$$

Under normal conditions, therefore, after one unit of time the ratio of transistor-to-diode failure rates would be close to 2.0, whereas under the accelerated test, the ratio would be nearly 54.

Put differently, the exponential coefficient resulting from the first failure factor is, at the stress of seven, 2.9 times as effective as that from the second failure factor, whereas at normal stress the first is only 1.7 times as effective. Such changes in the importance of failure factors are indicated in figure 1, page 28. The fact that the increased failure rate under accelerated testing is accompanied by a change in the distribution of failures as between transistors and diodes is characteristic of an accelerated test.

If the effects of several stresses are to be examined in the accelerated test, it will be necessary to conduct a series of tests in which each of the

stresses is varied independently. Since the results from any one test yield a value which is one of a statistical distribution of values which might be obtained by performing many tests of the same type, it is necessary to perform enough individual tests in each series so that the nature of the distribution and its characteristic parameters can be inferred.

#### 4.1.7.3 Accelerated Test Design

In the computations in paragraph 4.2, four equations were set up using mean values. The four equations were the failure rates for each of four devices, and from them there was calculated an implied value for each of four variables; namely, the failure factors, the  $K \lambda$ 's. The development also showed that weighting factors could be computed which brought the data with respect to capacitors into consistency with the remaining data.

On a very elementary basis, the computed  $K \lambda$ 's could be used directly in making analyses of the failure data, and by inserting them in standard equations, predictions on reliability would be indicated. The question is, how much confidence can be placed in such predictions, or even in the computed  $K \lambda$ 's. The physicist or electronic engineer is satisfied with such experimental values accompanied by a statement of probable error, which he usually regards as so small that it may be ignored. The problem here is a statistical one, in which error is not necessarily small, and confidence limits must be established.

The statistical problem which is faced by the reliability engineer is much more complex. For him, the problem that he is given is a set of equations

$$3K_L \lambda_L + 2K_J \lambda_J + K_V \lambda_V + K_s \lambda_s = K_T \lambda_T = h_T$$

$$2K_L \lambda_L + K_J \lambda_J + K_V \lambda_V + K_s \lambda_s = K_D \lambda_D = h_D$$

etc,

and, not a single experiment which gives the value of  $h_T$ , etc, as in the example given, but a number of experiments which yield a distribution of values of each with a mean  $h_i$  and a certain confidence limit determined by

the distribution, calculable from the sum total of experimental values. From these ranges of the  $h_i$ 's, for example, with a confidence limit of 90 percent

$$2.4 \leq K_T \lambda_T \leq 11.4,$$

$$3.9 \leq K_D \lambda_D \leq 6.8,$$

$$0.01 \leq K_R \lambda_R \leq 0.80,$$

$$0.15 \leq K_C \lambda_C \leq 1.1,$$

he must determine mean values and confidence limits of the  $K \lambda$ 's. The problem is a considerably more difficult one. It is essentially the substitution of functions considered over a range of values of the variable, in place of the constants in the matrix development.

If enough experiments have been performed to permit the representation of each of the  $h_i$ 's by a suitable distribution, the equations may be set up as in paragraph 4.2.4, except that the  $h_i$ 's are not numbers but functional expressions for the distribution. The present analysis has assumed exponential distributions; these are the simplest. Analogous techniques could be developed for other distributions at the expense of considerably greater processing effort. Formal solution of the matrix now yields not a number but a set of functional expressions for each of the failure factor  $K \lambda$ 's. These expressions will not necessarily be typical distributions used in statistical analysis. Either they must be approximated by a suitable type of statistical distribution, through plotting and fitting, or new techniques for working with the new types of functions must be developed statistically. If the former approach is used, another question arises; namely, to what degree are confidence limits changed by the use of the approximation.

To some extent, the difficulties may be mitigated by commencing the analysis with the use of several different possible groups of failure factors. Utilizing the same tests, the results of using each of these groups can be examined to see which group yields the best set of confidence limits. As the preciseness of the results increases, less difficulty can be anticipated from the overall distribution of values.

From the data calculated in paragraph 4.2.4, it is possible for the engineer to predict the reliability of a system. Similarly, it is possible for

him to analyze the results of a set of tests of failure in the system. However, the prediction and the analysis will be characterized by the fact that the user cannot tell how likely any future experiment, or how likely the performance of a military system in use, is to agree with the prediction or analysis. From the data at hand, it is the prediction of the most likely behavior; however, this is no guarantee that for any given percentage of military systems, the prediction will be found to be obeyed. Just as in any statistical reliability analysis, a number of experiments are necessary to establish such a confidence factor.

The design of accelerated testing experiments, therefore, requires both the performance of a number of experiments for each stress level, and a suitable choice of a statistical distribution function for the  $K \lambda$ 's.

Certain types of such distributions have been considered, and offer promise towards being utilizable within an accelerated test design. None has as yet completely fulfilled the desired characteristics.

However, it is evident that the response of the devices (and/or system) to increased stresses which may otherwise be apparently chaotic and random can be made more tractable by using the several failure factors connected with portions of the device as a set of quantities whose individual variation, as the stresses are increased, is considered separately. Thus, in figure 1, if the relative importance of a failure factor under various stresses is that shown, the total failure distribution at normal stress will be determined by the relative importance of the different failure factors, with I being the most effective and IV the least. With increased stresses, the relative importance changes, and eventually III is overwhelmingly the major cause of failures. The essential contribution which the failure factor approach has made is to provide a functional skeleton with which to put the data into order.

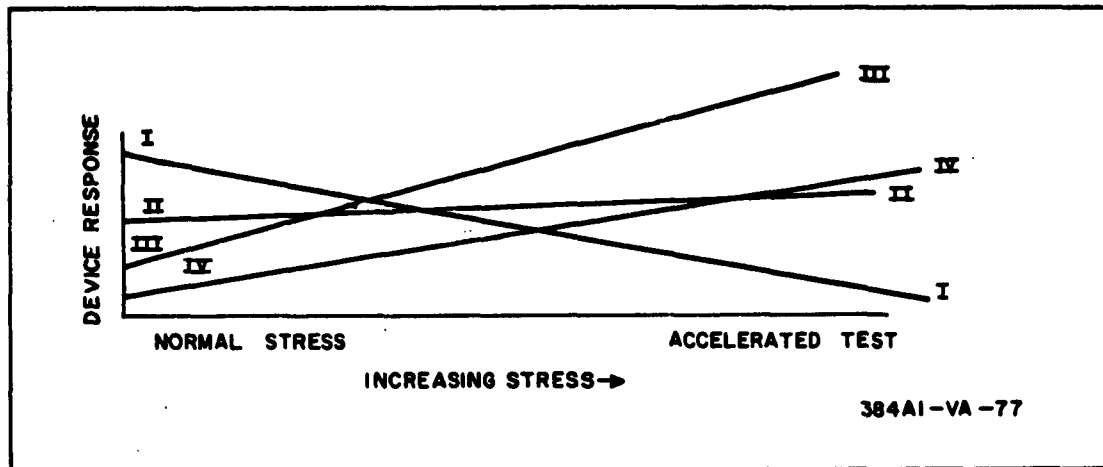


Figure 1. Device Response to Increasing Stress

#### 4.1.7.5 Conclusion

It has been shown that the failure factor analysis permits the use of a relatively few subdivisions for the analysis of the failure data, such subdivisions being chosen to contain, each, a number of other subfactors. The failure factors themselves can be computed (as in paragraph 4.2.4) from the failure data for a given system and stress environment. By confining the number of failure factors to a small number, it is possible to obtain relatively unambiguous values for them with a small number of devices being included in the test, and to do this while the devices are tested in a system, rather than individually. The results can be used either for accelerated test design, or for extending accelerated test results back to what would have been obtained if the test had been conducted under normal, unaccelerated, conditions.

Complete correction would require a large number of factors; it would also introduce nonlinearities and interdependent quantities. By choosing a reasonably small number of failure factors, each is a summation of a number of subfactors (and therefore of the effect of a number of failure mechanisms).

As is well known, such a summation over a reasonably large number of subfactors tends to smooth out the sum total effect, and the dependence of individual  $K \lambda$ 's upon the stress is likely to be smooth and monotonic rather than pathological. The mathematical manipulations become simpler and linear relations tend to be acceptable. In any case, a minimax decision must be made with respect to the number of failure factors necessary to provide for the different types of alteration of failure which increased stresses entail, while at the same time not unduly overloading the mathematical processing.

Once the  $K$ 's and the  $\lambda$ 's have been determined for the type of component, type of leads, etc , for the normal stress environment, and as a function of stress, any accelerated tests can be converted to values which may be used to predict reliability of life under normal use. The simultaneous determination of the weighting factors for the particular system permits using the values computed for normal stress environment for that particular system in predicting system reliability. Since this can be done with accelerated testing, the system reliability to be anticipated under normal stresses can be predicted in a period of test time which is not so great as to render a system or device obsolescent.

#### 4.2 FAILURE FACTOR MODEL FOR ANALYSIS AND PREDICTION OF COMPONENT RELIABILITY

The aim of the following treatment is to supplement present failure analysis techniques with one which can progressively be made more exact as knowledge of various failure mechanisms and the laws of their behavior becomes progressively more complete. Anticipated advantages which can result as the understanding of mechanisms of failure is incorporated into the model are: more complete analysis of what exactly is taking place in deterioration and failure of a component; more precise prediction of reliability and probable average life under various environments; and identification of particular areas which need to be examined to improve fabrication and handling processes so as to remove causes of failure.

Each failure factor is an easily identifiable part or structure of the component, or is a major property of the component sufficiently definite to be identifiable and controllable through the fabrication process. For example, the number of junctions in a device (transistor or diode or complex functional electronic block) is definite, and each mechanism of failure which requires the existence of a junction will have  $m$  times as many chances to operate in a component with  $m$  junctions as in a diode with a single junction. Similarly the types of mechanism which are related to the failure factor titled "leads" are described in paragraph 4.1.5 above.

The very large number of processes which are subsumed under present statistical failure formulation, and the small degree of knowledge which it is assumed is available with respect to each, are replaced by a formulation in terms of specifically identifiable factors, characteristic of the component, which are related to the mechanisms of failure. These failure factors furnish a finite number of categories to which the various known, and the as yet unidentified mechanisms of failure may be correlated. Being small in number, their mathematical treatment imposes a smaller complexity than if a very large number of categories were required. The uncertainty of the treatment of infinite numbers of processes or events is replaced by the corresponding



uncertainty as to the number of actual mechanisms which contribute to a particular failure factor. However, the failure factor as a category has a definite weight for a given environmental situation, given components, and given definitions of failure. As more knowledge is obtained about any particular mechanism of failure, this knowledge can be incorporated into the failure factor analysis by changing the weighting, or in extreme cases by suggesting the choice of an additional failure factor for consideration.

Philosophically, and presumably practically (as knowledge accumulates), each failure factor itself can be broken down into further subfactors, which take into account all the dimensional, material, structural, and manufacturing differences to be found among the various components or solid state devices. For the maximum degree of breakdown, the four-dimensional vector which is treated below would be replaced by an  $N$ -dimensional vector where  $N$  can be a very large number. The matrix formed by such a system would be nearly impossible to solve, and the data to support the solutions of such equations would be too costly to obtain. The failure factor mode of analysis, though not yet completely definite in the sense of a complete description of each mechanism, bears the same relation to the individual mechanisms as do the measurable quantities of a sample of gas or liquid, such as pressure, temperature, density, molecular weight, etc, to the precise description of the individual velocities, positions, and true individual masses of the molecules comprising the sample.

Error in measurement, and other uncertainties is still applicable, just as in the standard present methods of statistical analysis. These can only be reduced by increased knowledge and control. However, as the knowledge of natural processes connected with deterioration and failure increases, it can be incorporated into the failure factor model to increase the precision of description, and the practical utility of the analysis for planning fabrication operations and cleanliness and other safeguards, and for better analysis of causes of failure, and failure rates, and therefore reliability to be anticipated.

#### 4.2.1 Basic Formulation of Failure Factor Approach

Assume the negative exponential distribution of failures within the devices. The failure distribution function,  $F_r$ , of the  $r^{\text{th}}$  failure factor as a function of time,  $t$ , is

$$F_r(t) = 1 - \exp(-\lambda_r t) \quad (1)$$

where  $\lambda_r$  is the constant failure rate of the  $r^{\text{th}}$  failure factor. The reliability with respect to that factor at time  $t$  may be defined as the probability that the device has not failed as a result of the mechanisms connected with the failure factor:

$$R_r(t) = \exp(-\lambda_r t). \quad (2)$$

The reliability of the device itself is the probability that no failure has occurred as a result of any failure factor

$$R_{\text{DEVICE}}(t) = \prod_{r=1}^N \exp(-\lambda_r t) = \exp\left(-\left[\sum_{r=1}^N \lambda_r\right] t\right) \quad (3)$$

The unit in terms of which the failure rate is measured depends upon the basic unit of time; e.g., the number of hours the devices were operated or whether this is measured in hours or days, etc. Correction may be made for the time unit by substituting  $K\lambda$  for  $\lambda$  in the equations.

The introduction of the factor  $K$  can be made more useful. Different environments and different procedures of testing correspond to different stressing of the system being measured. If the  $\lambda_r$  is interpreted as the failure rate from the  $r^{\text{th}}$  failure factor under a standard set of stresses, more intense or less intense stresses than the standard can be indicated by changing the value of the  $K$  in the product  $K\lambda$ . The reliability of the component as measured in the system  $A$ , whose design and whose testing procedure impose a particular set of stresses upon the components is then

$$R_{\text{DEVICE}} = \exp\left(-\left[\sum_{r=1}^N A K_r \lambda_r\right] t\right). \quad (4)$$

In a different system so designed that different stresses exist, and under different environmental and test conditions, the measured reliability of the

component would be

$$R_{\text{Device}} = \exp \left( - \left[ \sum_{r=1}^N B_r^{K_r} \lambda_r \right] t \right).$$

Using a given unit of time, then, the  $r^{\text{th}}$  failure factor for system A with its stresses may be defined as  $B_r^{K_r} \lambda_r$ .

By analyzing the observed failures within a given system, and determining the numerical value of the exponential coefficient of  $t$  which must be used to express the reliability of the component in that system, a value is obtained for the sum of the failure factors. If this is done for each component analyzed in the system, a set of simultaneous linear equations results, and the solution of these yields the individual values. In paragraphs 4.2.3 and 4.2.4 it is shown that not only is it possible to determine the values of the failure factors, but also the ranges of appropriate weightings for each failure factor.

In certain cases, the weighting is obvious. A device with three leads will have three opportunities for the action of any mechanism which is connected with the failure factor related to leads. In other cases, the weighting is not obvious, and, as below, must be determined by analysis of the data.

#### 4.2.2 Cautions

Some misinterpretations which must be avoided should be specifically mentioned, and the correct point of view is formulated below.

The failure factor is a subdivision of the categories within which failure may, in general, occur. With the exercise of a little ingenuity, it would be possible to subdivide each failure factor into a number of further failure factors, as desired. Too great a subdivision defeats the purpose of the present approach, however.

The failure factor is not a summation of mechanisms of failure. It is a category within which the summation of effects of the various mechanisms can be included by knowledge of how these mechanisms behave as a function of the various stresses which exist in the system. Suitable use of the information obtained on the mechanisms of failure and their performance, permits closer definition of the failure factors.

Each mechanism of failure is more or less effective depending upon the environmental conditions. Changes in conditions such as temperature, mechanical shock, applied voltage, concentrations of chemical agents, etc, determine whether the mechanism actually contributes to failure, and to what extent or at what rate it does so. Lacking a word to define effects of such quantities upon the mechanisms, with respect to increasing or decreasing the effectiveness of the operation of that mechanism, or to whether the mechanism operates at all, quantities such as temperature or applied voltage will be termed activators of the failure mechanisms.

The failure factors themselves (the  $K\lambda$ 's) have values depending upon the environmental stresses, fabrication technology, and the time unit used. They do not have a given constant value such as "one." As shown below, their value is to be determined by solution of a matrix.

#### 4.2.3 Present Formulation: Four Failure Factors

For reasons described in the Quarterly Report 3 (pp. 20-22,) four failure factors were chosen for analysis of the results obtained in the detailed study of failures in the two military data processing systems during manufacture and test. These factors are: leads, junctions, and volume or bulk material, and the surface. This is an initial attempt to define the major failure factors which should be considered, and must be judged in terms of the consistency and utility of the results. Other choices of failure factors are possible; however, the ones chosen possess the advantage of clear definability, without confusion as to the correlatability of each of the component subfactors.

On a very elementary level, the weights which are to be assigned to each failure factor are evident in the cases of transistor and diode, the chief components which are candidates for failure study. These are:

$$\text{Transistors: } 3 F_L + 2 F_J + 1 F_V + 1 F_S \quad (5)$$

$$\text{Diodes: } 2 F_L + 1 F_J + 1 F_V + 1 F_S$$

where L denotes leads, J junctions, V semiconductor bulk or volume material, and S semiconductor surfaces. If only transistors and diodes

were under consideration, equations 5 could be satisfied by the choice unity for each failure factor, so that the ratio of failure factors in general in the two systems would become a model ratio of 5:7, i. e. 0.714, which is very close to the observed ratio in the two systems. The additional experimental data gathered indicates, however, that while the sums of the weighted failure factors are 7 and 5 respectively, the individual values of the failure factors differ markedly from 1 as shown below.

Since more or different failure factors could have been chosen, yielding a different ratio, some justification is necessary for this choice of four factors. The experiments under the present contract have shown the importance of both the surface and the bulk behavior of solid state components in the accumulation of mechanisms of failure. It is well known that failures occur at junctions, and the results on percentages of failures which are shorts between emitter, base, and collector in the two systems point to junctions as a major failure factor. Reasons for the importance of leads as a failure factor are given in Quarterly Report 3 on p. 20 and in paragraph 4.1.5 above. No other clearly identifiable portion of the structure of the component has the same definiteness or importance that the four chosen do, and those which come to mind can be shown to be categorizable under the four here chosen. Thus, suitable encapsulation may appear to be a failure factor. However, the various effects resulting from improper encapsulation may be shown to affect the surface or the leads, with some slight effect on the other two failure factors.

However, the consistency of the approach, and the justification of the choice of these factors, requires more support. Therefore, to test this approach, the utility of the application of the four factors to the other two components is examined. This is a more severe test, since various types of (not merely makes or processes) resistors of different materials and various types of capacitors operating on different principles are included in the failures analyzed in the two systems. The test is further complicated

by the fact that some major differences exist in system A as compared to the technology of system B, because of the necessity for higher reliability.\*

The weighting of the failure factors for resistors will be

$$\text{Resistors: } 2 F_L + 0 F_J + 1 F_V + 0 F_S \quad (6)$$

Because of the major differences in capacitors, two solution techniques were used: the first was to use the above three equations, and sharpen up the values by applying the requirement that all weightings and all failure factors must physically be positive valued quantities; the second was to assign undetermined weights to three capacitor failure factors, and see whether consistent weights (six unknowns) could be found that would satisfy the 14 conditions of nonnegativity; in addition to the excess of conditions to be met, physical consistency requires that the values obtained for the various quantities entering into the equations be reasonable.

#### 4.2.4 Computation of Failure Rates and Weightings of Failure Factors

##### 4.2.4.1 The Equations, and Matrix Formulation

The equations for the failure rates are therefore equations 5 and 6. If major changes had not been incorporated into the capacitor sample and environment, it would be natural to include a fourth equation, namely

$$\text{Capacitors: } 2 F_L + 2 F_J + 1 F_V + 0 F_S \quad (7)$$

$$\text{or } 2 F_L + 0 F_J + 1 F_V + 2 F_S$$

depending upon whether the metal-insulator interface in the capacitor is to be regarded as functioning more like a junction or more like a surface.

\* Specifications were tighter, design reviews were incorporated into the schedule and better heat disposal, better voltage regulation, and more protective circuitry was incorporated. Different types of physical processes were involved in the data acquisition and processing, which was more precise for system A. Capacitors were upgraded, HI RI types being used almost everywhere, and CPVO-8 and CPVO-9 types used in the most important locations; a derating policy was incorporated, so that no capacitor was used at more than 50 percent of its rated voltages; electrolytics (the only electrolytic condensers in B were tantalum, since aluminum may not be used) were designed out of the initial design wherever possible, there being included general-purpose ceramic (0.001 percent/1000 hours) quality mica or paper capacitors, and mylar types.

For reasons given in the footnote on page 37, and because, for example, the CPVO-8 capacitors contain two metal sheets rolled into a spiral with insulation between, and with some 15 to 20 or more layers of the metal intersecting a given radius because of the spiral winding, this cannot be done. Furthermore, it is desirable to determine the extent to which, in this type of formulation, the mechanisms of failure distribute themselves in capacitor failure as if the metal dielectric interface were a surface or as if it were a junction.

Using as a unit of time that time in which 7 transistors failed in system B, the notation:

$B^K \lambda_L$  = proportionate failure rate of the leads under the stress of system B

$A^K \lambda_J$  = proportionate failure rate of junctions under the stress of system A,

the equations and their associated matrices for system B become,

$$\text{Transistors: } 3 B^K \lambda_L + 2 B^K \lambda_J + B^K \lambda_V + B^K \lambda_S = 7 \quad (8)$$

$$\text{Diodes: } 2 B^K \lambda_L + B^K \lambda_J + B^K \lambda_V + B^K \lambda_S = 5$$

$$\text{Resistors: } 2 B^K \lambda_L + 0 + B^K \lambda_V + 0 = 0.25$$

$$\text{Capacitors: } 2 B^K \lambda_L + x_b B^K \lambda_J + x_3 B^K \lambda_V + x_4 B^K \lambda_S = 0.35$$

so that for system B,

$$\begin{bmatrix} 3 & 2 & 1 & 1 \\ 2 & 1 & 1 & 1 \\ 2 & 0 & 1 & 0 \\ 2 & x_b & x_3 & x_4 \end{bmatrix} \begin{bmatrix} B^K \lambda_L \\ B^K \lambda_J \\ B^K \lambda_V \\ B^K \lambda_S \end{bmatrix} = \begin{bmatrix} 7 \\ 5 \\ 0.25 \\ 0.35 \end{bmatrix} \quad (9)$$

For system A, the weights in the case of capacitors may be different. Therefore,

$$\begin{bmatrix} 3 & 2 & 1 & 1 \\ 2 & 1 & 1 & 1 \\ 2 & 0 & 1 & 0 \\ 2 & x_a & x_1 & x_2 \end{bmatrix} \begin{bmatrix} A^K \lambda_L \\ A^K \lambda_J \\ A^K \lambda_V \\ A^K \lambda_S \end{bmatrix} = \begin{bmatrix} 1 \\ 0.71 \\ 0.036 \\ 0.26 \end{bmatrix} \quad (10)$$

The numerical quantities in the vectors on the right hand side of the equal signs are measured values, and the consistency of the approach is tested by whether they yield suitable results.

#### 4.2.4.2 Solution: First Approach

Because of the uncertainty with respect to capacitors, the last equation is omitted in each case, and the remaining three are solved, treating one variable as a parameter. After solution, the condition that no failure rate be less than zero is imposed. The following mean proportionate failure rates are obtained:

$$\begin{array}{ll} B^K \lambda_L = 0.063 & A^K \lambda_L = 0.009 \\ B^K \lambda_J = 1.94 & A^K \lambda_J = 0.281 \\ B^K \lambda_V = 0.125 & A^K \lambda_V = 0.018 \\ B^K \lambda_S = 2.81 & A^K \lambda_S = 0.393 \end{array} \quad (11)$$

The decrease in the failure rate factor from system B to system A is nearly seven times in each case, or stated differently, the attention paid to improved reliability in system A resulted in a decrease of failure rates by a ratio of seven.

#### 4.2.4.3 Solution: Full Treatment of Statistical Weightings Using Mean Values

To determine relative weightings of failure factors for capacitors in the two systems, applying the most stringent test available to the experimental data in order to check the consistency of this approach, all four equations are used.



Solution of the equations yields:

$$\begin{aligned}
 A^{K_L \lambda_L} &= [\delta - 2.75 \eta] / \eta & B^{K_L \lambda_L} &= [\theta - 0.384 \epsilon] / \epsilon & (12) \\
 A^{K_J \lambda_J} &= [-\delta + 4.75 \eta] / \eta & B^{K_J \lambda_J} &= [-\theta + 0.674 \epsilon] / \epsilon \\
 A^{K_V \lambda_V} &= [-2 \delta + 5.75 \eta] / \eta & B^{K_V \lambda_V} &= [-2 \theta + 0.804 \epsilon] / \epsilon \\
 A^{K_S \lambda_S} &= \delta / \eta & B^{K_S \lambda_S} &= \theta / \epsilon
 \end{aligned}$$

$$\text{where } \delta = 5.85 - 5.75 x_1 - 4.75 x_a \quad (13)$$

$$\eta = 2 - 2 x_1 + x_2 - x_a$$

$$\theta = 1.028 - 0.804 x_3 - 0.684 x_d$$

$$\epsilon = 2 - 2 x_3 + x_4 - x_b$$

Since no failure factor can have a value less than zero, equations 12 supply eight conditions on the two ratios  $\delta/\eta$  and  $\theta/\epsilon$ . Expressing the Greek letter quantities in terms of the  $x_i$ 's, these eight conditions are applied to six parameters. Doing this in order, there are obtained

$$2.75 < \delta/\eta < 2.875; 0.384 < \theta/\epsilon < 0.402; \quad (14)$$

the mean values are

$$\delta/\eta = 2.81, \theta/\epsilon = 0.393. \quad (15)$$

In terms of them, the following values are obtained for the individual failure rates,  $K\lambda$ , in the two systems:

$$\begin{aligned}
 A^{K_L \lambda_L} &= 0.009 & B^{K_L \lambda_L} &= 0.060 & (16) \\
 A^{K_J \lambda_J} &= 0.281 & B^{K_J \lambda_J} &= 1.940 \\
 A^{K_V \lambda_V} &= 0.018 & B^{K_V \lambda_V} &= 0.130 \\
 A^{K_S \lambda_S} &= 0.393 & B^{K_S \lambda_S} &= 2.810
 \end{aligned}$$

These are nearly the same as the values (equation 11) but differ slightly since the capacitor equation has been considered explicitly.

For each  $x$ , value ranges which are compatible with the experimental results can be shown easily. Using the explicit expressions (13) for the

quantities represented by Greek letters in equation 14, there may be obtained two inequalities for each system. If these are plotted in triaxial coordinates, figures 2 and 3 are obtained. Here the ordinates are  $x_2$  and  $x_4$  respectively, the abscissas are  $x_1$  and  $x_3$  respectively, and the successive oblique lines are  $x_a$  and  $x_b$  respectively. In each case, one of the two extreme values in equation 14 yields an inequality involving only  $x_a$  and  $x_2$  (system A), or  $x_b$  and  $x_4$  (system B). This inequality states that a linear combination of the two variables have a value greater than a given amount. Therefore, it denies the region to the left and below the single line of smaller slope in each diagram. This region has been shaded. In each case, the other inequality is an expression in all three variables. For a given value of  $x_1$  (or  $x_3$ ), there is obtained a particular line, all such lines being parallel to each other. These inequalities, for a given line, state that the area to the right and above the line contains no acceptable set of values for the variables. The only possible values of the  $x$ 's are therefore those included in the non-shaded region of each graph.

If any particular value of  $x_1$  (or  $x_3$ ) is chosen, the values of  $x_2$  and  $x_a$  ( $x_4$  and  $x_b$ ) which are possible are those within the unshaded area to the left and below a line representing that value of  $x_1$  ( $x_3$ ). Thus in figure 2, if a value,  $x_1 = 0.5$ , is chosen, a line parallel to the oblique lines is drawn halfway between the lines  $x_1 = 0.4$  and  $x_1 = 0.6$ . All values of  $x_2$  and  $x_a$  contained in the unshaded area to the left and below this oblique line are then suitable; if for example,  $x_2$  is then chosen as 0.01, the permissible range of  $x_a$  is from 0.038 to 0.078.

The drastic limitation which the experimental data on these systems imposes upon the values of the parameters is of direct benefit to experimental design for accelerated testing.

The ranges of  $x$  values that are obtained all fall within reasonable limits. Within the permitted range are the values  $x_1 = x_3 = 1$ , which intuitively might be regarded as suitable, since there presumably is only one volume

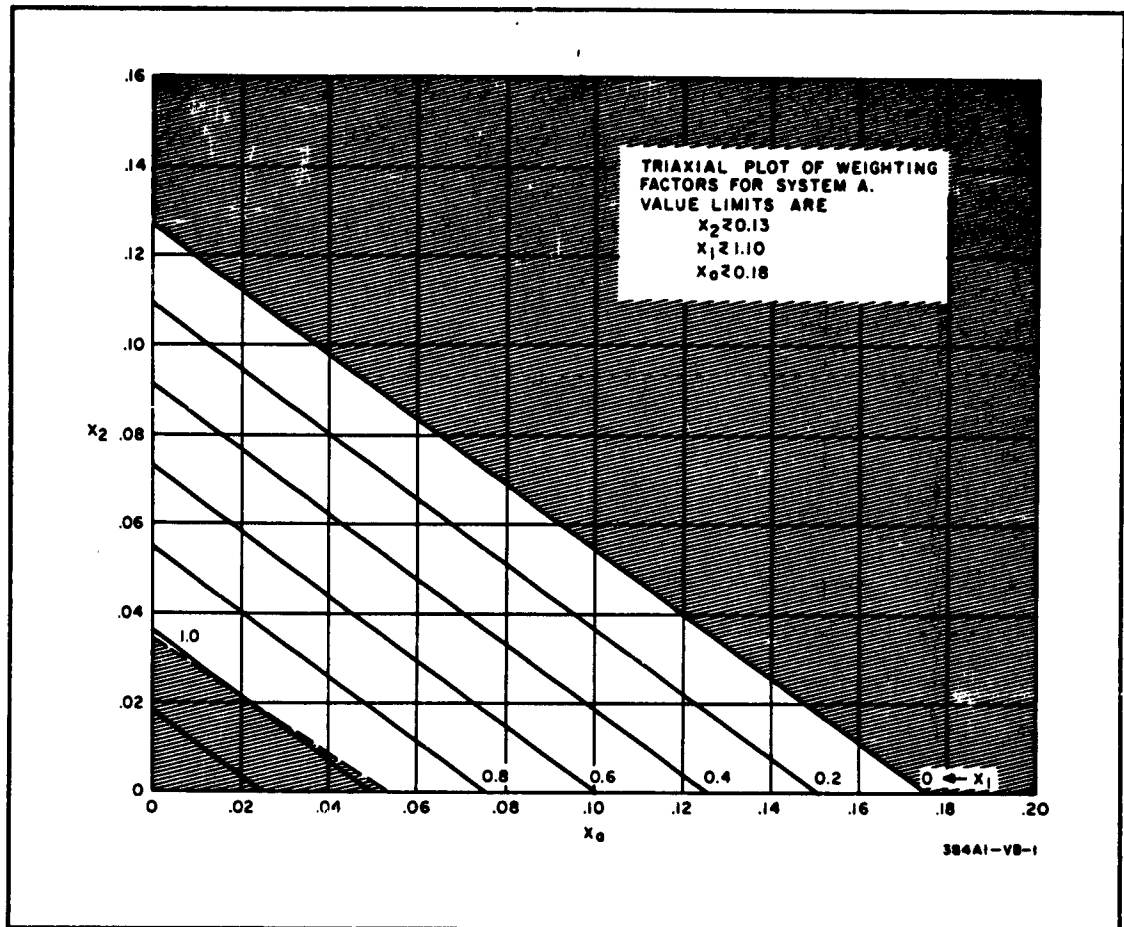


Figure 2. Weighting Factors for System A

within each capacitor; for this case, the other  $x$ 's are so closely confined that they may both be regarded as essentially defined. However, since the resemblance between capacitors and transistors with respect to possible subfactors of failure is considerably less than is that between diodes and transistors, other values of  $x_1$  and  $x_3$  may be more reasonable, such as 0.5 or 0.0.

The weighting of only two of the corresponding failure factors for the capacitors can be the same in the two systems. Examination of the figures shows the maximum possible value of  $x_2$  is less than the minimum possible

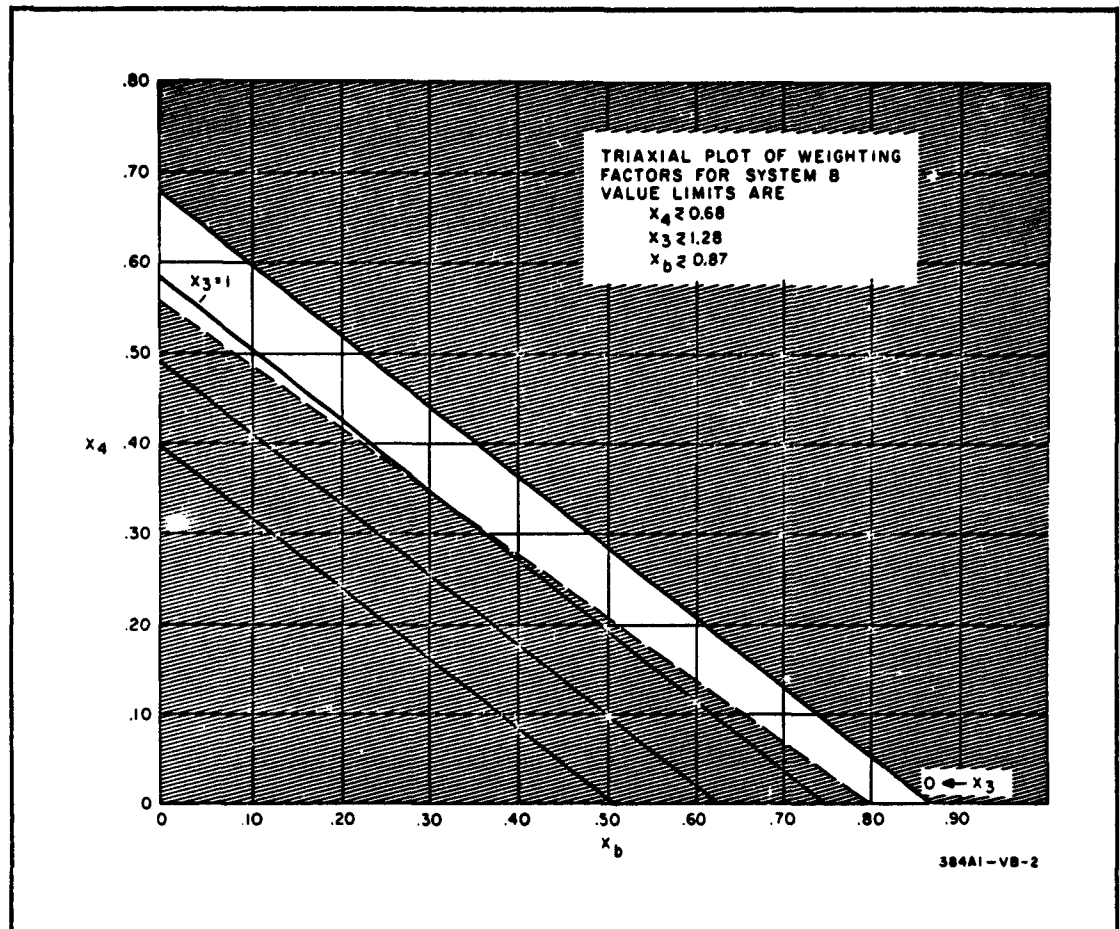


Figure 3. Weighting Factors for System B

value of  $x_4$  except in the region  $x_b > 0.60$ ; however, then  $x_a$  must be less than 0.18. If both triaxial plots were placed on the same diagram, that for system A would fall well down towards the origin in the lower forbidden region of the plots for system B. This again reflects the decreased importance of failure factors because of the emphasis upon design review and component choice in system A.

If it be assumed that the weighting factors for volume are equal to one for both systems, and those for junctions are equal to zero for both systems, then the surface dependent weighting factors have the values  $0.0364 < x_2 < 0.038$ ,  $0.557 < x_4 < 0.582$ , so that the weighting of the surface dependent

factor in system B is about 16 times that in system A. For  $x_1 = x_3 = 0.5$  or 0.0 this ratio is reduced to about 10, or 6, respectively.

Since each value on the right side of equations 9 and 10 is itself a mean and is surrounded by a distribution of values, the values of the failure factors themselves are means within a distribution based upon the original uncertainty of the experiment. Additional measurements would further sharpen the values.

#### 4.2.5 Summary and Discussion

The treatment has yielded consistent mean values for the failure factors, and has exhibited a decrease by a factor of seven in the failure rates occasioned by the greater attention to reliability in system A; although it does not eliminate the possibility that at least one of the failure factors does not operate in capacitors, it does leave open the likelihood that capacitor failure factors are distributed over surfaces, junctions, and bulk material. In the systems measured, it leads to no absurdities, and the values of failure factors and weightings are reasonable and acceptable. Whether these attributes of this approach will be retained in application to other systems or other environments remains to be seen. If so, there may be some advantage from the ability to define unambiguous categories (failure factors correlated directly with the structure of the component) in which to introduce the experimental results from the system of failure mechanisms.

### 4.3 SURFACE STUDIES: ELECTRONIC MATERIAL AND PROCESSING CHARACTERIZATION BY THE ELECTRICAL-FRICTIONAL PROBE

#### 4.3.1 Apparatus and Early Results

The construction of the electrical-frictional probe apparatus is discussed in the three quarterly reports. The sensitivity of the electrical charge transfer trace to surface properties, and the uniformity of its response is described in Quarterly Report 3. In particular, major changes in response, from negative to positive, are observed when the probe passes from n-type material to p-type material, and vice versa. In its passage over material of any one chemical composition, slight changes in the trace indicate chemical impurities and defects on the surface. Indications are most satisfactory on the semiconductor material itself, rather than the oxide.

In Quarterly Report 3, an experiment is described in which a bull's-eye wafer, figure 4a, was repeatedly traversed after several oxidizing and oxide-removal processes. The result showed that an oxide removal by HF left an active surface which deactivated on exposure to air; a second oxide removal by HF reactivated the surface, and, after this, only the n-type regions would be deactivated with atmospheric exposure. After a third HF etch, no further deactivation was observed. It is therefore not necessarily sound to assume that in processing a wafer the oxide removal by HF yields a surface which remains free of oxide. Unless several redox cycles are incorporated into the processing, any oxide-free surface produced may show inherent variability in electrical properties unless used in fabrication immediately.

A number of traces showing various experimental results are given in Quarterly Report 3. Two of these have been combined into one picture, which shows the sensitivity and uniformity of the method. (See figure 4b.)

#### 4.3.2 Surface and Volume Properties Measured by the Electrical-Frictional Probe

With zero voltage, the probe is most sensitive in measuring the slight changes in chemical composition or defects in the surface. With applied voltage, and depending upon the location of the return electrode, deeper and deeper regions in the volume of the material can be measured. The reason

for this is that conduction paths must traverse the volume of the material. The height of the trace as the probe travels over the material indicates the ease or difficulty of charge carriers pursuing their changing conduction paths through the material. This has been utilized as an indicator of conditions below the surface.

Also, the photovoltaic effect used as described in paragraphs 4.5 to 4.8, below, enables some examination of stresses or other effects within the volume of the material, not too far from the surface. However, additional methods of examining the interior of the material are desirable. To do this, the light transmitting properties of the semiconductor material have been utilized.

#### 4.3.2.1 Depth of Penetration

Elementary considerations of transmittance, absorption, and relative energy response or carrier density increase in the photovoltaic effect, as a function of light frequency, show that the responses which arise from a given depth in the material, change significantly as the frequency approaches an absorption peak or a cutoff point. Experiments with filters and a Brush recorder confirm this expectation and show that if due allowance is made for the nature of the contacts to the sample, increasing the wavelength of light in the range from 0.42 to 1.0 micron gives an increase in the apparent mean penetration of the measured results below the surface.

#### 4.3.3 Surface Investigation With Voltage Applied on Probe

Using a quarter of a bull's-eye diffused p-on-n wafer and the path of the probe and circuit arrangement as shown in figure 5, a traverse was made over successive n-and p-regions with external voltage in the circuit. The battery had a negligible internal resistance of 21 ohms. Generally, the current was uniform in each of the n-regions, but fluctuated in the diffused

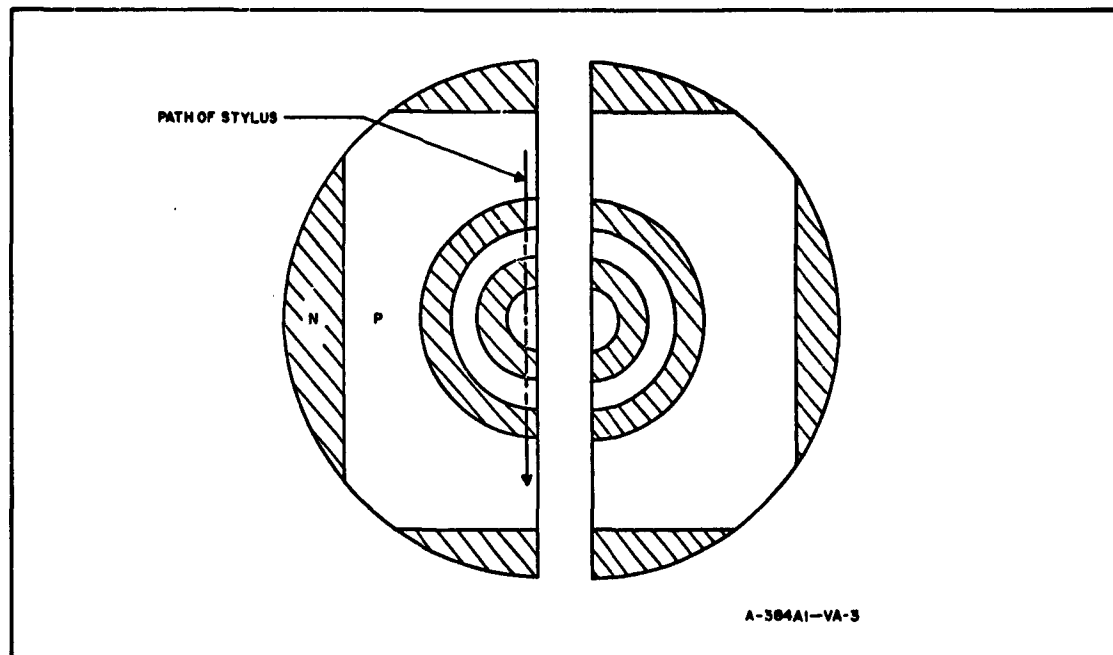


Figure 4a. Bull's-Eye Wafer Cut in Half

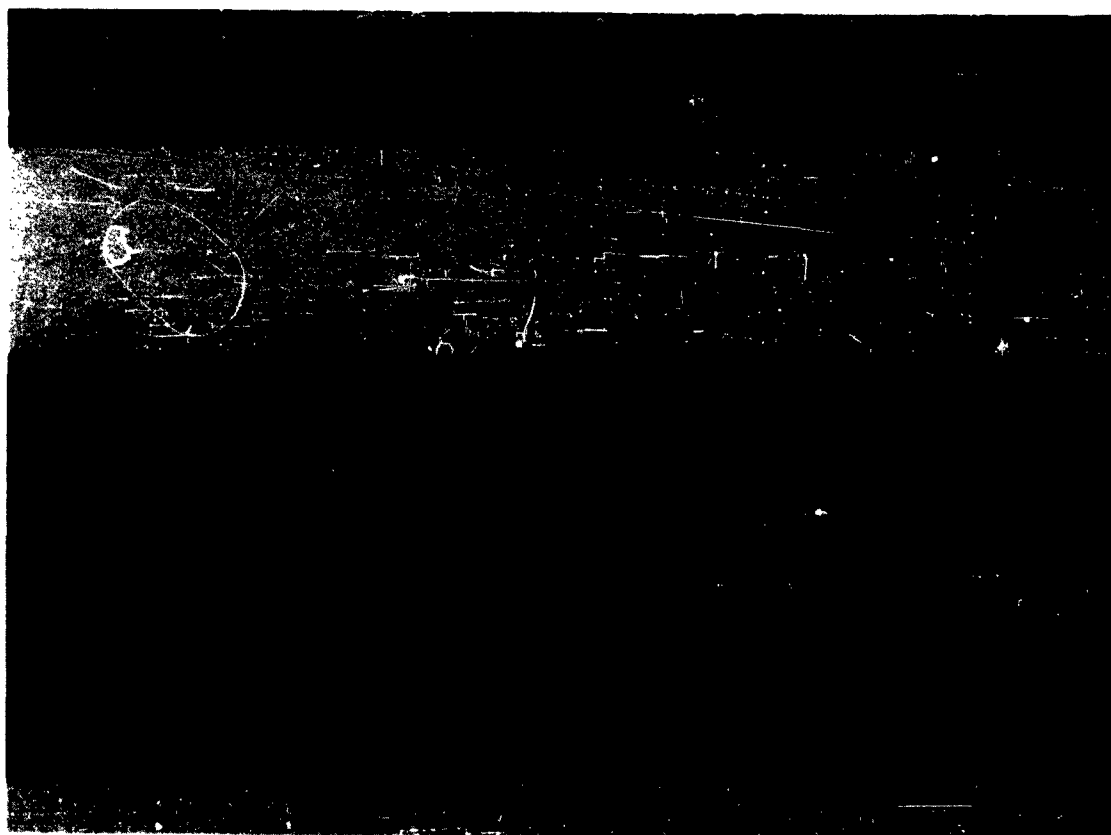


Figure 4b. Typical Response to Changes of Material Composition



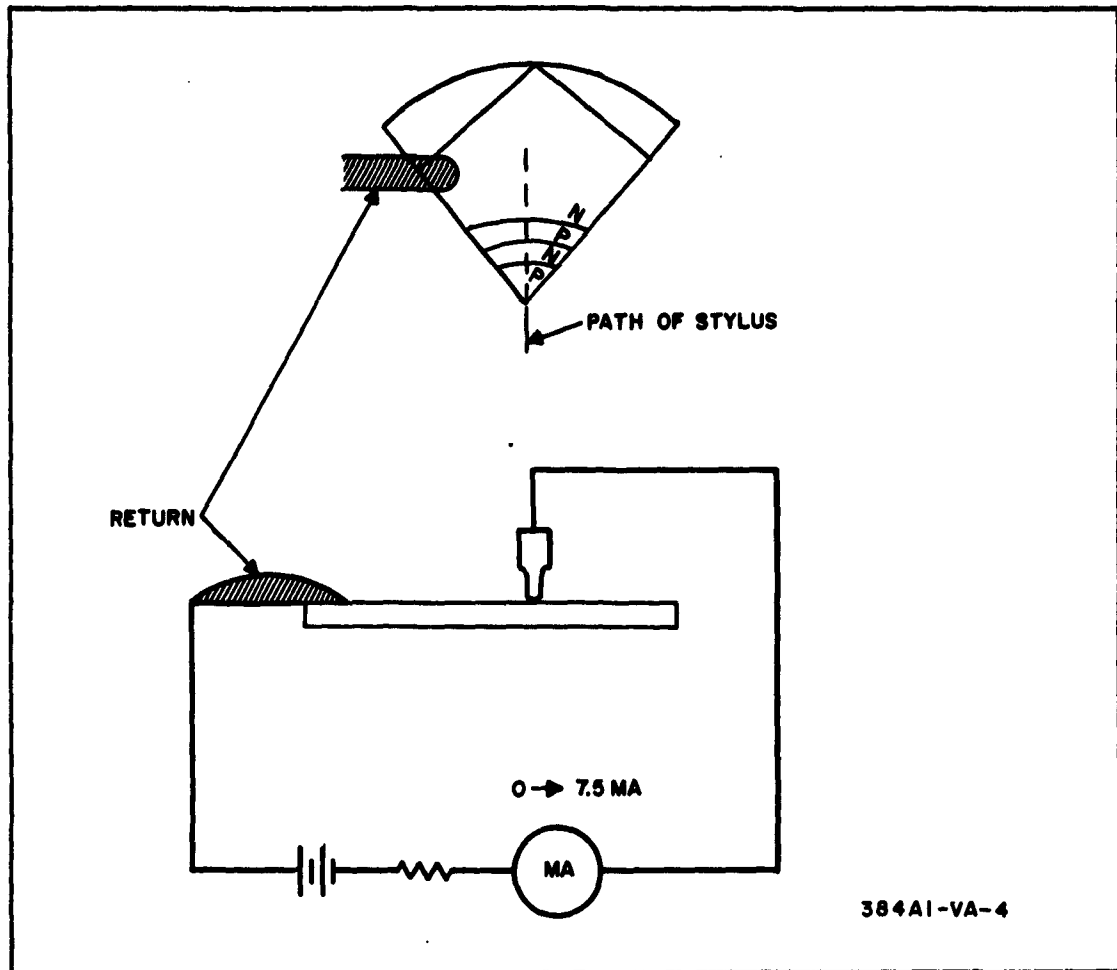


Figure 5. Circuit Arrangement Used in Surface Investigation

regions. In the last p-region, the current increased nearly logarithmically from 4.3 ma upon entry to 6.4 ma at the point of the quadrant, reflecting the concentration of current lines.

Repeating test with probe positive then negative, with and without illumination, results obtained are in Table 2. See also paragraph 4.3.4.2.

#### 4.3.4 Use of the Electrical-Frictional Probe Electrical Trace in Examining Fabrication Techniques. Effects of Water Spot

Since the traces shown above and in Quarterly Report 3 show reproducibility and considerable sensitivity, the use of the trace was studied as an aid to the examination of factors during fabrication which might be conducive to failure.

TABLE 2  
TESTS WITH EXPOSURE TO LIGHT

	Current in MA					Resistance in K Ohms			
	N <sub>1</sub>	P <sub>1</sub>	N <sub>2</sub>	P <sub>2</sub>		N <sub>1</sub>	P <sub>1</sub>	N <sub>2</sub>	P <sub>2</sub>
No Light (+) Stylus	.85 ma	3.5 to 4.0	.80	4.3 to 6.4	---	25.23	5.18 to 4.35	26.93	3.98 to 2.25
Light (+) Stylus	3.3	4.35	2.4 to 1.9	5.0 to 6.5	---	5.55	3.91	8.13 to 10.58	3.23 to 2.20
No Light (-) Stylus	0	4.0 to 4.1	Approx. 1 sec. 5.3 to 0		---	∞	4.35 to 4.23	∞	2.98 to 2.48
Light (-) Stylus	0	4.6 to 4.9	Approx. 1 sec. 5.2 to 0		---	∞	3.62 to 3.32	∞	3.06 to 2.48

#### 4.3.4.1 Preparation of Wafer and Water-Spot Flaw

An n-on-p bull's-eye wafer was purposely diffused with a flaw. The surface was oxidized using the bull's-eye mask for defining the limits of the oxide. A drop of deionized water was then sprinkled on the oxide, and the wafer immediately placed in the diffusion furnace. Presumably the water evaporated almost instantly. Diffusion completed, the wafer was examined with the oxide still on it. A multicolored spot was visible on the outer ring (oxide + diffusant). The wafer was then scribed and the oxide removed from one of the two half-wafers. No sign of a spot or defect was visible after oxide removal.

#### 4.3.4.2 Trace Shows Effect of Flaw in Detail

Traces were made across the wafer and irregularities of large magnitudes were observed when the probe came to this region (figure 6a). After angle-lapping the wafer at 2 degrees and staining, it appeared as in figure 6b. The correlation between the regions picked out by the stain, and those indicated by the trace is shown in the figure; it is exact if allowance is made for the time necessary to change the film and take the next picture at one point.

The wafer was exposed to the atmosphere for 14 days, cleaned in TCE and a 5-minute HF bath, 5-minute  $\text{HNO}_3$ , and another 5-minute HF bath. Another defective region was tested with the probe; when stained, it appeared as in figure 7. The trace from this region is shown in figure 8.

To compare the results from zero applied voltage using light as an activator, and applied voltage on the probe, traces were made under each condition (figure 8). The upper two show the repeatability of the trace. The lower one is with applied voltage. The correlation between the runs is evident. Also evident is the fact that the applied voltage trace shows less detail, tending to show maxima and minima with little detail. This is because the effect was primarily in the surface region.

#### 4.3.5 The Possibility of Precise Depth Measurement

It has been shown repeatedly that minute changes in surface chemistry are shown by the apparatus. To investigate the sensitivity to depth of

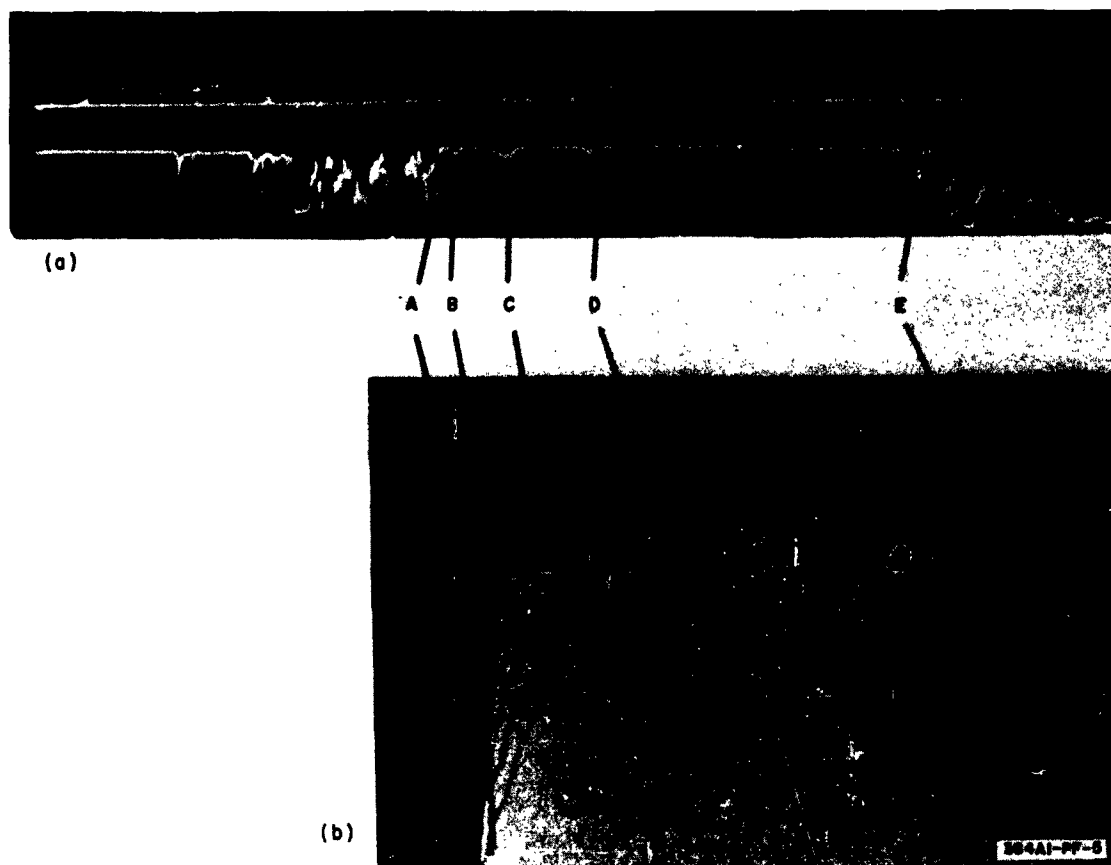


Figure 6. Wafer With Water Drop Flaw and Slip-Stick Response Across It

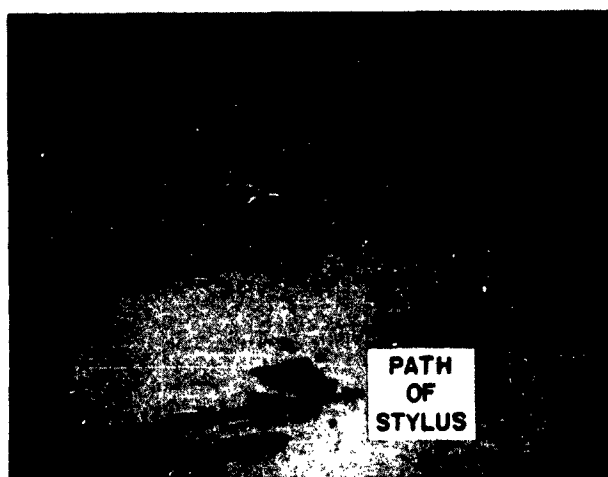


Figure 7. Magnified View of Stained Surface Flaw

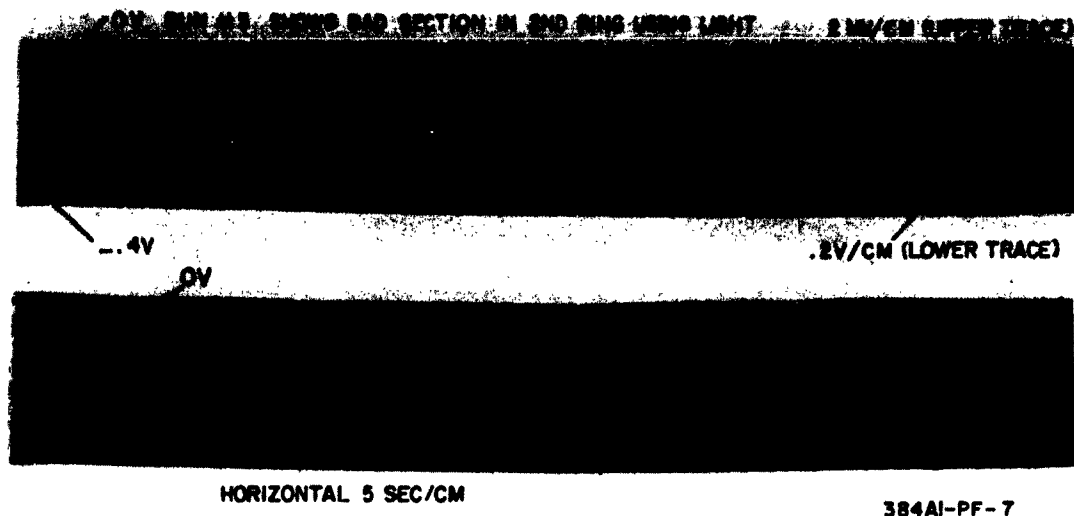


Figure 8a. Successive Traces From Defective Region of Figure 6. Upper Traces in Each Picture Are Mechanical Drag; Lower Traces Are Electrical; No Applied Voltage

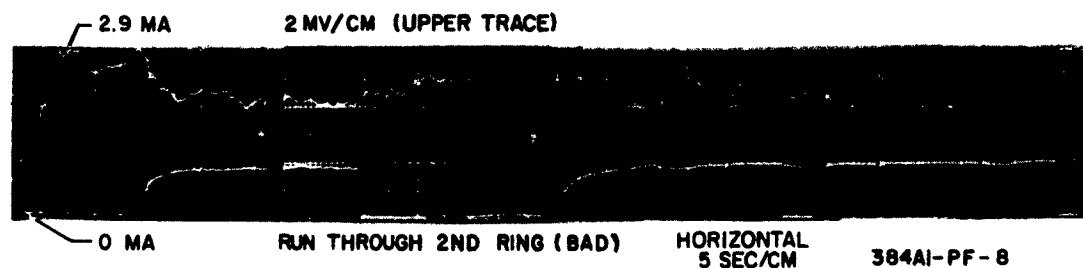


Figure 8b. Trace Over Same Region as in Figure 7a, With Voltage Applied to Probe. Note Smaller Amount of Detail on Electrical Trace

diffusion as well as to amount of doping, wafers were diffused in the temperature gradient region of the diffusion furnace, figure 9. Five 60 ohm-cm p-type wafers were lapped, chemically polished, oxide masked, and given a 5-minute predeposition and a 40-minute deposition, after which the oxide was removed.

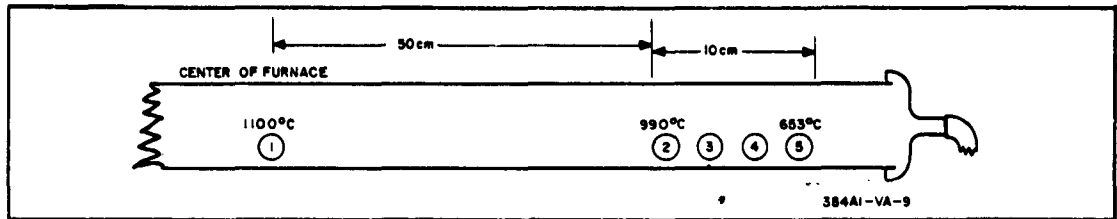


Figure 9. Schematic Diagram of Samples in Temperature Gradient Region of Furnace

Evidence was obtained for uneven deposition, but angle lapping and staining showed that the temperature gradient was insufficient to produce major differences in diffusion depth across an individual wafer.

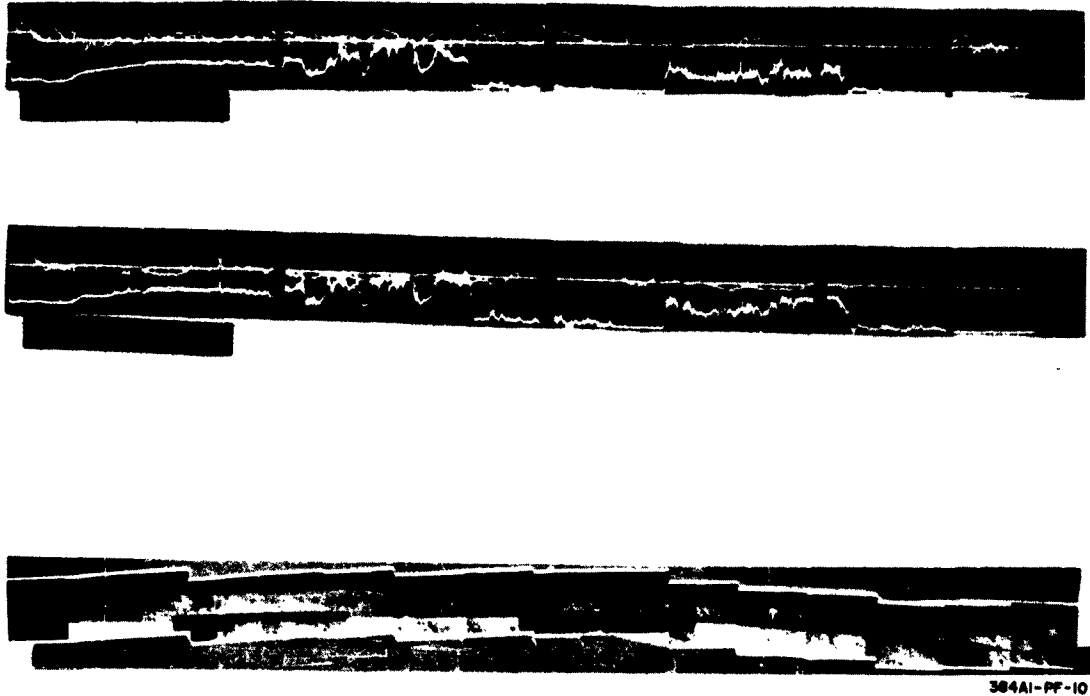


Figure 10. Similarity Between Repetitive Traces

#### 4.3.6 The Electrical-Frictional Probe is a Nondestructive Test for Defects

From traces published in Quarterly Report 3, and from other data, it has become evident that the electrical response obtained in a second trace over the same area is not noticeably different from that obtained in the first trace.

Note figure 8 and figure 10. Nearly the same effect is noted upon a third trace. Even these slight differences can be removed by a short etch which does not affect the characteristics of the wafer. Accordingly, the trace can be used as a method of examining the product of a step in the fabrication process and determining the efficiency of that step; the wafer tested can then be used for device manufacture if suitable.

The test therefore is a nondestructive test which can be correlated with performance and enable the rejection of samples of unsuitable characteristics or unsuitable preparation before further work is done on them. Thus it should be of value in decreasing the number of failures of completed devices.

#### 4.4 SURFACE STUDIES: SUPPLEMENTATION OF ELECTRICAL FRICTIONAL PROBE INFORMATION BY STICK-SLIP MEASUREMENTS

##### 4.4.1 The Stick-Slip Relaxation Cycle

The stick-slip phenomenon observed by Bowden and Ridler in 1936 has received much experimental and theoretical investigation. Morgan, Muskat, et al. early indicated the necessity for considering the dynamics of the motion of the surface element as well as that of the slider, and showed the need for considering the duration of stick. Perhaps the most thorough analysis of stick-slip is that of B. V. Derjaguin et al. who include explicit consideration of the duration of stick and of slip.

If the stick-slip traces are to be utilized for further information about the surface than can be obtained from the electrical transients during sliding, the physical motion of surface elements and their force constants and periods must be taken into account in the analysis.

Since a stick-slip cycle consists of a period of adhesion or temporary "weld" between slider and surface, followed by a release when the restoring force equals adhesion component and slip until stick again takes place, it follows that the primary information obtainable from a stick-slip cycle is the force interaction between probe and surface. The load transducer can also reflect irregularities in surface elevation. With a smooth surface, it has been shown experimentally that during the slip portion of the stick-slip, the instantaneous drag decreases to a very small fraction of its instantaneous value during stick, whereas little or no change is observed in the load; i. e., the instantaneous value of the coefficient of friction varies considerably, and the value observed in the usual experiment (if stick-slip is taking place) is an average value. The adhesion in the stick-slip cycle is usually regarded as time dependent, and stick takes place when adhesion has built up to where it exceeds restoring force. Stick continues as long as the adhesion component continues to build up fast enough so that its value equals or exceeds the restoring force, which is simultaneously increasing because of the distortion



that accompanies the gross relative motion of the surface with respect to the zero position of the slider. If breakfree occurs when the adhesion component is less than the surface shear strength, negligible wear accompanies it; if adhesion becomes equal to or tends to become greater than the shear strength of the surface of either the moving plate or the slider, breakfree is accompanied by the destruction of a portion of one of the surfaces, and gross wear is observed.

Experimentally, wear has turned out to be a relatively random variable. However, it is possible to set up experimentally a repetitive stick-slip relaxation cycle and use transducers to measure various physical constants of the cycle. From the duration of the stick phase, and of the slip phase, and from measurable mechanical constants, the adhesion between surface and slider can be determined. Adhesion is a chemical and electrical property of the two surfaces in contact; because of the catastrophic nature of break-free, the exact moment of individual breakfree and the corresponding adhesion are difficult to measure unless a repetitive relaxation cycle is established. If such a cycle is established, the adhesion at breakfree can be unambiguously computed from the equations of the cycle and various physical measurements which can be made with relative ease and accuracy.

#### 4. 4. 2 IBM 7090 Computer Analysis of the Stick-Slip Relaxation Cycle - Initial Results

An analysis of the stick-slip relaxation cycle, taking into account the dynamic properties of the slider and of the surface has been conducted. Under the present program, a considerable extension of this treatment has furnished the complete solution, and has been placed on the IBM 7090 computer. The results establish various correlations between the physical constants of the surface and of the slider, the observable variables of position and velocity of slider and of surface element at stick and at slip, and the duration of stick and of slip in the case when a repeating relaxation cycle has been established. Five major parameters are involved, of which probably the most important ones for a given system are the duration of stick and the duration of slip.

Several examples of the type of relation to be observed between the duration of stick, under conditions when stick-slip occurs, and the normalized force at breakfree were given in the Quarterly Report 3. One is shown in figure 11. Figure 12 shows the way in which the force at breakfree and the restoring force develop. The manner in which the buildup occurs, and the physical description of the resulting behavior was described nonmathematically in detail in Quarterly Report 3; the manner of making measurements to obtain the force information in cases when no stick-slip cycle is observed was also described in Quarterly Report 3. The subsequent period has yielded the complete solution.

In the analysis of the complete solution under this contract, the results of 15 hours computer time on the IBM 1401, and 3 hours computer time on the IBM 7090 have been incorporated to date. Of the parameters of the final equations, the values shown in table 3 have been computed for all values of the reduced variable representing duration of stick by steps of 0.01, 0.05, or 0.10, as necessary, in the range from 0 to 40. In view of future applications, both the results to be expected from the natural behavior of materials and the results from responses in which the restoring force has been artificially enhanced have been computed.

Radically different behavior is predicted for a metal slider against a plastic surface, as compared to a metal against metal or soft material against a metal surface. Forbidden regions of parameter combinations and type of response (e. g., figure 13) to be anticipated indicate that for the study of semiconductor surfaces, a relatively heavy and stiff stylus will yield the maximum amount of information.

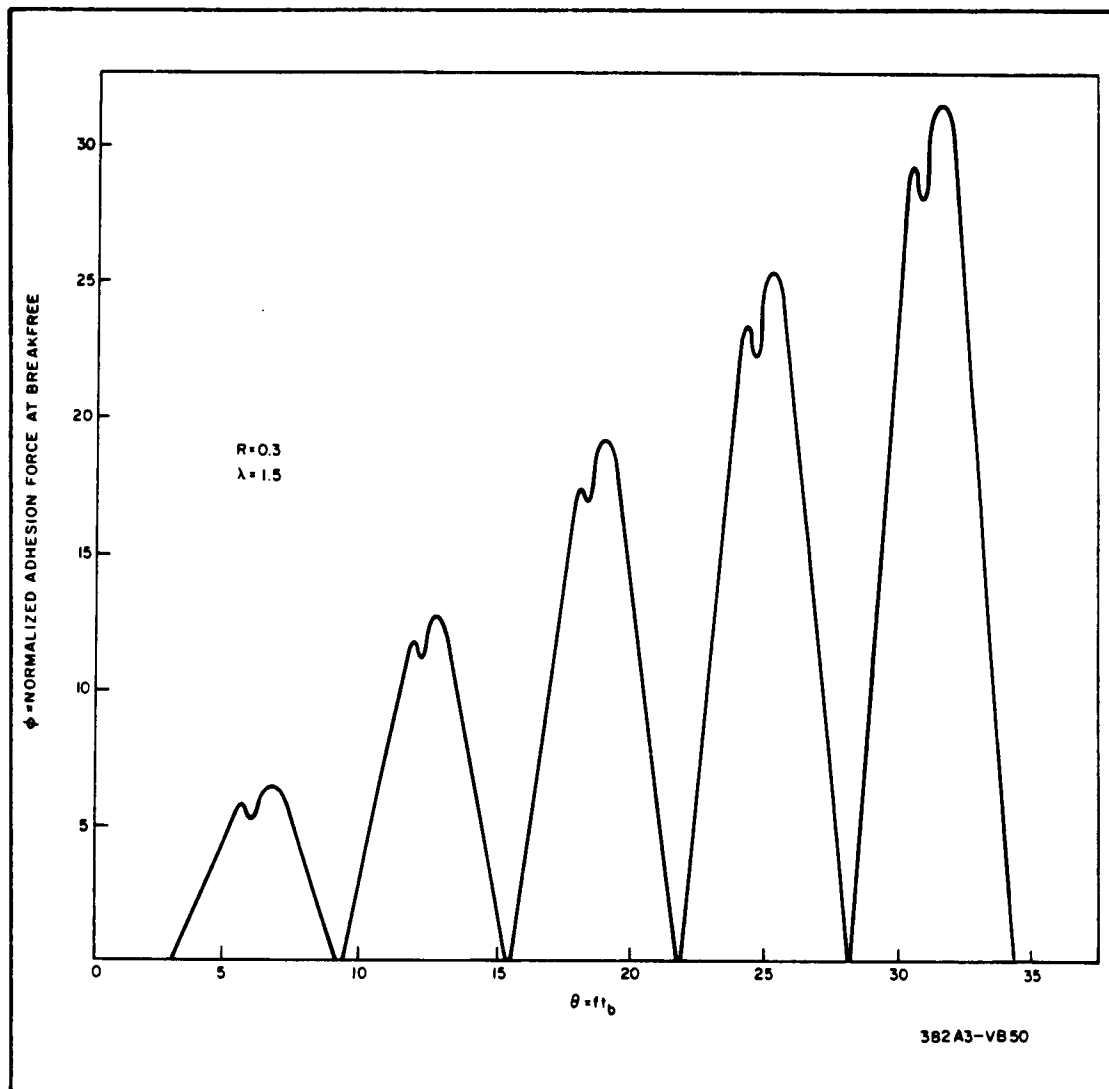


Figure 11.  $\phi$  the Normalized Force at Breakfree vs the Duration of the Stick-Slip Cycle Where  $\lambda$  Is Greater Than 1

For any given combination of material design parameters and relative speed of slider and moving surface, the adhesion force between the two, and therefore the horizontal component of the force, increases with time with a characteristic time-dependence curve which is a function of the nature of the materials in contact. The restoring force also increases, nearly linearly at first, but eventually very sharply. If the moment at which the restoring force equals the adhesional force corresponds to a point on the characteristic

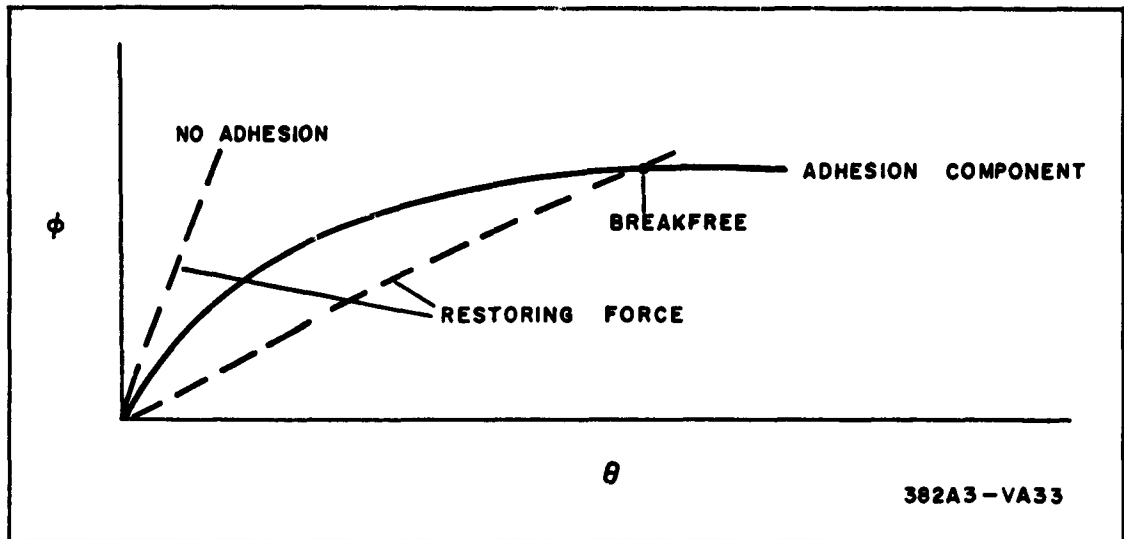


Figure 12a. Composite of  $\phi$  vs  $\theta$  Pairs That Yield a Stick-Slip Relaxation Cycle

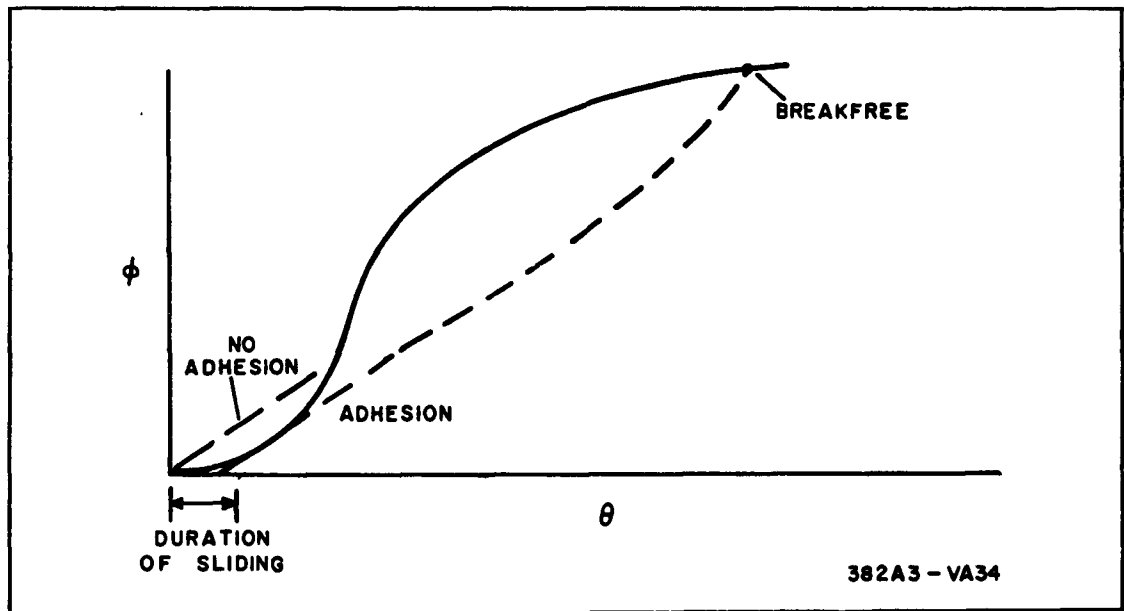


Figure 12b. Stick Observed as a Restoring Force Builds Up Nonlinearly

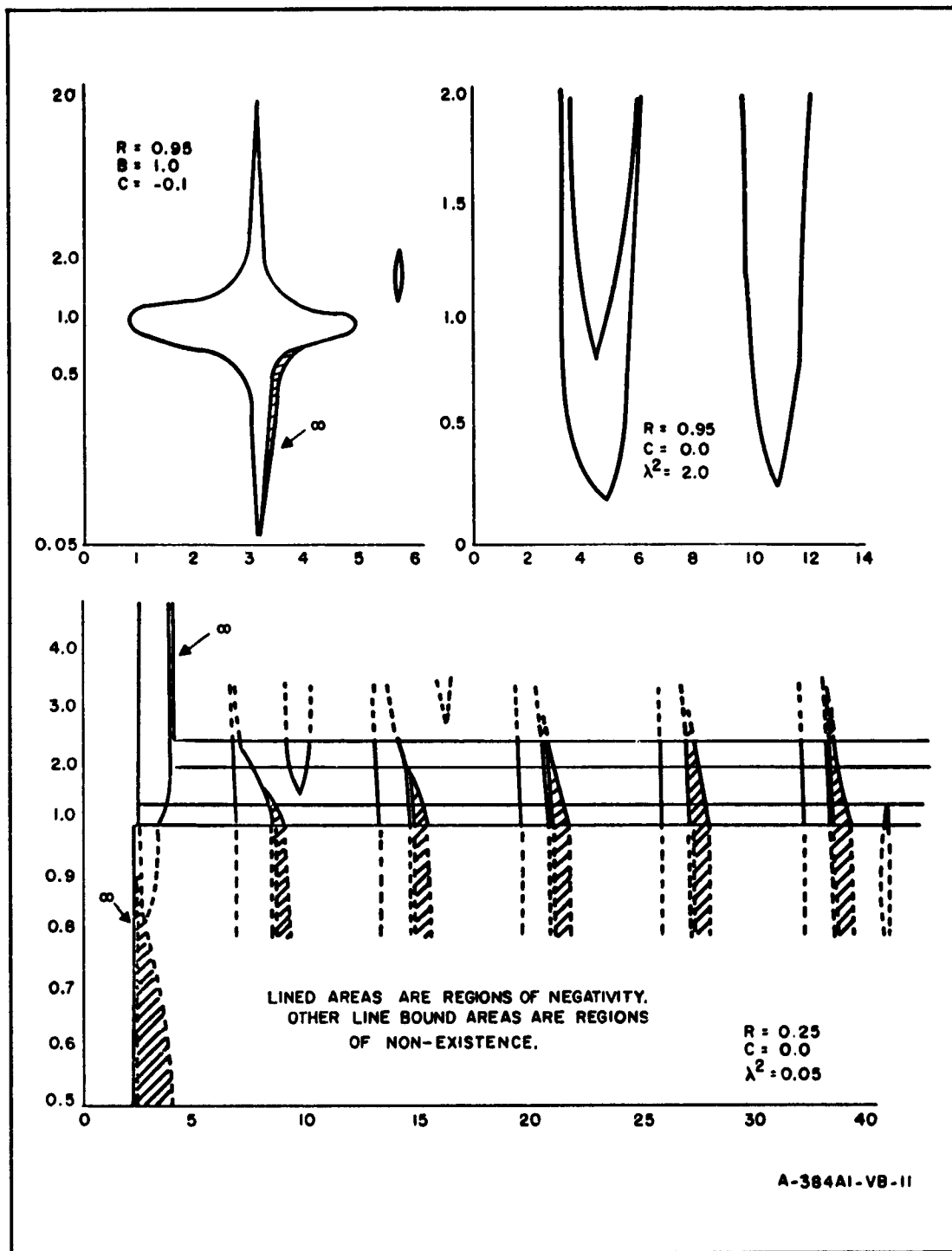


Figure 13. Existence Regions and Forbidden Regions of Stick-Slip Solution

TABLE 3  
COMPUTED PARAMETERS

$\theta_R$  = Range of  $\theta$   
 $\theta_I$  = Increments of  $\theta$

R = 0.250

$\lambda^2 = 0.05$									
C	B = 0		B = 0.250		B = 0.500		B = 0.750		$\theta_I$
	$\theta_R$	$\theta_I$	$\theta_R$	$\theta_I$	$\theta_R$	$\theta_I$	$\theta_R$	$\theta_I$	
-1.500	0-2.30	0.05	0-2.30	0.05	0-40	0.05	0-2.30	0.05	0.05
-0.375	0-2.30	0.05	0-2.30	0.05	0-2.30	0.05	0-2.30	0.05	
0	0-2.25	0.05	0-2.30	0.05	0-2.30	0.05	0-2.30	0.05	
0.375	0-2.25	0.05	0-2.30	0.05	0-2.30	0.05	0-2.30	0.05	
1.500	0-2.25	0.05			0-2.25	0.05			0.05
C	B = 1.00		B = 1.25		B = 1.50		B = 2.00		
-1.500	0-40	0.05					0-40	0.05	0.05
-0.375	0-40	0.05	0-40	0.05	0-40	0.05	0-3.95	0.05	
0	0-40	0.05	0-40	0.05	0-40	0.05	0-40	0.05	
0.375	0-23	0.05	0-23	0.05	0-40	0.05	0-40	0.05	
1.500	0-23	0.05					0-3.95	0.05	0.05
C	$\lambda^2 = 0.100$				$\lambda^2 = 0.125$				$\lambda^2 = 0.250$
	B = 1.25		B = 1.50		B = 1.50		B = 1.25		
-0.375	0-190	0.05	0-40	0.05	0-40	0.05	0-40	0.05	0.05
0	0-40	0.05	0-40	0.05	0-40	0.05	0-40	0.05	
0.375	0-40	0.05	0-190	0.05	0-170	0.05	0-40	0.05	

TABLE 3 (Continued)

R = 0.250

 $\theta_R$  = Range of  $\theta$   
 $\theta_I$  = Increments of  $\theta$ 

C	$\lambda^2 = 0.275$		$\lambda^2 = 0.500$			
	B = 1.50		B = 0		B = 0.250	
	$\theta_R$	$\theta_I$	$\theta_R$	$\theta_I$	$\theta_R$	$\theta_I$
-1.500			0-40	0.05		0-40
-0.375	0-40	0.05	0-40	0.05	0-40	0.05
0	0-40	0.05	0-40	0.05	0-40	0.05
0.375	0-40	0.05	0-40	0.05	0-40	0.05
1.500			0-40	0.05	0-40	0.05
C	$\lambda^2 = 0.750$		$\lambda^2 = 1.000$			
	B = 0.750		B = 1.000		B = 1.250	
	$\theta_R$	$\theta_I$	$\theta_R$	$\theta_I$	$\theta_R$	$\theta_I$
-1.500			0-40	0.05		
-0.375	0-40	0.05	0-40	0.05	0-40	0.10
0	0-40	0.05	0-40	0.05	0-40	0.10
0.375	0-40	0.05	0-40	0.05	0-40	0.10
1.500			0-40	0.05	0-40	0.10
C	$\lambda^2 = 0.500$		$\lambda^2 = 0.625$			
	B = 2.000		B = 1.50		$\lambda^2 = 0.775$	
	$\theta_R$	$\theta_I$	$\theta_R$	$\theta_I$	$\lambda^2 = 0.900$	
-1.500	0-40	0.05			B = 1.25	
-0.375	0-40	0.05	0-40	0.10	0-40	0.10
0	0-40	0.05	0-40	0.10	0-40	0.10
0.375	0-40	0.05	0-40	0.10	0-40	0.10
1.500	0-40	0.05	0-40	0.10	0-40	0.10

TABLE 3 (Continued)

$R = 0.250$

$\theta_R = \text{Range of } \theta$   
 $\theta_I = \text{Increments of } \theta$

C	$\lambda^2 = 1.000$							
	B = 0		B = 0.250		B = 0.500		B = 0.750	
	$\theta_R$	$\theta_I$	$\theta_R$	$\theta_I$	$\theta_R$	$\theta_I$	$\theta_R$	$\theta_I$
-1.500	0-40	0.10			0-40	0.10		
-0.375	0-40	0.10	0-40	0.10	0-40	0.10	0-40	0.10
0	0-40	0.10	0-40	0.10	0-40	0.10	0-40	0.10
0.375	0-40	0.10	0-40	0.10	0-40	0.10	0-40	0.10
1.500	0-40	0.10	0-40	0.10	0-40	0.10	0-40	0.10
C	B = 1.000		B = 1.250		B = 1.500		B = 2.000	
-1.500	0-40	0.10					0.40	0.10
-0.375	0-40	0.10	0-40	0.10	0-40	0.10	0.40	0.10
0	0-40	0.10	0-40	0.10	0-40	0.10	0.40	0.10
0.375	0-40	0.10	0-40	0.10	0-40	0.10	0.40	0.10
1.500	0-40	0.10	0-40	0.10	0-40	0.10	0.40	0.10
C	$\lambda^2 = 2.000$							
	B = 0		B = 0.250		B = 0.500		B = 0.750	
-1.500	0-40	0.10			0-40	0.10		
-0.375	0-40	0.10	0-40	0.10	0-40	0.10	0.40	0.10
0	0-40	0.10	0-40	0.10	0-40	0.10	0-40	0.10
0.375	0-40	0.10	0-40	0.10	0-40	0.10	0-40	0.10
1.500	0-40	0.10	0-40	0.10	0-40	0.10	0-40	0.10



$\theta_R$  = Range of  $\theta$   
 $\theta_I$  = Increments of  $\theta$

TABLE 3 (Continued)

R = 0.250

C	B = 1.000		B = 1.250		B = 1.500		B = 2.000	
	$\theta_R$	$\theta_I$	$\theta_R$	$\theta_I$	$\theta_R$	$\theta_I$	$\theta_R$	$\theta_I$
-1.500	0-40	0.10					0-40	0.10
-0.375	0-40	0.10	0-40	0.10	0-40	0.10	0-40	0.10
0	0-40	0.10	0-40	0.10	0-40	0.10	0-40	0.10
0.375	0-40	0.10	0-40	0.10	0-40	0.10	0-40	0.10
1.500	0-40	0.10					0-40	0.10
$\lambda^2 = 20.00$								
C	B = 0		B = 0.250		B = 0.500		B = 0.750	
	$\theta_R$	$\theta_I$	$\theta_R$	$\theta_I$	$\theta_R$	$\theta_I$	$\theta_R$	$\theta_I$
-1.500	0-40	0.10			0-40	0.10		
-0.375	0-40	0.10	0-40	0.10	0-40	0.10	0-40	0.10
0	0-40	0.10	0-40	0.10	0-40	0.10	0-40	0.10
0.375	0-40	0.10	0-40	0.10	0-40	0.10	0-40	0.10
1.500	0-40	0.10			0-40	0.10		
$\lambda^2 = 20.00$								
C	B = 1.000		B = 1.250		B = 1.500		B = 2.000	
	$\theta_R$	$\theta_I$	$\theta_R$	$\theta_I$	$\theta_R$	$\theta_I$	$\theta_R$	$\theta_I$
-1.500	0-40	0.10					0-40	0.10
-0.375	0-40	0.10	0-40	0.10	0-40	0.10	0-40	0.10
0	0-40	0.10	0-40	0.10	0-40	0.10	0-40	0.10
0.375	0-40	0.10	0-40	0.10	0-40	0.10	0-40	0.10
1.500	0-40	0.10					0-40	0.10

R = 0.750

TABLE 3 (Continued)

$\theta_R$  = Range of  $\theta$   
 $\theta_I$  = Increments of  $\theta$

C	$\lambda^2 = 0.050$							
	B = 0		B = 0.250		B = 0.500		B = 0.750	
	$\theta_R$	$\theta_I$	$\theta_R$	$\theta_I$	$\theta_R$	$\theta_I$	$\theta_R$	$\theta_I$
-0.500	0-2.90	0.05			0-15.45	0.05		
-0.125	0-2.90	0.05	0-2.90	0.05	0- 9.15	0.05	0-3.40	0.05
0	0-2.90	0.05	0-2.90	0.05	0- 9.15	0.05	0-3.40	0.05
0.125	0-2.90	0.05	0-2.90	0.05	0- 3.45	0.05	0-3.40	0.05
0.500	0-2.85	0.05			0- 2.90	0.05		
C	$\lambda^2 = 0.050$							
	B = 1.000		B = 1.500		B = 2.000		$\lambda^2 = 0.10$	
	$\theta_R$	$\theta_I$	$\theta_R$	$\theta_I$	$\theta_R$	$\theta_I$	$\theta_R$	$\theta_I$
-0.500	0-3.40	0.05			0-3.40	0.05		
-0.125	0-3.40	0.05			0-3.40	0.05		
0	0-40	0.05	0-3.40	0.05	0-3.35	0.05	0-3.50	0.05
0.125	0-3.40	0.05			0-3.35	0.05		
0.500	0-3.40	0.05			0-3.40	0.05		

R = 0.750

TABLE 3 (Continued)

 $\theta_R$  = Range of  $\theta$   
 $\theta_I$  = Increments of  $\theta$ 

C	$\lambda^2 = 0.125$		$\lambda^2 = 0.275$		$\lambda^2 = 0.500$			
	B = 1.50		B = 1.50		B = 0		B = 0.250	
	$\theta_R$	$\theta_I$	$\theta_R$	$\theta_I$	$\theta_R$	$\theta_I$	$\theta_R$	$\theta_I$
-0.500					0-40	0.05		
-0.125					0-1.90	0.05	0-1.90	0.05
0	0-3.55	0.05	0-3.85	0.05	0-1.90	0.05	0-1.90	0.05
0.125					0-1.90	0.05	0-1.90	0.05
0.500					0-1.90	0.05		
$\lambda^2 = 0.500$								
C	B = 0.500		B = 0.750		B = 1.000		B = 1.500	
	0-40	0.05	0-27.05	0.05	0-40			
	0-8.20	0.05	0-27.05	0.05	0-27.05			
	0-1.90	0.05	0-1.95	0.05	0-40		0-29.5	0.10
	0-1.90	0.05	0-1.90	0.05	0-1.95			
0.500	0-1.90	0.05			0-1.90			

R = 0.750

TABLE 3 (Continued)

 $\theta_R$  = Range of  $\theta$   
 $\theta_I$  = Increments of  $\theta$ 

C	$\lambda^2 = 0.500$		$\lambda^2 = 0.625$		$\lambda^2 = 0.775$		$\lambda^2 = 1.000$	
	B = 2.000		B = 1.50		B = 1.50		B = 0	
	$\theta_R$	$\theta_I$	$\theta_R$	$\theta_I$	$\theta_R$	$\theta_I$	$\theta_R$	$\theta_I$
-0.500		0.05					0-40	0.10
-0.125	0-4.40	0.05					0-40	0.10
0	0-4.35	0.05		0.10	0-40	0.10	0-40	0.10
0.125	0-4.35	0.05					0-40	0.10
0.500	0-1.90	0.05					0-40	0.10
$\lambda^2 = 1.000$								
C	B = 0.250		B = 0.500		B = 0.750		B = 1.000	
	$\theta_R$	$\theta_I$	$\theta_R$	$\theta_I$	$\theta_R$	$\theta_I$	$\theta_R$	$\theta_I$
-0.500			0-40	0.10			0-40	0.10
-0.125	0-40	0.10	0-40	0.10	0-40	0.10	0-40	0.10
0	0-40	0.10	0-40	0.10	0-40	0.10	0-40	0.10
0.125	0-40	0.10	0-40	0.10	0-40	0.10	0-40	0.10
0.500			0-40	0.10			0-40	0.10

R = 0.750

TABLE 3 (Continued)

 $\theta_R$  = Range of  $\theta$   
 $\theta_I$  = Increments of  $\theta$ 

C	$\lambda^2 = 1.000$				$\lambda^2 = 2.000$			
	B = 1.500		B = 2.000		B = 0		B = 0.250	
	$\theta_R$	$\theta_I$	$\theta_R$	$\theta_I$	$\theta_R$	$\theta_I$	$\theta_R$	$\theta_I$
-0.500			0-40	0.10	0-40	0.10	0-40	0.10
-0.125			0-40	0.10	0-40	0.10	0-40	0.10
0	0-40	0.10	0-40	0.10	0-40	0.10	0-40	0.10
0.125			0-40	0.10	0-40	0.10	0-40	0.10
0.500			0-40	0.10	0-40	0.10	0-40	0.10
$\lambda^2 = 2.000$								
C	B = 0.500		B = 0.750		B = 1.000		B = 1.500	
	$\theta_R$	$\theta_I$	$\theta_R$	$\theta_I$	$\theta_R$	$\theta_I$	$\theta_R$	$\theta_I$
	$\theta_R$	$\theta_I$	$\theta_R$	$\theta_I$	$\theta_R$	$\theta_I$	$\theta_R$	$\theta_I$
-0.500	0-40	0.10	0-40	0.10	0-40	0.10	0-40	0.10
-0.125	0-40	0.10	0-40	0.10	0-40	0.10	0-40	0.10
0	0-40	0.10	0-40	0.10	0-40	0.10	0-40	0.10
0.125	0-40	0.10	0-40	0.10	0-40	0.10	0-40	0.10
0.500	0-40	0.10	0-40	0.10	0-40	0.10	0-40	0.10

R = 0.750

TABLE 3 (Continued)

$\theta$  = Range of  $\theta$   
 $\theta$  = Increments of  $\theta$

C	$\lambda^2 = 2.000$						$\lambda^2 = 20.00$																	
	B = 2.000						B = 0																	
	$\theta$		$\theta_I$				$\theta$		$\theta_I$															
	$\theta_R$	$\theta_I$	$\theta_R$	$\theta_I$	$\theta_R$	$\theta_I$	$\theta_R$	$\theta_I$	$\theta_R$	$\theta_I$	$\theta_R$	$\theta_I$												
-0.500	0-40	0.10	0-40	0.10	0-40	0.10	0-40	0.10	0-40	0.10	0-40	0.10												
-0.125	0-40	0.10	0-40	0.10	0-40	0.10	0-40	0.10	0-40	0.10	0-40	0.10												
0	0-40	0.10	0-40	0.10	0-40	0.10	0-40	0.10	0-40	0.10	0-40	0.10												
0.125	0-40	0.10	0-40	0.10	0-40	0.10	0-40	0.10	0-40	0.10	0-40	0.10												
0.500	0-40	0.10	0-40	0.10	0-40	0.10	0-40	0.10	0-40	0.10	0-40	0.10												
C	B = 0.750						B = 1.000						B = 1.500						B = 2.000					
	0-40		0.10				0-40		0.10				0-40		0.10				0-40		0.10			
	0-40		0.10				0-40		0.10				0-40		0.10				0-40		0.10			
	0-40		0.10				0-40		0.10				0-40		0.10				0-40		0.10			

curves in the existence region of the solutions of the equations, a stick-slip cycle is set up. If this is not the case, noncyclic breakfree occurs. The nature of the existence regions of the solution is therefore of importance to the experimental characterization of the motions to be observed experimentally.

#### 4.4.3 Use of the Stick-Slip Cycle Measurements to Supplement the Surface Information Yielded by the Electrical Frictional Probe

The correlations between the physical constants of the surface and the observables in the stick-slip behavior of the probe progressing over the surface enable the utilization of these observables to determine the rate of growth of adhesion between the slider and the surface. This permits the calculation of the coefficient of friction, as well as information on transient behavior. Quarterly Report 3 indicated the way in which the information can be used and the information obtainable from the frictional drag of the probe when no stick-slip cycle has been set up.

Since the establishment of the adhesion between the slider and the surface depends upon the chemical nature and the surface geometry of the two surfaces in contact, additional information can be obtained and correlated against the processing of the particular semiconductor sample. More pertinent, it yields additional information which can be used in analyzing the overall nature of the material and its defects in a search for additional mechanisms likely to cause failure of electronic components.

#### 4.5 SURFACE STUDIES: THE NONUNIFORMITY AND AGING OF A SEMICONDUCTOR SURFACE, STUDIED BY PHOTOVOLTAIC RESPONSE

##### 4.5.1 Apparatus

The repetitive contacting apparatus, figure 14, described in Quarterly Reports 2 and 3, was used. The construction design permitted the contact at any desired point on the surface of the wafer to be examined and the pressure with which the probe touched the surface to be controlled. A copper probe, cleaned and polished, was used. The probe was well insulated from

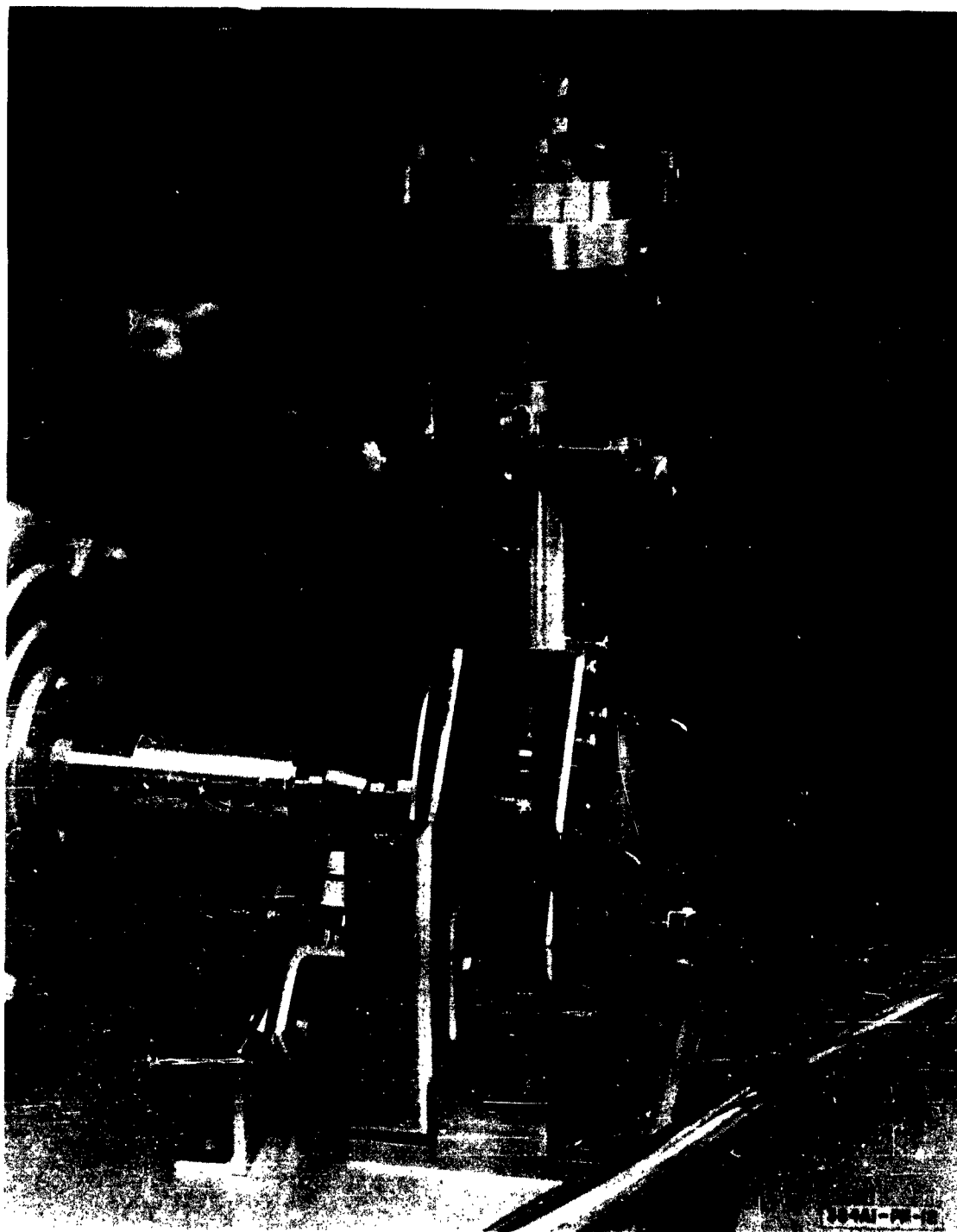


Figure 14. Repetitive Contacting Apparatus



ground and, connected to the input of a high gain oscilloscope. Visible light was directed at the point of contact of the probe and the sample, and chopped by a rotating baffle. The rise and fall times for intensity were of the order of a fraction to 1 millisecond, amply fast for the phenomena to be observed.

Several n- and p-type germanium and silicon samples were examined. At one point on the sample disc, an ohmic connection was made to ground. Therefore, instead of making connections to both ends of a sample and traversing a light spot over the free surface of the material, the probe was put into physical contact with each individual region to be examined. The same pressure was used for all contacts, and response was found to be the same for repeated contacts at the same spot, or upon returning to the area after having measured some other spot.

#### 4.5.2 Variation of Photovoltaic Response With Radius on Wafer

A freshly prepared disc of 1.2-ohm-cm p-doped silicon showed a dependence of the transient electrical response upon radial distance from the center, irrespective of angular position. In one case, the height of the initial voltage peak varied, increasing as the edge was approached. In another case, the characteristic time of the decay from the initial peak decreased as the edge was approached.

Since the photovoltaic response is related to the chemical and electrical properties of the material, such a difference in photo-EMF with radius, irrespective of azimuth, indicates that the fundamental electrical constants of the material differ somewhat as the circumference of the wafer is approached. If a number of transistors or microelectronic devices are fabricated on the same wafer, either the performance parameters of different devices will differ slightly depending upon whether their location on the wafer is in the center or at the edge, or slight changes should be incorporated into the design, as the location of the device on the wafer moves out toward the edge.

#### 4.5.3 Response to Chopped Light - Fresh Surface

Similar results were obtained on various materials. A 40-ohm-cm p-doped germanium wafer, with ohmic ground connection, will be described as an example. The wafer was mechanically polished, and etched with CP-4. Contact with different points on the surface yielded essentially the same response everywhere (left-hand column of figure 15), a sharp leading edge to a 50-mv peak followed by a small transient decrease to a steady state condition. Slight differences in the amplitude of the steady state value at different points on the surface were noted, but the waveform was the same.

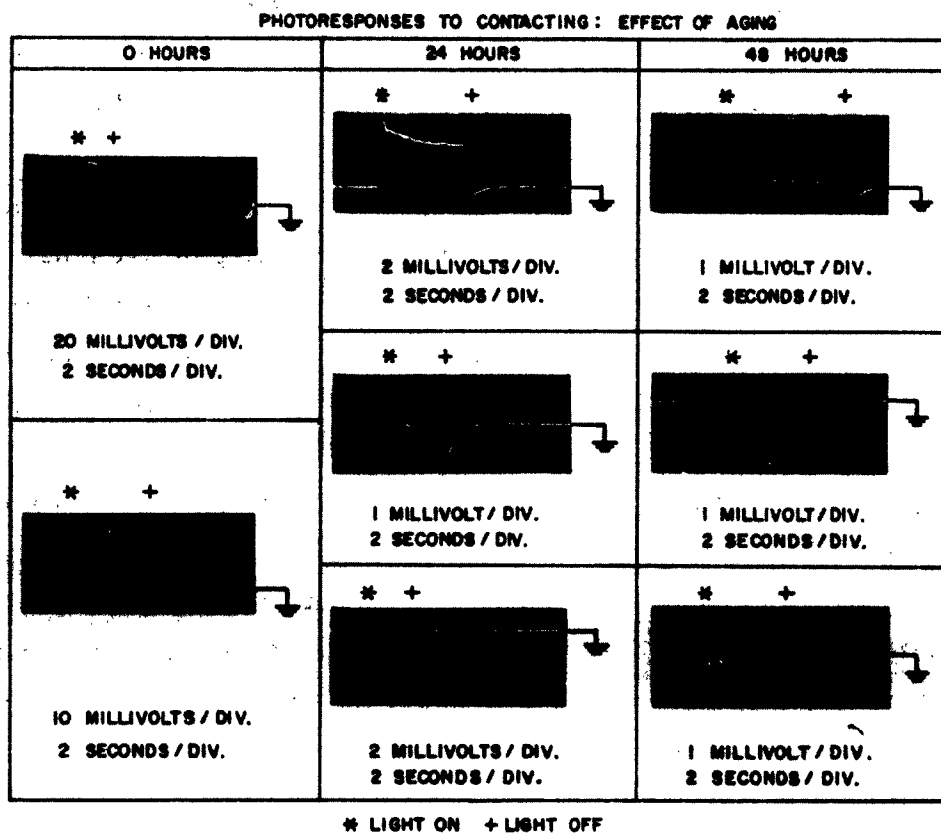


Figure 15. Response of Contact With Different Points on Surface

#### 4. 5. 4 Response to Chopped Light - Aged Surface

After 24 hours in air, five different types of transient shapes were observed, three of which are shown in figure 15. Each type of transient shape was characteristic of a particular point on the surface, and could be obtained repeatedly upon returning to that point of contact. Responses of the first type; i. e., like those obtained just after etching, but of smaller magnitude, were by far the most frequent, constituting approximately 80 percent of the total. The others evidently were characteristic of a different state of the surface at the point. Whereas the initial response, as well as the usual response after 24 hours, was positive, at several points the response after 24 hours was negative, and at others, it commenced positive and progressed to negative in a manner somewhat reminiscent of the shape of the curve in electret behavior. Surface changes were evidently not uniform across the sample.

After an additional 24-hour delay, the main type of response again decreased in amplitude, and again showed variations, being of five types, three of which are shown in figure 15. The percentage of responses which were of the same type as those originally observed had decreased somewhat, so that more regions of the sample were showing departures from original composition or state.

It may be concluded that the aging of a semiconducting disc surface does not take place uniformly. Instead, it commences independently at a number of separate points on the surface, and, to some extent at least, progresses outward from them. It is possible that a number of different reactions are taking place, depending upon the activity of different regions of the surface, distributions of defects, and the number of components present in the ambient atmosphere.

Each particular type of response has its own characteristic. For example, the right center trace in figure 15 is a negative rapid transient when the light

is cut on, followed by a slow rise in the negative direction. When the light is cut off, a positive transient is followed by a very slow decay time back to ground. The experimenter can easily distinguish the type from other types. Whether each type corresponds to only one chemical or energy state has not yet been determined, but it is reasonable to believe that each chemical or energy state is characterized by only one type of response.

The aging continues at a slow rate at all points presumably until no further photoresponse is observed.

Aging in air has two effects; the first is a decrease in amplitude of the original response; the second, progressive alterations of the surface so that portions of it show other types of response.

#### 4.6 SURFACE STUDIES: USE OF THE PHOTOVOLTAIC EFFECT FOR STUDY OF CHEMICAL PROCESSES ON PRECISE LOCATIONS OF SEMICONDUCTOR SURFACES

##### 4.6.1 Decrease of Initial Photovoltaic Response as a Function of Aging

The magnitude of the initial rise of the most common type of photovoltaic response described just above decayed with the length of time the wafer was in air after a CP-4 etch, as indicated in figure 16. For 40-ohm-cm In-doped p-type germanium, therefore, the decay curve is represented by

$$V_{\text{photo-EMF}} = V_o / [1 + (bt)^n], \text{ where } V_o = 50 \text{ mv, } b = 1.30 \text{ sec}^{-1}, n = 1.01.$$

Assuming that n really is equal to 1, the difference being the result of experimental error:

$$\frac{dV}{dt} = -aV^2 \tag{17}$$

where

$$a = 26 \text{ (volt sec)}^{-1}$$

This is the equation of a second order chemical reaction, and if it is assumed that the photovoltage is proportional either to the concentration  $x$  of a substance or to the difference in concentration ( $C_o - x$ ) between a given concentration and that observed as time passes, either of two usual chemical kinetics expressions for the change of the concentration with time is obtained.

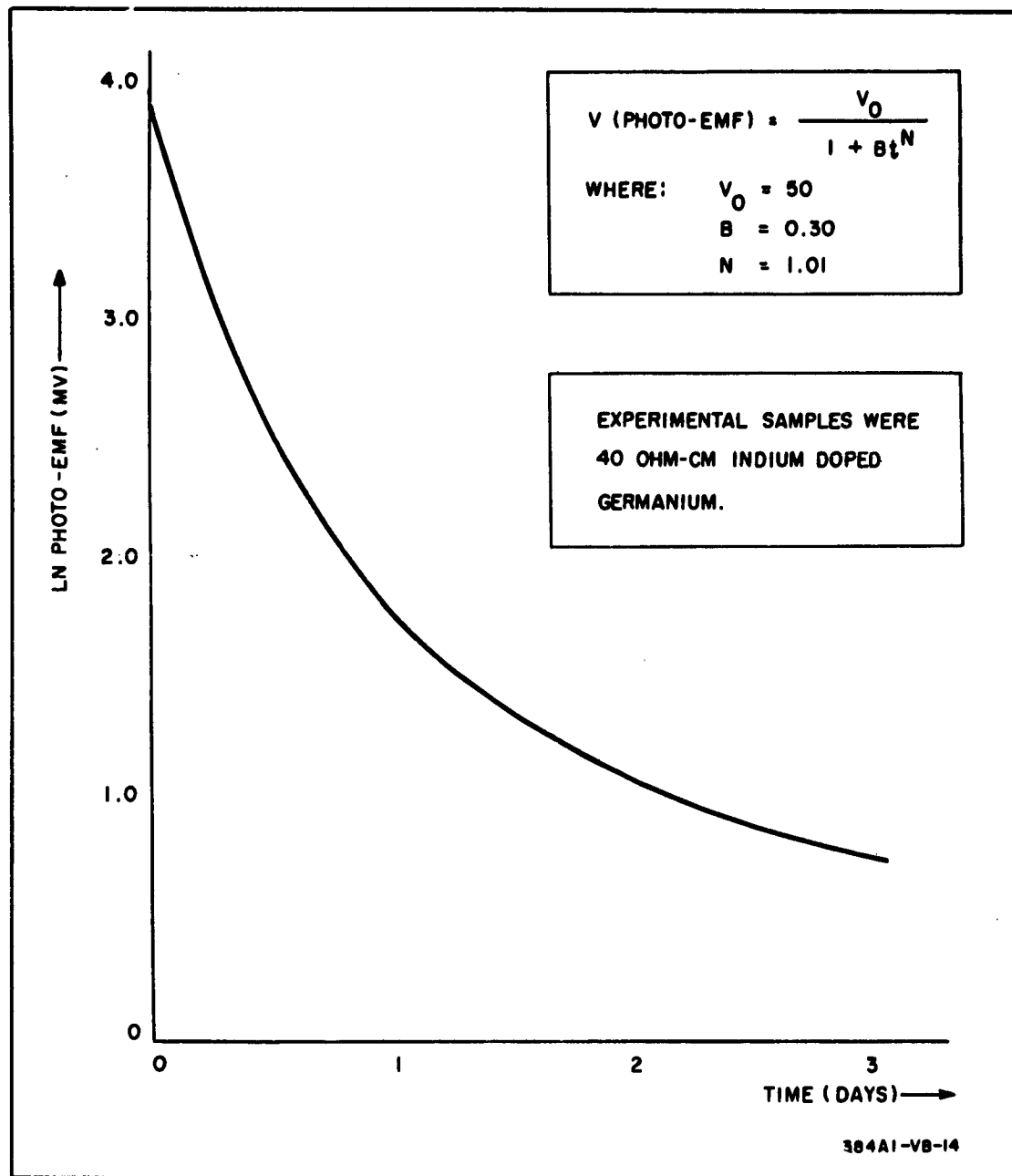


Figure 16. Photo-EMF Response Decay Rate  
for Extrinsic Germanium

#### 4.6.2 Effect of Chemical Treatments - Initial Results

If, at about 24 hours the surface is again cleaned by etching with CP-4, the original photoresponse is again obtained. If it is etched after 24 hours with HF instead of CP-4, the photovoltaic response remains unchanged. This implies that the chemical change responsible for the decrease of the voltage maximum is not a surface oxidation by ambient oxygen. From thermodynamic values of free energy, it would seem possible that the effective factor in restoring the original voltage is the free bromine which could enter into a weak combination with the freshly exposed surface germanium or indium and gradually decompose in an atmospheric ambient. Some doubt is cast on this by the experiments described in the next paragraph, however.

Grinding the surface with alumina in deionized water at the 24-hour period nearly restores the original response. It appeared possible therefore that the governing factor was the ability to restore a fresh nascent Si surface of interior composition, or of interior composition with an oxide layer of thickness of the order of a few Angstroms.

Because these experiments indicated information was implicit in photovoltaic studies of chemical processes, a more complete investigation was undertaken of the types of processes which might be taking place upon semiconducting wafers during various processes commonly used in solid state device technology. These are described in succeeding paragraphs.

#### 4.7 CHEMICAL STUDY OF ETCHING PROCESSES BY USE OF THE PHOTOVOLTAIC RESPONSE

As in the use of electrical effects to study chemical or mechanical properties or behavior of materials, it must be remembered that the electrical response is affected by chemical, thermal, mechanical, electrical, and other parameters. Sufficient control of the various parameters must be maintained to assure that the conclusions are justified. In general, it has been extremely difficult if not impossible to control, in a single experimental study, all of the many variables associated with surface electrical measurements on semiconductors. When undertaking such work, therefore, a choice must be made with respect to which parameters must be closely controlled and which may be left uncontrolled because of their relatively minimal effects on the outcome of the experiment.

In the present work, it was judged advisable to employ close control over experimental apparatus parameters and semiconductor sample conditions, with maintenance of relatively dust- and static-charge-free ambient conditions being the only controls over the normally random environmental variables. This most closely approximates conventional semiconductor device fabrication conditions, and should be of maximum value in detecting failure mechanisms and increasing reliability of the end product component.

With these procedural objectives as a goal, the experimental work was performed as described in the following paragraphs.

##### 4.7.1 Initial Sample Preparation

To maintain parameter control with respect to germanium samples chosen for the experimental work, a single 40-ohm-cm In-doped germanium wafer was scribed and broken as illustrated in figure 17. Because of their uniformity of size and similarity with respect to position on the original wafer, the eight center sections, numbered 7 through 14, were chosen as the main samples for study. The six edge sections were retained for future work. By using the center sections, any differences in dislocation densities and impurity concentrations between the center and edge of the original boule were avoided.

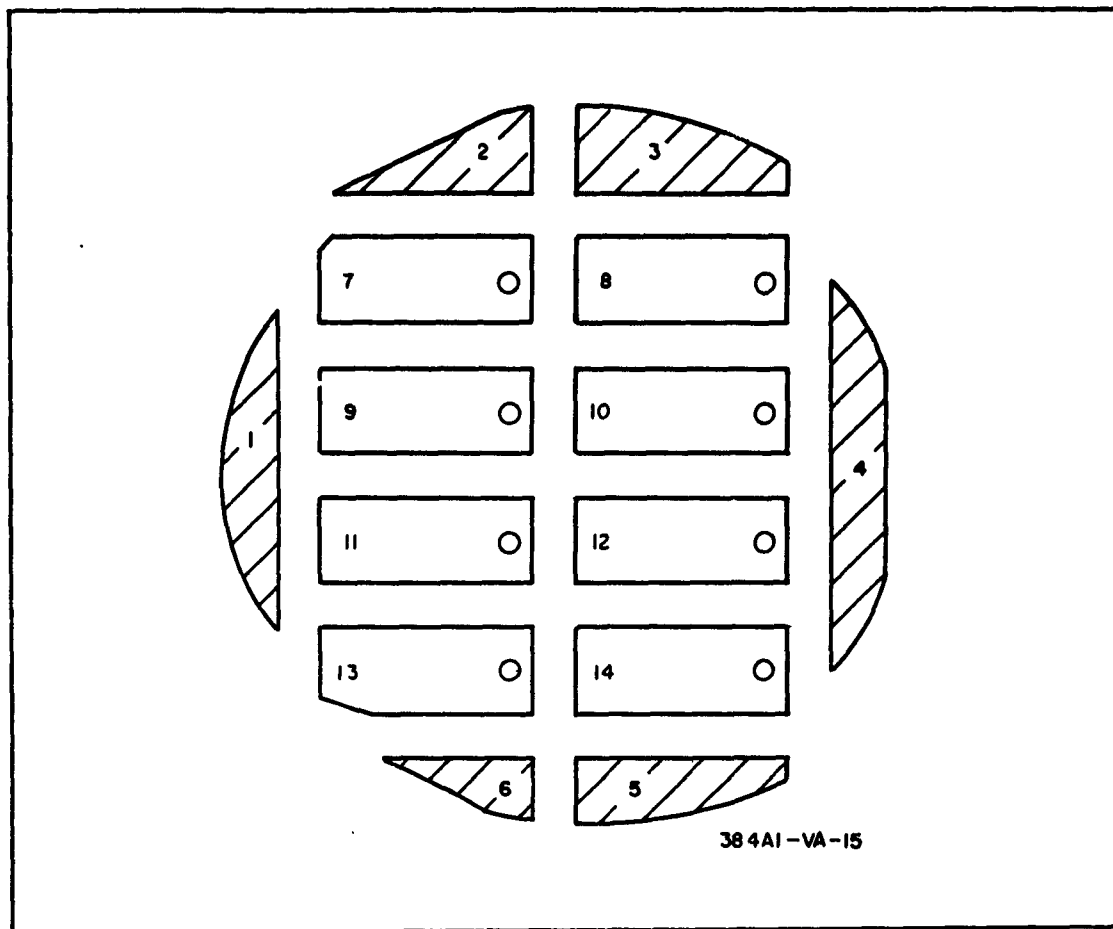


Figure 17. Germanium Wafer Sectioning Scheme

Preparation for the eight main samples proceeded according to the following stepwise scheme:

- a. All samples were degreased with boiling trichloroethylene in three successive wash operations and then dried in trichloroethylene vapor.
- b. To form ohmic junctions, a 5-mil-diameter silver lead was attached to each piece with tin-lead coreless solder, using a saturated water solution of zinc chloride as a flux. (To minimize sputtering and surface contamination, a minimum amount of this flux was used.) The position of lead attachment to each piece is indicated by the small circles in figure 17.



c. Immediately following lead attachment, all samples were thoroughly washed with clean deionized water to remove all traces of the acid zinc chloride soldering flux.

d. Each sample was then individually potted in an insulating polymer, utilizing small sections of aluminum microwave guide as potting molds (see figure 18). The polymer used for potting was an American Cyanamid Co.

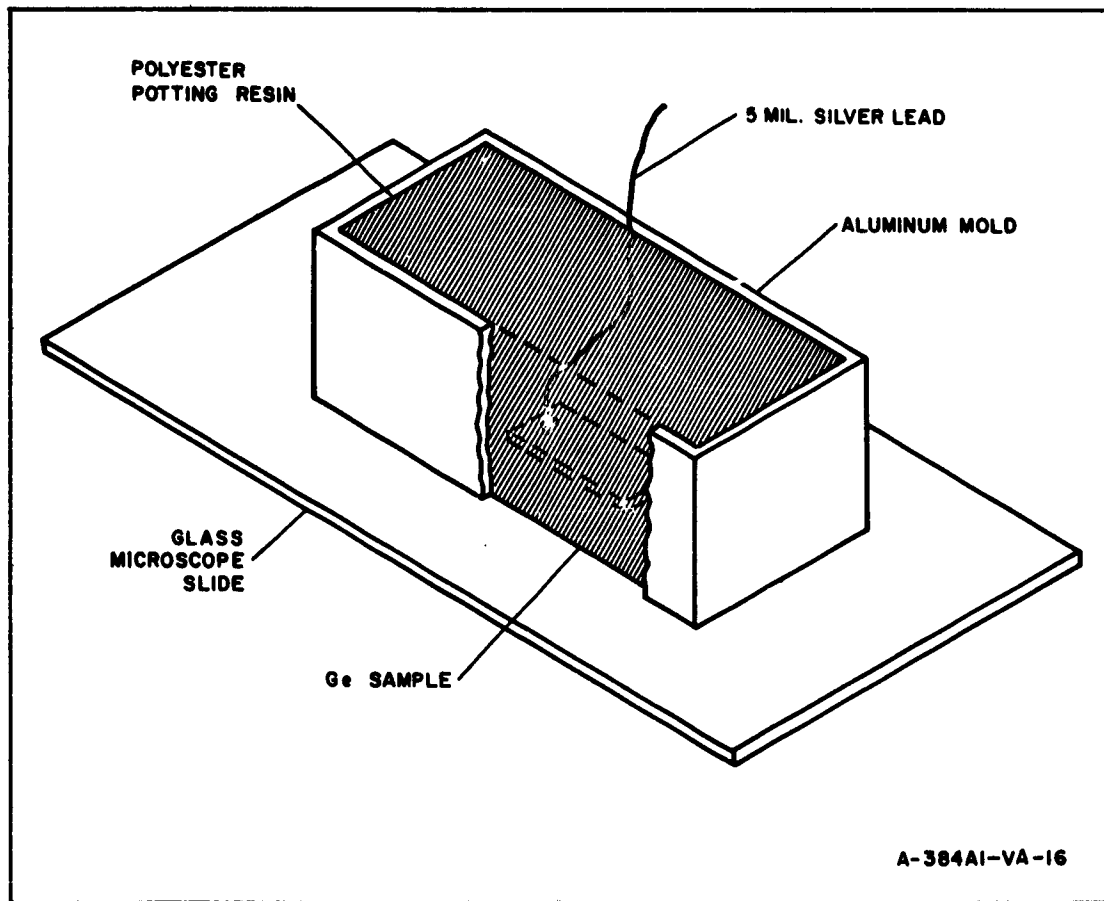


Figure 18. Sketch Showing Potting of Samples

(Laminac) polyester prepolymer dissolved in free styrene monomer. This solution was free radical catalyzed by the addition of 1.5 percent by weight of a 60-percent solution of methyl ethyl ketone peroxide in dimethyl phthalate.

Prior to potting, the entire mold interior and the glass plate top surface were coated with a mold release, consisting of a thin layer of Dow Corning high vacuum silicone grease. The potting compound was then added to the molds as a low viscosity liquid and was permitted an overnight cure before subsequent operations.

e. The potted samples were then removed from the molds and thoroughly degreased with hot trichloroethylene. (The finished sample is illustrated in figure 19.)

f. The samples were then desiccated against phosphorous pentoxide to await final treatment.

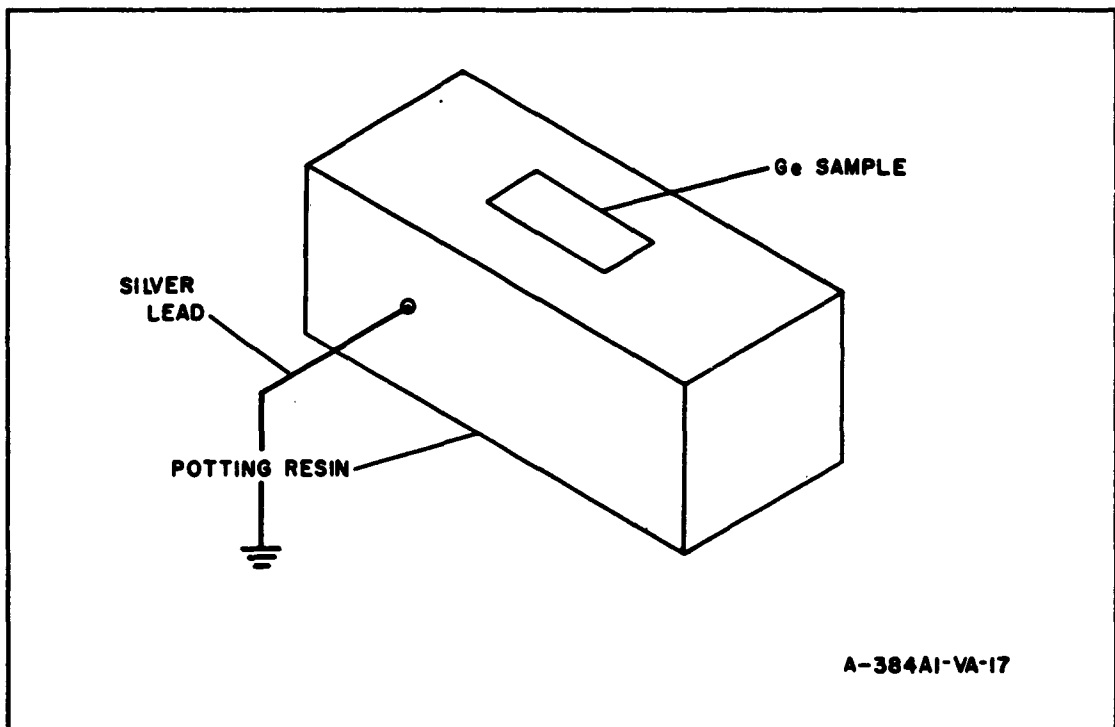


Figure 19. Sketch of Finished Potted Sample

#### 4.7.2 Design and Carrying Out of Experiment

As a first step in the experiment, all eight samples were uniformly lapped for 3 minutes using Lapmaster No. 1950 lapping compound on an optically

flat glass plate. These plates were then thoroughly cleaned in a three-stage ultrasonic wash with deionized water to remove all traces of the lapping abrasive. The grinding technique avoided contact between the mold containing the sample and the grinding bed.

Subsequent to grinding, the eight samples were divided into two groups of four samples each; Group A contained samples 7 through 10 and Group B contained samples 11 through 14. The experimental work for each group then proceeded according to the following stepwise procedures:\*

Group A Procedure

- a. Photoresponse measurement 1/
- b. Desiccation against phosphorous pentoxide for 70 hours
- c. Photoresponse measurement 1/
- d. Sample etch 2/

Sample No.	Etch	Etch Time (seconds)
7	CP-4	20
8	CP-3	20
9	HF-HNO <sub>3</sub> -1	20
10	H <sub>2</sub> O	20

- e. Photoresponse measurement 1/
- f. Desiccation against phosphorous pentoxide for 24 hours
- g. Photoresponse measurement 1/
- h. Desiccation against phosphorous pentoxide for 24 hours
- i. Photoresponse measurement 1/

\* In the figures of response as a function of processing, typical responses are assembled under letters such as a, c, e, g, etc; these groupings indicate that the wafer has completed the processing step in the list of processes below which is identified by that letter.

1/ See following section for description.

2/ See table 4 for etch formulations.

- j. Relap according to previously described procedure
- k. Sample re-etch<sup>2/</sup>

Sample No.	Etch	Etch Time (seconds)
7	CP-4	30
8	HF-HNO <sub>3</sub> -2	80
9	Superoxol	360
10	H <sub>2</sub> O	60

- l. Photoresponse measurement<sup>1/</sup>
- m. Desiccation against phosphorous pentoxide for 24 hours
- n. Photoresponse measurement<sup>1/</sup>

#### Group B Procedure

- a. Sample etch<sup>2/</sup>

Sample No.	Etch	Etch Time (seconds)
11	CP-4	20
12	CP-3	20
13	HF-HNO <sub>3</sub> -1	20
14	H <sub>2</sub> O	20

- b. Photoresponse measurement<sup>1/</sup>
- c. Desiccation against phosphorous pentoxide for 70 hours
- d. Photoresponse measurement<sup>1/</sup>
- e. Relap according to previously described lapping procedure
- f. Sample re-etch<sup>2/</sup>

1/ See following section for description.

2/ See table 4 for etch formulations.

Sample No.	Etch	Etch Time (seconds)
11	CP-4	20
12	CP-3	60
13	HF-HNO <sub>3</sub> -1	190
14	H <sub>2</sub> O	60

- g. Photoresponse measurement <sup>1/</sup>
- h. Desiccation against phosphorous pentoxide for 24 hours
- i. Photoresponse measurement <sup>1/</sup>
- j. Desiccation against phosphorous pentoxide for 6.5 days
- k. Photoresponse measurement <sup>1/</sup>
- l. Sample etched for 10 minutes in concentrated hydrofluoric acid
- m. Photoresponse measurement <sup>1/</sup>

The germanium etch formulations used in this experiment are presented in table 4.

TABLE 4  
GERMANIUM ETCH FORMULATIONS

Ingredient (Units By Vol.)	Etch Type					
	CP-4	CP-4	HF-HNO <sub>3</sub> -1	HF-HNO <sub>3</sub> -2	Superoxol	H <sub>2</sub> O
HF	15	15	15	15	10	
HNO <sub>3</sub>	25	25	25	25		
HC <sub>2</sub> H <sub>3</sub> O <sub>2</sub>	15	15				
H <sub>2</sub> O <sub>2</sub>					10	
Br <sub>2</sub>	0.3					
H <sub>2</sub> O			15		40	100

<sup>1/</sup> See following section for description.

<sup>2/</sup> See table 4 for etch formulations.

#### 4.7.3 Procedures in Photoresponse Measurement

The photoresponse measurements referred to in the test procedures just described were the most critical measurements in the experiment, since they provide a direct photoelectric measure of the effects of various physical and chemical processes upon the surface electrical properties of semiconductors. The procedures followed in making these measurements will therefore be described in detail.

The principal apparatus employed in this work was the "repetitive contact" device described in previous quarterly reports. The device was not used in the repetitive contact mode, but was employed as a stationary mechanism to permit a metal probe to contact a germanium sample with a controlled amount of contact pressure.

This device was used in making all of the photoresponse measurements according to the following stepwise procedure:

- a. The potted sample was placed on the sample platform of the device, and its single ohmic contact lead was soldered to a grounded metal post immediately adjacent to the platform.

- b. A small beryllium-copper spring probe was affixed in the normal probe position for the contact apparatus, and was then positioned over the point on the sample where contact was desired. The platform was raised to permit the probe to contact the sample surface and the platform height was adjusted to provide a constant spring-probe vertical deflection of 20 to 25 mils. (This corresponds to a very light contact pressure.)

- c. The sample surface was then exposed to high intensity illumination from a Sylvania Sun-Gun, and the electrical response of the sample was photographically recorded from the CRT of a Tektronix 545 oscilloscope. For each measurement, the light was shuttered on in a period of the order of 0.02 second, left on for 6 seconds, and then similarly shuttered off, so that each photograph illustrates the total effect of the illumination on-off

sequence. Five areas for photoresponse measurement were defined for each sample, as illustrated in figure 20. Photoresponse measurements were made only on those areas and the area measured was recorded for each measurement.

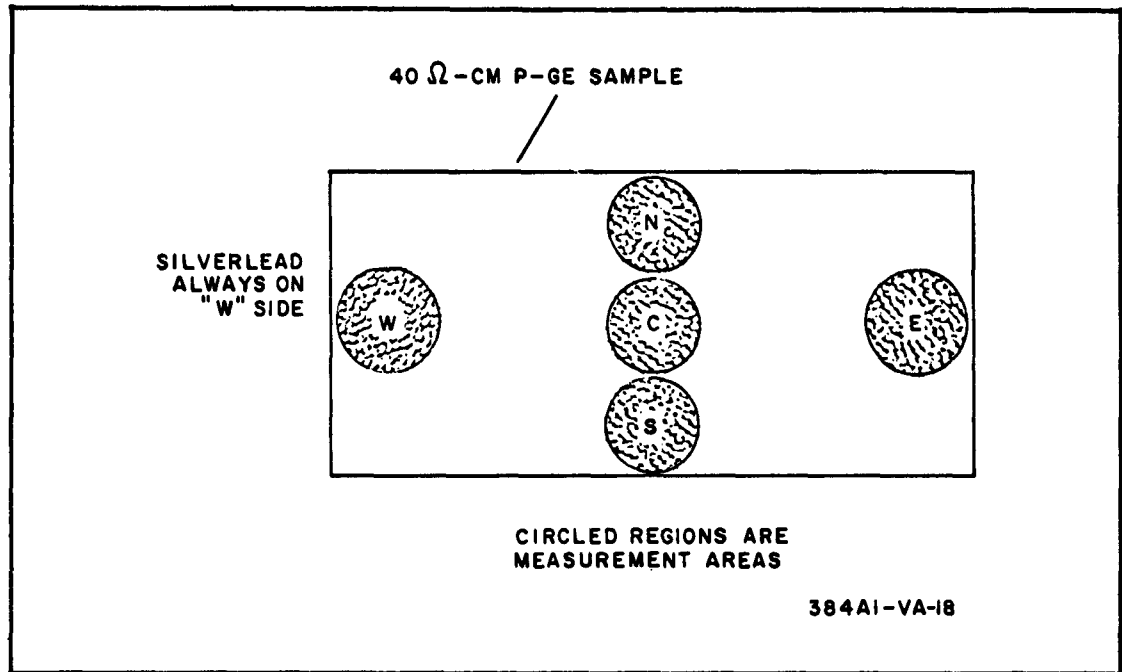


Figure 20. Sample Measurement Areas

This procedure permitted simpler and more accurate location of sample areas having special interest. Such areas might be spots of nonuniform etching, areas containing cracks or fractures, areas having unusually high dislocation densities, or simply areas close to a junction or near an edge of the sample. Such areas are easily distinguishable from normal sample areas in the experiment.

Table 5 summarizes the photoresponse measurements; typical responses are shown in the figures.

TABLE 5  
PHOTORESPONSE MEASUREMENTS

GROUP A										
Sample No.	Procedure Steps (Column Nos. show sample location and Photo. No. - e.g. W-33 is location W, Sample 33)									
	a	c	e	g	i	l	n			
7	N-1, C-2, S-3, W-4, E-5	N-35, C-36	N-51, C-52	N-67, C-68	N-73, C-74	N-110, C-111	N-120, C-121			
8	N-6, C-7, S-8, W-9, E-10	N-37, C-38	N-53, C-54	N-69, C-70	N-75, C-76	N-112, C-113	N-121, C-123, N-124*			
9	N-11, S-12, W-13, E-14	N-39, C-40	N-55, C-56	N-71, C-72	N-77, C-78	N-114, C-115	N-118, C-119			
10	N-15, S-16, W-17, E-18	N-41, C-42	N-57, C-58		N-79, C-80	N-116, C-117	C-125			
GROUP B										
	b	d	g	i	k	m				
11	N-19, S-20, W-21, E-22	N-43, C-44	N-59 C-60	N-81, C-82	N-96, C-97	N-102, C-103				
12	N-23, S-24, W-25, E-26	N-45 C-46	N-61, C-62	N-83, C-84	N-98,	N-104, C-105				
13	N-27, S-28, W-29, E-30	N-47, C-48	N-63, C-64	N-85, C-86	N-99,	N-106, C-107				
14	N-31, S-32, W-33, E-34	N-49, C-50	N-65, C-66	N-87, C-88	N-100, C-101	N-108, C-109				

\* Measurement with probe in deep etch groove.



#### 4.7.4 Responses From Lapped Surfaces

Results of photoresponse measurements made within 30 minutes after sample lapping with alumina abrasive definitely indicated a uniformity of response among all eight samples. In general, this response waveform was of the type shown in figure 21. The characteristics of this response curve were, except for small amplitude variations, precisely the same for all samples lapped in the same manner. Each response, in this regard, showed two distinct components (a and b in figure 21), a very fast low amplitude initial negative response followed by an exponential-like decay to some maximum negative value (on the order of 1 to 3 mv). The curve then either remained essentially flat or showed a slight positive response until illumination was removed, after which the procedure was reversed and the voltage decayed to zero.

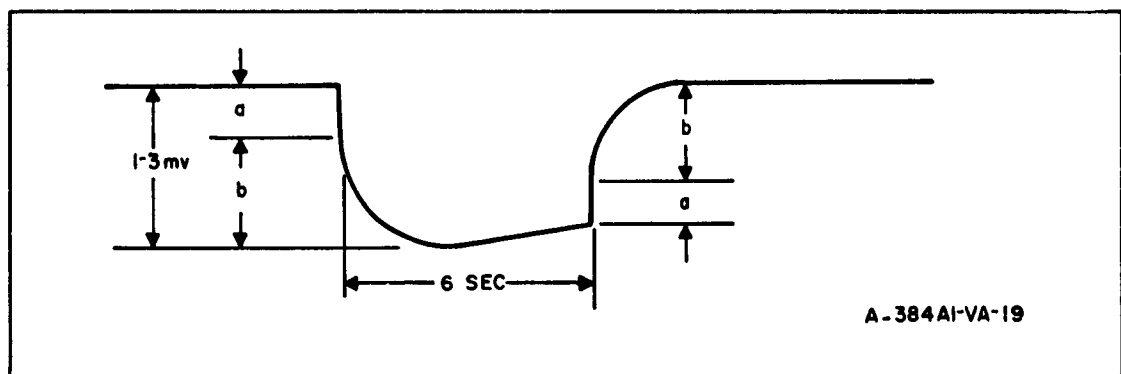


Figure 21. Photoresponse Waveform From Lapped Surface

Because of the extensive surface damage created by the lapping procedure, it would be expected that photovoltaic responses, under the conditions of the experiment, would be extremely small or nonexistent because of a very high surface carrier recombination rate. This proved to be the case, the photoresponse (a) being 0.5 mv or less and being typically very fast with respect to rise rate.

#### 4.7.4.1 Separation of Photovoltaic and Thermoelectric Components of Response

The remainder of the response is not so simply explained, since the behavior observed is not consistent with that which would be expected for any single conventional solid state phenomenon. This portion of the curve most probably represents the sum of two thermal-voltage curves, generated by the ohmic junction on the underside of the germanium sample and by the junction formed by the beryllium-copper probe contact to the exposed germanium surface.

Of the total energy output of the light source, a large percentage lies in the infrared portion of the spectrum. Irradiation of the sample with this source therefore causes the beryllium-copper probe, the germanium surface, and the polyester mount to rise in temperature.

A set of subsidiary experiments involving successive shielding of various parts of the sample and its surroundings indicated that heat conducted to the copper-germanium junction from the copper probe, and from the germanium surface itself was primarily responsible for the generation of a thermal voltage at this junction.

It was also shown that due mainly to direct infrared radiation through the polyester and heat conduction in the germanium, the ohmic junction on the unexposed surface of the sample generated a relatively small thermal voltage. Since this voltage and the thermal voltage generated by the probe junction are in opposition, the response in figure 21 is due to a summation of the two, the main transient being photovoltaic from the probe junction, and the ohmic contact on the underside contributing the positive sloping portion of the curve.

This summed thermal effect is present throughout this experiment, since measurement conditions remained essentially the same in all the work. The responses, however, are not necessarily of precisely the same form as those just described, since any treatment of a germanium surface (e.g., chemical etching) alters the nature of the probe contact with that surface, thus changing the form of the thermal response to a degree depending on the amount and nature of the contact change.

The thermal effects measured here are a separate means of investigation of surface properties of semiconductors. Here, they are used in combination with the photovoltaic effect; they are not detrimental to the experiment, since they can be subtracted from the total response in any given result to yield pure photovoltaic data. They alone have been utilized in other work under this contract to give information about materials and device behavior under temperature change which may be related to improper performance of the device function. Other utilization of this thermal response is also indicated.

#### 4.7.5 Responses from CP-4 Etched Surfaces - Effect of Etch Time

The composition of the CP-4 etch was shown in table 4. On germanium surfaces the photoresponse, except for isolated observations, was generally of the form of figure 22, where the (a) portions of the curve appear to be due to the thermal effects described in detail in the previous paragraph and the remainder is a photovoltaic response characteristic of the surface location being observed. The amplitudes of these responses varied over a relatively wide range, depending upon the following experimental conditions:

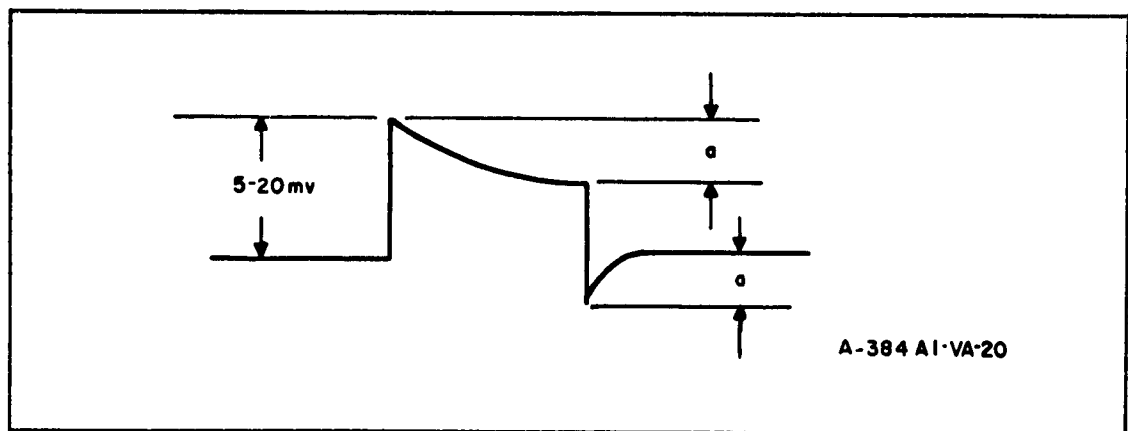


Figure 22. Photoresponse Waveform From CP-4 Etched Surfaces

- a. Degree of etching (controlled by etch time)
- b. Surface measurement location
- c. Elapsed time after etching

Responses obtained after 20-second etches appear reproducibly to have considerably different properties from those obtained after 30-second etches (see figure 23). After a 20-second etch, the responses were all of the above form, varying only slightly in magnitude with time, and becoming progressively noisier and more inconsistent from point to point on the surface. After a 30-second etch, however, the initially observed waveform, see figure 23, inverted with time, giving a response similar to the form of the 20-second etch.

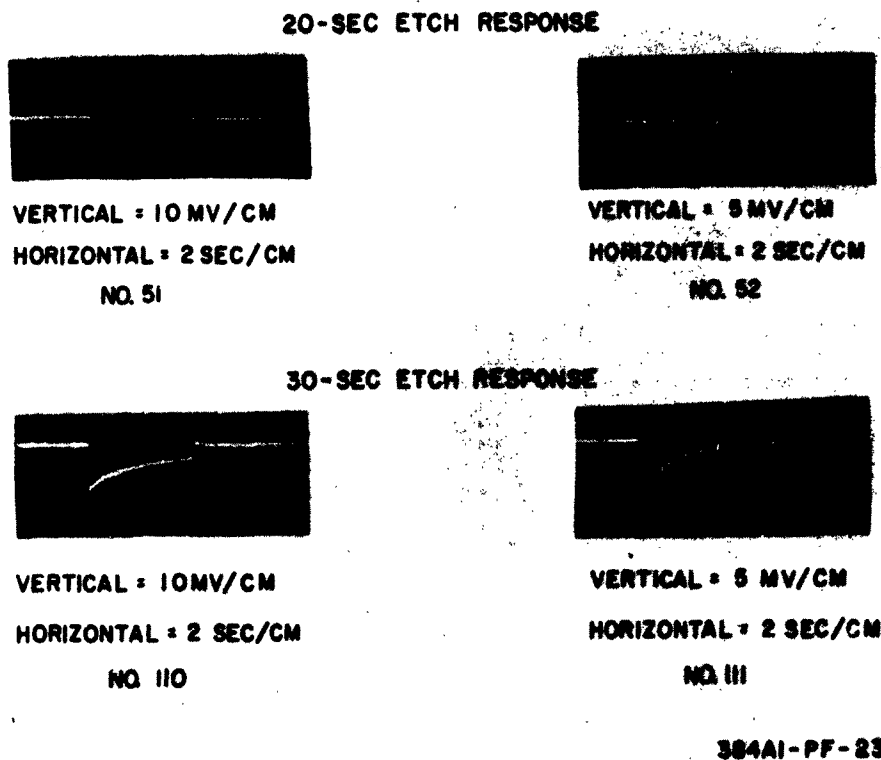


Figure 23. Photoresponse Waveform From CP-4 Etched Surfaces  
After 30-Second Etch

Since this difference in response occurring between the 20-second etch and the 30-second etch was reproducible, it portrays a real chemical difference of the surfaces in the two cases. The two most likely possibilities are (1) that a thin damaged layer is left on as a result of the grinding, and somewhat over 20 seconds is required to remove it, or (2) that the CP-4 has an induction period before maximum action. In either case, the implication for device technology is that CP-4 etch must be permitted to act for a minimum time depending upon the concentration, otherwise its purpose is not accomplished, and that increase of time or temperature of etch does not necessarily result in a smooth change of etch effects. CP-4 may leave an adsorbed layer of bromine.

#### 4.7.6 Responses From HF-HNO<sub>3</sub> Etched Samples

Simpler, slower, HF-HNO<sub>3</sub> etchants (than CP-4) may be preferred if chemical cleanliness is of prime importance.\*

Results from samples etched in HF-HNO<sub>3</sub> were extremely difficult to interpret in that the number of experimental factors to contend with was considerably larger than for other etches. Nevertheless, it has been possible, as a result of the experimental work, to outline some of the significant trends.

First, 20-second etches in HF-HNO<sub>3</sub> -1 (see table 4) produced essentially no change in response from that of the ground surface so long as the sample was etched immediately after grinding. If, however, a 70-hour desiccation period was observed between grinding and etching, the 20-second etch produced responses considerably different from those of the ground surface. Figure 24, for example, indicates not only a change in response form, but also a marked tendency toward noisiness.

A sample etched in the same formulation for 190 seconds immediately after grinding gave responses of relatively low amplitude and of the same general form (see figure 25) as was typical of CP-4 etches, but with considerably more noise. Responses from this sample as time elapsed after the etch,

---

\* Holmes, P.J., "The Electrochemistry of Semiconductors," Academic Press, London and New York, 1962, Chapter 5, p. 333.

**NO INTERVAL BETWEEN GRINDING AND ETCHING**



VERTICAL = 2 MV/CM  
HORIZONTAL = 2 SEC/CM  
NO. 55.



VERTICAL = 2 MV/CM  
HORIZONTAL = 2 SEC/CM  
NO. 56

**70-HOUR INTERVAL (DESICCATION) BETWEEN  
GRINDING AND ETCHING**



VERTICAL = 1 MV/CM  
HORIZONTAL = 2 SEC/CM  
NO. 47



VERTICAL = 1 MV/CM  
HORIZONTAL = 2 SEC/CM  
NO. 48

**384A1-PF-24**

Figure 24. Photoresponse Waveform From HF-HNO<sub>3</sub>-1 Etched Surface After 20-Second Etch (70-Hour Desiccation Interval)

tended to change in form, and to become inverted (see figure 26). Treatment of this sample with concentrated HF, 48 hours after etching, produced responses having considerably higher noise levels.

Samples etched for 80 seconds with HF-HNO<sub>3</sub>-2, (see table 4) however, gave responses of considerable amplitude and of the same form as was typical of CP-4. These tended to increase in noise and decrease in amplitude with increasing time.

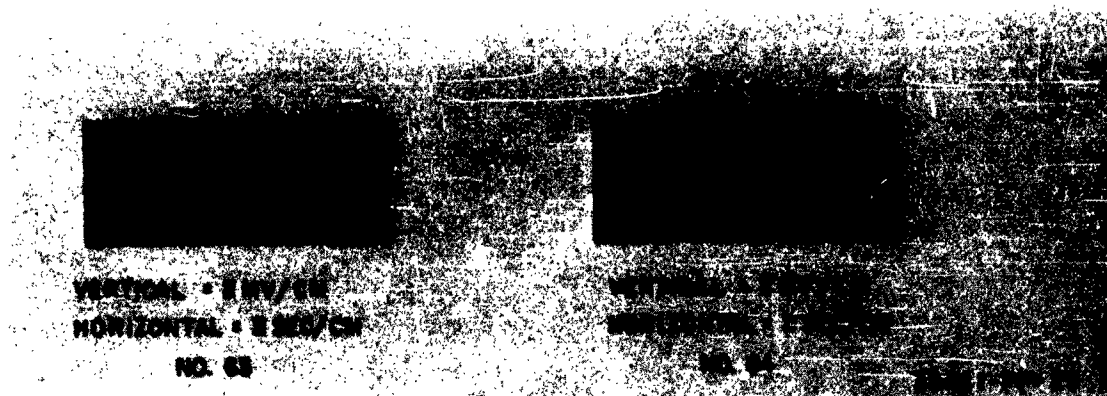
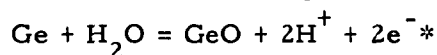


Figure 25. Photoresponse Waveform From HF-HNO<sub>3</sub>-1 Etched Surface After 190-Second Etch

In addition to the experimental results previously described, it was visually observed that throughout the course of the work with HF-HNO<sub>3</sub> - H<sub>2</sub>O etch formulations there was a marked tendency for the germanium surface to become yellow to brown in color during and after etching. These colored coatings developed in some etch formulations but not in others, were difficult to remove in HF, changed color from yellow to brown to black with heating, and tended to volatilize and disappear on prolonged heating. In other words, they had many of the characteristics of germanium monoxide formed in accordance with the following chemical reaction:



-E(volts) = +0.256 - 0.0591 pH (yellow)

-E(volts) = +0.100 - 0.0591 pH (brown)

-E(volts) = +0.089 - 0.0591 pH (black)

---

\* Ibid, p. 239.

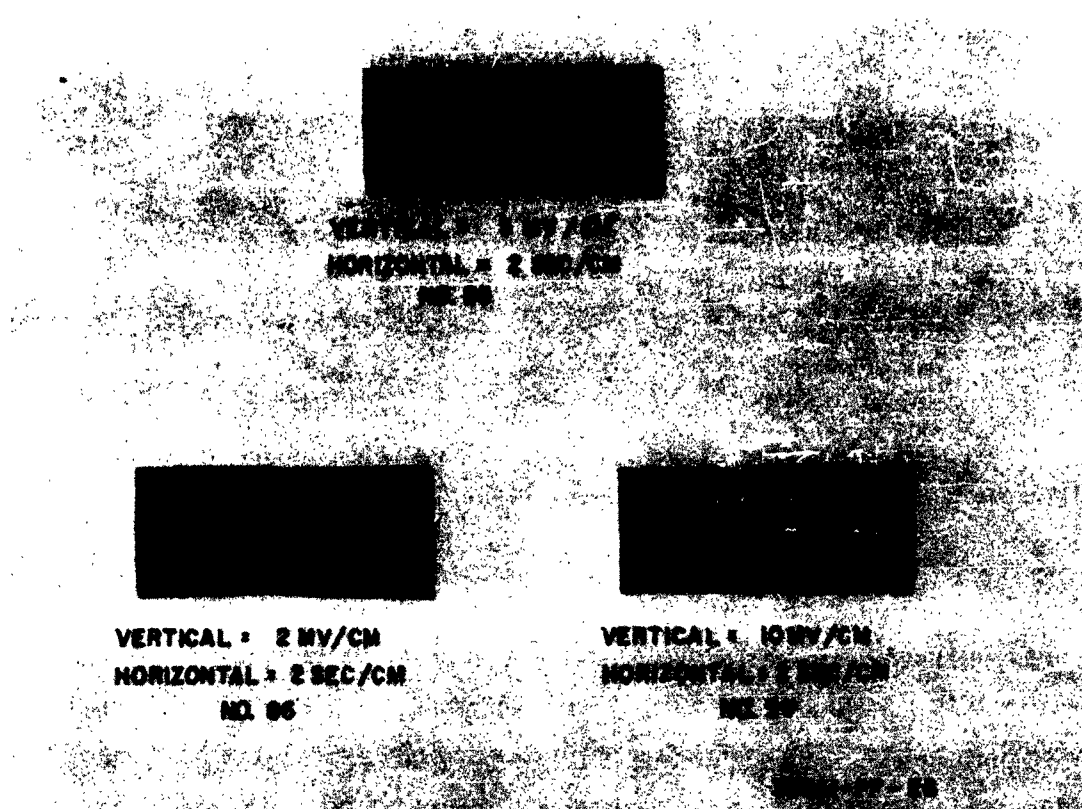


Figure 26. Photoresponse Waveform From HF-HNO<sub>3</sub>-1 Etched Surface After 190-Second Etch Showing Inversion After Long Time Interval

The formation of these coatings appeared to depend largely on the relative concentrations of HF, HNO<sub>3</sub>, and H<sub>2</sub>O in the etch formation, there being almost no tendency for coating formation in 15HF: 25 HNO<sub>3</sub> but a marked increase in oxidation tendency upon addition of water to this formulation. In fact, it was strongly indicated that the formation of this coating may define a definite region on an HF:HNO<sub>3</sub>:H<sub>2</sub>O ternary diagram.



The formation of such GeO deposits on the germanium surface may strongly influence the photoresponse measurements made on these surfaces. The presence of the deposits, or of their products under further processing, affects the electrical behavior of the surface under illumination. Therefore, the charge carrier atmospheres are different in their vicinity from what they would otherwise be. The effects of such deposits upon device performance and reliability are therefore of interest. The magnitude and the type of influence caused by the coatings are experimentally of interest, because of their relationship to semiconductor device fabrication techniques and on possible failure mechanisms.

#### 4.7.7 Responses From Superoxol Treated Surfaces

Superoxol is a recommended etch for germanium to leave a clean surface with no residues (see figure 27). The superoxol treatment on a freshly ground wafer gave the photoresponse shown in figure 28. Labeled steps of figure 28 are:

- a. Initial photoresponse with light on.
- b. Decay to steady-state value including the sum of thermal and photo-EMF.
- c. Final photoresponse with light off.
- d. Thermal voltage decay as probe cools to room temperature.

Table 6 below shows the change of the response with time.

TABLE 6  
TIME VS PHOTORESPONSE

Time	Photoresponse (in mv)			
	a	b	c	d
1 hour after etch	16	5	11	4
24 hours after etch	10	3	7	3

The decay between photo "on" and photo "off" was noisy revealing that the noise is directly related to irradiation.

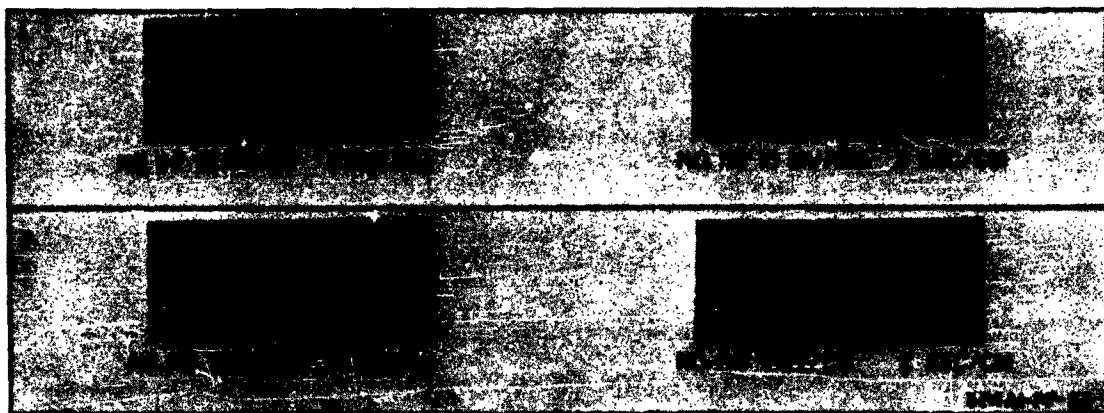


Figure 27. Photoresponse Waveform From Superoxol Treated Surface  
(See Table 5, Page 88)

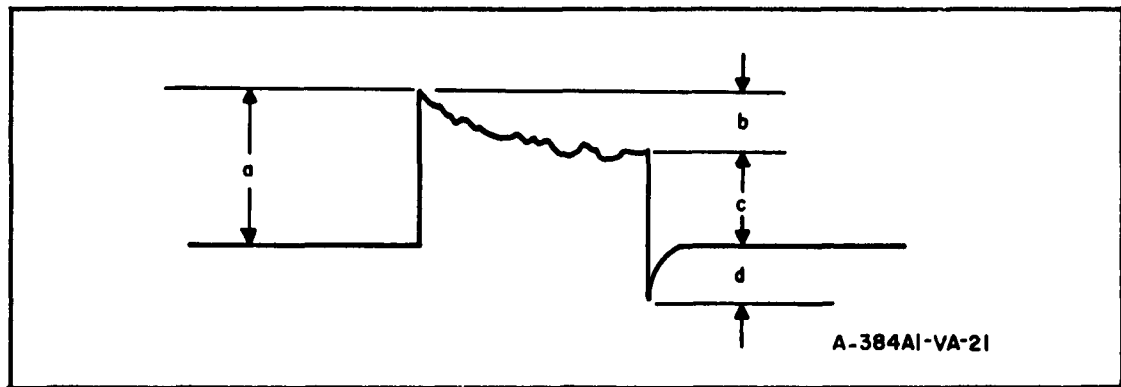


Figure 28. Photoresponse Waveform From Superoxol Treated Surfaces

The time-amplitude response change is of the order of 4 to 6 mv per 24-hour period. The thermal decay decreased by 1 to 2 mv in a 24-hour period. Two measurements per time period were made on the sample.

#### 4.7.8 Responses From CP-3 Etched Surfaces

The etch was looked at by a stepwise processing, consisting of a 20-second etch, a 24-hour hold in a dust-free moisture-free atmosphere, a 60-second CP-3 re-etch, and then a timewise following of the electrical response for 156 hours. A number of the samples were then subjected to a 10-minute HF treatment. Figure 29a and b shows the photoresponse of two groups of samples.

The CP-3 etchant introduced some interesting variations as shown in figure 30.

The first CP-3 etch (20 seconds) of the sample changed the photoresponse from (a) to (b) as shown in figure 30, where (a) has no photoresponses (only thermal) and (b) has both photo and thermal responses. The amplitudes of the thermal responses for (a) and (b) are approximately equal.

Following the 24-hour hold the initial photovoltage had diminished from 5 mv to 1.2 mv, a decrease of 3.8 mv or 76 percent. The thermal response diminished to 1 mv, a reduction of 40 percent.

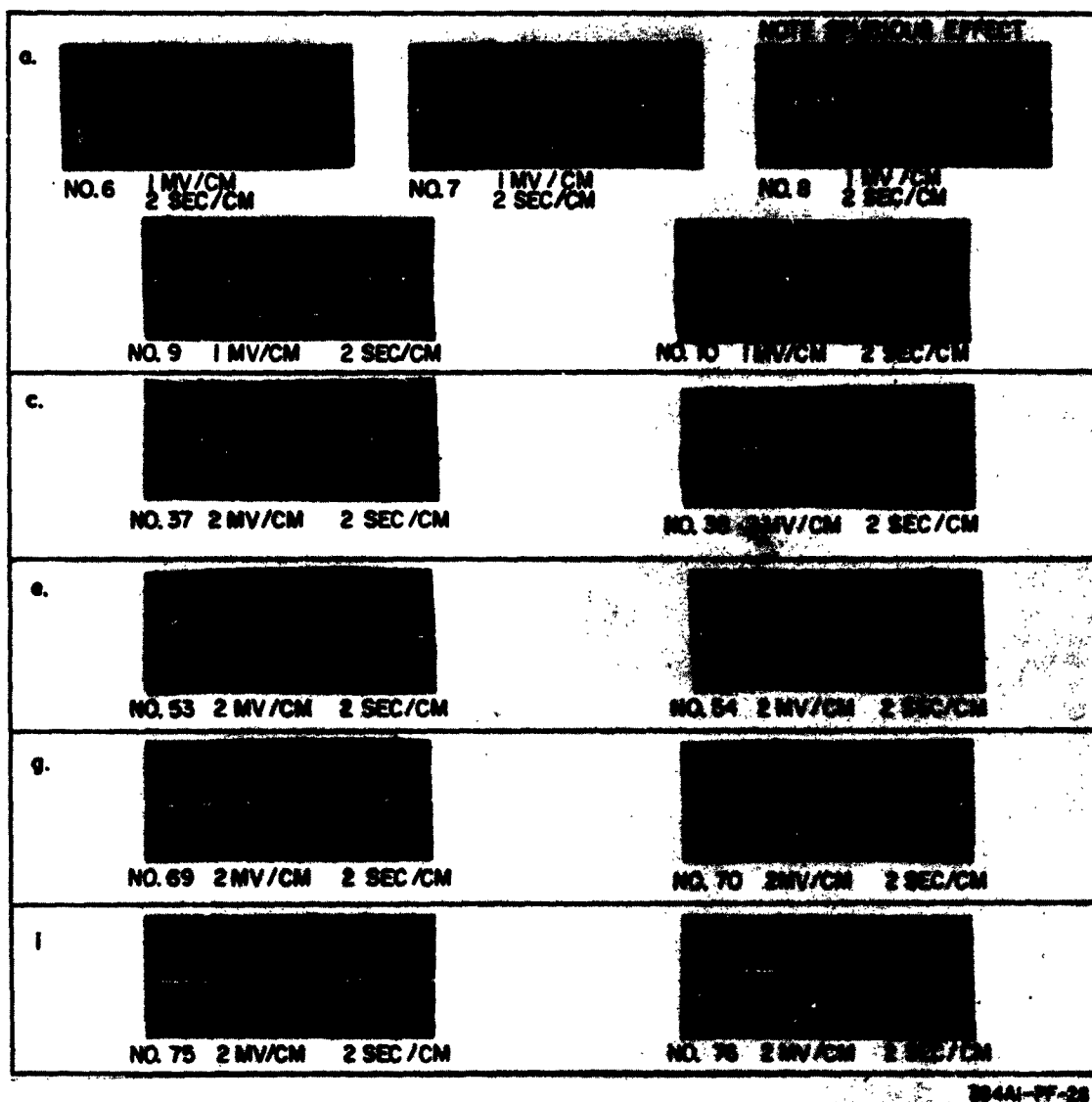
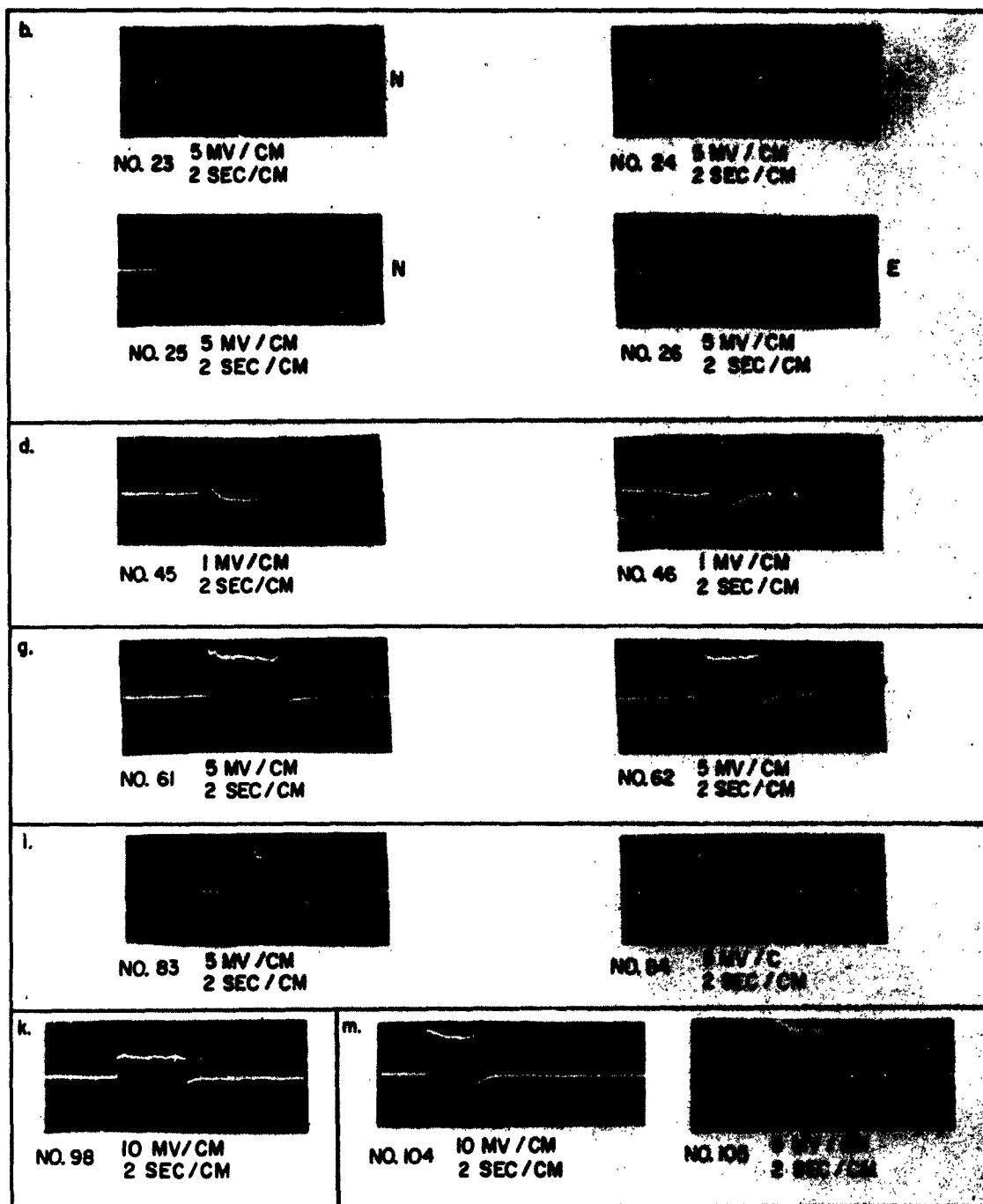


Figure 29a. Photoresponse Waveform From CP-3 Etched Surface  
(Group A, Sample 8, See Table 5, Page 88)



884AI-PT-29

Figure 29b. Photoreponse Waveform From CP-3 Treated Surface  
(Group B, Sample 12, See Table 5, Page 88)

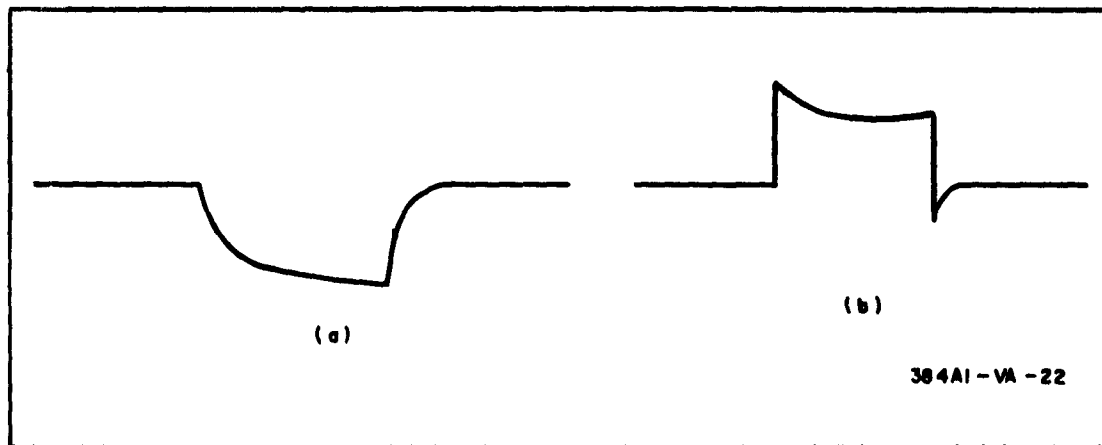


Figure 30. Photoresponse Waveform From CP-3 Etched Surfaces

A re-etch of the sample, this time 60 seconds (3 times the first etch), caused the amplitudes to increase. The photoresponse doubled (to 10 mv) the response after the first etch. The thermal response increased 2.5 times to 2.5 mv.

Twenty four hours after the second etch the thermal response increased from 2 to 7 mv. The leading edge of the photoresponse remained constant while the final photovoltage transient diminished from 10 mv to 4.5 mv.

Following the 156-hour delay after the second CP-3 etch, the thermal response changed from 7 mv to zero, while the photoresponse (initial and final) returned to 8 mv. This constitutes a decrease of 1 mv on the initial, and an increase to 8 mv (4 mv change) for the final photo-transient.

A subsequent HF treatment (10-minute duration) of the surface increased the photo-transient to 16 mv (approximately double the previous high following the second CP-3 etch (60 seconds)). The thermal transient returned to the same amplitude as that following the second CP-3 etch.

To further explore the effects of surface etchants on photovoltaic responses using P-Ge, three typical samples were lapped as previously reported and the photoresponses were measured immediately after the etching schedule as follows:

- a. Etch in boiling 30-percent  $\text{H}_2\text{O}_2$  for 5 minutes.
- b. Etch in 100 milliliters of 9:1  $\text{H}_2\text{O}$ :30-percent  $\text{H}_2\text{O}_2$  containing 8 grams of Na OH for 5 minutes.
- c. Unetched - immersed in deionized  $\text{H}_2\text{O}$  for 2 minutes. (Represents the control sample.)

Of particular interest was the comparison of etchants with HF to those without. The group (a, b, and c above) have no HF in the etchants.

Referring to figure 31, for each sample there are two photoresponses identified as (c) and (n) which represent two separate positions of contact on the given sample.

Samples 9 and 10 of figure 31 showed the usual characteristic positive photo-transient followed by a decay to a positive steady state photo-EMF, when irradiated, followed by the negative going transient and decay to ground potential when not irradiated. Sample 13 of figure 31 gave the usual response for a lapped nonetched surface.

Maximum response of sample 9 was 40 mv, while that of sample 10 was 28 mv. These magnitudes are comparable with typical freshly etched samples using HF etchants.

These results in no way indicate that the presence of HF in an etchant has no influence on photoresponse measurements made from germanium samples etched in such formulations. They do indicate strongly, however, that the presence of HF is not the controlling factor in determining the characteristics of such responses.

#### 4.7.9 Analysis of Equivalent Circuit

The equivalent circuit of the experimental setup including the variable, passive, and active parameters\* is shown in figure 32.

\* The photo-EMF due to the ohmic contact was omitted from the circuit because, after potting the sample, light passing through the sample to the ohmic junction was absorbed in the sample; light passing through the potting material to the ohmic junction was sufficiently attenuated to produce  $< 0.1$  mv (photo-EMF). It was noted that direct illumination of the ohmic junction (with no plastic encasement) generated  $< 0.4$  mv photo-EMF.

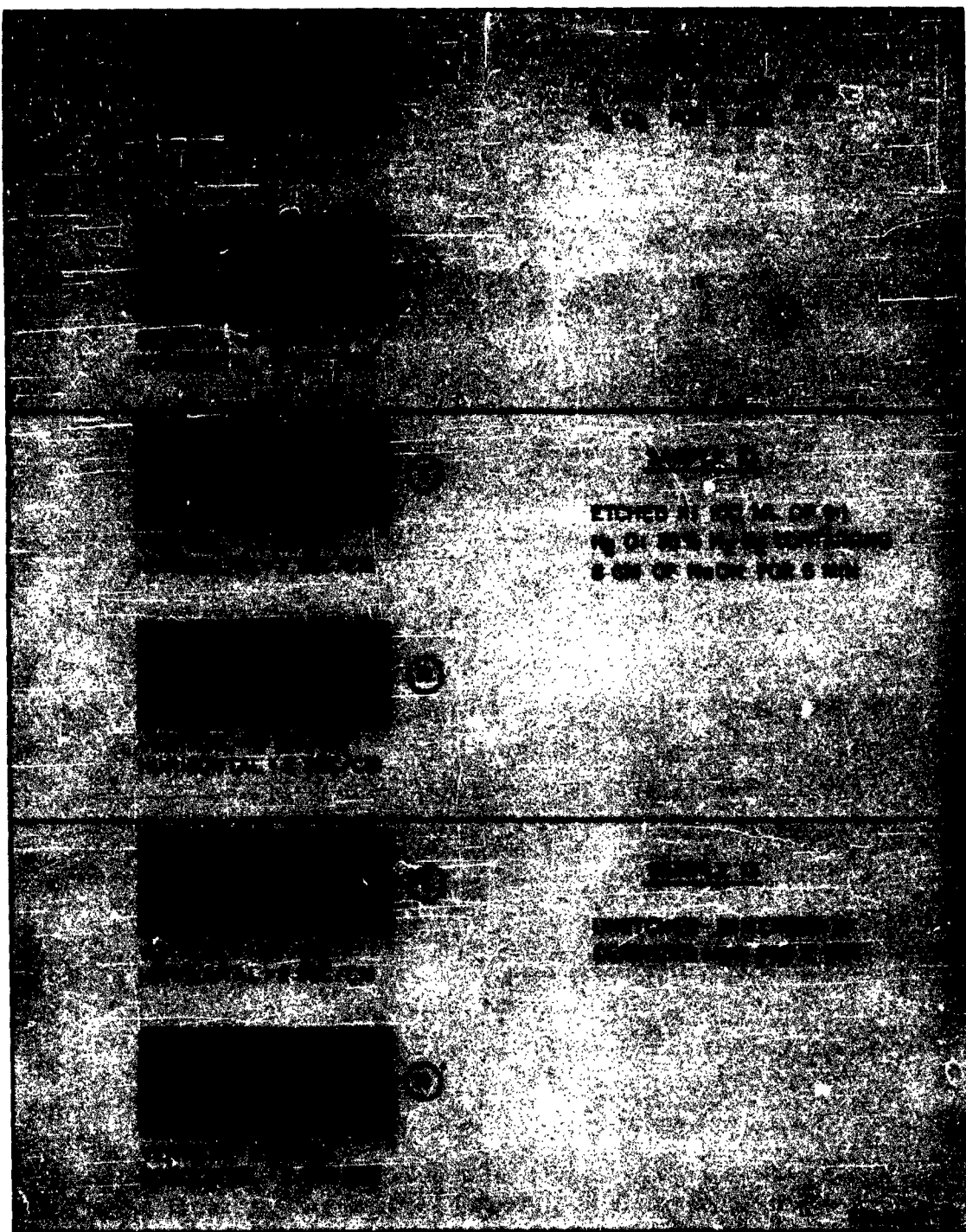


Figure 31. Photoresponse of Waveforms From Lapped Surfaces



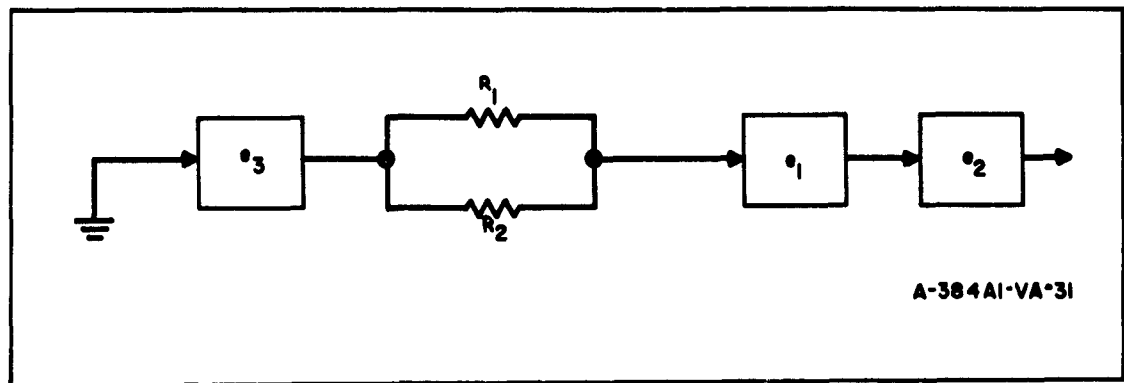


Figure 32. Equivalent Circuit of Experimental Setup

Terms used in figure 32 are defined as follows:

$R_1$  = bulk and surface resistance dependent on temperature

$R_2$  = bulk and surface resistance dependent on incident photons

$e_1$  = thermal-EMF from junction of probe with sample

$e_2$  = photo-EMF from junction of probe with sample

$e_3$  = thermal-EMF from ohmic junction with sample

The d-c polarity of  $e_1$  and  $e_3$  are opposing, and when  $e_1 = e_3$  the net thermal-EMF is zero. By lumping EMF's and resistances, an equivalent circuit including the CRO is shown in figure 33, where:

$E_1$  = lumped voltage of sample

$r_1$  = lumped resistances of sample

$r_2$  = input impedance of CRO

$E_0$  = voltage recorded on CRO

The current through  $r_2$  which biases the grid of the input tube to the CRO

is:

$$i = \frac{E_1}{r_1 + r_2} \quad (18)$$

The voltage applied to the CRO is:

(19)

$$E_0 = E_1 \frac{r_2}{r_1 + r_2} \quad (20)$$

When  $r_1 \ll r_2$ , a change in  $r_1$  has negligible effect on  $E$ .

In the experiment herein described,  $r_1 = 0.003r_2$ . A change in  $r_1$  due to illumination will, therefore, effect a change in  $E_0$  of less than 0.3 percent.

In this experiment, the effects of the variable resistance were considered negligible, and CRO voltage recorded was considered to be the thermal and/or photovoltage output of the sample.

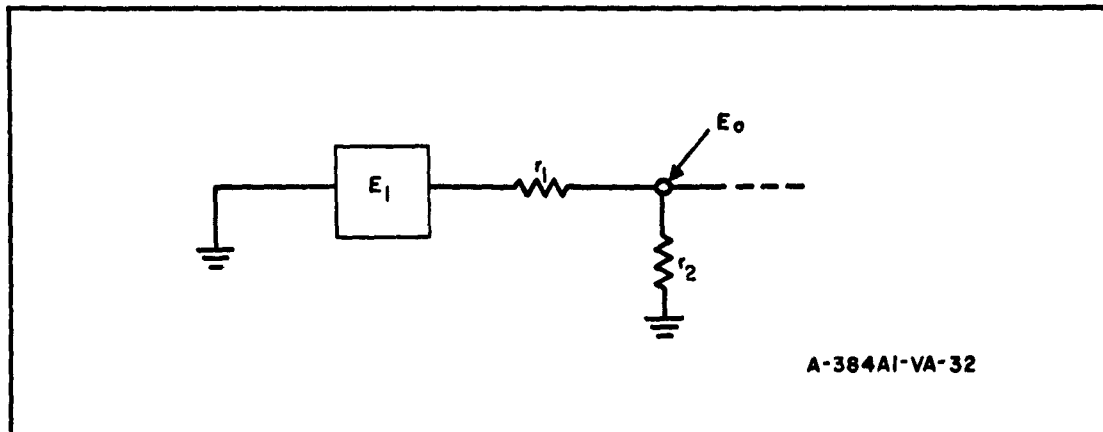


Figure 33. Equivalent Circuit, Including the CRO

## 4.8 DEPENDENCE OF PHOTOVOLTAIC RESPONSE UPON PRESSURE

### 4.8.1 Pressure Effects on Electronic Components

Electronic systems subject to acceleration, temperature changes, and varied external stresses, such as in missiles, or the acceleration incident to takeoff or maneuvering, necessarily will contain components which are subjected to external pressure. Also, changes in surface characteristics may be caused by the internal pressure effects of impurity regions, or major defects. To investigate these, the sensitive effects described in paragraphs 4.6 and 4.7 were used.

### 4.8.2 Apparatus and Experimental Method

The same apparatus was used, with a copper probe prepared as before, and a 40-ohm-cm p-doped germanium sample, mechanically polished and CP-4 etched. A strobe light at visible frequency, with a 1-millisecond pulse width, was directed onto the surface of the sample, while the stress was applied perpendicularly to the  $\{1:1:1\}$  surface of the sample.

### 4.8.3 Effect of Contact Pressure on Photoresponse of P-Germanium

The response to the chopped light was as indicated in figure 34. An increase of contact pressure changed the initial positive deflection from 6 mv to 2 mv to -4mv. Since the amount of oxide present was extremely small, if it existed at all, this is interpretable in terms either of change of Fermi level with lattice compression, or of change in contact potential with pressure. Increasing contact of the probe with the germanium under the thin or negligible oxide appears to be a less likely cause, since the initial response with light contact pressure immediately after a CP-4 etch and deionized water wash is positive, so that if increased contact were the only factor, the initial voltage would not be expected to become more negative.

### 4.8.4 Effect of Contact Pressure on Steady State Photo-EMF

A further experiment was performed to show the effect upon the steady state photo-EMF of externally applied pressure to a sample semiconductor material during illumination. A sample of 1.2-ohm-cm p-silicon was used,

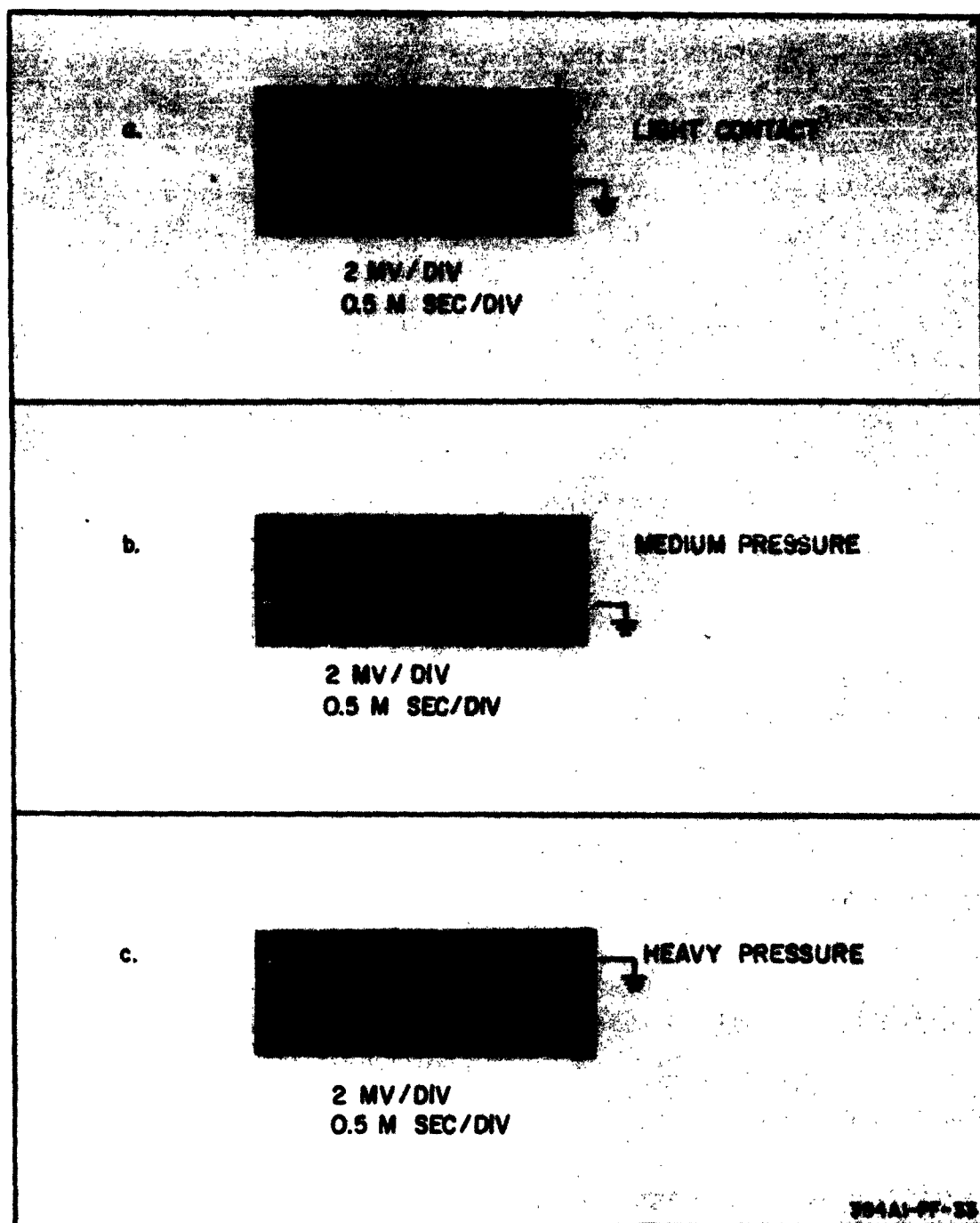


Figure 34. Effect of Repetitive Pressure on Photoresponse of 40 Ohm-cm P-Germanium

with ohmic ground connection and a copper probe. Illumination was by steady incandescent light, and the pressure on the probe was varied.

The results are shown in figure 35. The zero pressure steady state value of the EMF is indicated at the top. Pressure altered the value of the EMF approximately linearly - the higher the pressure, the greater was the deviation from the steady state conduction current.



Figure 35. Change in Photo-EMF with Repetitive Contact

A different type of experiment was performed in which repetitive contact was made, accompanied by coordinated chopped incandescent light. The change in the steady state photo-EMF with pressure is evident in figure 36.

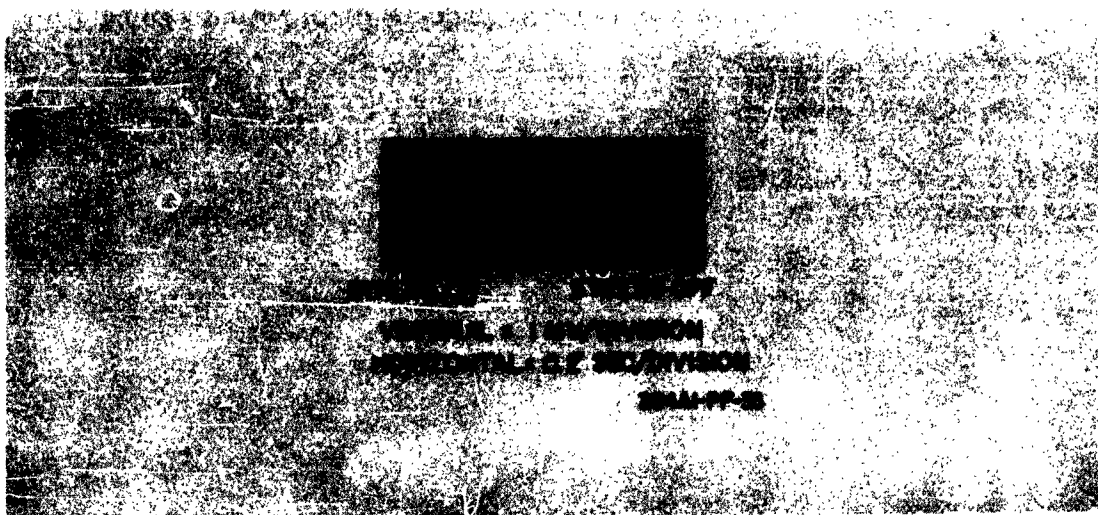
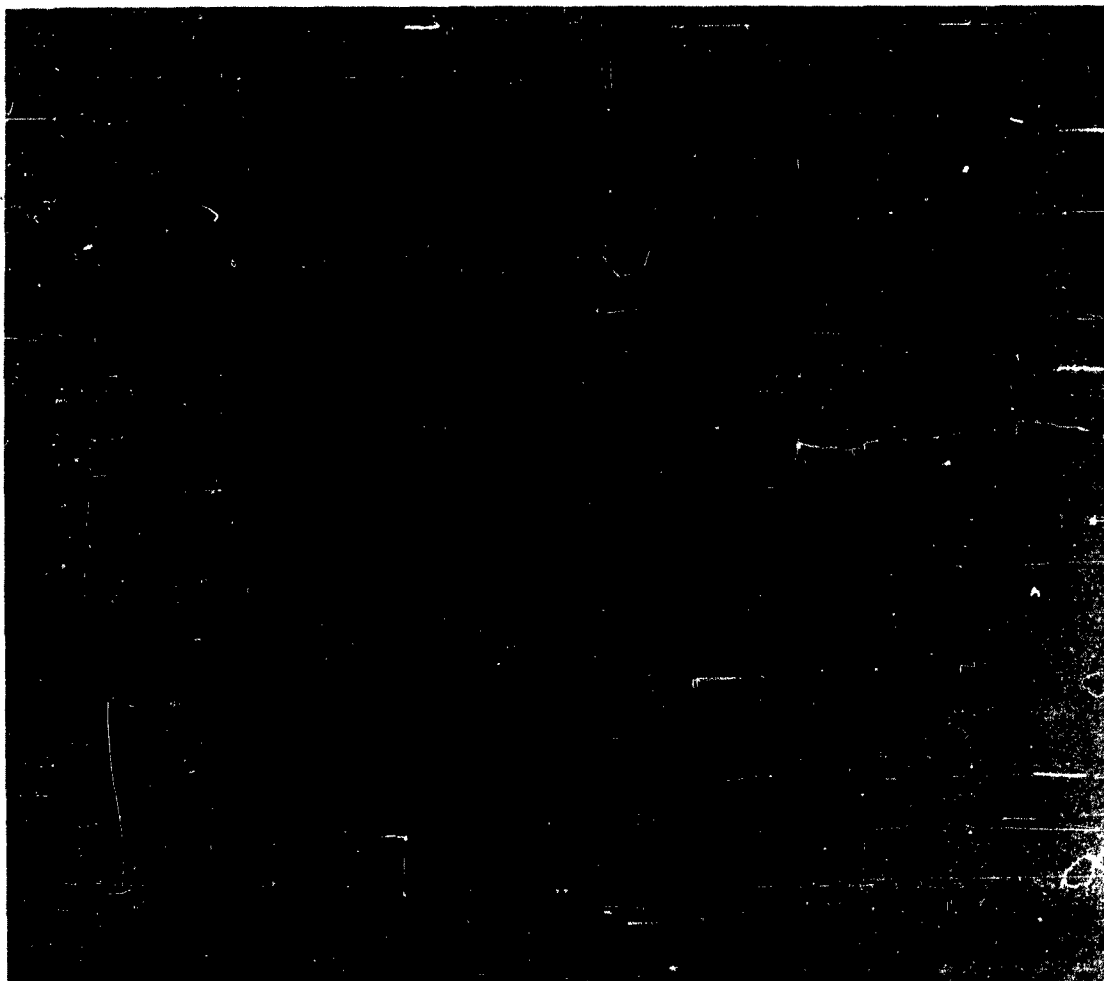


Figure 36. Effect of Repetitive Contact Accompanied by Coordinated Chopped Incandescent Light

That a response can be obtained without actual contact is shown by another experiment. The same apparatus was used, with ohmic connections to p-silicon, and pressure fixed for any one experiment. The light, chopped at 90 cps, was directed at the surface, and oscilloscope photos were taken. The various responses are evident in figure 37. Figure 37a shows the response when a 0.5-mil gap exists between the probe and the sample. Both a negative and a positive small response can be seen.

The succession of responses as the contact is made and stress is applied, shows a difference in the waveform of each wave of the periodic pattern (see figure 37b, c, and d).

Evidently, the probe is able to detect inductively small changes in charge carrier population of the surface occasioned by the illumination, even with close approach but no contact. The development of an intermediate peak in the downgoing portion of the waveform is noticeable in the lower two photographs.



**Figure 37. Response With Coordinated Chopped Incandescent  
Light and No Actual Contact\***

\*All applied stress is perpendicular to the surface of the sample.

#### 4.8.5 Effect of Temperature Change on the Pressure Variation of the Photo-EMF

The beginning and end results of an initial study of the effect of temperature on the thermal (not photo-) EMF from the ohmic junctions are shown in figure 38. Initially the thermal EMF outputs of the two ohmic connections, (one at the end and one in the center) were balanced.

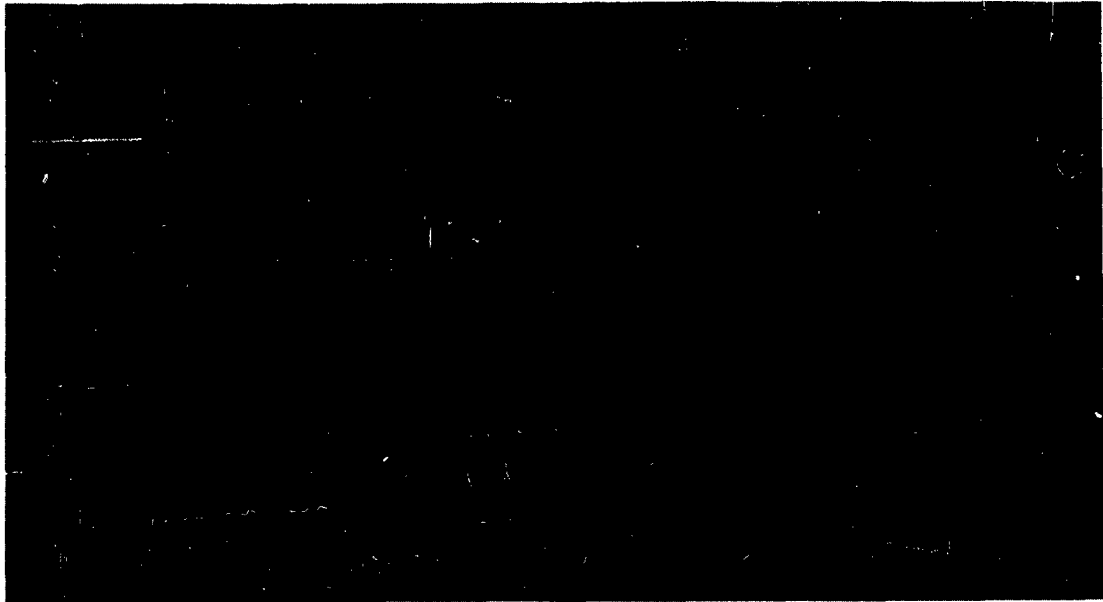


Figure 38. Beginning and End Results of Tests on Thermal EMF from Ohmic Junctions

The two connections, though ohmic, had temperature sensitivity and were therefore thermocouples; when the heat source under the sample was turned on, the two EMF's opposed each other. One and then the other dominates the polarity until the steady state is reached. When the heat source is turned off, another oscillation between the two thermocouples takes place as the temperature decreases to equilibrium throughout the substrate.

The photovoltaic response was then examined. An n-type silicon was provided with two ohmic connections, one grounded and the other in the center of the substrate to receive the copper probe contact. The contact area



between the copper and the silicon through the ohmic gold was therefore constant except for a slight thermal expansion. The sample was heated above room temperature by a heat lamp, and then with the lamp off, repetitive contacts were made between the gold and the copper probe. Figure 39 shows the response.

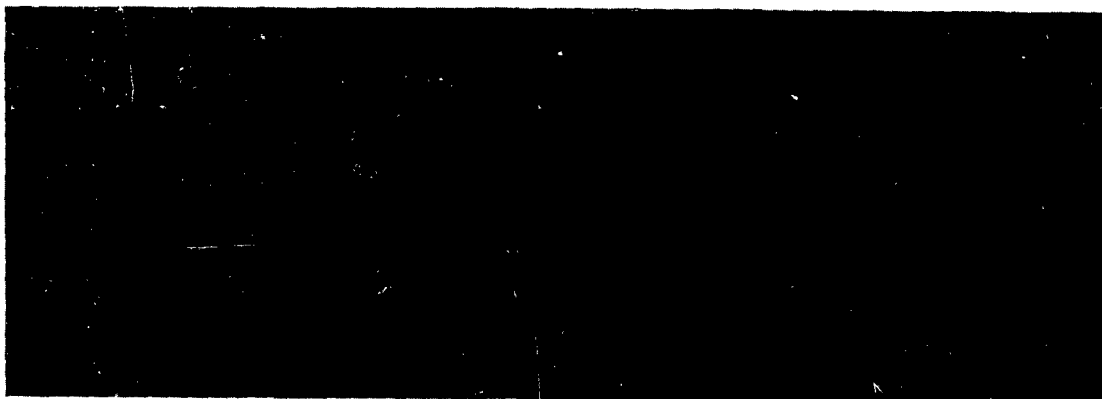


Figure 39. Voltage Response Caused by Dynamic Stress (by Repetitive Contact Applied Perpendicularly) to Ohmic Contact on Surface of N-Silicon

Light was then applied to the contact region. The response was that shown in figure 40. The effect of the light is in the opposite direction from that of the rise in temperature, heat producing positive current, and light negative current.

#### 4.8.6 Implication

Pressure, impact, or remanent stress may change surface properties and, if temperature rises or electron charge concentrations and their associated internal stresses occur in a solid state device, the pressures resulting may affect performance of the device. The complexity of the situation is evident from the results shown above. It is directly evident, however, that altered performance of electronic components may occur in military systems when stresses or accelerations are applied to them, and these altered performances may constitute failure when regarded against the objective desired for the system performance.



**Figure 40. Voltage Response of Combined Dynamic Stress and Incandescent Light Upon Ohmic Contact on Surface of N-Silicon**

#### 4.9 SURFACE STUDIES: LOW ENERGY ELECTRON BEAM SCANNING OF TRANSISTOR SURFACES

The variations in surface potential across the material surface can be used to obtain pictures of the nature and geometry of the surface. Low energy electron beams are directed at the surface in an electron-optical experimental setup which permits photography of the resulting surface indications. Any defects which may be observed can be examined for correlation with future or past failures of the device. Several such failed devices were examined under the electron-beam arrangement described in Quarterly Report 2. Examples were given in Quarterly Reports 1, 2, and 3. Since the resolution obtainable in the apparatus being used was insufficient to yield the information desired, the work is being transferred to an electron scanning microscope presently under construction, which will have a much higher resolution.

However, several significant observations were made, such as relative dielectric charge storage on different types of transistors, as discussed in paragraph 4.13.1.

Also, in several mesa transistors, bright V-shaped areas were seen extending from the emitter region as the collector voltage was applied and raised to the upper operating value specified for the transistor under observation.

In one fortuitous case, a stray dirt particle was observed on the surface, apparently critically influencing the field distribution in the vicinity of a junction.

#### 4.10 SURFACE STUDIES: ATTEMPT TO MAP CHARGE DISTRIBUTIONS ON SEMICONDUCTOR SURFACES

##### 4.10.1 Nature and Effects of Charge Distributions

The probability that charge distributions will be found at the sites of dislocations has been mentioned by Shockley. Thermodynamically, the existence of charge distributions is indicated at junctions, interfaces, or other departures from physical or chemical homogeneity.

The failure of transistors because of the accumulation of ions on their surface is described in paragraph 4.13; such ions may accumulate because the ambient atmosphere contains high concentrations of gaseous ions, or for other reasons. As a part of the understanding of the manner in which failure is induced, a closer look at the geometrical distribution of these ions is desirable; eventually, it is desirable to correlate the ion distribution with defect distribution in the material of which the transistor is made. Implications from the experimental work described elsewhere in this report lead to the possibility that effects of surface charge may be in part due to charge density variation, and in part to the geometrical location of the charges on the material.

Such mapping of charge distributions has been accomplished with good resolution on insulators (and with poorer resolution on transistors). While the problem here is somewhat less favorable to a similar experimental approach, the degree of information which may be obtained was examined.

##### 4.10.2 Techniques

In the past, such charge areas, particularly in the vicinity of p-n junctions in transistors, have been delineated by treatment of operating transistors with dispersions of finely divided particles of high dielectric constants in nonconducting liquids of low dielectric constant. It has been shown by researchers at Bell Telephone Laboratories that such dispersions are strongly field responsive, the dispersed particles tending to migrate and collect at surface locations, such as rectifying junctions, which are areas of high field intensity. It has also been shown that the ratio of dielectric constants, dispersed solid to dispersing liquid, should be a maximum and that both liquid

and solid should be nonconducting materials. P-N junctions in transistors were successfully delineated using dispersions of barium titanate in carbon tetrachloride, the dispersed barium titanate particles being collected at the junction. The collected particles were observed microscopically with considerable difficulty.

Dusting techniques with ZnS-CdS charged powders have been used to delineate charge locations on plastics. By mixing two oppositely charged and differently colored powders of small particle size, and dusting the plastic surface with this mixture, both positive and negative charge sites were exhibited simultaneously by color difference under ultraviolet light. It was shown that stationary charges can exist adjacent to one another in distinct patterns, the formation of which is related to the past history of the sample.

#### 4.10.3 Use of Dispersions

The present work was an attempt to map bound charges on device surfaces by similar techniques.

An operating mesa transistor was immersed in dispersions of fluorescent organic pigments in nonconducting media, such as n-hexane and xylene. Collected pigment particles were then viewed microscopically under ultraviolet light. This approach was largely unsuccessful because (1) the particle size of the commercial pigments used was too large to permit useful resolution, and (2) it was impossible to find fluorescent or phosphorescent pigments of sufficiently high dielectric constant to meet the solid-liquid ratio requirements necessary for adequate selective deposition.

#### 4.10.4 Use of Charged Powders

Because of prior successful use, another method, the charged powder technique was tried. An apparatus was constructed (figure 41), which permitted operating devices to be exposed to a controlled stream of air containing suspended charged phosphorescent particles. Preferential deposition of particles on charged device areas was strongly indicated. Table 7 lists the substances tried in various combinations. Two difficulties were encountered:

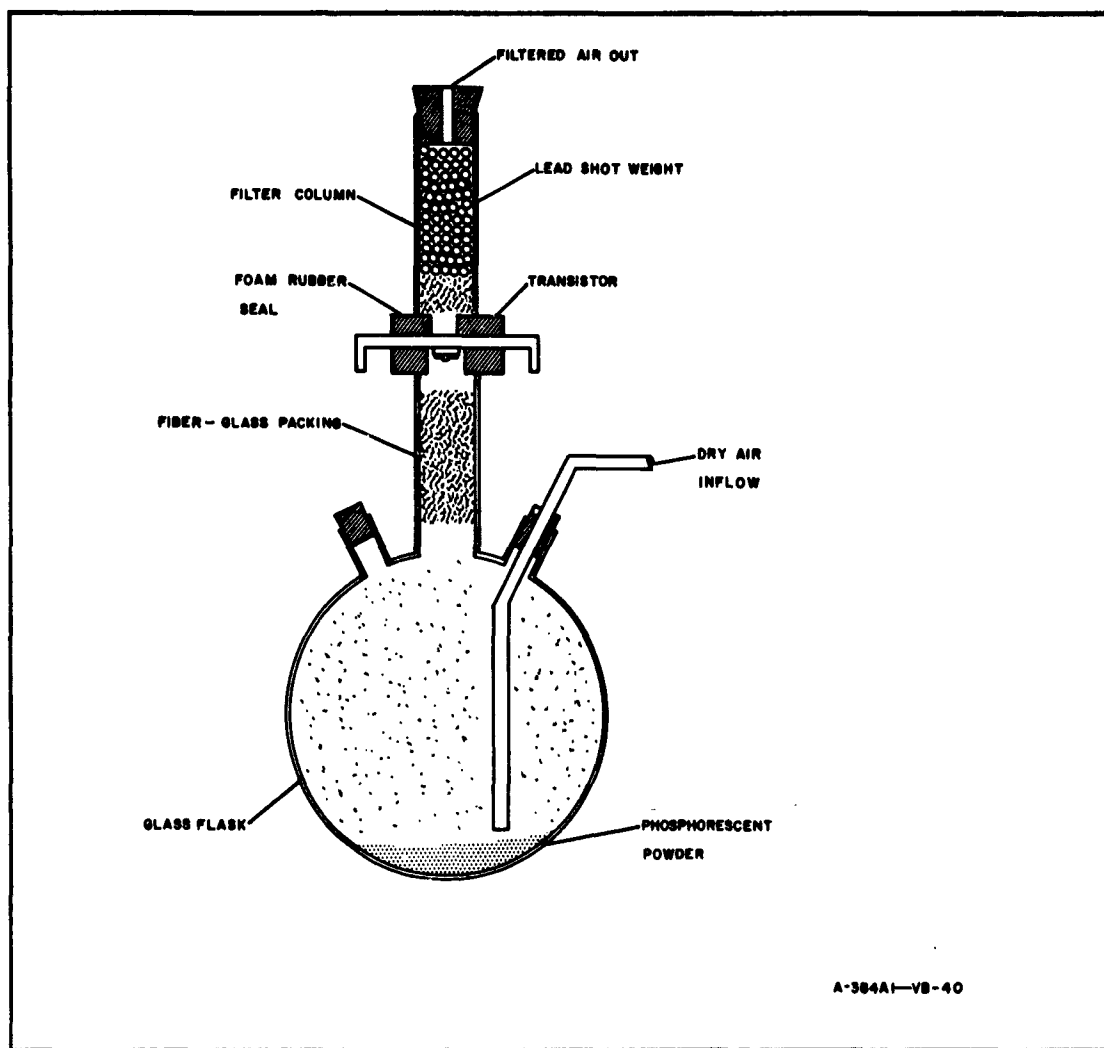


Figure 41. Apparatus for Charged Powder Technique

a. The suspended powder particle size was too large to permit adequate resolution (better resolution than that required with charged plastics was necessary for satisfactory results)

b. The suspended powder exhibited affinity for water; accordingly agglomeration could not be avoided for sufficient periods of time to obtain necessary resolving power.

TABLE 7  
EXPERIMENTAL CHARGE MAPPING MATERIALS

Trade Designation	Chemical Type	Manufacturer
1		
Helecon 2304	ZnS-CdS	United States Radium Corp.
Helecon 2315	ZnS-CdS	United States Radium Corp.
Helecon 2330	ZnS	United States Radium Corp.
2		
Lumigraphic Red X-2489	Organic Resin-Based Pigment	Imperial Color Chemical and Paper
Orange X-2490	Organic Resin-Based Pigment	Imperial Color Chemical and Paper
Yellow-R X-2491	Organic Resin-Based Pigment	Imperial Color Chemical and Paper
Yellow-G X-2522	Organic Resin-Based Pigment	Imperial Color Chemical and Paper
Green X-2523	Organic Resin-Based Pigment	Imperial Color Chemical and Paper
3		
Attagel 20	Attapulgitic Clay	Minerals and Chemicals Phillip Corp.
Attagel 30	Attapulgitic Clay	Minerals and Chemicals Phillip Corp.
ASP 100	Aluminum Silicate	Minerals and Chemicals Phillip Corp.
ASP 105	Aluminum Silicate	Minerals and Chemicals Phillip Corp.
ASP 106	Aluminum Silicate	Minerals and Chemicals Phillip Corp.
4		
Hi-viz Lemon Yellow 39	Organic Resin-Based Pigment	Lawter Chemicals, Inc.
Hi-viz Cerise Red 30	Organic Resin-Based Pigment	Lawter Chemicals, Inc.

(1) PHOSPHORESCENT      (2) & (4) FLUORESCENT      (3) NON-LIGHT RESPONSIVE



#### 4.11 VOLUME STUDIES: THE INCIDENCE OF CRACKS, VISIBLE OR SUB-VISIBLE, IN SEMICONDUCTOR MATERIALS

The application of mechanical stresses well within the range encountered during processing to semiconducting materials has been shown to cause cracks in the material, both those visible under a 1000x Leitz microscope, and those not visible, but demonstrable. These and other results of the apparatus built for the flexure-charge experiments are described below. The equations of motion of the flexure test apparatus are given in Appendix A.

##### 4.11.1 Apparatus Modifications

The flexure-charge apparatus described on pp. 40-43 of quarterly report 3 was modified by:

- a. Completely electrically shielding the sample and its immediate surroundings
- b. Providing precise means for the removal of undesired high frequency components of the electrical trace

##### 4.11.2 Sample Displacement Cycle

An analysis of the mechanical cycle performed by the material in flexure is given in paragraph 4.11.12, together with some indication of the reasons for the choice of the precise dimensions used. The actual displacement of the end of the sample is periodic, nearly sinusoidal, but with a slight displacement of the maximum.

##### 4.11.2.1 Deviation From Ideal Displacement Cycle

Using an extremely flat silicon dendrite-web sample, a complete cycle was traversed by hand in steps. From its highly reflecting surface, a 1-mm diameter collimated light spot from a zirconium arc point source was reflected to a translucent plastic screen at a distance of 6 feet. The position of the spot was plotted on the plastic screen for each 30 degrees of the cycle. The result of the measurement is the curve shown in figure 42. Since one end of the sample is fixed, the curve shows that a small but appreciable twisting or torsional stress component occurs simultaneously with flexure. This is being designed out of the apparatus. The actual displacement used in

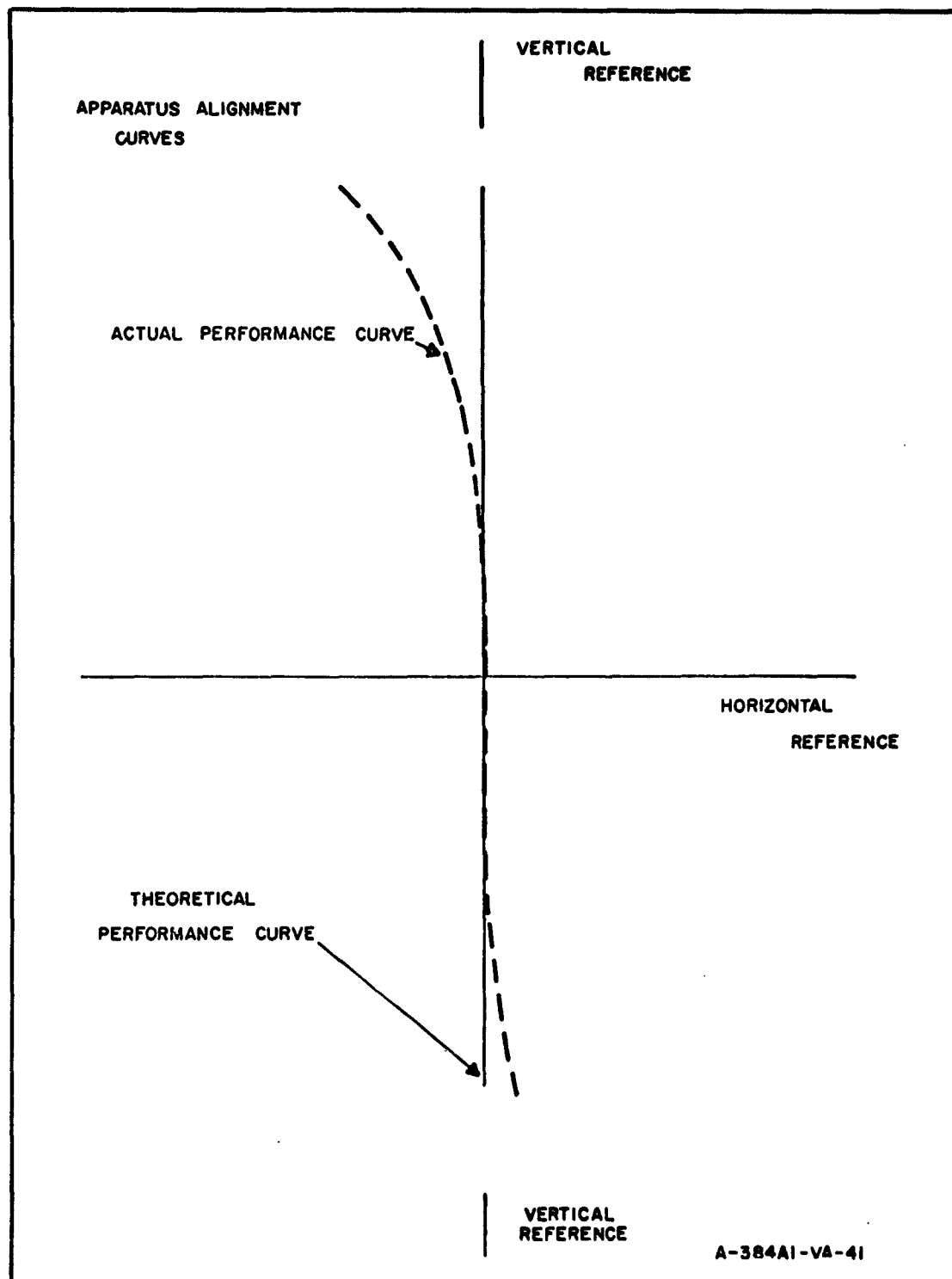


Figure 42. Results of Cycle of Flexure-Charge Apparatus

the experiments was small enough so that the twist was of minor effect. Its effect, however, is to make the two possible maxima in a complete cycle slightly different in stress concentration. This is indicated later in figure 50 by the notations "primary" and "secondary" flexure maxima.

#### 4.11.3 Sample Characteristics and Preparation

##### 4.11.3.1 Samples

Two types of samples were employed: (1) n-silicon dendrite-web samples of volume resistivities between 4.5 and 7.0 ohm-cm (figure 43), (2) 1/4-inch p-silicon slivers, diamond cut from 7/8-inch diameter production wafers ranging in thickness from approximately 5 to 15 mils.

The dendrite-web samples are preferred because they are of convenient width, they can be obtained in virtually any desired length, and because the edge dendrites are stronger and considerably more flexible than the web so that critical stresses invariably occur first in the center web section.

##### 4.11.3.2 Cleaning

Before the attachment of leads and junctions, the samples were subjected to a standard cleaning procedure to completely remove all organic surface contamination as well as all oxides of silicon. Besides providing optimum results with respect to surface cleanliness, this procedure yielded optimum performance in subsequent alloying operations. It included the following steps:

- a. Organic contamination was removed by immersing the samples in boiling trichloroethylene for 10 to 15 minutes.

- b. Surface oxides of silicon were next removed by a 15-minute immersion in concentrated hydrofluoric acid.

- c. Excess acid was then removed by a thorough rinsing in fresh deionized water.

- d. Retained water was then washed from the samples by rinsing in a 1:1 mixture of acetone and methyl alcohol. The samples were then left immersed in a fresh portion of the same mixture until ready for use in subsequent operations.

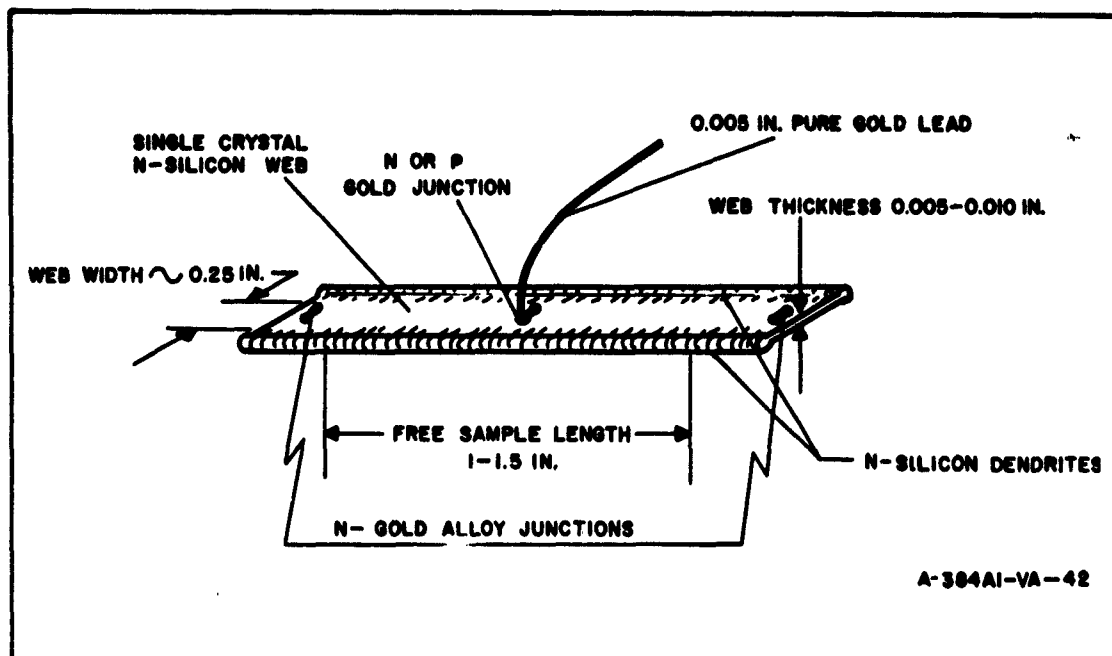


Figure 43. N-Silicon Dendrite Web Sample Schematic Diagram and Equivalent Circuit

#### 4. 11. 3. 3 Junction and Lead Attachment

Silicon-gold alloy connections gave the maximum mechanical strength as well as best reproducibility in electrical performance; nail-head bonding and thermal compression bonding techniques gave inferior results.

Following sample cleaning, the required alloy junctions were made in a hydrogen bell jar on a clean and thermally degassed carbon slab over a nichrome heater strip, and allowed to come to room temperature under continuous hydrogen flow.

The alloy junctions were positioned on the sample as shown in figure 43. For nonrectifying junctions, the two end junctions were doped the same as the silicon sample. The equivalent circuit of the n-silicon dendrite web is shown in figure 44. The center connection (lead to the oscilloscope) was made by alloying a 5-mil gold wire to the silicon surface simultaneously with an n-or p-doped piece of gold.

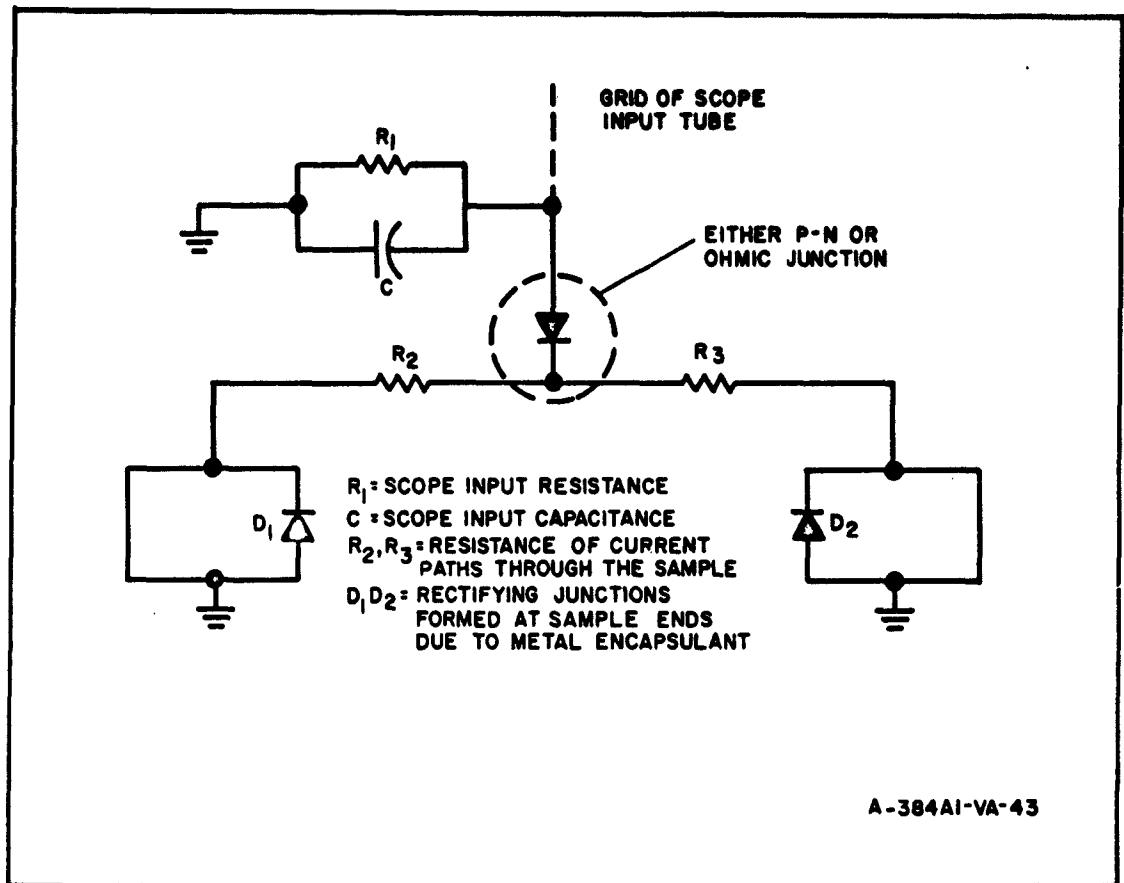
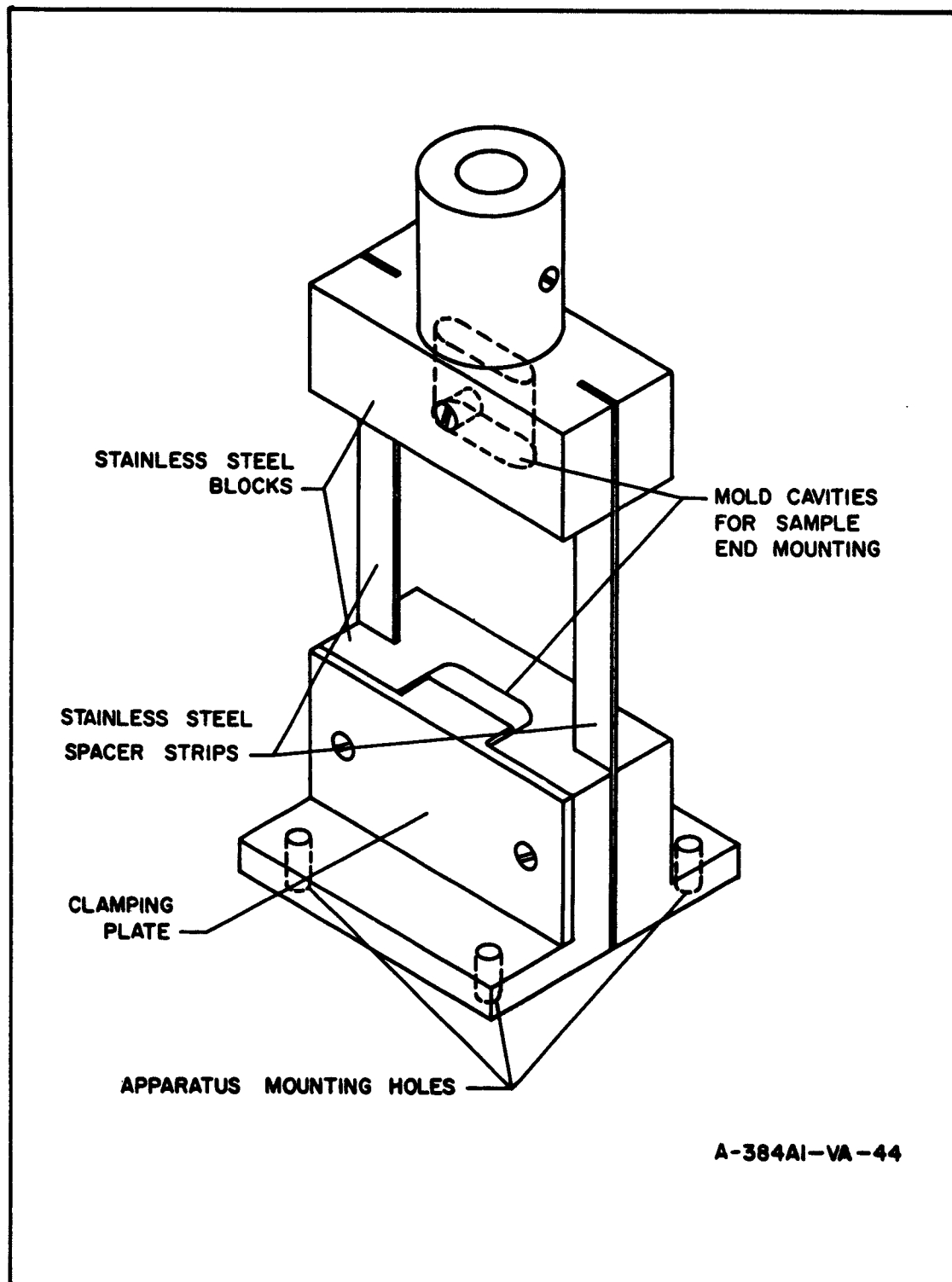


Figure 44. N-Silicon Dendrite Web Electrical Representation

#### 4.11.3.4 Sample Mount

The sample mount consisted of two stainless steel blocks positioned a fixed distance apart, each containing a mold cavity suitable for encapsulating the ends of the silicon sample in a low melting metal alloy (figure 45). For the experiments described here, an indium-tin eutectic, to which 10 percent of pure lead was added for increased rigidity, was used for end encapsulation. Provision was incorporated for additional pressure on the metal encapsulation to obtain a firm constant pressure contact across the uneven cross section of the sample ends.



A-384AI-VA-44

Figure 45. Sample Mount

#### 4.11.4 P-N Junction Experiments

Samples having gold-silicon p-n center lead junctions were prepared, mounted in the apparatus, and flexed at a frequency of 0.85 cps.

Practically no response was obtained with p-n junction samples when the experiment was run in darkness, but periodic responses typified by that shown in figure 46 were obtained when the junction was illuminated with a standard polychromatic light source.

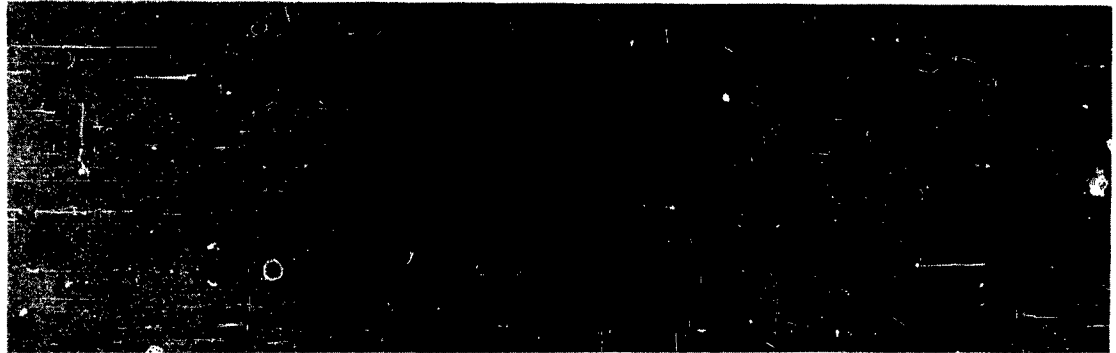


Figure 46. Illuminated P-N Center Junction Sample

#### 4.11.5 Ohmic Junction Experiments

When samples having ohmic center lead junctions were repetitively flexed, very low magnitude, but periodically repeated responses (figure 47) were obtained for experiments run both in darkness and with junction illumination. Junction illumination, in this regard, had little or no effect on the electrical response obtained.

#### 4.11.6 Variation of Position of Center Lead

Samples having ohmic center lead junctions attached in various positions along the sample length were prepared and tested in the apparatus. Results of this experiment indicated that the position of the lead attachment has no effect on the maximum magnitude of the response obtained, but that maximum

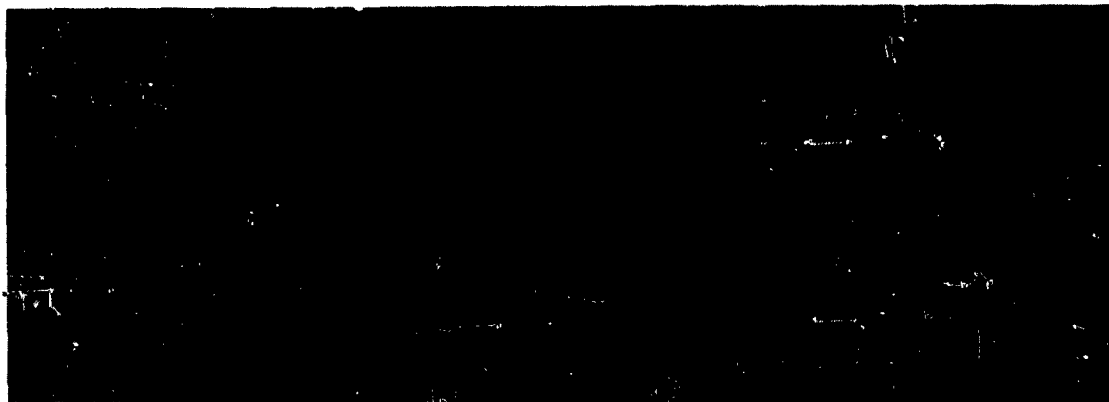


Figure 47. Ohmic Center Junction Sample

responses are obtained after fewer repetitive flexures when the leads are attached at points of maximum stress on the silicon sample surface.

#### 4.11.7 Fatigue Experiments

Significant electrical responses had been obtained from the short-term flexure of silicon dendrite-web samples, and therefore the effect of long-term flexure on performance was looked at. Samples with ohmic center-junctions were flexed repetitively and continuously at 0.85 cps for periods up to 12 hours. Electrical responses were recorded periodically, and ambient temperature close to the sample was recorded continuously by a platinum-platinum (10 percent rhodium) thermocouple and precision potentiometer. At stated intervals, the samples were removed and photographed microscopically with a Leitz microscope-camera combination, to correlate electrical response with mechanical damage at the surface. Figure 48 shows typical electrical responses.

The results of these experiments are discussed in paragraph 4.11.9 below.



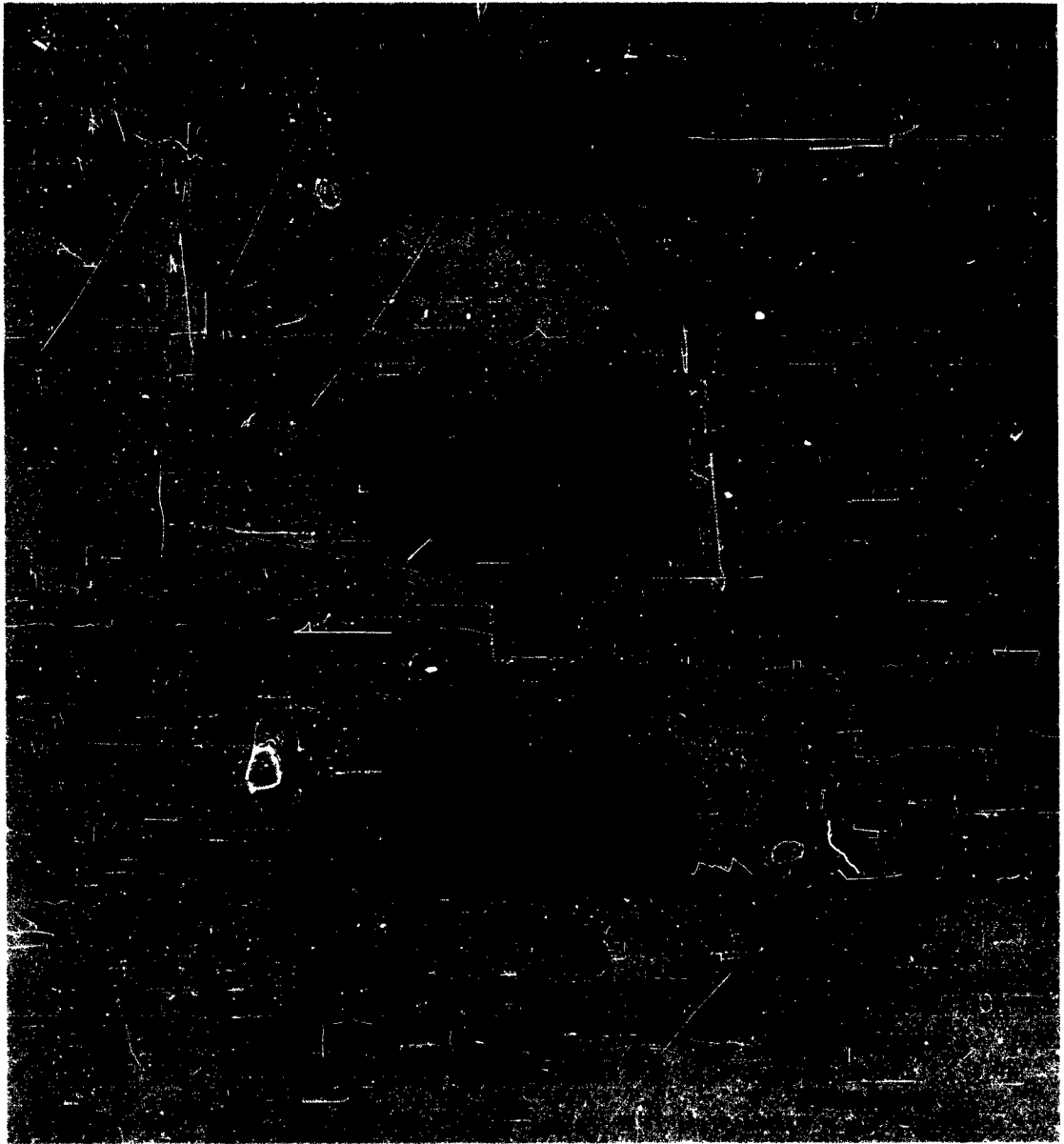


**Figure 48. Typical Electrical Responses of Samples  
Subjected to Fatigue**

#### 4. 11. 8 Elevated Temperature Experiments

Since semiconductor devices may often function in relatively high temperature environments, the temperature dependence of the phenomena related to device failure is important to a complete understanding of the mechanisms by which failures occur. And, since the fatigue experiments which were conducted have shown that mechanical damage in silicon can occur as a result of repetitive stressing, additional experiments were conducted to obtain information on the temperature dependence of these damage creation processes.

Samples of the same type used in the fatigue experiments were mounted in the flexure apparatus, and the sample, and its immediate surroundings, brought to a stable thermal equilibrium at a temperature higher than room temperature by heating with a forced stream of warm air. Since all of the junctions on the sample are small thermoelectric generators, the establishment of thermal equilibrium was assured by delaying the experiment until the electrical trace at the oscilloscope had reached a stable dc level, indicating overall thermoelectric equilibrium. Flexure was then begun at a frequency of 0.85 cps, and the electrical responses and surface damage were photographed periodically. The same procedure was then repeated for several different temperature levels, thus providing information regarding the electrical response change with variation in temperature.

Figures 49a and 49b are typical photographs of the responses obtained for this series of experiments.

#### 4. 11. 9 Visible and Subvisible Cracks in Semiconductor Materials

The results of the fatigue test are summarized in the sketch, figure 50 which shows the results with one sample and is representative of those with other members of the experimental series. Primary and secondary flexure maxima are explained in paragraph 4. 11. 2. 1 above.

As seen from this sketch, after 10 minutes of continuous flexure at a frequency of 0.85 cps, relatively "fast" responses began to appear at the maximum stress point on the flexure cycle. With an increasing number of

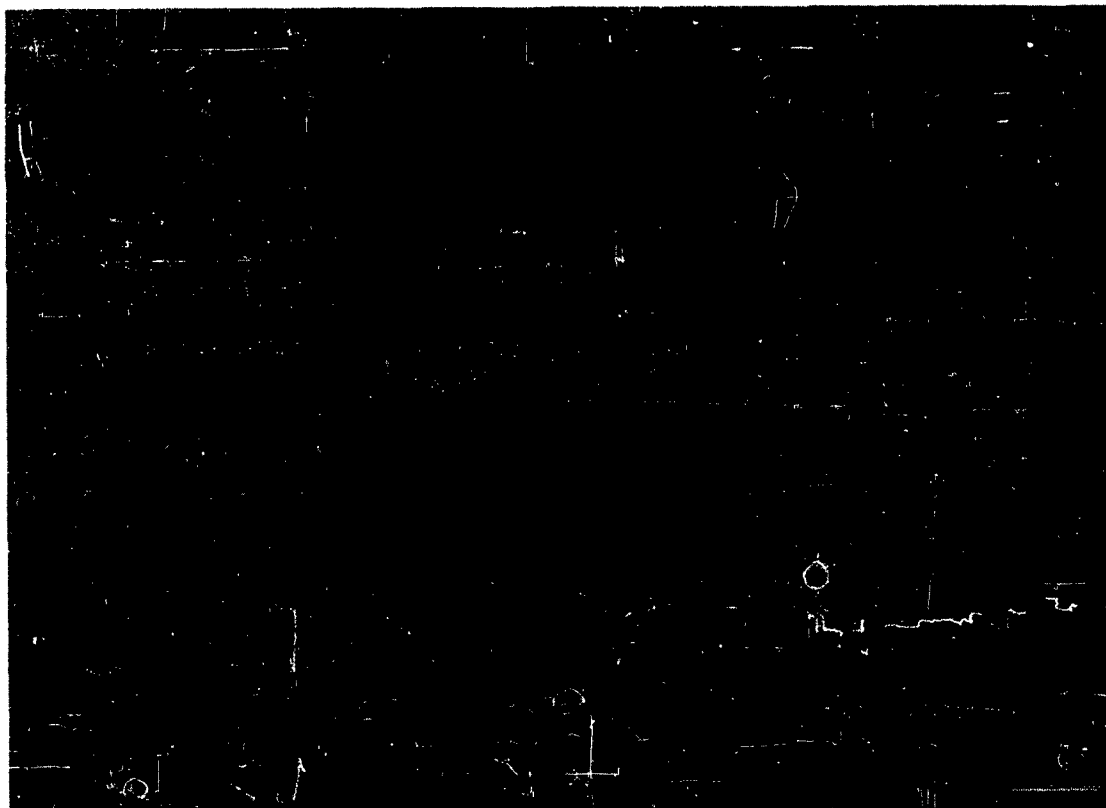


**Figure 49. Typical Electrical Responses of Samples  
Subjected to Fatigue**

flexure cycles, the responses above the steady state value never exceeded 1 millivolt, but additional responses began to appear at the opposite point of maximum flexure. Finally, in the specific experiment illustrated, voltage responses of a roughly repeating character were obtained over the entire flexure cycle after 8 hours of continuous flexure.

Microphotographs of the sample surfaces at various times throughout the course of the test produced the following generalized observations:

a. In general, no change in sample surface characteristics was discernible (for microscope magnifications up to 200x) for continuous flexure times of up to approximately 1 hour.

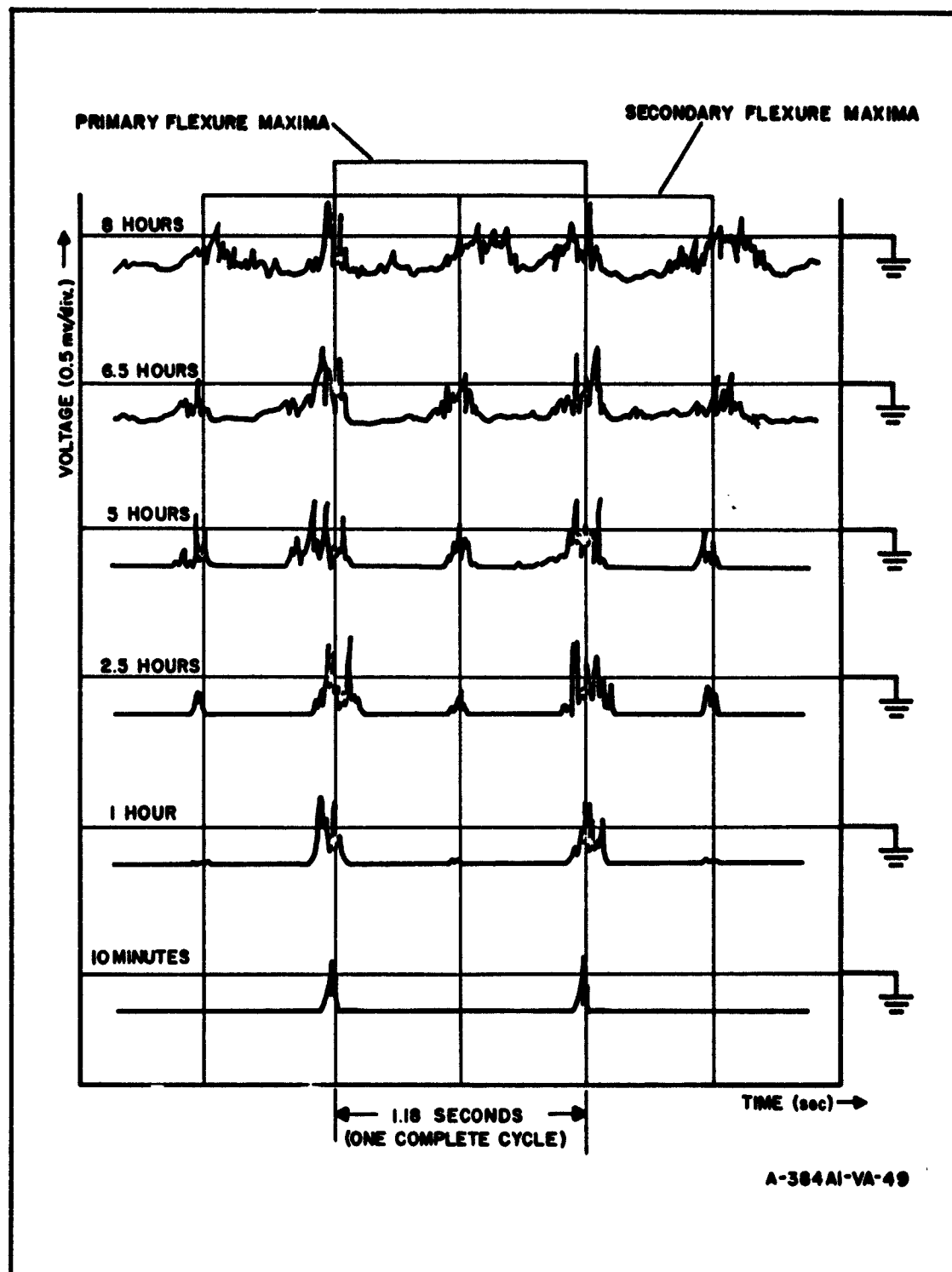


Figure 50. Pictorial Summary of Fatigue Experiment Results

b. After 1 hour, microscopically observable cracks or fractures began to appear at points of obvious stress concentration (e.g., around alloy junctions, surface flaws, etc, (figure 51). With increasing flexure time beyond this point, the creation of new fractures and enlargement of old ones occurred continuously.



Figure 51. Typical Junction Area Damage Resulting From Repetitive Stressing

On the basis of these results, it appeared reasonable to conclude that the electrical responses observed on repetitive flexure were directly related to the occurrence of fractures and other mechanical damage produced by

repetitive stress induced fatigue in the sample. It is probable that the voltage pulses observed in the present experiments stem from the following phenomena:

a. It is probable that the largest single contributor to the voltage response was the frictional generation of charges at fracture interfaces, caused by minute displacements of adjacent fracture planes relative to one another as the sample was flexed. This type of phenomena has been observed often in the past by other experimenters.

b. At the instant of formation of a new fracture in the silicon sample, a separation of charges similar to that observed by Skinner and Kern in insulating polymers probably occurred. This phenomenon then contributed continually to the voltage response as previously formed fractures became enlarged with repeated sample stressing.

c. In addition, it has been shown in other work on this contract that some contact charging can occur when similar materials are repetitively contacted. A similar phenomena probably occurs here as existing cracks and fractures open and close during the flexure cycle.

For continuous flexure times beyond about 1 hour, the appearance of a new voltage response in general always coincided with the formation of a new fracture, or the enlargement of an old one.

Responses occurring at continuous flexure times less than 1 hour, however, could not be correlated with readily observable gross mechanical damage.

Some experimental observations support the possibility that these responses may result from the formation of minute surface fractures similar to the "reversible cracks" observed in flexurally stressed glasses by Finkel and Kutkin. When the surface on which these cracks occur is stressed in tension, the cracks open sufficiently to permit microscopic observation, but they have the ability to close or possibly heal almost completely upon removal of the applied stress. This explanation of the results obtained in the

present study is supported by the results of the following supplemental experiments:

a. Samples which had been repetitively stressed for less than 10 minutes were lightly etched with a hydrofluoric-nitric-acetic acid mixture (designated CP-4), a strong silicon-silicon oxide etchant, and compared with similarly etched but unstressed samples. Those samples, which had been stressed, revealed patterns of very fine etch lines in far greater abundance than the unstressed samples.

Since it is known that preferential etching will occur at sites of discontinuity on silicon surfaces, it can be tentatively concluded that the line patterns obtained were due to preferential etching of the acid at microscopically invisible fractures sites on the silicon surface.

b. A simple experiment showed that the gradual application of pressure at a point on a silicon wafer surface can result in observable fracture patterns which completely disappear upon removal of the stressing force.

#### 4. 11. 10 Elevated Temperature Results

The sketch, figure 51, prepared in a manner similar to that for the "fatigue test" results, summarizes the results of the elevated temperature experiments which were conducted in accordance with the previously described procedure.

The most significant observations with respect to these results are the following:

a. An increase in sample ambient equilibrium temperature was invariably accompanied by an increase in magnitude of the voltage response obtained on repetitive flexure.

b. A correlation of sample surface microphotographs with voltage response data indicated that increased temperature shortened the continuous flexure times required for gross mechanical damage to first occur in the sample.

If the explanation for the phenomena observed in the "fatigue tests" can be tentatively assumed correct, then result a, cited above, is completely

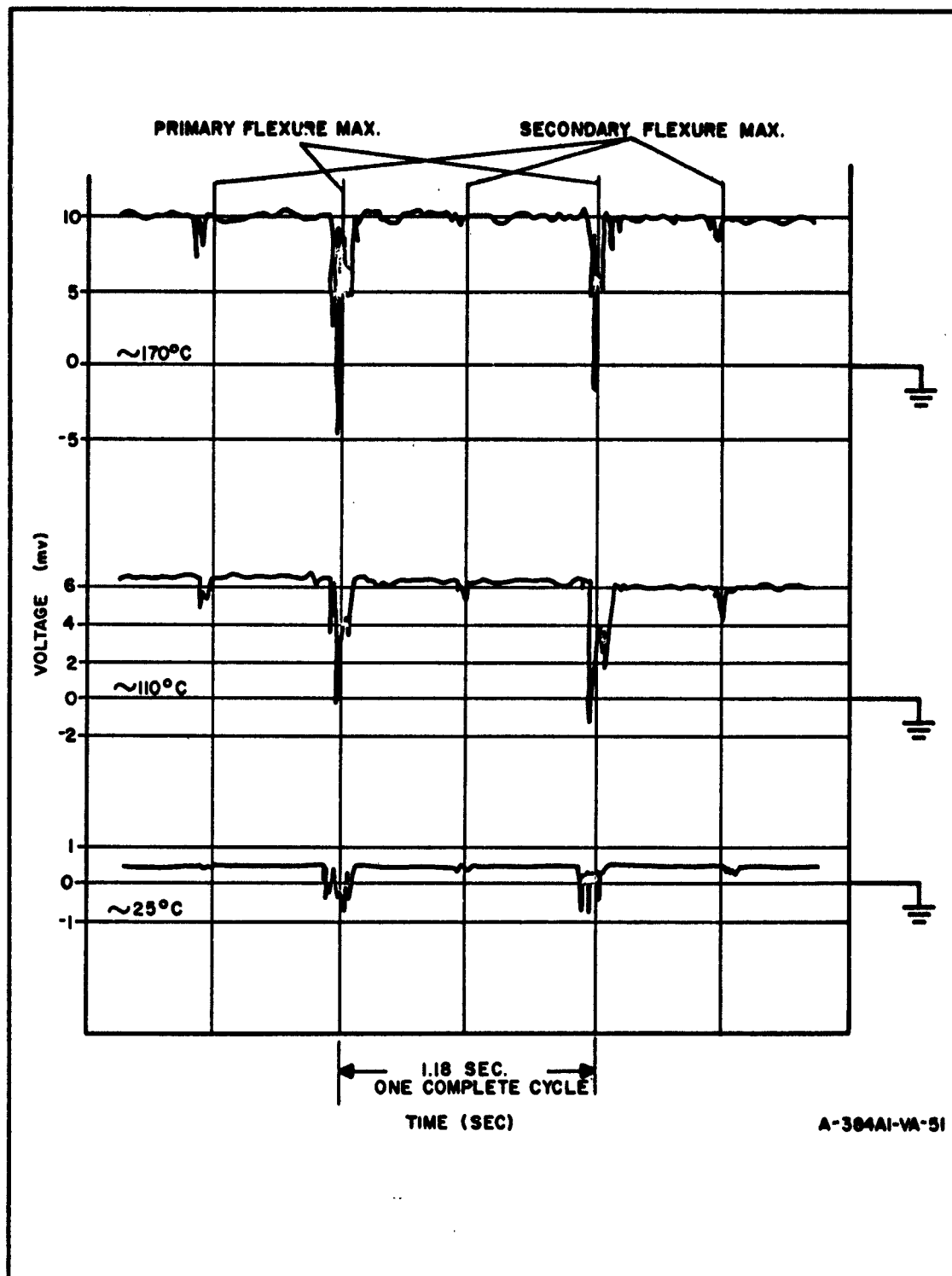


Figure 52. Pictorial Summary of Elevated Temperature Experiments



consistent. It is well known that an increase in temperature in a semiconductor results in an increase in the number of carriers above the quasi-Fermi level (determined by the electro-chemical potential). With respect to the present experiment, this increase would logically manifest itself in an overall increase in the magnitude of voltage responses, both at steady state and on repetitive sample flexure.

#### 4.11.11 Conclusions

Oscillatory and repeated stresses in silicon and probably in other semiconductor materials of similar mechanical properties can cause deterioration of the overall performance of devices made of the material.

Such stresses can be applied without its being evident in the course of grinding, polishing, scribing, etc.

The mechanical degradation that is caused by flexural stresses in silicon has been shown to concentrate at alloy junctions and other sites of discontinuity. It also is hastened by elevated temperature.

Some of the damage, though existing, may become microscopically invisible upon removal of the stress.

The above phenomena appear to occupy a significant position with regard to fundamental mechanisms of failure in semiconductors.

#### **4.12 VOLUME STUDIES: UTILIZATION OF THE ELECTRICAL-FRICTIONAL PROBE FOR VOLUME STUDIES OF SEMICONDUCTOR MATERIALS**

As described in paragraph 4.3, the frictional probe electrical response gives information on the nature of material under the surface, by either suitable utilization of frequency of light illuminating the material, or of applied voltage on the probe. Indications of effects occurring under the surface are also given by the techniques described in paragraph 4.5, although the electrical-frictional probe is regarded as more informative. In those sections are described some of the experiments which showed the utility of each apparatus for volume studies, and the results obtained.

#### **4.13 TRANSISTOR FAILURE CAUSED BY SURFACE CHARGING**

Detailed descriptions of the work performed which resulted in the discovery that surface charging could cause transistor failures is given in Quarterly Reports 2 and 3. A few typical curves from the curve tracer showing the alteration in transistor characteristics with charging are given in figure 53. The difference in the effects of charging the surface near the emitter, and near the collector, is described in Quarterly Report 3.

The charging may occur because of a number of different causes. In the manufacturing process, frictional electricity may unwittingly be created by the operator's movement relative to some surface, during encapsulation and flow onto the transistor. The transistor may be in regions containing strong electromagnetic fields before encapsulation. Any of the effects described below may be responsible. If the charge does not flow off rapidly, the retained charge can cause the type of performance failure shown in the diagrams, in which its characteristics change from that of a transistor to that of a resistor of low resistance. Later recovery may occur over long periods of time.

Since most transistor surfaces are passivated, a thin nonconducting layer is on the surface, which tends to retain the charge; because of its thinness, the charge is close to the surface of the semiconducting material. The

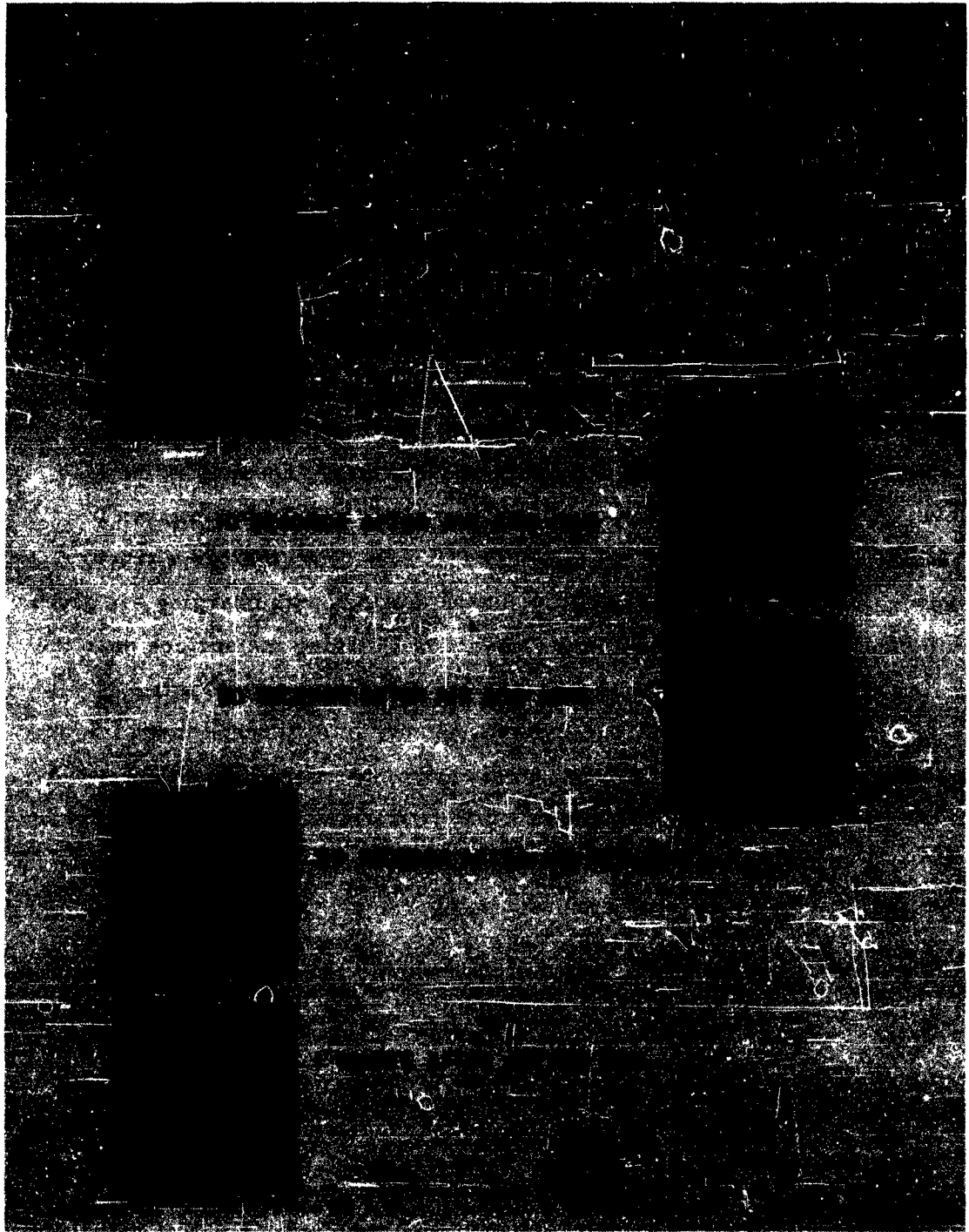
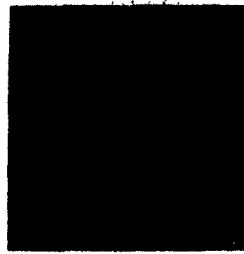


Figure 53a. Ions and Air on Surface of a Transistor



NO CHARGE



EMITTER CHARGED



COLLECTOR CHARGED

$V = 0.5 \text{ MA}$

$H = 1V$

$S = 0.2$

$R_C = 500 \text{ OHMS}$

382A3-PF-21

Figure 53b. Separate Charging of Emitter and Collector

change in characteristics can be caused by any one of a number of effects, some of which are: field effect because of the charge layer being an extremely small distance from the operating transistor region, dielectric breakdown of the passivating layer because of the steep gradient across it, electron-hole generation favored by the sharp field gradient, dielectric polarization of the passivating layer, or formation of channels by the added charge density. Chemical change of the layer may or may not be involved.

#### 4.13.1 Failure From Charging by Application of Ions to the Transistor Surface

In summarizing the experiments using gas carriers of ions, argon, nitrogen, and air, it can be concluded that the integrated effect of air or nitrogen is greater than of argon as the ion carrier. The small differences in ionization potential were negligible for the voltages used in ionizing. Flow rate was the same. The charge decay time on the transistor is much shorter when argon is used. Whether this is because of the greater mean velocity of the lighter atom at the same temperature or because of a smaller affinity of the charged ion to the surface was not determined.

When the partially ionized gas is directed at the emitter of a rate-grown transistor, the collector current will decrease by 20 percent. (Quarterly Report 3, paragraph 4.6.4). If the gas stream is directed at the collector area, the collector current increases by over 100 percent.

The ion-charging studies were conducted on several types of transistors (grown-diffused, planar, and mesa). The charging effect of the ion generator was much smaller on the mesa and planar type transistors.

The condition of the transistor prior to ion-charging was important. Transistors with minor damage or exceptionally low betas were much more susceptible to accepting a charge, as compared to a new transistor meeting specifications. After being charged and discharged, the transistor surface was more susceptible to accepting a charge, even after days of inactivity.

When the surfaces of various transistors were scanned with an electron beam (paragraph 4.9 above), the ceramic base material under the

grown-diffused transistor retained a charge that distorted the image of the surface of the device under inspection. However, when a mesa type transistor was scanned with an electron beam, definite patterns could be determined, even though the mesa transistor was only a fraction of the size of the grown-diffused transistor.

Further experimentation is desirable to pin down the precise types of effects operating in the failure by surface charging, but the failure is real though not necessarily permanent, and has been demonstrated. The fact that the surfaces become more susceptible to charging after being once charged would argue for a chemical change or for dielectric breakdown. However, it was also observed that: the effect disappears when the charge has time to leak off (permanent chemical change by dielectric breakdown would favor the retention of a charge though not at all so great as that originally applied); ultraviolet light causes the effect (paragraph 4.13.2 below); similar effects are caused by frictional charging by shaking a transistor with loose desiccant; and the effect can be produced by a steep low-peak voltage pulse with recovery shortly thereafter. Since UV causes it, and since the gases without their ions do not cause the effect, it is attributable to the charge rather than the chemical nature of the gas. Irrespective of the cause or group of causes, it is a demonstrated, previously unsuspected, mechanism of failure.

To minimize the ability of a transistor to retain an electrical charge, it is recommended that dielectric material be reduced to a minimum or be provided with sufficient leakage to minimize the RC time constant for charge storage.

#### 4.13.2 Charging by Ultraviolet Light

This process is described in Quarterly Report 3. A sample of its effect is shown in figure 54. It is a mechanism of failure, but unlikely to be encountered in the normal use of encapsulated transistors.



**Figure 54. Longwave UV on Surface of Alloyed Junction Transistor**

#### **4.13.3 Failure Resulting From Transistor Vibration or Acceleration: Charging by Frictional Contact With Loose Desiccant Particles**

The effect of loose desiccants in transistors was observed. Several transistors commercially available are manufactured with loose desiccants. From the previous results, it was felt that frictional charging from this desiccant would affect transistor performance.

The transistors were vibrated at a frequency of 1200 cps, so that accelerations of 15 to 25 g's were applied. Pictures were taken of the collector curve characteristics. The collector curves, figure 55, resemble normal curves but appear to be modulated with white noise. The fogginess; i. e., the traces which leave the regular curves and appear to go downwards in a random fashion, all with the same slope, are the effect of the frictional charge resulting from the rubbing of the desiccant particles on the passivating layer or elsewhere during the shaking.

The change in electrical characteristics was a slight increase (> 5 percent) in collector current.

It is recommended that desiccants not be incorporated loose, or in such form that they can crack free or powder; instead the desiccant should be thoroughly secured internally, in the transistor's cover.

#### **4.13.4 Failure Resulting From Nonoverload Steep Voltage Pulse**

In these experiments, as distinguished from those in paragraph 4.13.1, the pulse charging of the transistors was carried out on encapsulated transistors: i. e., as they arrive from the supplier.

Transistors, all of a similar type (grown-diffused), but varying in beta and in previous condition, were subjected to a 0.6- $\mu$ sec pulse, with a rise time of 0.1  $\mu$ sec and pulse height of 100 volts, at a repetition rate of 500 cps; the pulses were fed directly into the base of the transistor from a pulse generator for 15 seconds. The circuit is shown in figure 56. The pulse generator was then disconnected, and the transistor switched to the collector curve tracer. The electrical effect as viewed on the collector curve tracers showed a 10 to 15 percent increase in collector current. This increased



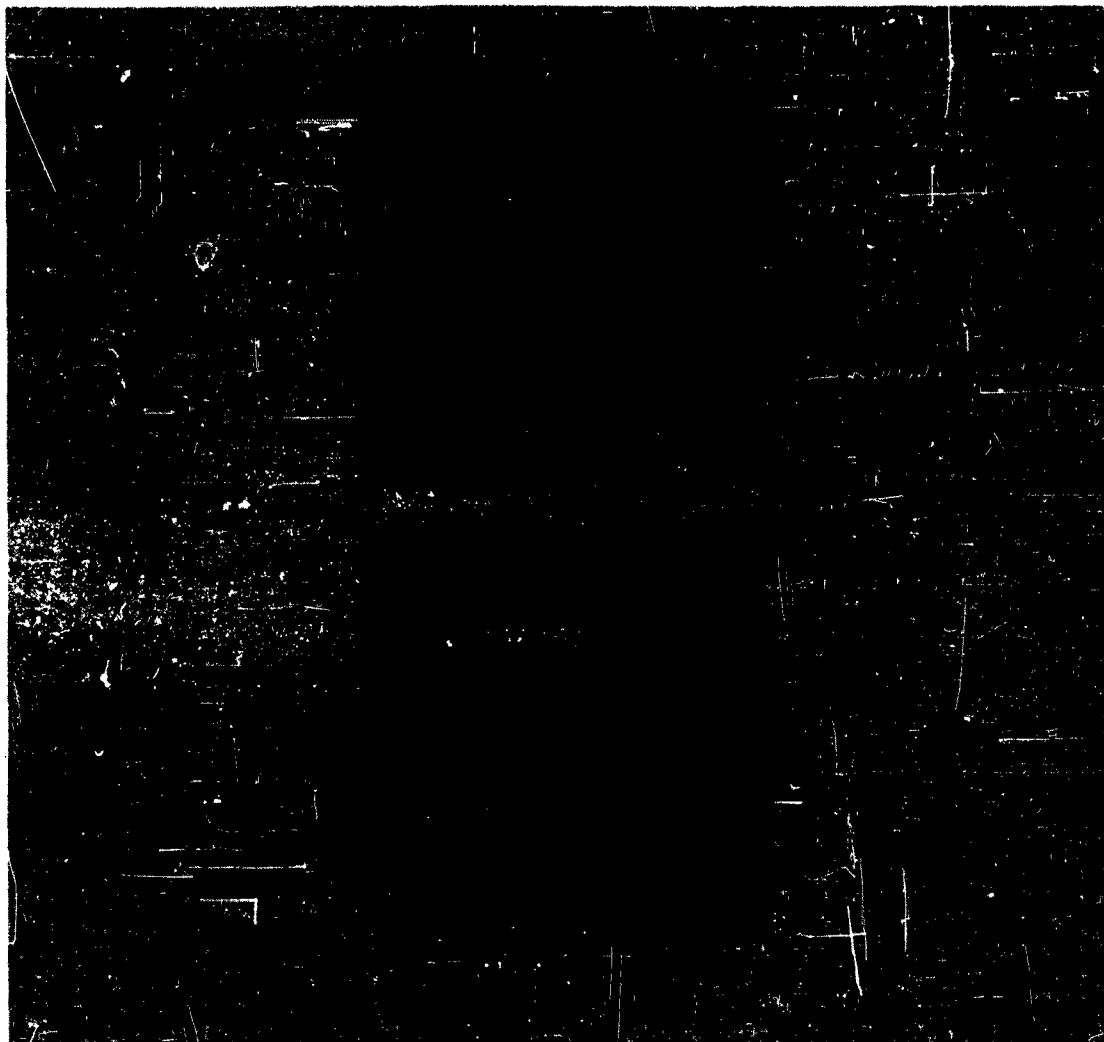


Figure 55. Effect of Loose Desiccant Under Vibration

current returned to the original value of collector current in approximately 25 seconds.

As in the experiments described in paragraph 4.13.1, the magnitude of the increase in collector current and the decay time were dependent upon the condition of the transistor: the transistors with the lowest beta exhibited the greatest increase in collector current and the longest recovery time.

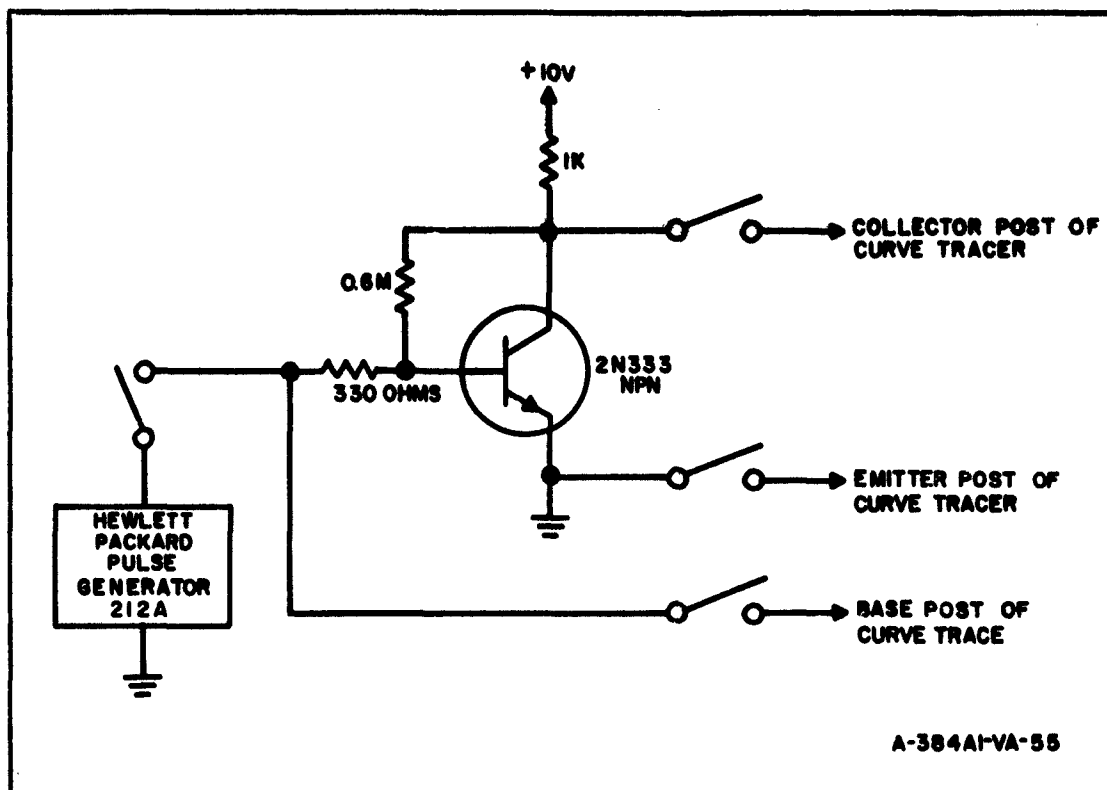


Figure 56. Circuitry for Pulse Charging

In the performance of its circuit function, a transistor used at nearly the specification voltages may suffer this kind of change of characteristic. It is reasonable to believe that even though the voltages used here were below the overload range, a decrease of peak voltage will decrease the undesired effect. The likelihood of changes in transistor performance from this effect would then be decreased if a derating procedure is used, so that the transistor is not subjected to voltage peaks above some fraction, say 50 or 30 percent of its rated values.

#### 4.14 SPECIFIC FAILURE MODES RELATED TO FABRICATION AND PROCESSING TECHNIQUES: LIAISON AND CORRELATION WITH PRODUCT RELIABILITY GROUP

Accompanying the investigation described in paragraph 4.1, a number of devices, principally transistors and diodes, have been examined physically

by removal of the can and subjecting them to various physical and microscopic tests. A small amount of this work has been performed in liaison with the Product Reliability Group, as a means of obtaining clues as to mechanisms of failure.

Since similar results have been obtained by other contractors under the Mechanisms of Failure program of the sponsor, and since the items were studied not to identify modes of failure, but to yield clues to mechanisms of failure not presently recognized, they will not be described in detail.

Examples of such failed devices, from different manufacturers, include:

a. A glass diode which exhibited suitable forward current characteristics, but broke down at one-third its rated value of 180 volts when operated in the back current direction. Chemical cleaning removed the paint, and inspection through the glass showed that the inside of the glass envelope was coated with a fine deposit of Pb particles. The particles would move when the glass envelope was tapped, and contributed microphonics on the forward current curve. The opened diode was examined under the microscope, figure 57, and the silicon disc appeared to have two passivating covers. The outer one which was a transparent silicone grease about the consistency of a heavy oil (containing some of the Pb particles) was removed with trichloroethylene. The diode completely recovered. Apparently, the breakdown was due in part to discharge between the metal particles in the silicone grease.

b. A diode reported shorted was examined. It showed 0.5 megohm resistance and on examination was found to be not shorted but approaching an open condition from a fracture occurring near the bonding of the anode lead. The stresses apparently were bimetallic from alloying, and actual cracking may have resulted from additional external stresses, during use.

c. Two power transistors, silicon-alloyed, that failed in a system were checked and found to look resistive, with no beta. After applying heat to remove the transistors from their heat sink, both showed some transistor action. Both were opened and subjected to ammonium fluoride etch, washed,

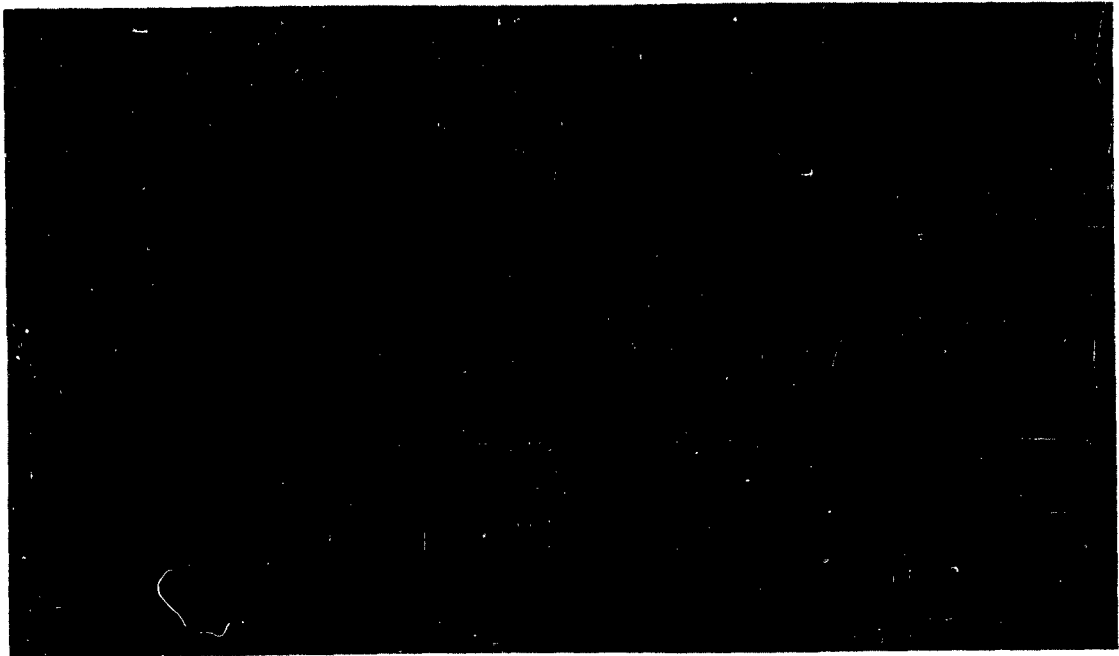


Figure 57. Microscopic View of Opened Diode

and rechecked on a curve tracer. Both had recovered to more than 80 percent of their maximum operating limits. The partial recovery after application of heat and the almost complete recovery after a surface etch indicates surface failure; no test was made for any effect of deterioration of the silicone varnish at the transistor operating temperature.

d. Two diodes submitted by the Product Reliability group had failed during high ambient heat ( $262^{\circ} - 266^{\circ}\text{C}$ ) tests. No diode action could be detected. Solder rivulets had formed between the anode and cathode, fused into the side of the Si-pill, and continuing underneath into a pool of solder (figure 58). After etching the solder rivulets nearly off, diode action was restored.



Figure 58. View of Diodes Failed During High Ambient Heat

e. Direct comparison was made between two 2N333 transistors which were initially good (as received); after subjecting them to an overload voltage pulse, one failed, and the other one withstood many such voltage pulses without failure. Upon removing the cap and observing the two transistors under the microscope, it was clearly visible that in the failed transistor the alloy used to solder down the emitter end of the silicon bar to the ceramic base had run over and bridged across the entire base region, and onto the collector. At this point, the question was why the transistor had tested good initially. Apparently a thin layer of natural oxide on the silicon surface prevented the alloy bridge from actually shorting. However, the initial overload

pulse electrically punctured this oxide layer, and produced the short indicated by the visual examination. As a final step, the metal shorting bridge was carefully etched away, and the transistor was found to be restored to its normal operating condition.

This instance illustrates the need for good control of even the noncritical steps in the manufacture of the transistors, and also the need for visual inspection to pinpoint cases where units may appear good when tested electrically, but still be susceptible to failure.

## 4.15 THE EFFECT OF CARRIER DIFFUSION IN SEMICONDUCTOR MATERIALS

### 4.15.1 Introduction

The effects of carrier diffusion are fundamental to the solid state explanation of conduction, and to analyses of the behavior of rectifying junctions, transistor action, etc. Diffusion effects may be responsible for space charge concentrations, diffusion potentials at junctions, non-ohmic behavior, etc. It is the purpose of the present development to show that the thermodynamically consistent picture of the diffusion component of the current flow can be responsible for circuit transients not usually included in the conceptual analysis of devices made of semiconducting materials.

Effects in circuits containing devices made with semiconductor materials, such as delay times in traversal of a region, lag caused by the detailed behavior of carriers in the vicinity of a p-n junction, etc., have been considered in a number of studies, partly in the search for solid state analogs of inductive action. Here, the distinction between such inductive-type response and that considered in conventional inductances must be recognized.

The conventional inductance introduced into a circuit performs two main functions. Both may be derived from Maxwell's equations. First, it causes a phase lag in the current, behind applied voltage; second, it stores energy in the electromagnetic field. The solid state analogs of inductance, which have been discussed in the literature, perform the first function adequately; the frequency and temperature dependence of the phase lag may be different than usually expected in conventional inductances, but this can be allowed for in circuit or microcircuit design. The solid state analogs do not perform the second function in the same way in which an inductance does.

It is not the intention of the present development to discuss the questions of lossless storage of energy in the electromagnetic field, the Poynting vector and its justification at high frequencies, and the effect of radiation upon total circuit energy. It may be assumed in a solid state material, that

current flow is governed by the conduction-diffusion equation, at least at frequencies in the ranges used in solid state technology; i. e. , below microwave frequencies. For convenience, the derivation below considers only a single carrier, but generalization to two is immediate and not difficult.

If a thermodynamically consistent derivation (reference 1) is made of the flow of a single carrier in a semiconducting material, neglecting carrier generation and recombination, the electrochemical potential is:

$$U = \psi + kT \ln n + \text{constant} \quad (22)$$

where  $\psi$  is  $e$  times the electrical potential  $V$ ,  $n$  is the volume density of carriers, and  $k$  and  $T$  are Boltzmann's constant and the absolute temperature. The current through the material is given by:

$$j = -n \mu \nabla U = -n \mu \nabla \psi - \mu kT \nabla n = n e \mu E - eD \nabla n \quad (23)$$

in which  $D$  is the diffusion constant, and  $E$  the electrical field. Equation 23 is the conduction diffusion equation for a single carrier, analogous to these for majority and minority carrier developed by Shockley and co-workers (reference 2). From the development (reference 1), it is possible also to determine other thermodynamic quantities, including the Maxwell forces within material through which the current is flowing or in which the charges are. These forces agree with those expected on the basis of a treatment of the charge content and current flow as an electron gas.

#### 4.15.2 General Formulation

Consider a sample of semiconductor material within a device. Because of the operation of contiguous portions of the device, time-dependent electrical fields are created in the vicinity of the sample being considered, (figure 59). To examine the effects of these electrical fields, blocked boundaries will be considered; the volume of the material between the two surfaces is therefore subject to internal currents and potentials because of the fields, but no net current flow occurs across the surfaces. The question to be considered is what transients and what heat dissipation are found in the volume of material.



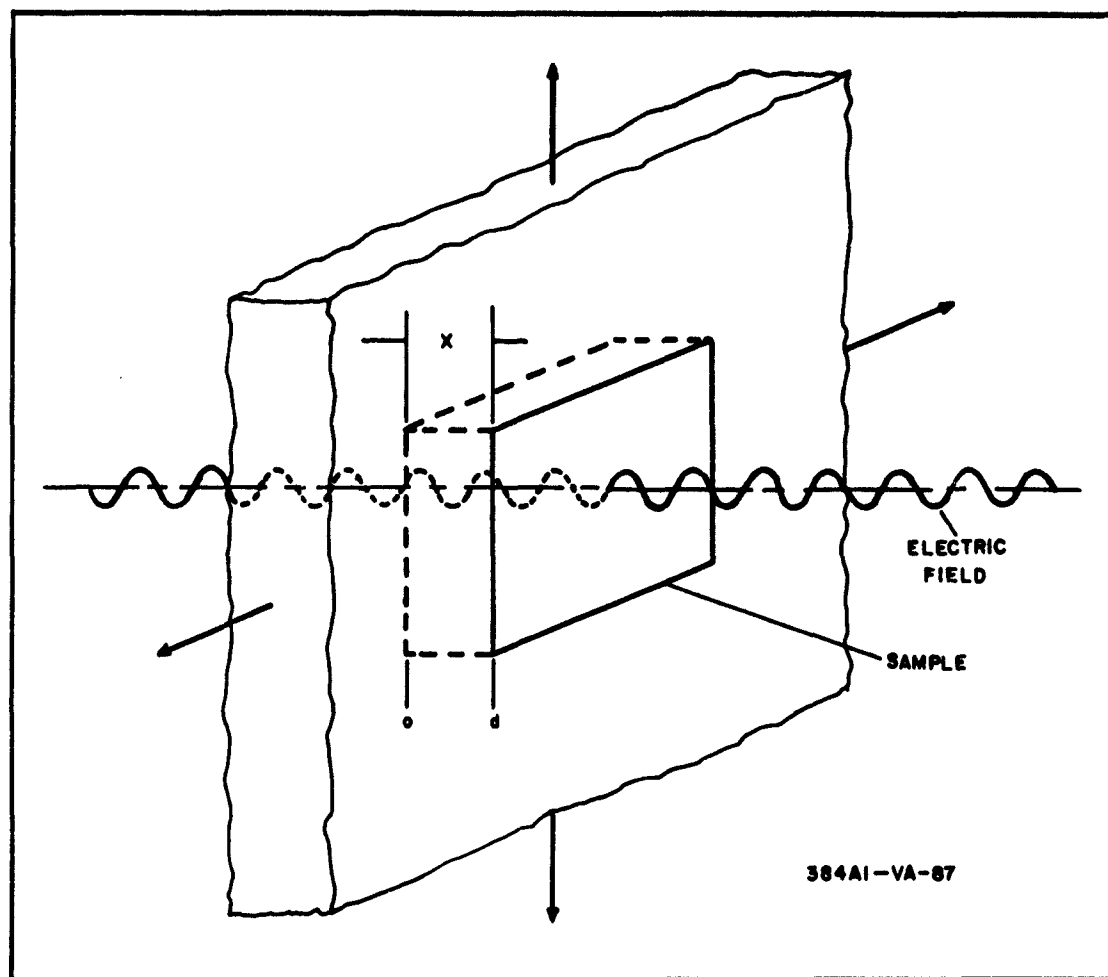


Figure 59. Electric Fields in Vicinity of Sample

The one-dimensional model considered here is depicted in figure 60.  $E_a(t)$  represents the electric intensity of an applied field;  $E_i(x, t)$ , the internal field due to the displacement of charge carriers;  $E_T(x, t)$ , the net electric intensity,  $E_a + E_i$ ; and  $j(x, t)$ , the current density within the dielectric sample. It is assumed that only one type of charge carrier is present, having been released from a bound state by a suitable agency such as thermal or photon excitation, leaving behind an oppositely charged core density fixed in space. It is assumed that the current density consists of both conduction and diffusion components, and that related time-dependent phenomena are described sufficiently well by the steady state conduction-diffusion equation, viz.,

$$j(x, t) = \mu e n(x, t) E_T(x, t) + e D \nabla n(x, t) \quad (24)$$

where  $\mu$  is the mobility constant;  $n$ , the negative charge carrier density;  $D$ , the diffusion constant; and  $e$ , the electron charge.

By obvious reformulation, the treatment is applicable to those cases in which the charge carrier is positive, as when holes instead of electrons, or protons or other ions (in, for example, alkali or silver halides, or certain polymeric materials), are the carriers. Although in many cases, the Nernst-Einstein diffusion equation will be applicable:

$$e D = \mu k T, \quad (25)$$

the treatment will, for generality, continue to use the diffusion constant, and equation 25 will be introduced where appropriate in considering certain consequences of the treatment.

Treating the applied field as a boundary perturbation of the form,  $\lambda E_a(t)$ , the various physical variables can be expanded in terms of the perturbation parameter  $\lambda$  as follows:

$$E_T(x, t, \lambda) = \sum_{k=0}^{\infty} E_{T k}(x, t) \lambda^k = \lambda E_a(t) + \sum_{k=0}^{\infty} E_{i k}(x, t) \lambda^k, \quad (26)$$

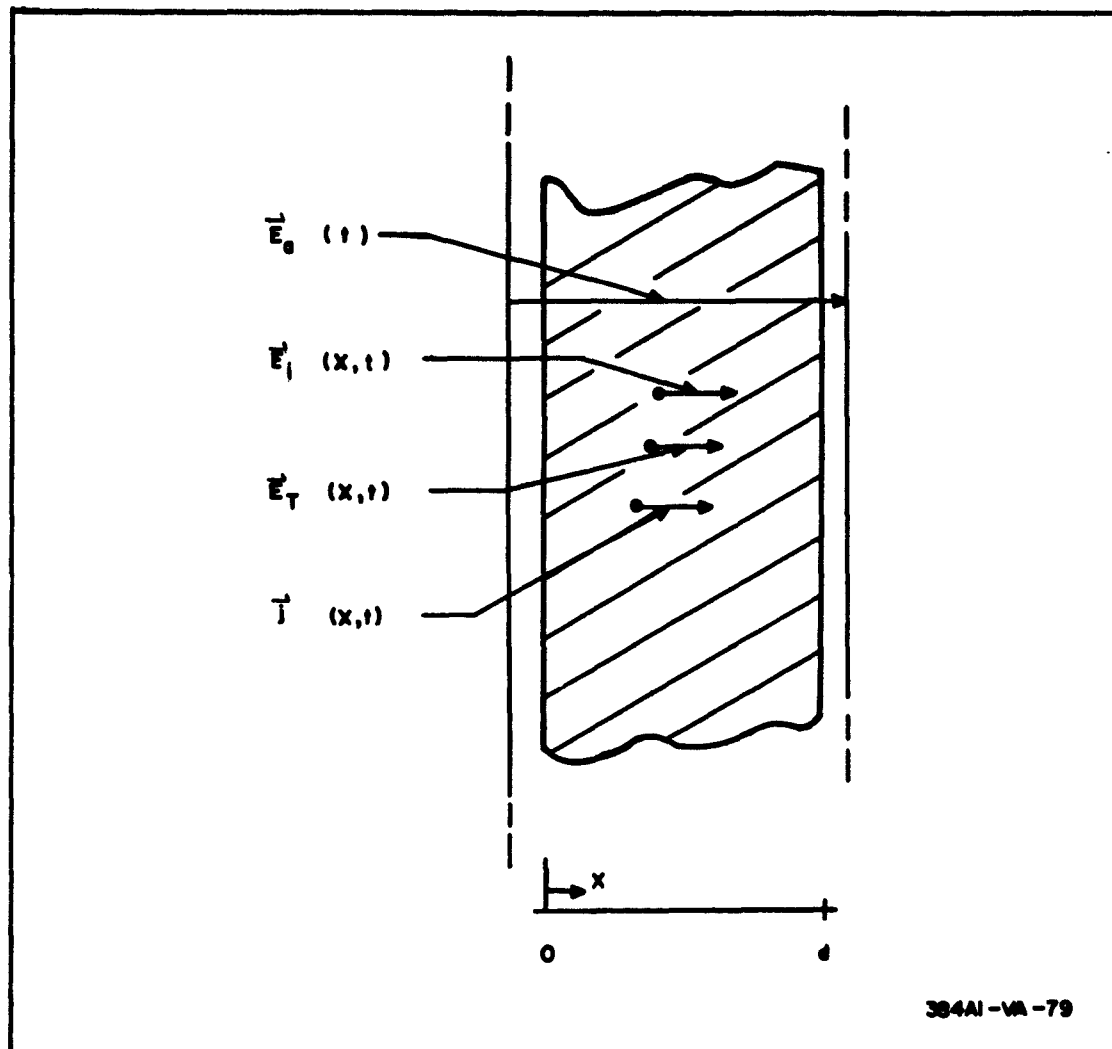


Figure 60. Model for Transient Conduction-Diffusion of Carriers

$$j(x, t, \lambda) = \sum_{k=0}^{\infty} j_k(x, t) \lambda^k \quad (27)$$

$$n(x, t, \lambda) = \sum_{k=0}^{\infty} n_k(x, t) \lambda^k \quad (28)$$

$$\sigma(x, t, \lambda) = \mu e n(x, t, \lambda) = \mu e \sum_{k=0}^{\infty} n_k(x, t) \lambda^k = \sum_{k=0}^{\infty} \sigma_k \lambda^k \quad (28a)$$

As verified below, a set of appropriate boundary conditions is

$$E_{T0}(x, t) = E_{i0}(x, t) = 0 \quad (29)$$

$$E_T(0, t) = E_T(d, t) = \lambda E_a(t) \quad (29a)$$

$$j(0, t) = j(d, t) = 0 \quad (30a)$$

Equation 29 implies that in the unperturbed state the specimen is electrically neutral, and equation 30a implies that the boundary interfaces are "blocked."

Both equations 29a and 30a give:

$$E_{ik}(0, t) = |E_{ik}(0, t)| = E_{ik}(d, t) = 0; \quad k = 1, 2, \dots \quad (29b)$$

$$j_k(0, t) = j_k(d, t) = 0; \quad k = 1, 2, \dots \quad (30b)$$

Together with Poissons's equation and the continuity relation:

$$\nabla \cdot E_T = (4\pi e/\epsilon) (n_+ - n), \quad \epsilon = \epsilon_0 \epsilon_R; \quad (31)$$

$$\nabla \cdot j = e (\partial n / \partial t); \quad (32)$$

Equation 24 to the first order reduces to:

$$\left. \begin{aligned} L \cdot \{E_{i1}(x, t)\} &= \frac{\partial^3 E_{i1}}{\partial x^3} - \frac{\partial^2 E_{i1}}{\partial x \partial \tau} - K \frac{\partial E_{i1}}{\partial x} = 0 \\ \tau &= Dt, \quad K = 4\pi \mu e n_+ / \epsilon D; \end{aligned} \right\} \quad (33)$$

where  $n_+$  is the constant positive "core" density, and  $K$  is the square of a parameter with the dimensions of a reciprocal length analogous to that introduced in the Debye-Hückel treatment of electrolytes. If the Nernst-Einstein diffusion relation (equation 25) is applicable,  $K$  is the reciprocal of the square of the "Debye shielding distance,"  $h$ , so that if  $h$  is small with respect to  $d$ , (i. e.,  $K$  large in comparison with  $d^{-2}$ ) the electron gas may be considered as behaving as a plasma (reference 3).

In the above equations,  $\epsilon_0$  is the permittivity of free space, with the value unity if electrostatic units are employed.  $\epsilon_R$  is the relative permittivity, which, for values greater than one, accounts for the classical polarization of a linear dielectric (reference 4), and is commonly called the dielectric constant. The physical phenomenon associated with  $\epsilon_R$  is purely an energy storage and, under an applied alternating field, a material characterized only by  $\epsilon_R$  would show no loss. A Cole-Cole diagram for such a material would consist of a single point on the abscissa at  $\epsilon_R$ . In the experimental investigation of the loss associated with alternating fields, an additional mechanism is being studied which modifies  $\epsilon_R$  into a frequency-dependent quantity. The complex dielectric constant  $\epsilon^* = \epsilon_R f(\omega)$ ; in paragraph 4.16, the functional form of  $f(\omega)$  is obtained for a semiconducting material showing loss originating in conduction and diffusion.

In addition to the above equations, we have:

$$j_1(x, \tau) = (\epsilon D / 4\pi) \left\{ K E_{T1}(x, \tau) - \frac{\partial^2}{\partial x^2} E_{T1}(x, \tau) \right\} \quad (34)$$

Defining a Green's function by the following equation:

$$\tilde{L} \{g(x, \tau | x_0, \tau_0)\} = -\frac{\partial^3 g}{\partial x^3} - \frac{\partial^2 g}{\partial x \partial \tau} + K \frac{\partial g}{\partial x} = \delta(x - x_0) \delta(\tau - \tau_0) \quad (35)$$

with boundary conditions:

$$(\partial g / \partial x)_{x=0} = (\partial g / \partial x)_{x=d} = 0; \quad g(x, \tau_0^+ | x_0, \tau_0) = 0, \quad (36)$$

There is attained from equation 33, with  $E$  standing for  $E_{i0}$ :

$$\begin{aligned}
 E_{i1}(x, \tau) &= \int_0^t \int_0^d \{ E(x_0, \tau_0) \tilde{L} \cdot g(x_0, \tau_0 | x, \tau) - g(x_0, \tau_0 | x, \tau) L \cdot E(x_0, \tau_0) \} dx_0 d\tau_0 \\
 &= \int_0^t \left\{ \frac{\partial g}{\partial x_0} \frac{\partial E}{\partial x_0} - E \frac{\partial^2 g}{\partial x_0^2} - g \frac{\partial^2 E}{\partial x_0^2} + K g E + g \frac{\partial E}{\partial x_0} \right\}_{x_0=\tau}^{x_0=d} d\tau_0 - \int_0^d \left\{ E \frac{\partial g}{\partial x_0} \right\}_{\tau_0=0}^{\tau_0=\tau} dx_0
 \end{aligned} \quad (37)$$

Equations 29b, 30b, 34, 36, and 37 yield:

$$E_{i1}(x, \tau) = \int_0^t K \{ g(0, \tau_0 | x, \tau) - g(d, \tau_0 | x, \tau) \} E_a(\tau_0) d\tau_0 + \int_0^d E_{i1}(x_0, 0) \left( \frac{\partial g}{\partial x_0} \right)_{\tau_0=0} dx_0 \quad (38)$$

The boundary conditions utilized in evaluating equation 37 emerge from the Green's function treatment as the appropriate and consistent boundary conditions for the physical problem. They have not been arbitrarily chosen prior to the development, as would be the case for the steady state closed form of the solution. This is related to the fact that a steady state solution, obtained directly, rather than through a general solution which represents the summation of the actual physical transient (or relaxation) responses, will describe only the steady state, and not permit generalization to more general situations.

It is readily verified that the Green's function:

$$\begin{aligned}
 g(x, \tau | x_0, \tau_0) &= - \sum_{n=1}^{\infty} \left[ (2/n\pi) \sin(n\pi x_0/d) \cdot \cos(n\pi x/d) \cdot \right. \\
 &\quad \left. \exp \{ \beta_n (\tau - \tau_0) \} \cdot \mu(\tau - \tau_0) \right]
 \end{aligned} \quad (39)$$

$$\beta_n = K + (n\pi/d)^2, \quad \mu(\tau) = \begin{cases} 0, & \tau < 0 \\ 1, & \tau \leq 0 \end{cases}$$

satisfies equation 35 and the boundary conditions of equation 36. If there is no initial carrier displacement, the second term on the right-hand side of equation 37 vanishes and, by equations 26 and 39, the first order solution for the electric intensity is:

$$E_{T1} = E_a(t) - \sum_{n=1}^{\infty} \left\{ 4KD/(2n-1)\pi \right\} a_{2n-1}(t) \cdot \sin \left\{ (2n-1) \pi x/d \right\} \quad (40)$$

where

$$a_{2n-1}(t) = \int_0^t E_a(t_0) \cdot \exp \left\{ -\beta_{2n-1} D (t - t_0) \right\} dt_0$$

and that for the charge density is:

$$n_0 = n_+, \quad n = n_+ + n_1 \lambda + O(\lambda^2),$$

$$n_1 = -(\epsilon/4\pi e) (4KD/d) \sum_{n=1}^{\infty} a_{2n-1}(t) \cdot \cos \left\{ (2n-1) \pi x/d \right\} \quad (41)$$

The term  $n_+$  describes a uniform density and is primarily a number, its identification with a charge opposite to that of the carrier being the result of a multiplicative term. By equation 31:

$$n = n_+ - (\epsilon/4\pi e) \nabla \cdot E_T \quad (42)$$

so that  $n_+$  may also be regarded as the reference uniform distribution of carriers which has been disturbed by the applied field and diffusion to yield the actual distribution,  $n(x, t)$ . This also follows from the zero order terms of equations 24 to 32. Since  $n_+$  is a number, the term  $n_+$  appearing in the definition of  $KD$  (equation 33) establishes the value of  $KD$  in terms of the mean carrier density.

Here  $\lambda$  is a separation variable which may be dropped after terms of the same order of perturbation have been collected together. Since the phenomenon is nonlinear, the physical response will be different in quality as well as

in magnitude, as the applied field changes. Additional terms in the expansion will be taken up elsewhere; for the present purpose, they are not necessary. It is shown below that for dielectric constant and loss factor, it is appropriate that  $\lambda$  be infinitesimal and therefore a suitable perturbation parameter. Equations 40 and 41 will in general be approximations for large applied fields, since, for them, the higher order terms of the boundary problem solution are important.

Equation 33 is equivalent to:

$$e \frac{\partial n}{\partial t} = e D \frac{\partial^2 n_1}{\partial x^2} + \sigma_o \nabla \cdot E_{i1} \quad (43)$$

in which the subscripts refer to the first order terms in the expansions, and  $\sigma_o$  is the conductivity computed for the unperturbed charge carrier density. Therefore, the regarding of  $\lambda$  as infinitesimal amounts to retaining the terms in which the electric field intensity, charge density, or current, show the primary dependence upon the applied field and upon quantities such as the mobility and diffusion constant, but rejecting those which describe the product of two such effects or the secondary change in one such quantity brought about by the primary change in another.

The parameter  $KD$  is independent of the diffusion constant,  $D$ , and may be restated as:

$$KD = 4\pi (n_+ e \mu / \epsilon_o \epsilon_R) = \sigma_o / \epsilon \quad (44)$$

where  $\sigma_o$  is the conductivity which would be observed if an infinitesimal direct current field were applied to the dielectric. The diffusion term, in  $\beta_{2n-1} D$ , i. e.,  $[(2n-1) \pi/d]^2 D$ , becomes important or negligible as  $D$  becomes large or small, but also as the thickness of the dielectric,  $d$ , becomes small or large. It is more important for the higher order terms in  $n$ .

The results in equations 40 and 41 constitute time-dependent first order solutions applicable to the study of recovery and transient phenomena, as well as loss factor investigations.



#### 4.15.3 The Transients Resulting From the Diffusion Component of the Current

The diffusion represents an uncoordinated type of carrier motion, as compared to that of the field-dependent carrier flow. Therefore, any change in applied field will result in a change in internal field, potential, charge carrier density, and distributions which will not completely follow those of the applied field. These changes will be time-dependent, since the diffusion equilibrium cannot be attained instantaneously for the new condition; therefore, a time-varying applied field will bring into existence a time-varying set of electrical quantities within the material. To determine the nature of the transients, the equations developed above will be applied to various types of time-dependent applied electrical fields.

##### 4.15.3.1 Sinusoidal Applied Field

If the applied field is sinusoidal,  $E_a = \lambda \cos \omega t$ . Then:

$$E_{T1}(x, t) = \cos \omega t - \sum_{n=1}^{\infty} \left( \frac{4KD}{(2n-1)\pi} \right) \left\{ \frac{\omega \sin \omega t + \beta_{2n-1} D (\cos \omega t - \exp \beta_{2n-1} Dt)}{\omega^2 + (\beta_{2n-1} D)^2} \right\} \sin \left\{ (2n-1) \pi x/d \right\} \quad (45)$$

Evidently, the added transient is unimportant at the surfaces of the semiconductor material, and reaches a maximum halfway between these surfaces. To see the nature of the dependence upon the frequency, it is more convenient to examine the complete transient potential. By integrating over the thickness of the material:

$$V(t) = - \int_0^d E_{T1}(x, t) dx$$

$$d^{-1} V(t) = - \cos \omega t - \sum_{n=1}^{\infty} \frac{8KD}{(2n-1)^2 \pi^2} \left\{ \frac{\omega \sin \omega t + \beta_{2n-1} D (\cos \omega t - \exp \beta_{2n-1} Dt)}{\omega^2 + (\beta_{2n-1} D)^2} \right\} \quad (46)$$

Considering the case in which, for all terms of the expansion which are significant,  $\beta_{2n-1} D \gg KD$ , the steady state term becomes

$$d^{-1} V(t) = S \cos (\omega t - \alpha),$$

where

$$\begin{aligned} A &= 1 - (4\pi\sigma_0 KD/\Delta), \quad B = 4\pi\sigma_0 \omega/\Delta, \quad \Delta = \omega^2 + K^2 D^2, \\ \tan \alpha &= B/A, \quad S^{-2} = A^2 + B^2 \end{aligned} \quad (47)$$

The transient, therefore, consists of an exponentially decreasing term which reduces the potential across the sample, and a steady state term which lags the applied field by an amount dependent upon the frequency. As the frequency applied to the carriers in the material increases from zero to large values, this lag increases from zero up to a maximum of  $\pi/2$ .

Slightly different behavior derivable from equation 46 is obtained if the approximation  $\beta_{2n-1} D = KD$  is not valid.

#### 4.15.3.2 Pulsed Field

Calculation of the effect of a pulse can be done the same way.

$$\begin{aligned} E_a(t_0) &= 0, & t_0 < 0 \\ &= c, & 0 \leq t_0 \leq b \\ &= 0, & t_0 > b \end{aligned}$$

then,

$$\begin{aligned} a_{2n-1}(t) &= -c(\beta_{2n-1} D)^{-1} \left[ 1 - \exp(-\beta_{2n-1} Dt) \right. \\ &\quad \left. - \left\{ 1 - \exp(-\beta_{2n-1} D(t-b)) \right\} \right] \end{aligned} \quad (48)$$

consisting of two transients, attributable respectively to the initial rise in field and the fall in field at the end of the pulse. Here,

$$\begin{aligned}
 -(cd)^{-1} V(t) &= 1 - \sum_{n=1}^{\infty} \frac{8KD}{(2n-1)^2 \pi^2 a_{2n-1}} (t) & t \leq b \\
 &= - \sum_{n=1}^{\infty} \frac{8KD}{(2n-1)^2 \pi^2 a_{2n-1}} (t) & t > b
 \end{aligned} \tag{49}$$

If  $\beta_{2n-1} D \approx KD$ ,

$$\begin{aligned}
 -(cd)^{-1} V(t) &= 1 + (KD)^{-1} [\exp(KDb) - 1] \exp(-KDt) & t \leq b \\
 &= (KD)^{-1} [\exp(KDb) - 1] \exp(-KDt) & t > b
 \end{aligned} \tag{50}$$

#### 4.15.3.3 Impulse

The response to an impulse may be calculated directly but can be obtained more readily from the results of the last paragraph. Let  $bc = 1$ ,  $c \rightarrow \infty$ .

The response to a unit impulse at  $t = 0$  is:

$$-d^{-1} V(t) = - \sum_{n=1}^{\infty} \frac{8KD}{(2n-1)^2 \pi^2} \exp(-\beta_{2n-1} Dt) + \delta_t^0 \tag{51}$$

From equation 51, it is evident that the response to an impulse is a distribution of exponential decays. If conduction is predominant, these all have the same decay constant and sum up into a simple exponential decay. If diffusion is predominant, they differ in decay constant and sum up into a curve whose departure from a pure exponential depends upon the relative weights of conductivity and diffusion constant. Using the Nernst-Einstein relation, the diffusion broadening of the curve will be more effective at higher temperature:

$$\beta_{2n-1} D = \mu \left[ \frac{4\pi en}{\epsilon} + \frac{(2n-1)^2 \pi^2}{d^2} \frac{kT}{\epsilon} \right] \tag{52}$$

If the mobility is unchanged, increased importance of diffusion affects the decay curve through the ratio of temperature to charge density. From equation 52, it is obvious that this will be more effective in thinner samples, and such effects should be more easily observed in thin films.

#### 4.15.3.4 Application of a Steady Field

If a sample with no field applied to it is suddenly inserted into a field,  $c$ , or a field is suddenly applied to it (no net current over the boundaries, since blocked boundaries are under consideration),

$$a_{2n-1}(t) = c (\beta_{2n-1} D)^{-1} [1 - \exp(-\beta_{2n-1} Dt)] \quad (53)$$

so that the field and potential across the sample increase exponentially like the charging of a capacitor. The current at the center plane of the specimen is

$$\frac{\epsilon KD c}{4\pi} \sum_{n=1}^{\infty} \frac{4}{(2n-1)\pi} \exp(-\beta_{2n-1} Dt) \quad (54)$$

and if conduction is predominant:

$$j_x = \frac{d}{2} = \sigma \exp\left(-\frac{\sigma}{\epsilon} t\right). \quad (55)$$

#### 4.15.3.5 Geometrical Location of Transient Effects

From the equations, it is evident that, because of the blocked boundary, the field transients are greatest in the center of the sample, farthest away from the surfaces. The same is true for the internal current. The average power loss is computed in paragraph 4.16.4.

#### 4.15.4 Effect on Charge Carrier Distribution

From equation 41, it is evident that the effect of such transients on charge carrier distribution will be greatest near the surfaces. Since the same  $a_{2n-1}$ 's are involved, the time dependence of the effect upon the charge carrier distribution has essentially the same functional form as in the cases just discussed, deviating more as diffusion becomes more important. The dependence on distance from the surface, while different from, is analogous to the well-known skin effect.

#### 4.15.5 Equivalent Circuit

The impedance  $Z(i\omega)$  per unit area can be written as:

$$Z(i\omega) = [Y(i\omega)]^{-1} = (d/i\omega\epsilon) \left[ 1 - \frac{8K}{\pi^2} \sum_{n=1}^{\infty} \left\{ (2n-1)^2 \beta_{2n-1} \right\}^{-1} \right] \quad (56)$$

$$+ \sum_{n=1}^{\infty} \left[ \frac{8KD}{\epsilon\pi^2 (2n-1)^2 \beta_{2n-1}} \right] / (i\omega + \beta_{2n-1} D)$$

from which the equivalent circuit in figure 61 can be derived. In the figure,

$$C_o^{-1} = \frac{d}{\epsilon} \left[ 1 - \frac{8K}{\pi^2} \sum_{n=1}^{\infty} \left\{ (2n-1)^2 \beta_{2n-1} \right\}^{-1} \right] \quad (57)$$

$$C_n = \epsilon\pi^2 (2n-1)^2 \beta_{2n-1} / 8KD$$

$$G_n = \beta_{2n-1} D \cdot C_n$$

- From a network standpoint, figure 61 shows why the curves in para. 4.16.3 show only one maximum rather than a series of peaks corresponding to the individual relaxation times. An RC network, as in figure 61, has an infinite set of alternating poles and zeros on the negative real axis of the frequency plane. Such a distribution of poles and zeros can give rise only to one maximum peak in the impedance magnitude, or, equivalently, in the dielectric loss, even though an infinite number of relaxation mechanisms are present.

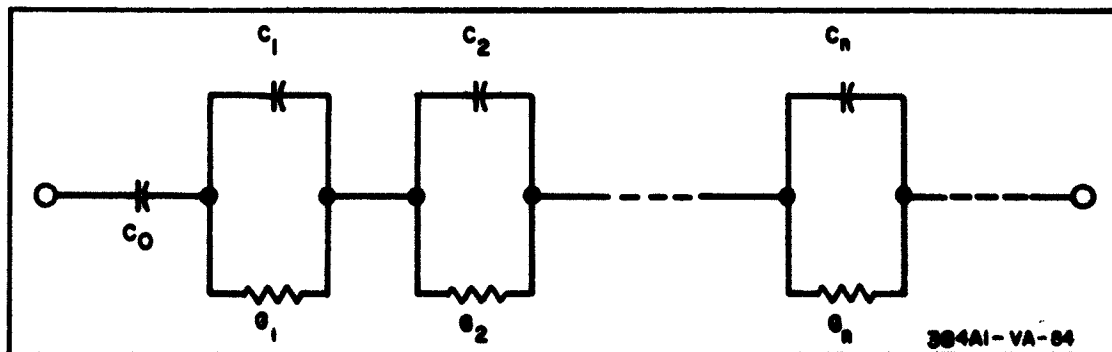


Figure 61. Equivalent Circuit for Conduction-Diffusion in a Semiconducting Material

## 4.16 FAILURE IN SOLID STATE DEVICES FROM INTERNAL HEAT GENERATION

### 4.16.1 Introduction

In paragraph 4.15, it was shown that the diffusion component of conduction diffusion in a solid state material introduces transients, and produces a lag in the response to a sinusoidal field. Any such lag is accompanied by conversion of electrical into heat energy. In this paragraph, the complex dielectric constant and loss factor will be developed, and the power loss to heat calculated. Since the result is important at low frequencies, it becomes one of the mechanisms which should be included in the consideration of losses in the presently insufficiently understood frequency range below 100 cps. The present calculation also shows the consistent way to include conduction in the specimen into loss factor calculations, and this turns out to be not additive.

### 4.16.2 Dielectric Loss From Conduction and Diffusion

#### 4.16.2.1 The Complex Dielectric Constant

The solutions result from a consideration of combined conduction and diffusion alone. No other loss mechanism is invoked to account for a dependence between the complex dielectric constant and frequency. Nonlossy material exhibiting ideal polarization is represented adequately by the conditions,  $\epsilon_R > 1$ ,  $\mu = 0$ . The effect of additional loss mechanisms will be described subsequently.

In the present case, the effective complex dielectric constant is most conveniently derived from the zero order admittance between the boundary interfaces. The applied field is  $E_a = \lambda \exp(i\omega t)$ . With the interface voltage  $V(t)$ , and displacement current at the boundary,  $i(t)$ , given by:

$$V(t) = \int_0^d E_T(x, t) dx \quad (58)$$

and

$$i(t) = d [E_a(t)] / dt \quad (59)$$

respectively, the zero order admittance per unit area is defined as:

$$Y(i\omega) = \lim_{\lambda \rightarrow 0} \left[ \mathcal{F} \cdot \{i(t)\} / \mathcal{F} \cdot \{V(t)\} \right] \quad (60)$$

where  $\mathcal{F}$  is the Fourier transform operator; i.e.,

$$\mathcal{F}\{f(t)\} = \int_{-\infty}^{\infty} f(t) \exp(-i\omega t) dt \quad (61)$$

Combining equations 40, 45, 46, and 47:

$$Y(i\omega) = i\omega(\epsilon/d) (a + i\beta)^{-1} \quad (62)$$

where

$$a = 1 - (8 KD/\pi^2) \sum_{n=1}^{\infty} \beta_{2n-1}^2 D/\Delta_{2n-1} \quad (62a)$$

and

$$\beta = (8 KD/\pi^2) \sum_{n=1}^{\infty} \omega/\Delta_{2n-1} \quad (62b)$$

and

$$\Delta_{2n-1} = (2n-1)^2 (\omega^2 + \beta_{2n-1}^2 D^2). \quad (62c)$$

Therefore, the complex dielectric constant,  $\epsilon^*$ , is given by:

$$\begin{aligned} \epsilon^*(\omega) &= \epsilon'(\omega) - i\epsilon''(\omega) = Y(i\omega)/i\omega(\epsilon_0/d) = \epsilon_R/(a + i\beta) \\ &= \epsilon_R \left[ 1 - \frac{8 KD}{\pi^2} \sum_{n=1}^{\infty} \frac{\beta_{2n-1}^2 D}{(2n-1)^2 (\omega^2 + \beta_{2n-1}^2 D^2)} \right. \\ &\quad \left. + i \frac{8 KD}{\pi^2} \sum_{n=1}^{\infty} \frac{\omega}{(2n-1)^2 (\omega^2 + \beta_{2n-1}^2 D^2)} \right]^{-1} \end{aligned} \quad (63)$$

The (real and frequency dependent) dielectric constant, and loss factor are:

$$\epsilon' = \epsilon_R a/(a^2 + \beta^2); \quad \epsilon'' = \epsilon_R \beta/(a^2 + \beta^2) \quad (64a)$$

and the loss tangent is:

$$\tan \delta = \epsilon' / \epsilon'' = \beta / \alpha. \quad (64b)$$

Equation 63 for  $\epsilon^*$ , although obtained by a perturbation method, is an exact solution. The dielectric loss in a nonlinear mechanism such as this will depend upon both the frequency,  $\omega$ , and the amplitude,  $\lambda$ , of the applied field. However, a dielectric constant is a property of the material, and not of both the material and the amplitude which the investigator happens to apply in the experiment. Accordingly, to be meaningful,  $\epsilon^*(\omega, \lambda)$  is defined in practice as  $\lim_{\lambda \rightarrow 0} \epsilon^*(\omega, \lambda)$ . The limiting process removes the importance of the succeeding order perturbations, and leaves the complex dielectric constant defined in equation 63 as the exact solution.

The series for  $\alpha$  and  $\beta$  may be expressed in dimensionless variables as:

$$\alpha = 1 - (8s^2/\pi^2) \sum_{n=1}^{\infty} \left[ s^2 + (2n-1)^2 \right] / (2n-1)^2 \left[ x^2 + \left\{ s^2 + (2n-1)^2 \right\}^2 \right],$$

$$\beta = (8s^2 x / \pi^2) \sum_{n=1}^{\infty} (2n-1)^{-2} \left[ x^2 + \left\{ s^2 + (2n-1)^2 \right\}^2 \right]^{-1} \quad (65)$$

where

$$x = \omega d^2 / \pi^2 D, \quad s^2 = KD d^2 / \pi^2 D$$

If the diffusion constant, as is often the case, is expressible as:

$$D = \nu_m a^2 \exp(-U/KT)$$

then

$$x = (2/\pi) (\nu/\nu_m) (d^2/a^2) \exp(+U/KT)$$

This expresses the ratio of the product of the applied frequency times  $d^2$  to the product of the characteristic lattice maximum or average frequency and the lattice constant squared corrected by a Boltzmann factor. The parameter  $s$  is essentially the ratio of  $d$  to the Debye length; if the Nernst-Einstein relation, equation 25, is valid,  $s^2 = (4e^2/\pi\epsilon k) (n_+ d^2/T)$ , and is proportional



to the density of carriers. In the figures,  $s^2$  is represented by the parameter,  $r$ .

#### 4.16.2.2 The Particular Case of Conduction but No Diffusion: Low Temperature

If equation 25 is valid, diffusion will become negligible with respect to conduction at low temperatures and only at low temperatures. Equation 23 has been shown to be experimentally valid when the conducting and diffusing entities are identical; i.e., under a wide number of equilibrium conditions (reference 5) and to be appropriate to the steady state (nonequilibrium) flow of current in a semiconductor. Even if the flow does not precisely obey equation 25, it would be expected that a qualitatively similar experimental behavior would characterize the temperature dependence of  $D$ . Since the diffusion term in  $\beta_{2n-1} D$  is  $[(2n-1)^2 \pi^2 / d^2] D$ , an infinitely thick specimen will show the same type of behavior as if  $D = 0$ .

At very low temperatures, or in an infinitely thick specimen, the expressions above become, for all  $n$ ,

$$\beta_{2n-1} D = KD$$

$$a_n(t) = \exp(-KDt) \int_0^t E_a(u) \exp(KDu) du \quad (66a)$$

$$= a(t)$$

$$E = E_a - KD a(t)$$

For the special case,  $E_a = \lambda \exp(i\omega t)$ :

$$\alpha = \omega^2 / [\omega^2 + K^2 D^2] = \alpha^2 + \beta^2$$

$$\beta = \omega KD / [\omega^2 + K^2 D^2]$$

so that

$$\epsilon' = \epsilon_R$$

$$\epsilon'' = \epsilon_R \frac{KD}{\omega} = 2\sigma_0 / f \epsilon_0$$

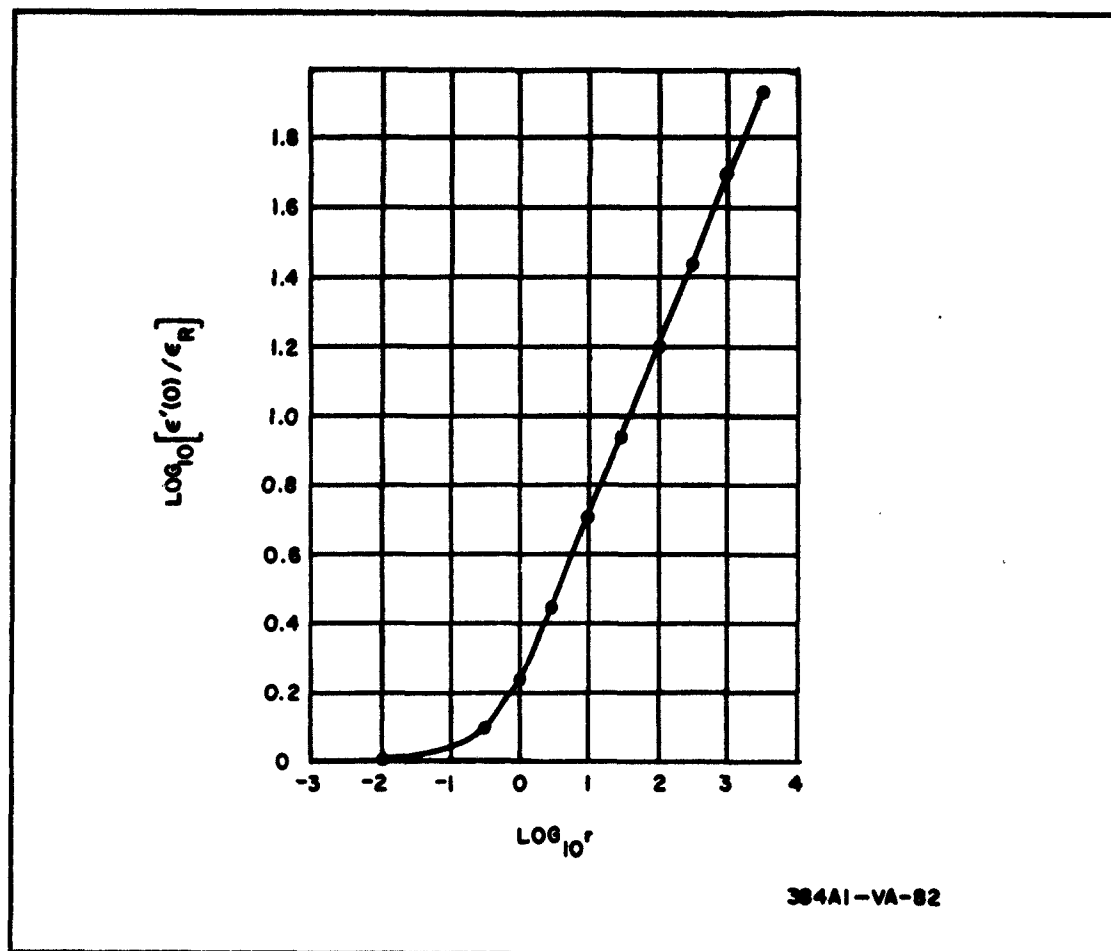


Figure 62. Dependence of Dielectric Constant on Relative Importance of Diffusion and Conduction

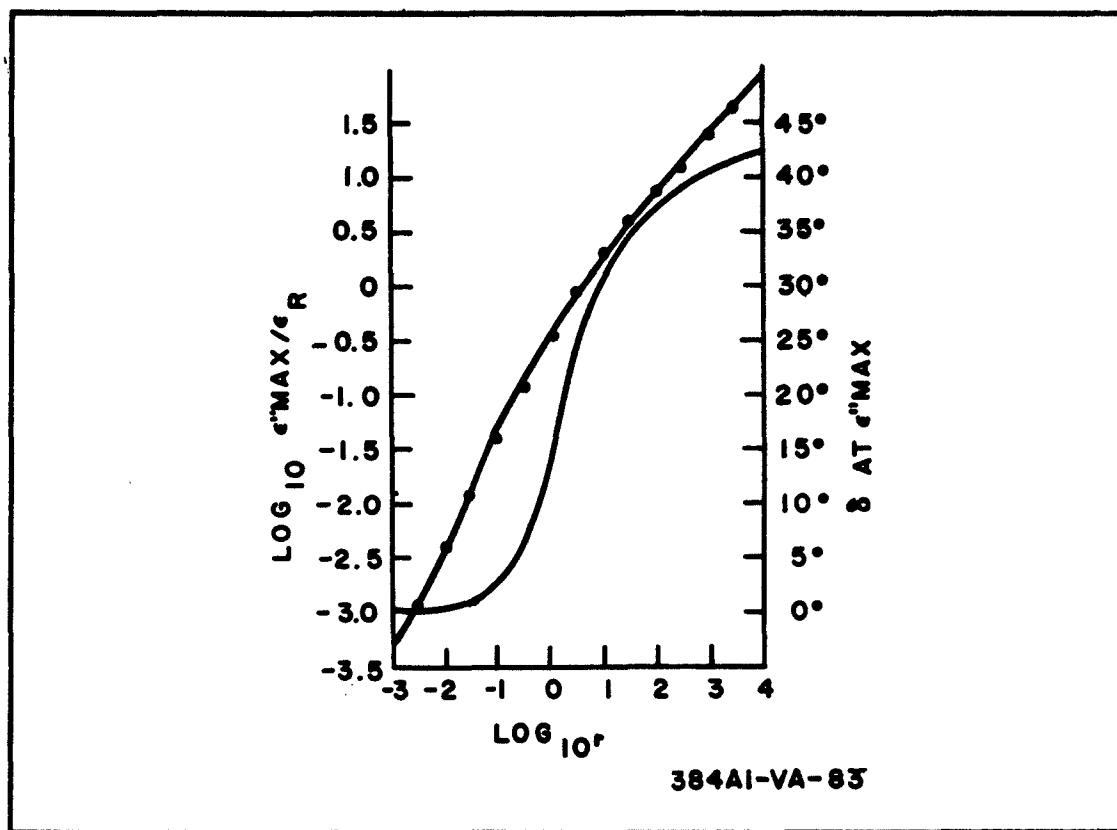


Figure 63. Dependence of Maximum  $\epsilon''$  and  $\delta$  on  $r$

The last two equations for the dielectric constant and loss factor are, of course, standard relations (reference 6), when no diffusion takes place.

#### 4.16.2.3 The Static Dielectric Constant, and Diffusion

If the frequency is set equal to zero, the static dielectric constant,  $\epsilon' (0)$ , is obtained. This will here be denoted by  $\bar{\epsilon}$  without a subscript to avoid confusion with the  $\epsilon$  previously defined.  $\beta$  and  $\epsilon''$  are, of course, zero, and  $\bar{\epsilon}$  becomes

$$\bar{\epsilon} = (\epsilon_R/a) = \frac{\pi \epsilon_R}{8 \sum_{n=1}^{\infty} [s^2 + (2n-1)^2]} = \epsilon_R (\pi s/2) \coth (\pi s/2) \quad (67)$$

so that  $\bar{\epsilon} = \epsilon_R$  for small  $s$ , but becomes therefore  $\bar{\epsilon}$ , are large. Increase of the importance of diffusion relative to conduction decreases  $\bar{\epsilon}$ , until when diffusion is predominant,  $\bar{\epsilon}$  approaches  $\epsilon_R$ . All else being the same, lower temperatures or higher mobile charge density increase  $s$ . The first effect agrees with the well-known usual decrease of the dielectric constant as the temperature increases (reference 8).

If the carrier density,  $n_+$ , increases without limit, so does  $s$ . From equation 67, the static dielectric constant increases without limit, proportionally to  $(n_+)^{1/2}$ . This increase of the dielectric constant as the carrier density increases is consistent with classical electrostatic solutions of dielectric bodies in space, in which a conducting body (metal) behaves like a dielectric body of infinite dielectric constant.

If the Nernst-Einstein relation, equation 25, is valid; i.e., if the conducting and diffusing charge carriers are identical, and if account is taken of the factor  $d^2$  in  $s^2$ , it is possible therefore to designate certain limiting conditions. Thin films of insulators, especially at medium to high temperature, will show small dielectric constants; examples are the usual polymeric insulators. Thick samples of conducting material, especially at low temperatures should show high dielectric constants. A sample of fixed thickness being raised in temperature will show discontinuities in the static dielectric

constant when a new crystal form appears in which the barrier energy to the release of carriers into the mobile state is significantly changed.

#### 4.16.3 Frequency Regions of Loss

Figures 64 - 66 show the frequency regions in which the maximum loss is to be anticipated. These frequency regions have been determined in the manner shown in Quarterly Report No. 3, paragraph 4.7.4 "Application - Frequency Regions Conducive to Failure." Reference should be made to figures 31 and 32 of that report, and the accompanying text. The cross-hatching shows the general frequency regions which are important from the point of view of heat dissipation, for different values of the characteristic parameters; i.e., for different values of specimen thickness, temperature, and conductivity. By avoiding such combinations of frequency and constructional and operational parameters, a minimum of power dissipation will result in devices of semiconducting materials.

To check the predictions of the loss factor method, it is also possible to calculate directly the average power in the equivalent circuit. This is done in the next paragraph.

#### 4.16.4 Average Power

The average power per unit volume for the material specimen under consideration, to which is applied an electric field of the form  $E_a(t) =$

$E_{am} \sin(\omega t)$  is:

$$P_{avg} = \lim_{t \rightarrow \infty} (td)^{-1} \int_0^t \mathcal{V}(t)i(t)dt$$

$$= \frac{4KE_{am}^2}{\pi^2} \sum_{n=1}^{\infty} \left[ (\omega/D)/(2n-1)^2 \left\{ (\omega/D)^2 + \beta_{2n-1}^2 \right\} \right]. \quad (68)$$

This expression exhibits the nature of the power absorption as the summation of a denumerably infinite number of relaxation mechanisms, each with its characteristic frequency. All have the same frequency if conduction is the only carrier action. In the case of conduction only, the average power is:

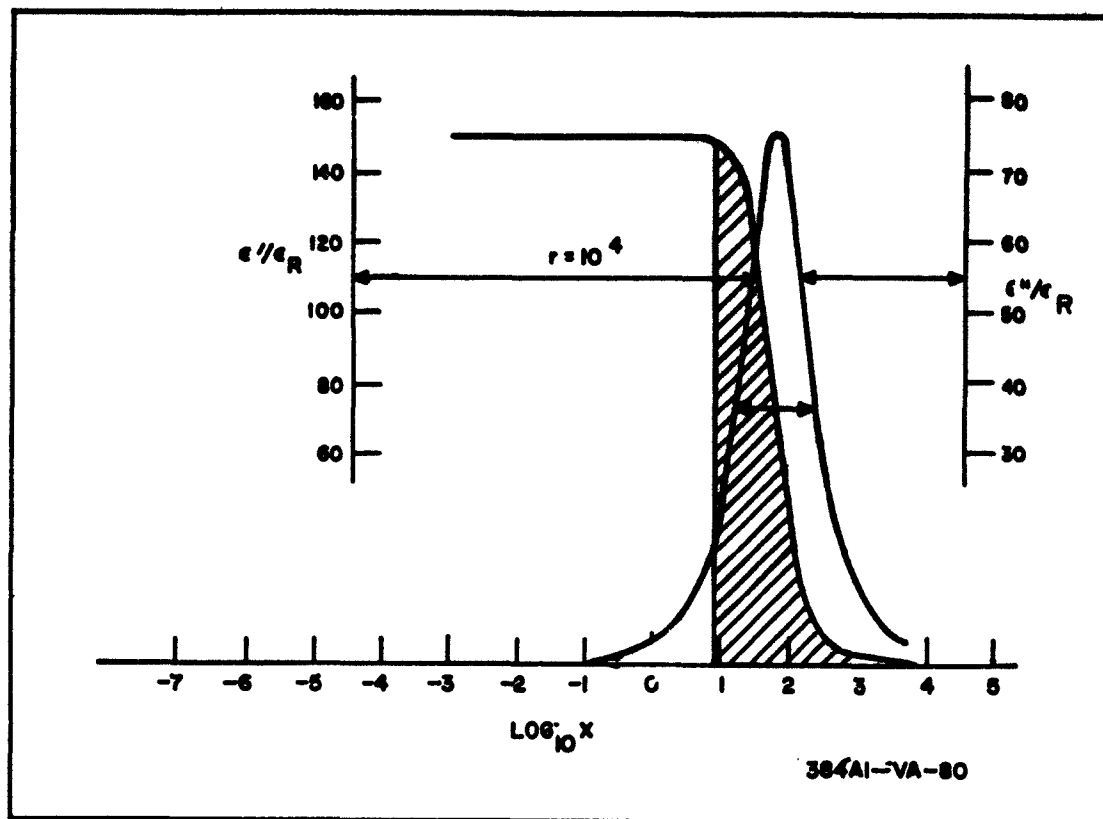


Figure 64. Important Frequency Regions of Loss,  $r = 10^4$

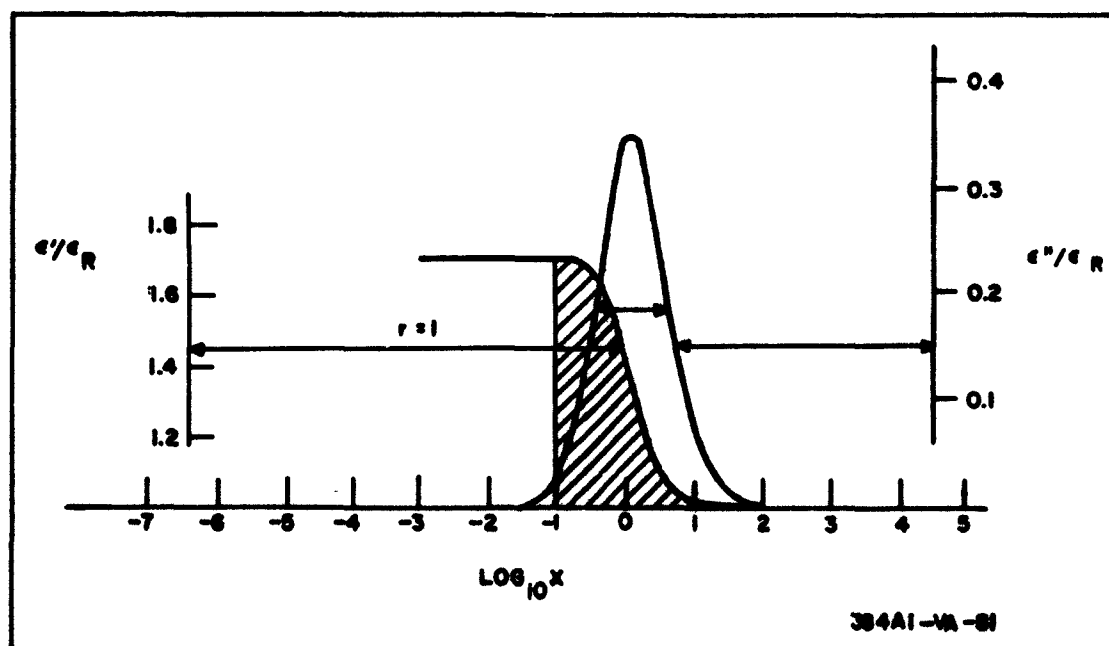


Figure 65. Important Frequency Regions of Loss,  $r = 1$

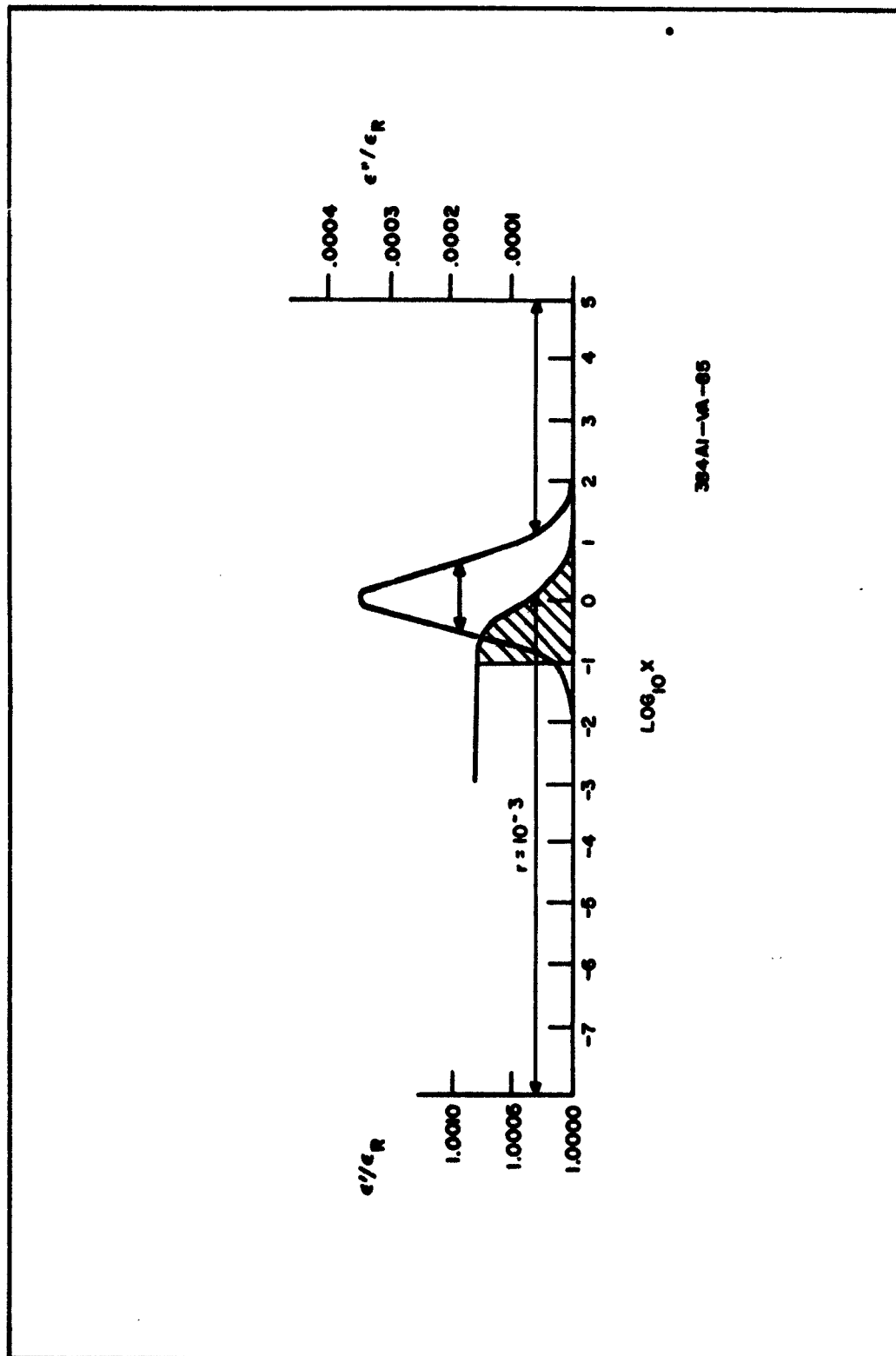


Figure 66. Important Frequency Regions of Loss,  $r = 10^{-3}$

$$P = (E_{am}^2/2) \left[ \frac{\omega KD}{\omega^2 + (KD)^2} \right] \quad (69)$$

$$= \frac{E^2}{4} \sin 2 \alpha$$

where  $\alpha$  is defined as in paragraph 4.15.3.1. The maximum power loss occurs at a frequency of  $KD$ , for which the phase lag is  $\pi/4$ . When diffusion accompanies conduction, changes are brought into the individual frequencies, so that the contribution of each term of the summation to the total is decreased, and the precise frequency of maximum loss changes. Accordingly, the power dissipation for a given frequency in the specimen of material will be temperature dependent, as will the frequency of maximum dissipation.

#### 4.16.5 Modes of Failure and Failure Processes

These results show that during normal operation of solid state devices, heat may be generated through the diffusion component of the device response. Figures 64-66 show how frequency ranges may be determined in which significant heat production occurs. By avoidance of certain design and construction parameter values, the likelihood of failure from excessive heat production may be minimized.

It is also possible from the equations to calculate the geometrical locations at which heat production from this cause will be a maximum. Since the effects of radiation to and from the environment must also be considered in any specific case, this portion of the development has not been carried further. If large currents pass through the device, it would be desirable to consider one more stage of approximation than that here developed; the means for doing this are obvious from the above.

The various modes of failure which may result from such heat release, such as chemical diffusion, lead disengagement, change of beta, etc, depend upon the design of the device, and will not be taken up further here.



#### 4.17 FAILURE IN THIN FILMS AT BENDS OR STEPS IN SUBSTRATE

A problem in the deposition of thin films of metal or semiconductor substrates, particularly on insulating substrates, is that of the continuity of the film as it passes over sharp bends, steps, or other surface inequities. In some cases, the film cracks and separates; in other cases it separates from the substrate without cracking.\* Both effects may be damaging. Lack of adhesion is a separate problem requiring investigation on its own. The purpose of the limited investigation undertaken here and reported below was to identify the causes of cracking, and to examine the improvement obtainable by certain technique approaches.

The films in a thin film circuit are usually processed by evaporation through a mechanical mask or by photoetching. The high surface-to-volume ratio characteristic of a film can emphasize interactions not normally significant. Energy and free energy considerations depend upon the topology of both the film and the underlying substrate, and may be quite different from those normally assumed for ideal flat faces.

A number of necessary techniques connected with the deposition create problems related to failure; examples are: oblique incidence in vacuum evaporation, pinholes or their equivalent in thin films, and the relationship of these and other changes in surface energy distributions to the kinetics of the chemical etching process. Primary emphasis in this study was placed on the discontinuities associated with conductors crossing surface irregularities. To obtain the maximum amount of information for the experimental work undertaken, a model was used which introduced differences in the coordinate normal to the surface by means of graduated step heights.

---

\* "The opens occurred where evaporated jumpers crossed the sharp edges of etched lines. An electropolishing technique to remove the sharp edges is being developed to rectify the situation." Planar Integration of Thin Film Functional Circuit Units, 3rd Quarterly Report Signal Corps Contract DA-36-039-SC-87246, p. 6, 31 May 1962. IBM Command and Control Center, Kingston, New York.

#### **4.17.1 Experimental Procedures**

##### **4.17.1.1 Design**

The design of the specimen investigated was based on an actual circuit which exhibited failure. This circuit was a magnetic film memory plane having bits 0.010 inch wide, 0.040 inch long, and 8000 Angstrom units high, assembled in an array of columns on 0.020-inch centers, and rows on 0.080-inch centers (figure 67). Film insulation separated these bits from conductors which were contiguous with the surface of the insulation and superimposed over the bits. These conductors were made by photoetching continuous films of gold. At first, KMER (Kodak Metal Etch Resist) was used as insulation, but since the solvent used to develop the mask for conductors also attacked the KMER insulator slightly, an alternate process was developed. A composite film of SiO and arsenic glass<sup>1/</sup> (30 percent As, 34 percent S, 36 percent Th) was tried as an improvement. This insulation, although eliminating the original objection to the KMER, created a new problem, namely a number of conductor failures of undetermined origin.

For control purposes, a pilot run prior to etching of the multilayer circuits consisted of etching single layer films which had been deposited on glass. In contrast to the multilayer circuits, the pilot runs always showed electrical continuity.

Because of the high incidence of failure for multilayer circuits, the first study was of the effect of step height on the reliability of the conductor. Other parameters studied were self-shadowing from the evaporation process and attack of the insulation through pinholes in the conductor during the etching process. Self-shadowing impedes deposition, and if insufficient metal is deposited in the corners of the step, a potential open circuit exists in the conductor. The evaporated glass can be attacked by the etchants, and if

<sup>1/</sup> McDermott, P. S., and E. R. Stack, "Studies on the Vacuum Deposition of the Low Melting Temperature Glass System of Arsenic, Sulfur, and Thallium," 1960 Vacuum Symposium Transactions, Pergamon Press, London (1961).

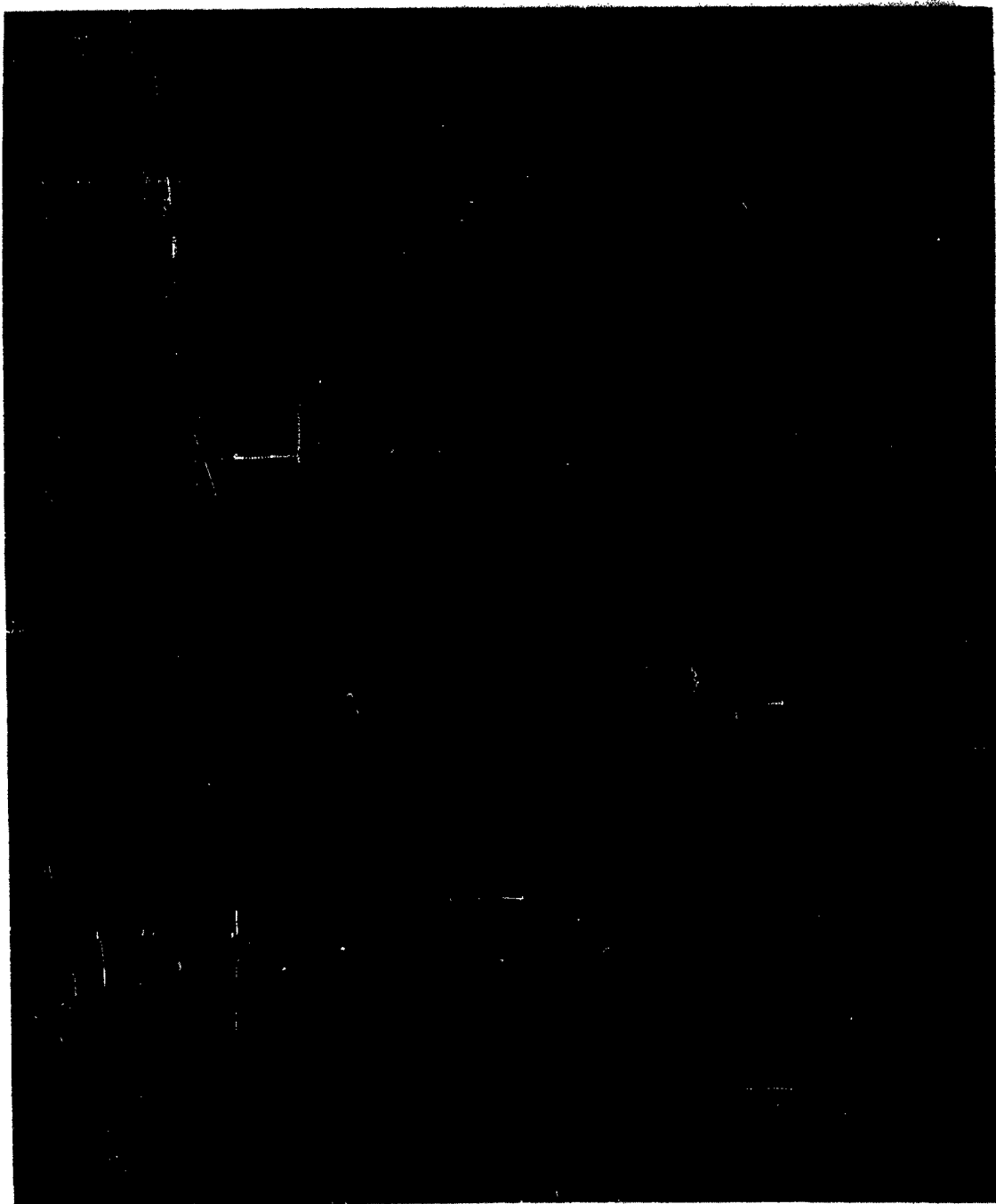


**Figure 67. Design of Magnetic Film Memory Plane**

penetration through pinholes in the conductor takes place, chemical attack of the insulation can proceed. The alteration of the underlying layer then can lead to mechanical failure of the conductors.

#### 4.17.1.2 Processing of Samples

The sequence of operations, starting with glass substrates, consisted of evaporating a conducting film (figure 67a), then electroplating a magnetic film (figure 67b) and etching the magnetic film into rectangles. Figure 67c shows the magnetic film with the KMER mask before etching and figure 67d shows the film after etching. An insulating film was then applied (figure 67e). Conductors were formed on top of the insulation by one of the processes indicated. Figure 67f shows the substrate with a conducting layer evaporated over the insulation. Depending on the orientation of the bit pattern, this layer was etched into either the pattern shown in figure 67g or that in figure 67h. Figure 67h was taken from the bottom of the substrate and shows how the conductors covered the bits. An example of the conductor evaporated through a mask is shown in figure 67i.

#### 4.17.1.3 Plating

Etched conductors and substrates without magnetic bits yielded completely reliable conductors. To investigate the first parameter, a step height was introduced in the plating process. Films were plated to thicknesses of 12,000, 8000, and 1500 Angstroms.

#### 4.17.1.4 Insulation

By dividing the total number of slides into three groups and using one of each, three different types of insulation were used in the study.

On the first third of the slides from each thickness group, SiO was evaporated while the slides were rotated at 3 rpm at 45 degrees to the source of vapor. This angle was chosen to obtain a maximum amount of filling of the step junction.

The second third of the slides was given two coatings of spun-on KMER as its insulating layer. The last third was given an SiO layer while positioned normal to the vapor source. On both of the SiO insulator slide groups, a final covering layer of the low temperature glass was evaporated to improve the adhesion of the gold to the SiO.

#### 4.17.1.5 Conductors

For conductor application, the slides were divided into three groups, each containing at least two slides from each of the above permutations. In the first group, the slides were positioned normal to the vapor source for the gold evaporation.

For the second group, six gold sources were positioned uniformly around, and approximately 6 inches below the substrates. The sources were evaporated one at a time to simulate a rotation technique, while holding the substrates still. The rotating substrate technique used for SiO could not be used because the desired gold thickness required separation between substrates and source to be as small as possible. If the substrates were placed in a holder positioned at an angle to the vapor source, one side of the holder would be two to four times as far from the source as the other side. Also, because of the small spacing between the boat and substrates, self-shadowing would still exist.

The conductors of the third group of slides were evaporated through a mask made by photoetching thin sheet iron. Shadowing was minimized by magnetically tightening the masks against the substrate. The conductor length required limiting the number of conductors per slide to three. The three lines were so spaced that the mask could be used with either orientation of the bit pattern. Figures 67d and 67e show these two bit pattern orientations.

#### **4.17.2 Observations and Conclusions**

##### **4.17.2.1 Adhesion of Insulation**

The SiO deposited at 45 degrees to the vapor source showed poor adhesion; this was not observed on the samples in which the deposition surface was normal to the vapor beam. Where the adhesion was poor, the difficulty was overcome by ion bombardment of the substrate after the SiO source was out-gassed.

##### **4.17.2.2 Failures**

Approximately 10 percent of the slides which passed the previous tests failed because a contaminated gold evaporation caused poor initial adherence. Another 10 percent failed during etching because of faulty conductor masking.

No failures were observed from conductor discontinuity over a step edge. Apparently step height, oblique incidence, and attack of the insulator by etching were not significant parameters in the failures observed earlier.

In the contaminated evaporation, a failure of adhesion between gold and insulator occurred. The gold layer cracked and curled away from the bits at their edges.

In an extreme case of poor adhesion, the stress is maximum at the bit edge, and failures would be expected to initiate there. With good adhesion, cracks at step edges are not observed. If no steps are included, the maximum stresses at step edges are avoided, and therefore the circuits should show fewer failures. This was true of the KMER insulated circuits, and the controls with no bits.

The tentative conclusions may be drawn that, under the circumstances of the present experiment, failure is primarily due to poor adhesion between gold and SiO arsenic glass layer, and that parameters such as step height, oblique incidence, or attack of insulator by the etchant are of secondary importance.

#### 4. 18 MULTIPLE-PARAMETER TRANSISTOR TRANSIENT OVERLOAD STUDY

In the study of failed components described in paragraph 4. 1, it was found that a substantial number of transistor failures during the manufacture and testing of two data processing systems occurred as a result of shorts between emitter and collector in one, and between emitter and base in the other. To understand this difference, a limited study was performed to explore the effect of voltage and power stresses on transistor performance in terms of the effect of a particular stress on device parameters.

##### 4. 18. 1 Transistors Used and Experiment Design

The transistors included in the test were chosen from those representative of the best available transistors on the market by the standards appropriate to their use in military systems. Selection was based on the fact that a large number of the existing transistorized airborne systems in present use utilize silicon grown junction and grown diffused transistors. On the other hand, systems now in design or in early stages of production contain silicon diffused, mesa, planar, and epitaxial. In all, 46 silicon n-p-n samples were chosen which include these different processing techniques, thus representing devices in present and future use. The samples also represent five major semiconductor manufacturers.

Thirteen parameters were measured on the test samples and used as references for the post-stress tests. These parameters include breakdown voltages and leakage currents of each junction, the small signal "h" parameters and high frequency beta. Each transistor was measured for pre- and post-stress readings with the same individual items of freshly calibrated test equipment.

Ten transistors, including two from each process type, were subjected to each of six stress tests. Thirty-two devices were submitted to only one test. The remaining fourteen were submitted to two tests; post-stress readings for the second test were compared to the post-stress readings for the preceding test to determine the extent of parameter change.

Tests No. 1 through 4 applied a voltage stress to the transistors on a pulse basis with the devices operating in a manner closely simulating actual circuit conditions.

Test No. 5 applied a power stress to the transistors operating at maximum power while Test No. 6 stressed only one junction at a 100-percent duty cycle.

#### 4.18.2 Types of Overload and Test Measurements

Figure 68 shows the circuits used in the tests described below.

##### 4.18.2.1 Test No. 1

The transistors were operated in the common-emitter configuration with the power supply voltage set at approximately three times the measured  $BV_{ce0}$  as recorded in tables 8 and 9. The devices were biased such that the collector-to-emitter voltage was equal to approximately one-half of the  $BV_{ce0}$  value and the dissipation was equal to approximately one-half the manufacturer's recommended maximum power rating.

The amount of current the transistors sustained during breakdown was determined by the size of the collector resistor and the device itself. The range of currents during breakdown was 1 to 3 milliamperes. A relatively low impedance appears between the base and emitter of the transistor because of the pulse generator at the input. Therefore, during off time the base-to-emitter appears relatively shorted so that the high voltage pulse on the collector appears across the collector-to-base junction. Essentially, the collector-to-emitter voltage, base-to-emitter shorted, is seen at the collector which is, in effect, the collector-to-base voltage, emitter open. The collector voltages measured with an oscilloscope during the off time verify this fact. Test No. 1 was run for 4 consecutive hours.

##### 4.18.2.2 Test No. 2

Operating conditions for this test were identical to those described above for Test No. 1, including the use of the pulse generator to turn the transistor off and allow the collector voltage to see the power supply voltage. The



TABLE 8  
TRANSISTOR OVERLOAD TESTS, INITIAL MEASUREMENTS

Unit No.	$I_{cbo}$ ( $\mu$ a) $V_{cb}=30v$	$I_{cbo}^*$ ( $\mu$ a)	$BV_{cbo}$ (volts) $I_c=100\mu a$	$I_{ceo}$ ( $\mu$ a) $V_{ce}=30v$	$I_{ceo}^*$ ( $\mu$ a)	$BV_{cbo}$ (volts) $I_c=100\mu a$	$I_{ebo}$ ( $\mu$ a) $V_{eb}=5v$	$BV_{ebo}$ (volts) $I_e=100\mu a$	$h_{ib}$ (ohms) $V_{cb}=5v$	$h_{ob}$ (ohms) $f=1.0kc$	$h_{rb}$ $\times 10^{-6}$ $I_c=1.0ma$	$h_{fe}$	$h_{fe}$ $V_{ce}=10v, I_c=20ma,$ $f=10mc$
DIFFUSED MESA N-P-N													
1	7	650	200	8	440	87	440	14.4	33	0.89	220	36.0	1.61
2	84	1000	124	160	1250	86	0.3	20.5	31	0.94	140	36.0	1.35
3	7	440	196	8	780	82	140	14.6	30	0.95	165	39.0	1.40
4	310	840	113	1600	8000	87	0.3	16.7	30	0.87	145	51.6	1.36
5	36	470	236	39	690	102	3	20.5	32	0.77	150	37.5	1.51
6	8	240	242	11	190	111	1.0	16.1	31	0.82	160	44.4	1.47
						$I_c=10ma$		$I_e=5\mu a$					$V_{ce}=5v, I_c=5ma,$ $f=20mc$
7	3	40	167	24	60	87	2	8.7	39	0.47	210	24.6	5.82
8	0.1	1100	172	0.1	3600	102	10	7.8	34	0.10	105	36.0	6.39
					$V_{ce}=15v$			$I_e=100\mu a$					$V_{ce}=10v, I_c=20ma,$ $f=20mc$
9	62	510	88	72	140	29	8200	6.8	31	0.28	105	19.0	2.60
10	58	480	70	70	120	23	1900	7.4	31	0.35	130	24.6	2.20
DIFFUSED PLANAR N-P-N													
	$V_{cbo}=60v$			$V_{ce}=40v$						$V_{cb}=5v,$ $I_c=1.0ma,$ $f=1.0kc$			
11	3	8.3	114	2	2	45	2	11	31	0.25	295	49.0	4.81
12	4	9.2	86	2	1.4	41	2	11.7	31	0.26	245	44.4	4.47
13	4	10	106	5	5.6	43	0.9	11.5	30	0.19	255	70.5	4.81
14	4	6.2	85	3	2	36	1.0	10.1	30	0.20	305	4.63	4.63
15	9	17	90	6	3.7	36	2	10.1	31	0.21	320	76.0	4.47
16	0.2	0.4	104	0.7	0.7	48	0.02	10.5	30	0.17	70	51.6	2.45
17	0.1	0.6	142	0.2	0.4	82	0.1	9.2	28	0.11	105	82.3	4.72
18	0.2	0.7	132	0.3	0.8	83	0.2	9.2	30	0.11	110	90.0	4.63
19	0.2	0.6	158	0.2	0.7	140	0.04	10.6	30	0.11	70	49.0	2.94
20	8	8	156	78	80	119	0.04	10.2	29	0.12	65	57.8	2.91
EPITAXIAL MESA N-P-N													
	$V_{cb}=30v$			$V_{ce}=30v$		$I_c=10ma$				$f=1.0kc$			$V_{ce}=10v, I_c=20ma,$ $f=20ma$
21	105	500	96	275	550	35	36	8	31	0.15	110	37.5	5.16
22	70	300	86	2100	1550	32	250	7.7	31	0.23	145	30.2	5.27
23	245	520	240	430	240	38	215	7.9	32	0.35	145	23.4	5.99
24	97	420	111	165	400	40	300	7.9	31	0.26	140	29.3	6.12
25	48	290	98	69	100	36	270	7.6	32	0.45	210	27.7	6.18

\* Measured at 90 percent of voltage at reverse breakdown knee

TABLE 8 (Continued)

EPITAXIAL MESA N-P-N (Continued)													
Unit No.	$I_{cbo}$ (na) $V_{cb}=15v$	$I_{cbo}$ (na)	$BV_{cbo}$ (volts) $I_c=10ua$	$I_{ceo}$ (na) $V_{ce}=10v$	$I_{cec}$ (na)	$BV_{ceo}$ (volts) $I_c=10ma$	$I_{ebo}$ (na) $V_{eb}=5v$	$BV_{ebo}$ (volts) $I_e=10ua$	$h_{fb}$ (ohms) $V_{cb}=5v$	$h_{ob}$ (ohms) $f=1.0kc$	$h_{rb-6}$ $X10^{-6}$ $I_c=1.0 ma$	$h_{fe}$	$h_{fe}$ $V_{ce}=10v, I_c=20ma$ $f=20ma$
26	32	290	70	71	210	20	11	8.5	32	0.18	205	39.0	17.10
GROWN DIFFUSED N-P-N													
	$V_{cb}=30v$		$I_c=50ua$	$V_{ce}=30v$		$I_c=1.0ma$	$V_{eb}=1.0v$	$I_e=1.0v$		$V_{cb}=5v, I_c=1.0ma, f=1.0kc$			$V_{ce}=5v, I_c=1.0ma$ $f=1.0mc$
27	0.7	14	156	0.8	10	76	0.18	7.9	43	0.12	125	49.0	13.2
28	1.0	2	127	2	10	74	0.06	7.6	45	0.14	195	61.5	15
29	10	205	175	18	50	95	0.16	7.5	47	0.15	140	37.5	10
30	4	94	122	6	80	68	0.04	6.4	42	0.10	130	65.7	9.8
31	1.0	2.4	138	1.0	2.6	68	0.08	6.9	40	0.08	90	70.5	12.3
32	0.5	2	166	0.9	5	87	0.08	6.0	43	0.14	195	65.7	15
33	1.0	64	162	18	65	104	0.10	6.2	40	0.16	195	57.8	16.2
34	0.5	11	170	0.5	7	89	0.30	5.9	39	0.09	105	70.5	14.6
35	0.4	0.6	134	1440	1890	87	0.04	8.7	43	0.11	130	54.5	9.4
36	0.9	34	174	4	60	85	0.09	6.2	39	0.12	200	76.0	16.5
GROWN JUNCTION N-P-N													
								$I_e=100ua$					
37	32	210	97	58	700	81	0.4	4.1	61	0.31	680	65.7	19.2
38	3	14	92	20	60	79	86	3.1	48	0.24	375	70.5	20.6
39	11	52	90	110	240	88	945	2.3	53	0.27	270	39.0	14
40	15	390	124	410	730	74	3000	1.8	45	0.27	440	70.5	15.4
41	79	510	74	330	410	77	2	6.6	69	0.34	790	54.5	18.8
42	4	10	68	5	20	73	92	2.7	56	0.23	370	57.8	17
43	37	640	104	80	610	80	28	3.4	67	0.30	645	57.8	18.4
44	7	60	101	13	100	76	185	2.5	49	0.26	370	44.4	13.2
45	6	30	82	34	190	75	0.3	33.2	105	0.25	895	51.6	13.7
46	96	1130	112	225	370	88	88	2.9	55	0.23	300	49.0	15.6

\* Measured at 90 percent of voltage at reverse breakdown knee.

TABLE 9  
TRANSISTOR OVERLOAD TEST, PARAMETER CHANGES FROM OVERLOAD

Process Type	Unit No.	$I_{cbo}$ (na)	$I_{cbo}^*$ (na)	BV <sub>cbo</sub> (volts)	$I_{ceo}$ (na)	$ceos^*$ (na)	BV <sub>ceo</sub> (volts)	$I_{ebo}$ (na)	BV <sub>ebo</sub> (volts)	$h_{ib}$ (ohms)	$h_{ob}$ (umhos)	$h_{rb}$ $\times 10^{-6}$	$h_{fe}$ (percent)	$h_{fe}$ (hi-freq) (percent)
Change in Parameters Following Test No. 1														
Diffused Mesa	9	+1	+5	+1	+1	+10	0	+100	+0.1	0	+0.01	+1	+14	-4
Diffused Planar	10	0	+20	0	+1	+10	-1	+50	+0.1	-1	-0.01	0	+13	0
Epitaxial Mesa	15	+1	-1	-1	0	+0.3	-1	0	+0.1	-1	0	+1	+6	-0.7
Grown	16	0	0	+1	0	0	+1	0	+0.1	0	+0.01	-2	-18	-6
Diffused	25	+50	+20	-50	-2	-50	0	0	0	0	+0.01	-10	-13	-3
Epitaxial	26	0	+115	0	-26	-12	+1	0	-0.1	-1	0	+2	0	-6
Grown	30	0	-4	-1	0	-1	+1	+0.04	0	-1	0	0	0	-3
Diffused	31	+0.1	+0.6	+1	+0.1	-0.1	0	+0.02	-0.1	0	+0.02	0	0	-8
Grown	41	0	+20	-1	+2	+5	+1	0	+0.2	-1	0	+2	0	-2
Junction	46	+2	+5	+1	+5	+5	-1	+2	-0.2	+2	0	+70	+11	+8
Change in Parameters Following Test No. 2														
Diffused Mesa	1	+1	+400	+3	+5	0	-1	-20	+0.1	-2	-0.01	-25	+4	+4
Diffused Planar	2	-10	-50	+13	-73	+300	+2	+0.2	0	-1	0	+15	-10	+7
Epitaxial	11	0	-1.5	0	+0.2	+0.6	-1	0	-0.2	+1	0	-15	-5	+4
Mesa	12	0	-1.6	0	-1.1	+0.1	+1	0	0	0	0	-5	-4	+2
Grown	23	-5	+50	+1	+90	+40	0	-35	0	+1	+0.01	0	+5	+4
Diffused	24	-5	-80	0	+15	-70	-1	-20	0	-1	0	0	0	+3
Grown	35	0	+0.1	-1	-90	-90	0	-0.02	0	0	-0.01	-20	-5	0
Junction	36	-0.2	+18.9ua	-4	0	+100ua	-1	-0.06	0	0	0	-10	-7	0
Grown	42	0	0	-2	-1	+20	0	+13	-0	-2	0	+20	0	+4
Junction	45	0	0	+1	-29	+10	0	-0.1	+0.3	-10	-0.06	-290	0	+9
Change in Parameters Following Test No. 3														
Diffused Mesa	6	-2.1	+40	-2	-3.2	+50	-1	-0.08	-0.2	0	-0.01	-25	-4	-7
Diffused Planar	7	-1.9	-16	-3	-22.1	-57.4	0	-0.6	-0.1	-2	-0.30	-90	+13	-2
Epitaxial	14	0	+0.5	-2	-0.5	-0.2	+1	+0.3	0	-1	0	0	-6	-2
Mesa	18	-0.03	+0.02	+1	-0.08	-0.14	+1	0	0	-2	0	0	0	-2
Grown	21	+25	+100	-2	-30	-80	0	+3	0	-2	+0.01	+10	+4	-4
Diffused	22	-11	+30	-2	+200	+250	+1	0	0	-3	-0.01	0	+7	-10
Grown	27	+0.05	+1	+2	+0.02	+2	0	+0.02	0	-2	-0.01	-15	-5	0
Junction	28	+0.05	0	-20	-0.6	+4	-1	-0.01	0	-2	0	-5	0	-7
Grown	37	-1	+30	-1	0	-340	-1	+4.3	0	-1	-0.08	-200	-12	-3
Junction	38	-0.3	+2	0	-16.4	-26	+1	-10	0	-2	-0.05	-95	0	-4

TABLE 9 (Continued)

Process Type	Unit No.	I <sub>cbo</sub> (na)	I <sub>cbo</sub> * (na)	BV <sub>cbo</sub> (volts)	I <sub>ceo</sub> (na)	I <sub>ceo</sub> * (na)	BV <sub>ceo</sub> (volts)	I <sub>ebo</sub> (na)	BV <sub>ebo</sub> (volts)	h <sub>ib</sub> (ohms)	h <sub>ob</sub> (umhos)	h <sub>rb-6</sub> X10 <sup>-6</sup>	h <sub>13</sub> (percent)	h <sub>40</sub> (hi-free) (percent)
Change in Parameters Following Test No. 4														
Diffused Mean	5	+6	+70.5ua	-140	-1	-630	-72	-1	0	0	+0.01	0	0	-5
	8	+89.9	+7100	-9	+219.9	-1400	-2	+11	0	+1	+0.02	+15	-4	-20
Diffused Planar	12	-1.2	0	-1	-2	-1.6	0	0	+0.1	0	+0.01	+5	-7	-17
	17	0	0	+2	0	0	0	0	0	+1	+0.01	+20	-8	-15
Epitaxial Mean	25	-51	+1090	+50	-17	+20	0	+5	0	-1	-0.02	+10	+15	-15
	26	0	+95	0	-17	+156	0	0	-0.1	0	0	+3	-4	-18
Grown	29	-2.6	+615	-1	-3	+70	-2	0	0	-3	0	+5	0	0
Diffused	32	+0.4	+308	+7	+174.1	100ua at 92V	-2	+0.06	0	-2	0	-10	-6	+2
Grown	39	-1	+8	0	-95	-80	+1	+15	0	-1	-0.01	-10	-8	-2
Junction	40	0	+140	+3	-387	-550	0	+1200	0	0	-0.02	-110	-17	+5
Change in Parameters Following Test No. 5														
Diffused Mean	3	-2	+23.5ua	0	-1	-260	+3	-10	+0.1	+1	0	0	-4	-7
	4	-165	+14.2ua	+22	-1030	-2.9ua	-1	0	+0.1	0	+0.02	-20	-5	-4
Diffused Planar	19	0	+759.4	+8	0	0	0	0	0	-1	+0.01	+25	-9	-16
	20	-1	-0.5	+2	-14	+2	-1	0	0	+2	+0.02	+30	-11	-16
Epitaxial Mean	21	-10	+13.4ua	+2	-5	-30	0	-5	0	+1	0	+5	-4	-8
	22	+5	+5670	+2	0	-100	+1	0	0	+1	+0.01	+5	-3	-16
Grown	33	+4.1	+776	+10	+60	-1	+1	+0.15	0	+1	0	-20	-27	-6
Diffused	34	-0.1	-1	+2	-0.1	-4	+1	-0.09	0	-1	+0.01	+10	-13	-2
Grown	43	-1	+120	+2	-14	-150	0	-2	0	-1	-0.01	-55	-6	-2
Junction	44	+0.2	0	0	-1.3	+50	0	-5	0	-2	-0.05	-50	+30	+23
Change in Parameters Following Test No. 6														
Diffused Mean	1	+3	-270	-2	0	0	+1	-20	-0.3	0	-0.04	-5	+4	-10
	2	+4	+250	-2	+13	-500	+1	+0.5	0	-1	0	-25	-12	-7
Diffused Planar	11	-0.4	+0.2	0	+0.2	+0.6	+1	+0.6	-0.2	0	-0.01	0	+5	-21
	12	-1	-1.4	0	+0.5	+0.5	0	+0.1	-0.1	0	-0.02	+10	+5	-19
Epitaxial Mean	23	+30	+150	-1	-130	-20	+1	+60	+0.1	-2	-0.01	+5	-9	-24
	24	-10	+40	0	-62	-30	+1	+30	+0.1	0	0	+5	-5	-22
Grown	30	-1.6	-54	0	-2.9	-43	0	+0.18	0	-1	+0.02	0	-25	-8
Diffused	31	+0.1	0	-6	-0.5	+0.5	0	+0.06	+0.1	-1	+0.01	+20	-13	-3
Grown	42	-0.4	-1	-1	-0.3	-24	+1	-13	0	+2	0	-20	-19	-9
Junction	45	-0.9	0	-3	+1.2	-144	0	0	+0.6	+20	+0.06	+135	-21	-18

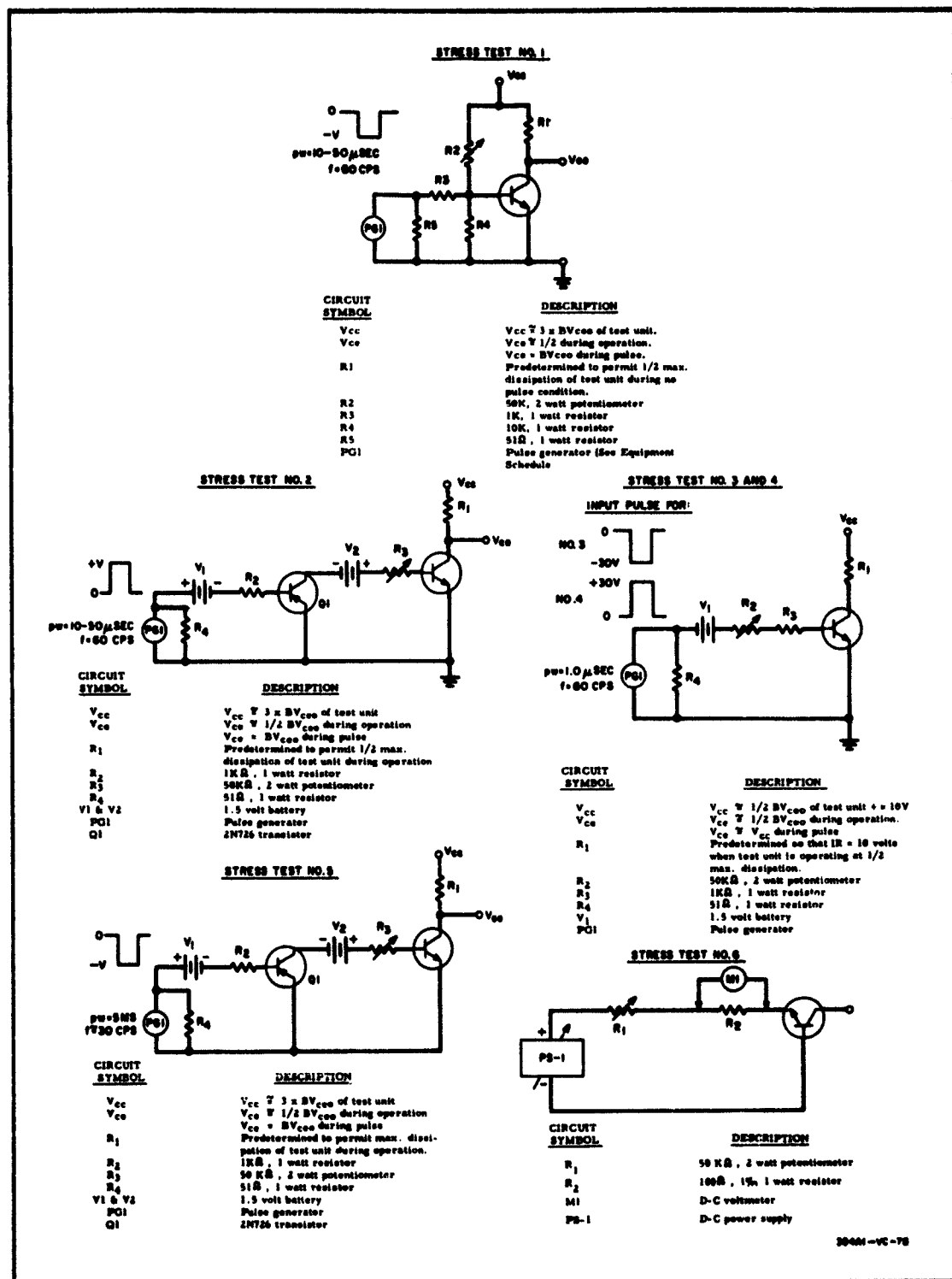


Figure 68. Stress Test Circuits

pulse widths were between 10 and 100  $\mu$ sec, depending on the device, and the frequency was 60 cps.

The purpose of this test was to apply high voltage, short duration pulses across the collector-to-emitter junctions. To accomplish this, a p-n-p fast switching transistor was used to drive the test samples so that, with a positive pulse into the base of the p-n-p which would turn it off, a high impedance would appear between the base and emitter of the test device, thus effectively appearing as an open base. The collector voltage seen would then be determined by the collector-to-emitter, base open, breakdown voltage of the individual transistors.

The currents sustained by the various transistors were limited to a range of 1 to 15 milliamperes during breakdown.

This test was conducted for 12 hours at a pulse width of 10 microseconds on the planar, grown diffused and epitaxial mesa transistors and for 4 hours at 100 microseconds and 18 hours at 50 microseconds on the grown junction and diffused mesa transistors.

#### 4.18.2.3 Test No. 3

The purpose of this test was to apply high voltage, short duration pulses to the base-to-emitter junction in the reverse direction, thus attempting to simulate hard turn-off conditions or high voltage transients which may be encountered in equipment switching circuitry. The transistors were again operated as described above except that the power supply was set to a low voltage such that during turn-off no breakdown of the junction would occur.

With the transistors biased on, the pulse generator applied a 30-volt negative pulse to the bases of the transistors at a frequency of 60 cps. The pulse width was 1 microsecond.

All transistors subjected to this test have a base-to-emitter reverse breakdown voltage of less than 30 volts so that during the turn-off pulse, each transistor base-to-emitter junction was broken down. The current was limited to a range of 2 to 25 milliamperes depending on the device.

This test was run for 20 hours.

#### 4.18.2.4 Test No. 4

With the transistors operating as described in Test No. 3, a positive 30-volt 1-microsecond pulse was applied to the bases of the transistors at a frequency of 60 cps.

The purpose of this test was to simulate excessively hard turn-on conditions of high voltage transients which may appear in switching circuitry.

Forward current during the positive pulse varied from 4 to 45 milliamperes.

The test samples were subjected to 20 hours of this type of voltage stressing.

#### 4.18.2.5 Test No. 5

The purpose of this test was to determine the effects of dissipating an amount of power equal to or greater than the manufacturer's recommended maximum power rating during breakdown and while the junction is at its maximum temperature due to operation at maximum rated power.

With the power supply set at a voltage equal to approximately three times the measured  $BV_{ceo}$ , the transistors were operated at their maximum rated power. Collector-to-emitter voltage was set at approximately one-half of the measured  $BV_{ceo}$ . A p-n-p fast switching transistor was used to drive the test samples as in Test No. 2. Thus, the collector-to-emitter, base open voltage was again seen at the collector during the turn-off time.

This stress test was conducted for 20 hours at a frequency of 30 cps and a pulse width of approximately 5 milliseconds for a duty cycle of approximately 15 percent.

#### 4.18.2.6 Test No. 6

The purpose of this test was to determine the effect of prolonged reverse emitter-to-base breakdown at low levels of current.

With the collector of the transistors open, a reverse bias was applied to the base-emitter junction. This reverse bias exceeded the  $BV_{ebo}$  reading as recorded in the initial data. Current was limited to approximately 1 milliamperes.

Time duration for this test was 20 hours.

#### 4.18.3 Test Results

The first stress test, in which the collector-to-base junctions were subjected to short duration, high voltage pulses, produced significant changes ( $\Delta h_{fe} \geq \pm 10$  percent) in the low frequency  $h_{fe}$  of four of the five process types tested. In addition, the two epitaxial units exhibited collector-to-base junction degradation. On one device the  $BV_{cbo}$  degraded to less than 50 percent of its initial reading while on the second,  $I_{cbo*}$ , the leakage near the breakdown knee, increased from 290 to 405 na (nanoamperes). One each of the planar and grown junction devices and both of the grown diffused devices had no significant change in parameters.

The second stress test, in which short duration, high voltage pulses were applied to the collector-to-emitter junction, produced the most significant changes in leakage characteristics. One of the mesas exhibited an increase of 400 na in  $I_{cbo*}$  while the other had an increase of 300 na in  $I_{cbo*}$ . A grown-diffused unit exhibited extreme degradation of  $I_{cbo*}$  and  $I_{ceo*}$  by several orders of magnitude. One grown junction had a change of 290 in its  $h_{rb}$  parameter. No significant parameter changes were noted in one grown-diffused, one grown junction, both planars and both epitaxial mesas.

The base-to-emitter junctions were subjected to short duration, high reverse voltage pulses in Test No. 3. There were no significant changes in parameters for one each of the mesa, grown-diffused, and grown junction types. The planars and epitaxial mesas also exhibited no changes. One mesa device had an increase of 13 percent in low frequency  $h_{fe}$  while a grown junction unit had a decrease of 12 percent in the same parameter. There was a significant drop in  $BV_{cbo}$  of 20 percent on one grown-diffused unit.

Test No. 4 was identical to Test No. 3 except that now the base-emitter diode was stressed in the forward biased direction. All devices tested, with the exception of one grown junction unit, exhibited significant changes of one or more parameters. The mesa units degraded orders of magnitude in  $I_{cbo}$ ,  $I_{cbo*}$ ,  $I_{ceo}$ , and  $I_{ceo*}$  plus a drop in high frequency  $h_{fe}$  of 20 percent on one



unit. The planars and one epitaxial unit exhibited high frequency  $h_{fe}$  fall-off greater than 10 percent. The other epitaxial had an increase in low frequency  $h_{fe}$  of 15 percent in addition to an order magnitude increase in  $I_{cbo*}$ . Both grown-diffused units also suffered significant increases in the collector-to-base and collector-to-emitter leakage parameters. The other grown junction device had a low frequency  $h_{fe}$  drop of 17 percent.

The fifth stress test in which excessive power was dissipated for short time periods produced parameter changes in all but one grown junction device.  $I_{cbo*}$  increased orders of magnitude on both mesas and one planar. This same planar unit had a drop in high frequency  $h_{fe}$  of 16 percent while the other planar also had a 16 percent drop in the same parameter in addition to a low frequency  $h_{fe}$  fall-off of 11 percent. Both epitaxial units and one grown-diffused unit also had orders of magnitude increase in  $I_{cbo*}$ . The low frequency  $h_{fe}$  decreased by 27 and 13 percent respectively, for the grown diffused types. The grown junction unit that was affected exhibited an increase of 30 percent in low frequency  $h_{fe}$  and 23 percent in high frequency  $h_{fe}$ .

Test No. 6 which continuously stressed the base-to-emitter junctions in the reverse direction at 1 milliamperes, and therefore at a very low power level, significantly affected the  $h_{fe}$  of all devices tested. One mesa, both planars, and both epitaxials suffered decreases of 10 to 24 percent in high frequency  $h_{fe}$ . The most significant change was exhibited by the epitaxial mesas and the least significant by the mesa. The other mesa device, both grown-diffused devices, and both grown junction devices exhibited decreases in low frequency  $h_{fe}$  of from 12 to 25 percent. The most significant decrease was for a grown diffused unit (25 percent) and the least significant was for the mesa (12 percent).

#### 4.18.4 Analysis of Results

In all of the stress tests performed, the most sensitive parameters for all types appear to be  $h_{fe}$  and the collector leakage current near the breakdown knee. Voltage degradation resulted in only one junction, collector-to-

base, on only two devices. The only other parameter affected significantly was the small signal reverse voltage transfer ratio,  $h_{rb}$ , on one grown junction device.

It is believed that those devices in which the collector leakage current near the knee was most affected by a particular stress suffered some alteration of the crystalline structure of the semiconductor near the surface. Both the collector depletion area and the surface provide most of the leakage current near the knee. However, since any effects on the collector depletion area would affect the high frequency  $h_{fe}$  to some extent, the greatest contribution to leakage in this case would appear to be surface leakage.

Low frequency  $h_{fe}$ , which is a product of emitter efficiency, base transport factor, and collector multiplication factor would be affected by  $\pm 10$  percent if any one of these factors changed by 0.2 to 0.3 percent.

High frequency  $h_{fe}$  would change significantly if either the collector depletion area and/or the emitter transition area were altered.

During Tests No. 1 and 2, varying pulse widths were required to allow a device to see the supply voltage during the turn-off period. Devices with a fast response time, such as planar and epitaxial types, would see the supply voltage during a 10-microsecond turn-off pulse. The other types required up to a 50-microsecond turn-off pulse. A high frequency, high speed switching type of transistor, therefore, would see a voltage transient of short duration, while some of the slower transistor types would see no transient because they could not respond fast enough.

Test No. 3 and 6 are similar tests except that the former is pulsed and the latter steady state. Little or no change in parameters occurred following Test No. 3. In fact, the planar and epitaxial units exhibited no significant changes whatsoever. Test No. 6, on the other hand, produced changes in  $h_{fe}$  on every device tested but no significant change in any other parameter. Every device was affected; steady state back biasing of the base-emitter junction in the breakdown region affects the  $h_{fe}$  of the device. Pulsed operation of the base-emitter junction in the breakdown region apparently has little or no effect.

Generally, it can be concluded that voltage stressing and power stressing (Test No. 5) produce roughly the same results; i.e., order of magnitude increase in collector leakage current near the reverse breakdown knee, and significant changes in either low frequency  $h_{fe}$  or high frequency  $h_{fe}$ . Only continuous operation in the reverse breakdown region appears to give characteristic changes in a particular parameter. No other test produced identifiable results.

The planar type appears least affected by the various tests and only  $h_{fe}$  appears sensitive at all. Mesa and grown-diffused types appeared most affected by all stress tests.

The more severe stress appears to be caused by high voltage turn-on pulsing (Test No. 4), excessive power dissipation in the collector breakdown region (Test No. 4), and continuous operation in the reverse breakdown region of the emitter-base junction (Test No. 6).

## 4.19 HIGH ENERGY RADIATION INDUCED FAILURE IN THE SOLID STATE - STUDY OF FERRITES USING MÖSSBAUER EFFECT

### 4.19.1 Introduction

The Mössbauer spectra were obtained for hexagonal ferrites with the magnetoplumbite structure and also for yttrium iron garnet. Samples of the hexagonal ferrites were studied both in powdered form and in oriented sintered discs, for two different divalent ions, and in one case over a range of temperatures. The spectra of the hexagonal ferrites revealed two hyperfine fields, as also observed in garnet. Tentative assignments of ions to sets corresponding to the observed fields were made.

Selected samples were subjected to intense electron bombardment up to a maximum dose of  $10^{11}$  rads. There were no systematic changes in the Mössbauer spectra of these after irradiation. This and magnetic measurements confirm that there were no gross changes in chemical structure, so that any failure mechanisms introduced by the radiation must have been of a lower order than gross structural mechanisms.

#### 4.19.1.1 Purpose of Work

Ferrites are magnetic materials derived from oxides of iron which are of increasing technical importance. Because of their very low conductivity compared to the more conventional metal magnetic materials, they have found wide application in high frequency circuits and computer memories.

In most studies of the effects of radiation upon magnetic materials, the magnetic properties are measured before and after irradiation. This information is of immediate practical value, but it is not necessarily useful in learning about the basic changes in the chemical structure at the material. Particularly in the case of ferrites, which are ferrimagnetic, it may be difficult to infer the nature of the structural changes from the macroscopic magnetic measurements which reflect only the net resultant of the two opposed internal magnetic fields.

It is fortunate that of all the elements which display the Mössbauer effect, iron is in practice the most convenient to study. From the Mössbauer

spectrum of a ferrite sample, one may determine a measure of each internal field individually, so that if changes in the macroscopic magnetic properties occur it should be possible to properly relate them to the changes in chemical structure. For any given set of iron ions which yield an absorption line (or set of absorption lines), the Mössbauer spectrum reveals not only a measure of the local internal field, but also a measure of the electric field gradient (which produces a quadrupole interaction), and in addition a measure of the electron density which is in turn an indication of the valence of the ion.

The purpose of this work was to study the radiation induced changes in ferrites by means of the Mössbauer effect. In addition, the examination of the undamaged samples itself was novel and so contributed to our understanding of the ferrite structure. Finally, the work can be considered a pilot study in the applicability of this new technique to the study of iron containing electronic materials.

#### 4.19.1.2 Materials of Interest

Of the wide variety of ferrites available with which to begin the work, two kinds of samples were chosen: (1) simple hexagonal ferrites of the magnetoplumbite structure, and (2) yttrium iron garnet, and of these the most work was done on 1. These samples were not chosen on the basis of previous radiation damage studies which have indeed been very meager, but for other reasons as discussed below. The spinel-type ferrites, on which there have been a number of radiation studies, had also been the subject of Mössbauer studies. Aside from  $\text{Fe}_3\text{O}_4$  itself (reference 7) there was some indication (reference 8) that the Mössbauer spectra were broad lines and not readily interpretable. On the other hand, the yttrium iron garnet was the subject of two Mössbauer studies (references 9 and 10) which were more successfully interpreted. Another reason for our interest in garnet was that it was a more timely material, more on the forefront of technology. The hexagonal ferrites were of interest for the same reason, especially with reference to their usefulness in computer memories, although previously there were little radiation damage data and no Mössbauer data. An additional quality of

the hexagonal ferrites was their capability to be made into oriented samples which, kin to single crystals, greatly clarified the interpretation of their spectra.

#### 4.19.1.3 Radiation Studies

Magnetic materials are generally regarded as having good radiation resistance, being far superior to organic materials and to semiconductors, and almost in the same class as structural metals and ceramics. A vast amount of literature is available on radiation damage to semiconductors and organic materials because of their great susceptibility to damage. At the other end of the scale there is also a vast amount of literature available on damage to metals and ceramics because, despite their resistance, they are damaged by the severely high fluxes to which they are subjected when used as structural materials in nuclear reactors. Because magnetic materials with their superior resistance rarely have to be subjected to such severe environments, there has not been a great demand for radiation damage studies. Such studies of ferrites are so few and scattered that one cannot even profitably review the field in order to make generalizations.

In a recent study, Taimuty and Mills exposed a variety of commercial ferrites to fast neutron doses of  $10^{16}$  to  $10^{18}$  nvt. The observed changes in the various magnetic properties were small, not necessarily monotonic with dose, and prompted the conclusion that the operation of devices incorporating these materials would not be significantly affected within this dose range. For the most part, the more significant changes could be ascribed to the formation of structural defects which interfere with domain wall motion during the magnetization process. However, there was an anomalous increase in small signal permeability in Mg-Mn ferrites at low doses which suggested that a significant transfer of Mg ions into tetrahedral sites occurred in the thermal spikes.

Additional evidence for site-interchange upon irradiation has been cited by other authors. Moss, et al. (reference 12) found an increase of 10 percent in saturation magnetization in a nickel ferrite exposed to  $3 \times 10^{18}$  nvt. At

the same dose, there was a decrease of 14 percent in the saturation magnetization of YIG (yttrium iron garnet). Schindler (reference 13) reported that after  $6.3 \times 10^{18}$  nvt there was a decrease of 15 percent in the saturation magnetization of a commercial  $\text{Fe}_3\text{O}_4$  composition, which he attributed in part to oxidation. However, he reported no decrease in garnet and some other ferrites. It has been reported (reference 15) that after  $4 \times 10^{20}$  nvt the open circuit induction of a barium ferrite (such as the hexagonal ferrites reported on in this paper) was reduced 63 percent (oriented sample) and 54 percent (nonoriented).

In contrast, other work has indicated that the predominant changes are in the dynamic rather than d-c properties. For instance, Gordon and Sery (reference 15) reported that a nickel ferrite exposed to  $2.7 \times 10^{18}$  nvt showed no change in d-c properties, but an increase of 50 percent in the core loss at 50 kc (worse at higher frequencies). Schindler (reference 13) also reported cases of up to 100 percent increase in coercive force in various ferrites exposed to  $6.3 \times 10^{18}$  nvt. These materials had shown no change in Curie temperature indicating that there were no gross changes in structure.

The work cited above involved neutron irradiation in all cases. An investigation (reference 6) at Westinghouse Central Research Laboratories was carried out by the Magnetics Development Laboratory (in part using the facilities of the author's laboratory) in which neutron irradiation was the principal means of damage and samples were observed for changes in magnetostriction and anisotropy. In addition, some irradiations were made with 2 Mev electrons up to an integrated flux of  $1.3 \times 10^{19}/\text{cm}^2$  in which positive indications of damage were observed in some cases. This suggested that electron irradiation might be tried first in the present investigation, since neutron irradiation would introduce additional problems in the Mössbauer measurement due to induced radioactivity.

The preceding discussion of some of the present radiation damage data on ferrites indicates that many problems could be clarified by measurements of the relative populations of each kind of crystal site and the magnetization per ion in each kind of site. This is the information obtainable from the

Mössbauer spectrum. Specifically the magnitude of the Zeeman splitting is a measure of the magnetization per ion, and the line intensity for any given set of lines is a measure of the population. In addition, as noted earlier, the position of the set is a measure of valence and the dissymmetry a measure of the electric field gradient at the site. It should be noted that in those cases where changes in magnetic properties are primarily attributable to defects which interfere with domain wall motion, there may be little or no change in the Mössbauer spectrum, because only a very small fraction of the absorbing nuclei may be involved in such structural defects.

#### 4.19.1.4 Principles of the Mössbauer Effect and Its Measurement (reference 16)

Just as the emission and absorption of light quanta by atoms are just inverse resonant processes, so it was expected that nuclear gamma rays should also undergo resonant absorption. Such an absorption process was sought for many years without success until Rudolf Mössbauer demonstrated it in 1958 in the case of  $\text{Ir}^{191}$ . From the wealth of investigations which followed, one can now elucidate the conditions required to carry out useful experiments in resonant gamma ray absorption.

The main reason that resonance absorption was not seen earlier was that the emitted photon gives up some of its energy to the recoiling nucleus and is thus "detuned" from resonance. It is now understood that if the emitting nucleus is in a solid lattice there is a finite probability of emission of a recoilless photon. The fraction,  $f$ , of emissions which are recoilless is given (reference 18) by:

$$f = \exp \left\{ - \left[ \frac{3}{2} \frac{E_o^2}{2Mc^2 k\theta} \left( 1 + \frac{4T^2}{\theta^2} \int_0^{\theta/T} \frac{x dx}{e^x - 1} \right) \right] \right\} \quad (70)$$



where  $E_0$  is the gamma ray energy,  $T$  the absolute temperature,  $\theta$  the Debye temperature,  $M$  the mass of the recoiling atom,  $c$  the velocity of light,  $k$  Boltzmann's constant, and  $x$  a dummy variable. In the case of iron metal for which  $\theta \sim 420^\circ\text{K}$ ,  $f \approx 0.8$  at room temperature. In the case of ferrites which have high  $\theta$ ,  $f$  is closer yet to unity at room temperature. One can see from equation 70 that the chance of observing the Mössbauer effect in any substance is increased if  $E_0$  is small ( $\sim 100$  Kev is an upper limit for convenience), if  $M$  is large, and if  $\theta$  is high. This means it is favored in "hard" metals and alloys, oxides, most salts, and glasses. It would be less favored in molecular crystals of covalent compounds, and has never been obtained in liquids.

The energy dependence of the recoilless gamma rays is determined by the uncertainty principle, the line width being greater the shorter the half life of the excited state. In the case of  $\text{Fe}^{57}$ , the nuclide of interest in this work, the line width is  $\sim 10^{-8}$  ev. As will be seen, this is a very convenient value. Very broad lines are undesirable because they do not permit the observation of fine structure. On the other hand, extremely narrow lines (long half lives) are very difficult to observe at all because minor, second order energy shifts can throw the emitter and absorber completely out of resonance.

Finally, since the interest is in short lived excited states, there must be available a suitable parent isotope to supply continuously the excited state of interest. Some other problems involved in the applicability of an isotope for the Mössbauer effect are (1) interfering radiations, (2) loss of gamma-ray intensity through internal conversion, and (3) isotopic abundance. Accordingly, there are relatively few isotopes for which the Mössbauer effect has had much application. Besides  $\text{Fe}^{57}$ , some of these are  $\text{Sn}^{119}$ ,  $\text{Dy}^{161}$ ,  $\text{Tm}^{169}$ ,  $\text{Ir}^{191}$ , and  $\text{Au}^{197}$ .

The Mössbauer effect can be observed by measuring the counting rate of a source through an absorber containing the ground state are nuclide and comparing this rate under conditions of resonance and nonresonance. The non-resonant condition can be achieved in various ways such as (1) heating to

reduce  $f$ , (2) magnetically cross polarizing emitter and absorber, or (3) the most common method, vibrating source, or absorber to doppler shift the gamma rays.

To obtain an energy spectrum of the absorber with respect to the source, precise and very small increments of energy must be added. The simplest way to achieve this is to move the absorber relative to the source, thus imposing a doppler shift, and for each value of relative velocity determine the corresponding count rate. In the case of  $\text{Fe}^{57}$ , the energy scale is so small that the largest velocity required is about 10 mm/sec. For  $\text{Fe}^{57}$ , 1 mm/sec  $\approx 4.8 \times 10^{-8}$  ev. Two kinds of velocity spectrometers are in use. The first is a constant velocity machine in which total counts are determined for a fixed interval ( $\sim 1$  minute) at constant velocity, and the process repeated at a number of other velocities. The other type, which is employed in the Westinghouse laboratories, scans all velocities rapidly (19 cps) and sorts the counts received in a multichannel analyzer as a function of the instantaneous velocity of the source.

#### 4.19.1.5 Interpretation of Mössbauer Spectra

The energy level of the excited nuclear state is influenced by the chemical environment of the nucleus to a small extent ( $\sim 10^{-7}$  to  $10^{-6}$  ev), which is however large compared to the line width. Accordingly, a fine structure and a shift are discernible in the spectrum obtained by the doppler shift procedure described above.

Figure 69 is an energy level diagram for  $\text{Fe}^{57}$  which illustrates the possible splitting and shifts. The scale is exaggerated greatly, the spacing between ground state and excited state actually being  $\sim 10^{13}$  times the other spacings.

The center shift observed experimentally consists of the shift depicted in figure 69, called the isomer shift, plus the second order doppler shift. The largest and most interesting (from the point of view of this study) contribution

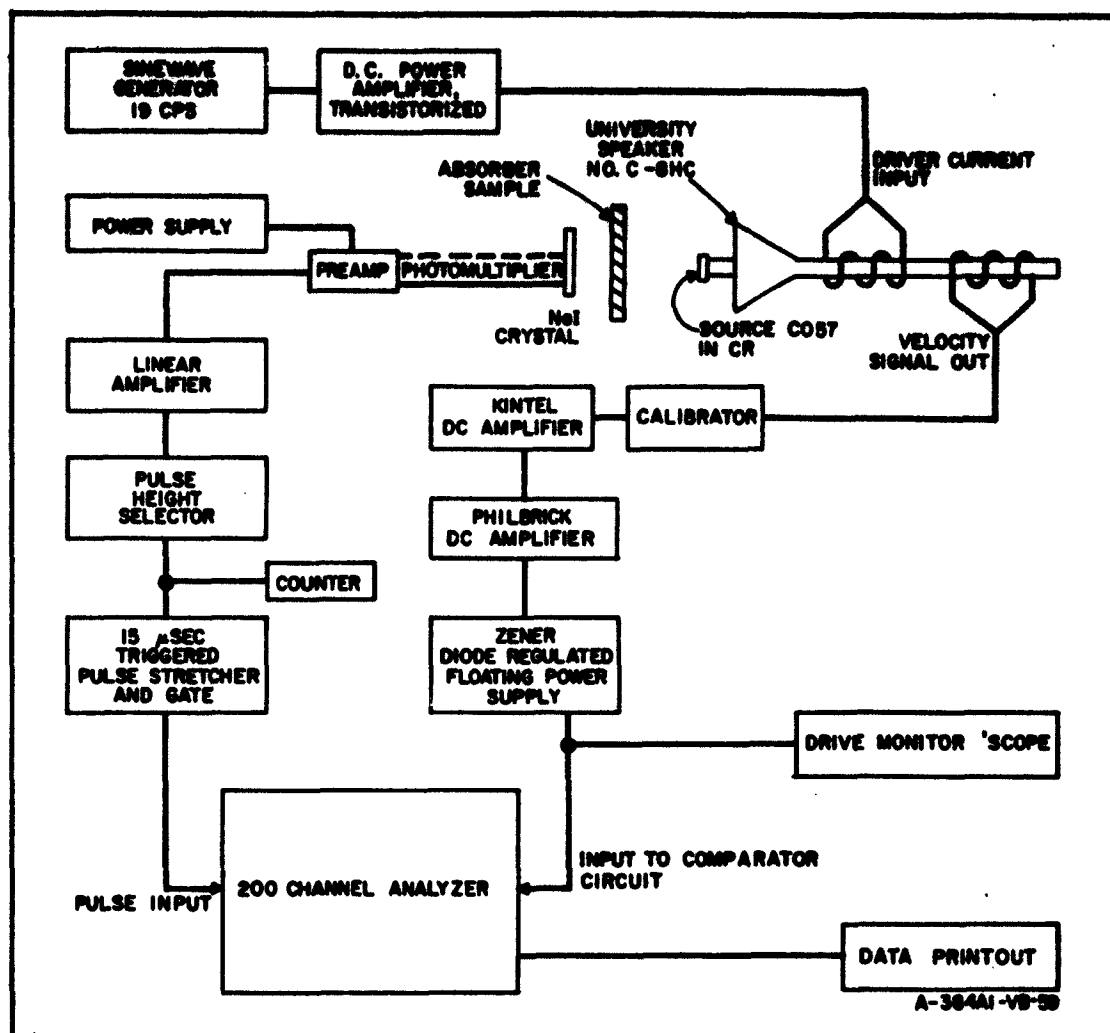


Figure 69. Block Diagram of Mössbauer Velocity Spectrometer

is the isomer shift which arises from the nuclear expansion accompanying the downward transition. This is a measure of the difference between source and absorber in the electron density at the nucleus, and thus indicates the valence of the iron. The second order doppler shift arises from the difference in average vibrational energy and is negligible when source and absorber are at the same room temperature. A correction of  $0.00073 \text{ mm/sec/}^{\circ}\text{C}$  is applicable around room temperature.

In the case of paramagnetic atoms, the ground state is unsplit and the upper state is either split into two levels or unsplit depending on whether or not there is an electric field gradient to interact with the quadrupole moment of the  $\text{Fe}^{57}$  nucleus. In magnetic materials, there is a large hyperfine field at the nucleus which interacts with the nuclear magnetic moments of the ground and excited states to form the six-line Zeeman pattern shown. As indicated, the magnetic moment of the ground state is greater than that of the excited state ( $A > B$ ). For iron metal at various temperatures it has been shown that the hyperfine field is proportional to the domain field, but this proportionality factor is not exactly the same for all materials. However, it apparently does not vary widely. The dissymmetry of the six-line pattern caused by the quadrupole interaction is shown in figure 69 for the simple case of an axially symmetric field gradient which is parallel to the magnetic axis. This provides a fair fit to the data obtained on the materials considered in this report.

The assignments of spectral lines in this work was based on the assumption that there exist in the sample two sets of iron atoms, each with its characteristic hyperfine field. Each set gives rise to six absorption lines numbered 1 to 6 in order of increasing energy, and subscripted (a) in the case of the larger field and (b) in the case of the smaller field. In the case of lines 3 and 4, set (a) was not always distinguishable from (b).

The following numerical relationships which can be deduced readily from figure 69 were used to analyze the spectra.

$$A = 4 - 2 = 5 - 3 \quad (71)$$

$$B = 5 - 4 = 3 - 2 \quad (72)$$

$$\epsilon = \frac{6 - 5 - 2 - 1}{4} = \frac{6 - 4 - 3 - 1}{4} \quad (73)$$

$$\text{Center Shift} = \frac{4 + 3}{2} + \epsilon \quad (74)$$

The quantities A, B,  $\epsilon$ , and the center shift are all measured in mm/sec.

Where equivalent calculations were not quite equal, the average of the two was listed. In some cases, lines 2 and 5 were difficult to measure and were not considered in the calculation.

The hyperfine field in koe may be computed as follows, where the numerical constant is obtained by comparison to the spectrum of pure iron for which the hyperfine field at room temperature is known to be 333 koe.

$$H_f = 31.4 [6 - 1] \quad (75)$$

or

$$H_f = 86.5 A \quad (76)$$

Expression 75 was used for all values listed in table 10. Actually, it is only applicable if figure 69 is applicable. In more complex cases, e.g., nonparallelism of field gradient and magnetic axes, the uppermost level and lowest level of the excited state are not equally shifted as shown. Expression 76 is always applicable. However, it requires a precise value for either line 2 or 5, which was not always obtainable.

The absence or poor resolution of lines 2 and 5 is a direct consequence of the nature of the hexagonal ferrites, which tend to have their direction of easy magnetization perpendicular to the plane of the sample, especially in the case of the oriented samples. It can be shown that when the direction of radiation is parallel to the magnetization, as in this situation, the  $\Delta m = 0$  transitions corresponding to lines 2 and 5 (see figure 69) are strongly forbidden. One can, in fact, readily distinguish the oriented samples by the very weak lines 2 and 5 in their Mössbauer spectra.

TABLE 10  
MÖSSBAUER SPECTRA OBTAINED IN THIS PROGRAM

Run No.	Material	Hyperfine Fields Koe (eq. 6)		Center Shifts mm/sec		Quadrupole Inter- actions, mm/sec		Hyperfine Fields Koe (eq. 7)		Notes
		HA(a)	HB(b)	(a)	(b)	(a)	(b)	HA(a)	HB(b)	
487	W (PMMA)	510	420	0.28	0.42	0.084	0.228	512	442	liquid N <sub>2</sub> ; ~7% scale correction in field ~5000 oe; ~7% scale correction ~7% scale correction subsequent runs were made using Cr source
489	W (HBO <sub>2</sub> )	515	424	0.39	0.54	0.088	0.244	505	434	
495	Ref. 489	481	454	0.30	0.24	0.189	0.132	468	459	
496	Ref. 487	508	414	0.41	0.54	0.036	0.167	488	432	
498	Ref. 440	518	428	0.42	0.40	0.068	0.265	506	436	scale suspect scale suspect scale suspect liquid N <sub>2</sub> ; scale trouble cured
499	Ref. 444	523	428	0.37	0.44	0.130	0.200	526	464	
502	Ref. 446	496	406	0.43	0.55	0.057	0.175	500	406	
506	W (HBO <sub>2</sub> )	489	399	0.48	0.58	0.050	0.156	497	413	
507	Ref. 447	475	392	0.40	0.48	0.100	0.175	527	432	-78°C -78°C -10.5°C 100°C
509	W (PMMA)	546	509	0.45	0.49	0.144	0.175	543	519	
510	Ref. 509	496	413	0.31	0.40	0.082	0.175	500	524	
511	Ref. 509	516	454	0.42	0.56	0.013	0.248	549	450	
515	Ref. 509	530	465	0.47	0.52	0.169	0.219	533	486	poor resolution very sharp spectrum
516	Ref. 509	518	436	0.51	0.66	-0.038	0.114	527	456	
517	Ref. 509	490	410	0.34	0.48	0.013	0.157	488	406	
518	W (Li <sub>2</sub> CO <sub>3</sub> )	476	366	0.47	0.59	0.019	0.138	482	385	
521	Ref. 443; 1 x 10 <sup>11</sup> rad	514	420	0.36	0.46	0.058	0.129	528	436	poor spectrum, sample ground up and disoriented
522	Ref. 450, 454; 1 x 10 <sup>11</sup> rad	498	400	0.43	0.48	0.120	0.185	-	374	
523	Ref. 439, 453; 1 x 10 <sup>11</sup> rad	498	413	0.37	0.51	0.044	0.185	500	428	
524	Ref. 445; 1 x 10 <sup>11</sup> rad	487	404	0.43	0.55	0.075	0.201	480	381	
527	Ref. 475; 4 x 10 <sup>10</sup> rad	492	398	0.54	0.41	0.113	-0.019	449	400	

TABLE 10 (Continued)

Run No.	Material	Hyperfine Fields Koe (eq. 6)		Center Shifts mm/sec		Quadrupole Inter- actions, mm/sec		Hyperfine Fields Koe (eq. 7)		Notes
		H(a)	H(b)	(a)	(b)	(a)	(b)	H(a)	H(b)	
402	W (Duco cement)	492	414	0.40	0.48	0.115	0.190	-	-	spurious peaks, 0.23 and ~ 8.8
403	YIG pwr. (Duco)	466	398	0.18	0.24	-0.040	0.020	492	404	6a unresolved
418	Indox V or.	-	424	-	0.49	-	0.262	-	-	spurious peaks, 0.00 and 2.99
439	BV13	510	411	0.37	0.45	0.085	0.165	519	436	lines 2 and 5 very weak not used for $\epsilon'$ 's
440	BV25 or., mag.	495	440	0.54	0.41	0.350	0.220	551	464	lines broad
441	BV25 or.	498	410	0.33	0.40	0.080	0.155	525	450	spurious peaks, -2.40, 0.25, and 2.90
442	15A6	488	403	0.24	0.38	0.144	0.281	454	389	spurious peak at 3.10
443	15A8 mag.	526	430	0.39	0.45	0.094	0.156	516	448	lines 2 and 5 weak, not used for $\epsilon'$ 's
444	Indox I	520	423	0.34	0.43	0.043	0.125	520	446	spurious peak at 0.1
445	Indox I mag.	515	427	0.28	0.47	0.125	0.219	502	430	spurious peak at 2.85
446	Indox V or., mag.	511	419	0.35	0.39	0.125	0.163	533	446	spurious peaks at 0.00, 2.90, 6.40
447	Indox V or.	520	427	0.28	0.35	0.100	0.150	518	387	spurious peaks at -2.40, 0.10, 2.90
450	BV25 or.	506	411	0.31	0.36	0.137	0.188	548	428	~7% scale correction required
451	Indox V or.	502	413	0.44	0.54	0.112	0.219	533	444	~3% scale correction required
452	Indox I	515	424	0.36	0.40	0.187	0.225	520	441	
453	Ref. 439, $5 \times 10^9$ rad	506	410	0.35	0.48	0.075	0.206	503	426	
454	Ref. 450, $1 \times 10^{10}$ rad	504	408	0.45	0.44	0.075	0.163	511	394	
475	YIG pwr. (LiBO <sub>2</sub> )	495	397	0.35	0.28	0.083	0.008	-	-	
476	YIG pwr. (PMMA)	501	408	0.45	0.31	0.085	-0.003	517	366	

TABLE 10 (Continued)

Run No.	Material	Hyperfine Fields Koe (eq. 6)		Center Shifts mm/sec		Quadrupole Inter- actions, mm/sec		Hyperfine Fields Koe (eq. 7)		Notes
		H <sub>A</sub> (a)	H <sub>A</sub> (b)	(a)	(b)	(a)	(b)	H <sub>A</sub> (a)	H <sub>A</sub> (b)	
528	Ref. 506; $4 \times 10^{10}$ rad	497	415	-	-	-	-	-	-	poor spectrum
529	Ref. 440, 498, $4 \times 10^{10}$ rad	502	412	0.34	0.50	0.069	0.226	478	406	
530	Ref. 446, 502; $4 \times 10^{10}$ rad	505	415	0.36	0.54	0.056	0.244	504	435	sample reground and disoriented
531	Repeat 524	499	412	0.31	0.61	0.008	0.105	524	419	
532	Repeat 528	496	400	0.48	0.56	0.058	0.130	502	423	



#### 4.19.2 Experimental Work

##### 4.19.2.1 Sample Materials

The materials reported on in this work are (1) hexagonal barium ferrite,  $\text{BaO} \cdot 6\text{Fe}_2\text{O}_3$ ; (2) hexagonal alkaline earth ferrite,  $\text{MO} \cdot 6\text{Fe}_2\text{O}_3$ , where M is an alkaline earth; and (3) yttrium iron garnet,  $\text{Y}_3\text{Fe}_5\text{O}_{12}$ .

The barium ferrite was made by Indiana Steel Corporation and is called Indox. Samples were obtained in the form of sintered discs, about 5/8-inch in diameter and 2 mils thick. Samples labelled Indox V were oriented in manufacture so that the axis of easy magnetization was perpendicular to the plane of the disc, whereas those called Indox I were not oriented. Some measurements were also made on each of these after they were magnetized (perpendicular to the plane of the disc).

The alkaline earth ferrite was prepared in the Westinghouse Research Laboratories. Discs similar to the various Indox samples were prepared. In addition, powder consisting of single domain particles was made available. Additional experiments were performed on absorbers prepared from this powder by mixing it with a large volume of polymethyl methacrylate powder (PMMA) and pressing into a disc. These absorbers were termed "disoriented," since in their dilute state there was little chance of adventitious orientation of the powder during pressing as appears to have occurred in the "unoriented" sintered discs to some extent.

Additional dilute disoriented discs were made by pressing the powder with a boric acid polymer. These samples were subjected to electron irradiation, assuming that the boric acid polymer would be much more radiation resistant than the organic polymer. Radiation damage was nonetheless severe at the highest doses used. For one elevated temperature run, a dilute disoriented absorber was made by pressing the powder with  $\text{Li}_2\text{CO}_3$ .

Runs were made on YIG in the form of powder in plastic discs as described above. The source of the powder was small rough crystals synthesized by a

sinter technique. In addition, melt grown single crystals were cut parallel to the 110 planes and ground to 2 to 3 mils, but the spectra obtained were too complex to be analyzed for purposes of this project. The YIG was made in the Westinghouse Research Laboratories.

Samples of the Westinghouse ferrite were also made in the form of slender rods suitable for magnetic measurements, and also of small enough diameter to permit penetration of the electron beam. These were used to determine the effects of irradiation upon the magnetic properties of the material since the Mössbauer absorbers were of improper shape.

#### 4.19.2.2 Mössbauer Equipment and Measurement Procedure

The Mössbauer velocity spectrometer is block diagrammed in figure 69a. This is the system which has been in use in the Westinghouse laboratory for 2-1/2 years and has been widely described. Several modifications have recently been incorporated. The transistorized driver amplifier was required for the new high compliance speaker now being used in order to drive it faithfully and reproducibly. The new speaker contains two voice coils, one of which is used as a driver and the other as a velocity transducer. This is superior to an external transducer in regard to ruggedness and constancy of calibration. The combination of new speaker and driver amplifier are also necessary for the parabolic drive system which has just been completed and is now being installed.

A device was installed to introduce a constant dead time after each pulse being fed to the analyzer. This avoids a "tilted" spectrum which arises because the time required to store a pulse is a function of the channel number. Accordingly, the analyzer dead time is a function of channel number unless otherwise controlled.

In the velocity signal route, a Zener diode and associated power supply was installed to improve the freedom from zero drift.

During this contract period, a new radiation source was made and installed. About two millicuries of Co<sup>57</sup> was electroplated onto a highly polished

chromium wafer. This was annealed in vacuum at 1000°C for one-half hour. (Prolonged annealing would "bury" the Co in the thick wafer.) This source was superior to the previously used stainless steel with regard to line width, and was also of much higher activity, giving about 10 times the former count rate. With the present count rate, a 4-hour run is sufficient to fill the memory of the analyzer, i. e.  $\sim 65,000$  counts per channel. Longer runs are made if better statistics are required to see small effects. The improved line width is illustrated in figure 71, which shows the new data obtained with the new Cr source and an absorber of enriched  $K_4Fe^{57}(CN)_6$ . The uncorrected line width is only 0.34 mm/sec. The isomer shift (center shift) is 0.08 mm/sec compared to 0.05 mm/sec for stainless steel. The isomer shift of -0.03 mm/sec for Cr versus stainless steel was checked using the chromium source and a stainless steel absorber.

To make a run, the following procedure was used. First, with the velocity coil shorted, the velocity train was calibrated using the d-c calibrating box. By varying the bias, channel 100 was made to correspond to zero velocity (zero volts) and by varying the gain channels 20 and 180 were made minus and plus 8.0 mm/sec, respectively. The appropriate calibrating d-c was 4.13 mv/mm/sec, which was determined and checked periodically by running the spectrum of pure iron foil for which the peak-to-peak Zeeman splitting at room temperature is well established as 10.65 mm/sec. Second, the amplitude of the source vibration was set to exceed slightly the velocity range of the analyzer and left fixed for the run. A "form run" was then stored using random counts and printed out, the counts in each velocity channel representing the relative measuring time at that velocity. Next the single channel analyzer was adjusted to feed only the 14.4 Kev counts to the analyzer and the spectrum was stored and printed out. Storage of the spectrum required much more time than the "form" because of the limited count rate of the 14.4 Kev gammas. After printing the spectrum, it was customary to repeat the

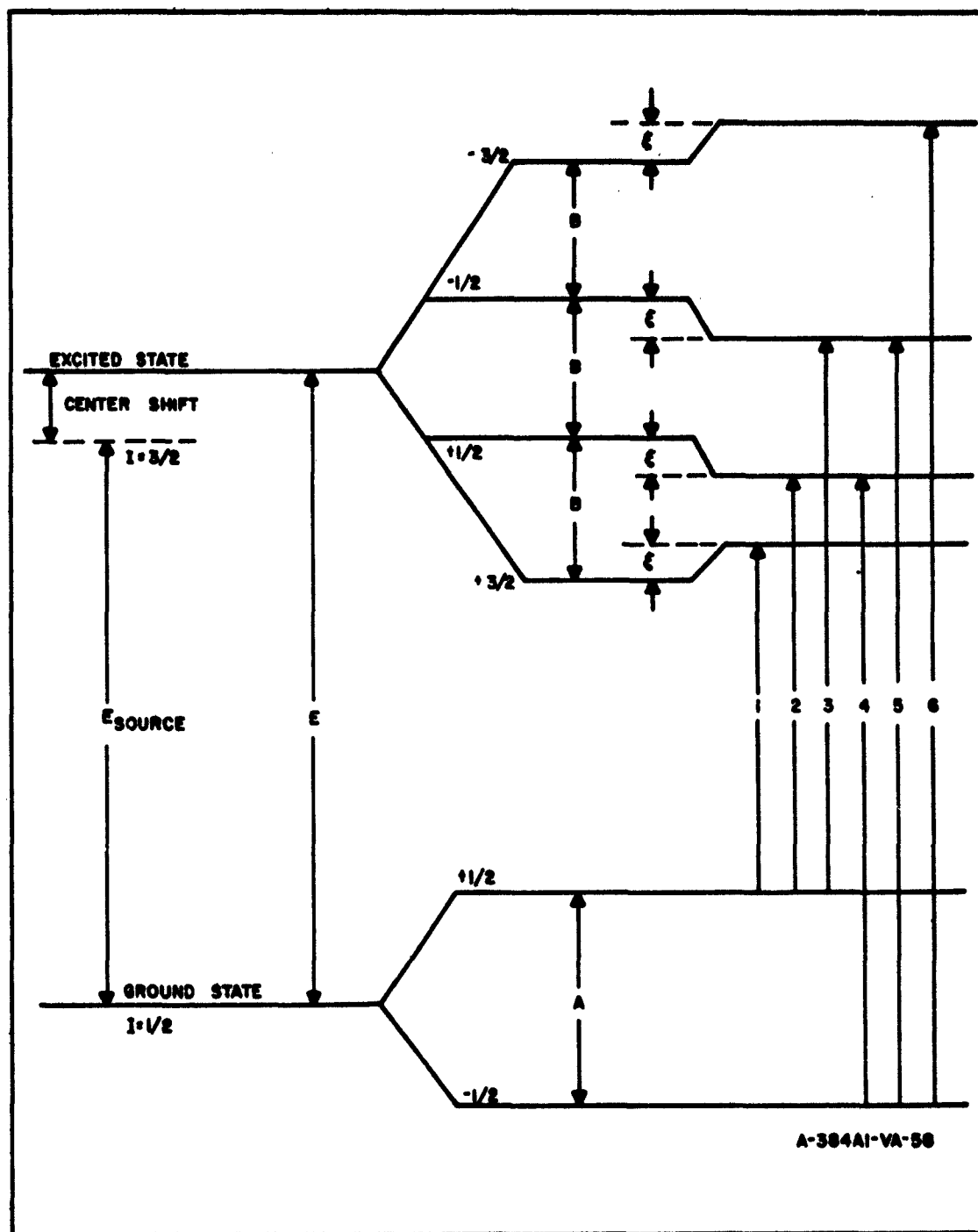


Figure 70. Energy Level Diagram for  $\text{Fe}^{57}$  Nucleus Showing Zeeman Splittings (A, B) Quadrupole Interaction ( $\epsilon$ ) and Center Shift

form and add the two forms to average out any slight drift in the pattern of motion of the drive, drift in the velocity train bias, and amplification. Any drift of bias or amplification was measured by repeating the d-c calibration procedure, and small drifts of one or two channels (i.e., 0.10 or 0.20 mm/sec), which occurred occasionally, were corrected for. The raw spectrum data was divided channel by channel by the form data to give a normalized spectrum with a flat background.

Before determining the positions of the absorption lines, smooth curves were drawn to match the data, based on the assumption that the curve was composed of lines which were Lorentzian in shape and about 0.5 mm/sec wide. The curve fitting was not done analytically but by trial and error manual sketching and visual inspection. The positions listed for the lines are the peak positions. No attempt was made to measure peak heights or areas.

The total count rate when the single channel analyzer was set for 14.4 Kev included 30 to 80 percent non-14.4 Kev background depending on absorber thickness. The percent background was determined for each sample by measuring the apparent 14.4 Kev rate with and without a 1/16-inch Al absorber. This measurement made it possible if desired to convert observed percentage Mössbauer effects to an absolute basis (although this was not necessary in this work), and also to estimate in advance the total number of counts required for a given net 14.4 Kev total. Since net effects were only about 9 percent at best, samples were run until the equivalent of 10,000 net 14.4 Kev counts ( $\pm 1$  percent counting statistics) were received.

#### 4.19.2.3 Irradiation Procedures

Because of the exploratory nature of the project, the main objective of the irradiation procedure was to obtain a high dose with some sacrifice of dose uniformity, accuracy of dosimetry, and temperature control. The radiation source was a 2 Mev Van de Graaff electron accelerator. The first two

samples (maximum dose  $10^{10}$  rad) were irradiated one at a time using an unfocused beam which after scattering by the window and by air was roughly uniform over the 5/8-inch diameter sample area. For subsequent irradiations, this beam was magnetically swept from side to side rapidly to cover a row of four samples.

Samples were placed on a thick aluminum base plate which was water cooled internally. They were held in place gently by 1/2-mil aluminum foil clamped to the base plate around the edges of the samples. A blast of air at the Al foil cooled the samples from above. In this arrangement, neither the foil nor the surrounding metal were warmed significantly. It was very difficult to measure the temperature of the actual samples during irradiation, but it was presumed that they were thin enough so that they too were not warmed. A serious experimental difficulty in this work was that the samples were too fragile to risk a more firm thermal contact during the irradiation. The small rods irradiated for magnetic properties effects may have suffered higher temperature rises because they were thicker (with respect to beam penetration) and had very poor thermal contact.

The dose rate and its distribution over the sample area were obtained by short irradiations on the same set up of blue cellophane, which has been calibrated and used for this general purpose in our laboratory for several years. Although its accuracy is not better than 5 percent, this method automatically corrects for such factors as backscatter (as long as the samples are thin), and maps the dose distribution conveniently and in detail.

Doses have been given in rads (1) since they were determined by a chemical method and (2) because it was anticipated that damage would be due to ionization primarily. If damage is to be ascribed to direct impact displacements, it is pertinent to give the flux, which corresponds to roughly  $3 \times 10^{17}$  electrons/cm<sup>2</sup> per  $1 \times 10^{10}$  rad.

#### 4.19.2.4 Results

Table 10 is a chronological listing of all the interpretable spectra obtained in this program (exclusive of calibrations) giving the nature of the sample and the parameters of the two six line sets calculated from the line spacings. The alkaline earth hexagonal ferrites are designated by their Westinghouse code numbers, with the exception of the powder which is simply labelled W followed by the binder material. Sintered discs are labelled "or" if oriented and "mag" if magnetized. Irradiated samples are referred to by their original run number and dose. Repeated runs on the same absorber are referred to the original run number. All samples were run with both source and absorber at room temperature unless the absorber temperature is otherwise listed in the notes.

The early runs were made against a stainless steel source; those beyond 499 employed the Cr source. No correction for the source difference was made. To compare center shifts, 0.03 mm/sec should be subtracted from the Cr source values; the other numbers are unchanged. Center shifts were corrected for 2nd order doppler effect when necessary.

Values for Hf computed by equation 76 will not be used in discussing Hf, but were listed in order to indicate, by comparing with Hf (equation 75), how reliable lines 2 and 5 were.

In runs 475 through 507 there was some difficulty in maintaining a constant scale calibration, and a correction factor was applied to the spacings, based on the results of pure iron calibration runs. The agreement of results indicates that in most cases this correction was legitimate, but run 495 gave anomalously low spacings. The trouble seems to have originated when the Zener diode regulated power supply was substituted for batteries in the velocity train. For some reason, the analyzer then became more sensitive to overdrive. Subsequent careful attention to drive amplitude eliminated further scale difficulties.

Figures 71 to 78 illustrate some of the spectra referred to in table 10. In figures 71 and 72, runs 439 and 453, the absorption lines are pointed upward since the reciprocal of the count rate had been calculated then. Despite the normalization procedure in reducing the data, some distortion of the base line appears in a few cases as a result of slight bias shifts and gain changes in the velocity train, plus a greatly expanded vertical scale. Such distortions are gradual and do not interfere with the determination of line position but do contribute to the difficulty of interpreting peak heights quantitatively.

Figure 79 is a plot of the hyperfine fields in the disoriented absorbers of the Westinghouse ferrite as a function of temperature using the data in table 10 from runs 509 to 518.

Table 11 lists the results of the magnetic measurements of the rod samples of Westinghouse hexagonal ferrites which were irradiated. As can be seen, these samples survived the electron bombardment without any significant change. The differences in table 11 are below the experimental error for the measurement.

TABLE 11  
MAGNETIZATION OF SMALL FERRITE RODS  
FOR ELECTRON IRRADIATION

	Control Samples	Irradiated Samples; 10 <sup>11</sup> rad
Magnetized parallel to axis of rod	70.5	70.1
Magnetized perpendicular to axis of rod	69.5	69.4
Average	70.0	69.75



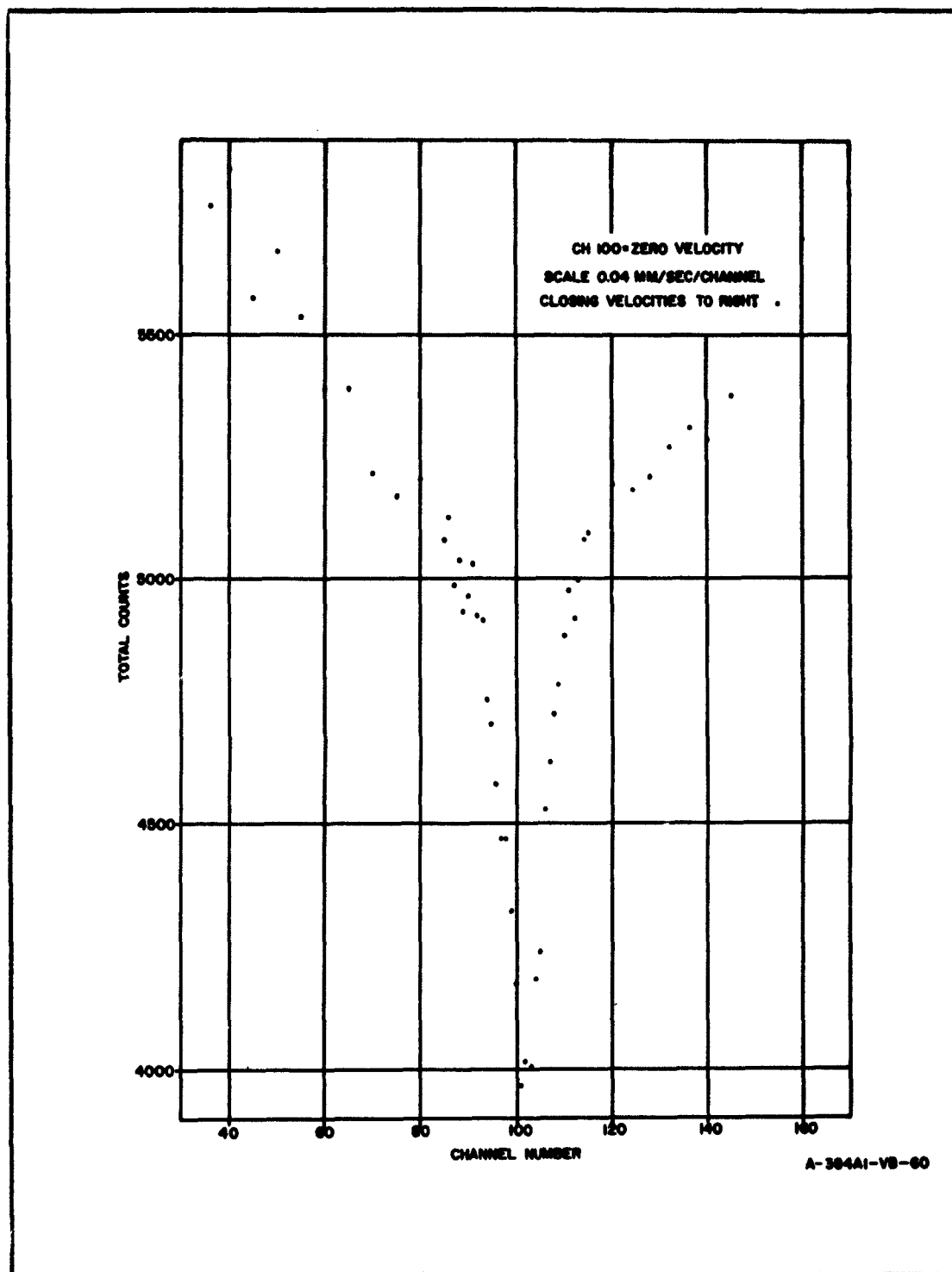


Figure 71. Spectrum of  $K_4Fe^{57}(CN)_6$  With Cr Source

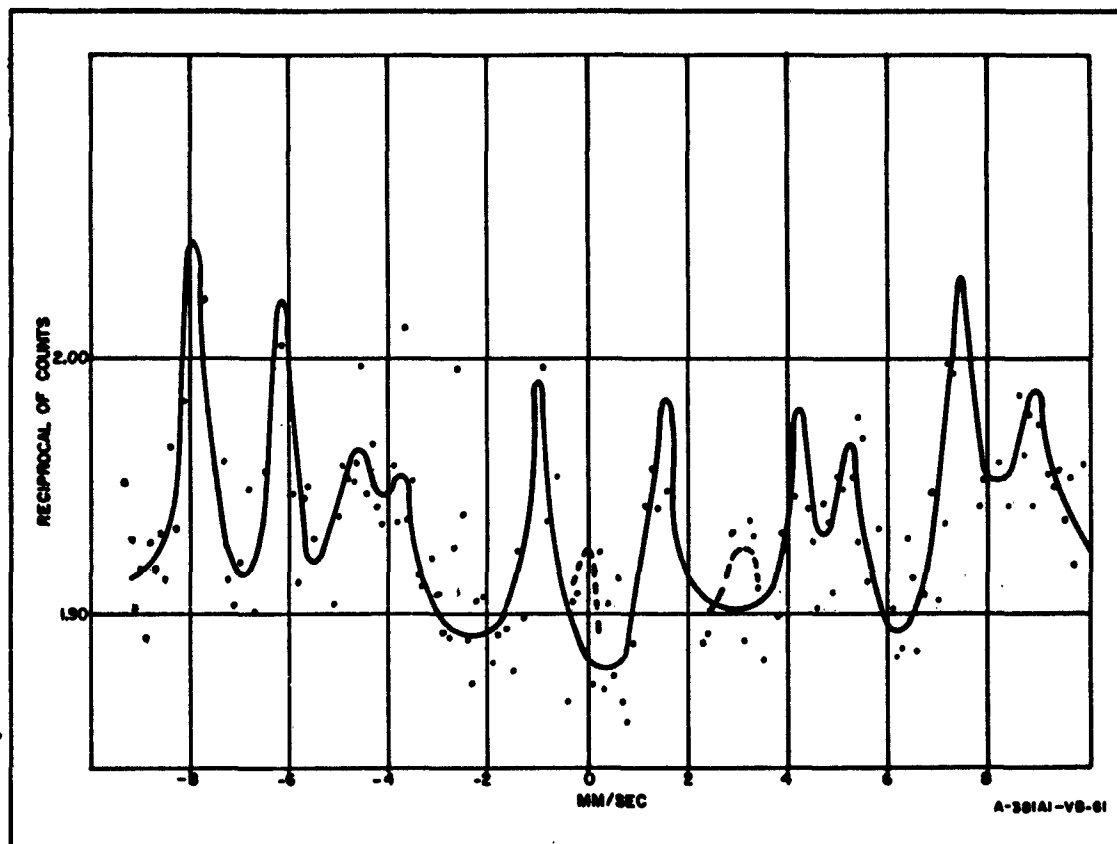


Figure 72. Plot of Mössbauer Spectra, Run 439, BV13

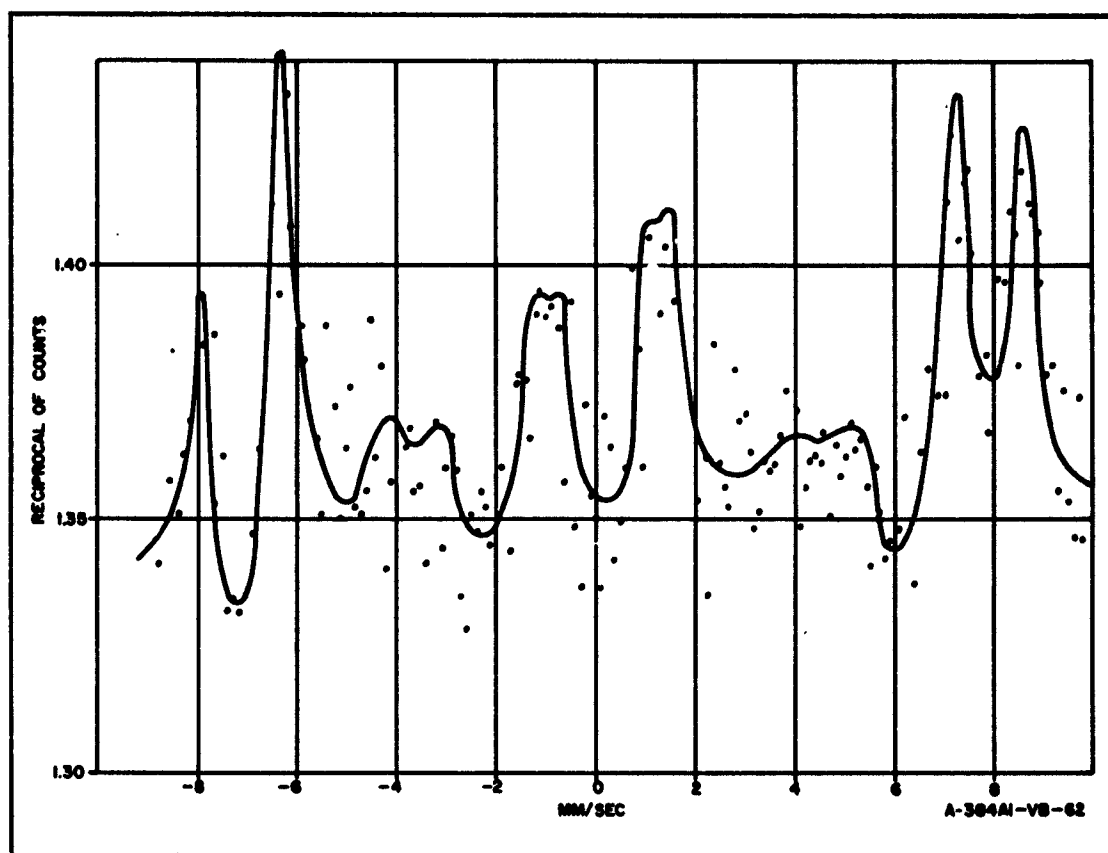


Figure 73. Plot of Mössbauer Spectra,  
Run 447, Indox V Oriented

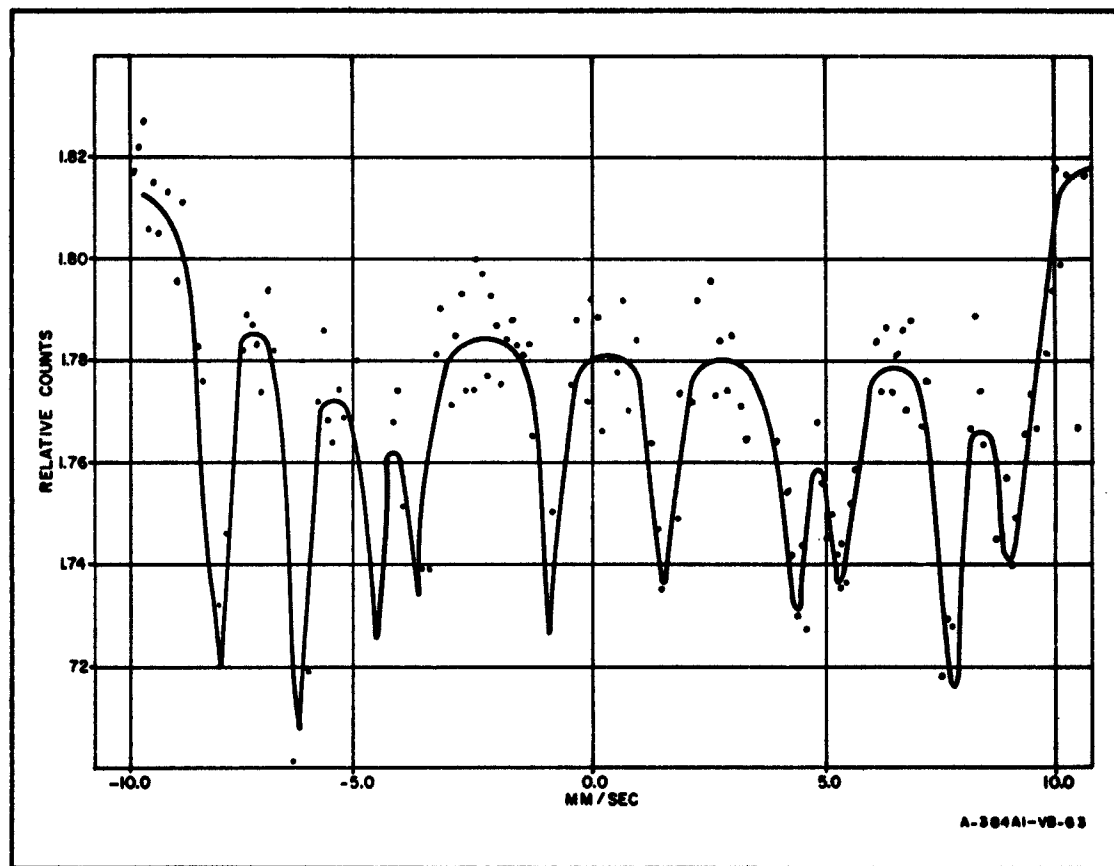


Figure 74. Plot of Mössbauer Spectra, Run 523,  
BV13 After  $10^{11}$  Rad

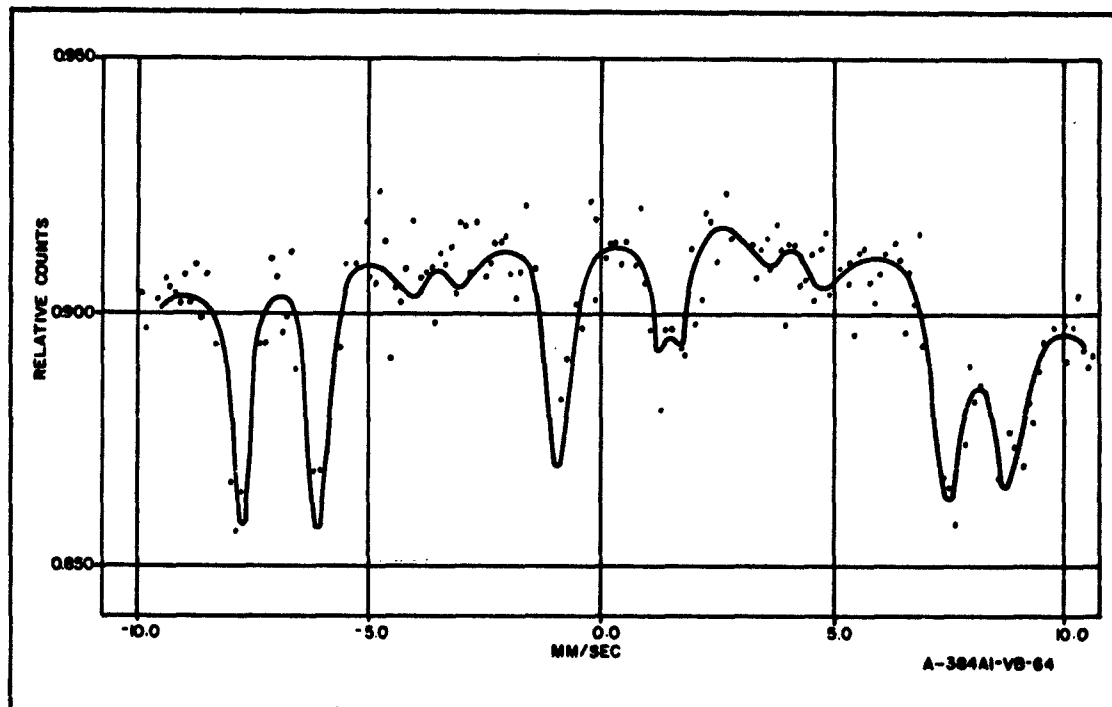


Figure 75. Plot of Mössbauer Spectra, Run 498,  
BV25 Oriented and Magnetized

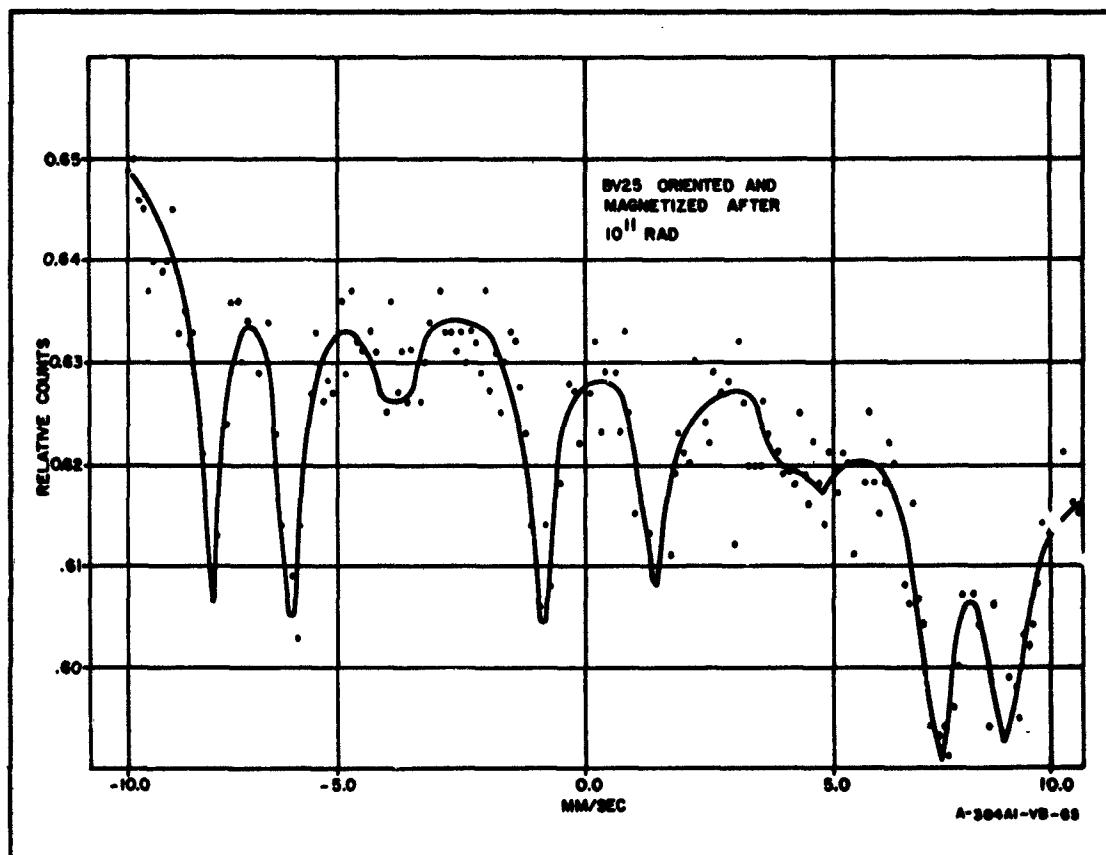


Figure 76. Plot of Mössbauer Spectra, Run 529, BV25  
Oriented and Magnetized, After  $10^{11}$  Rad

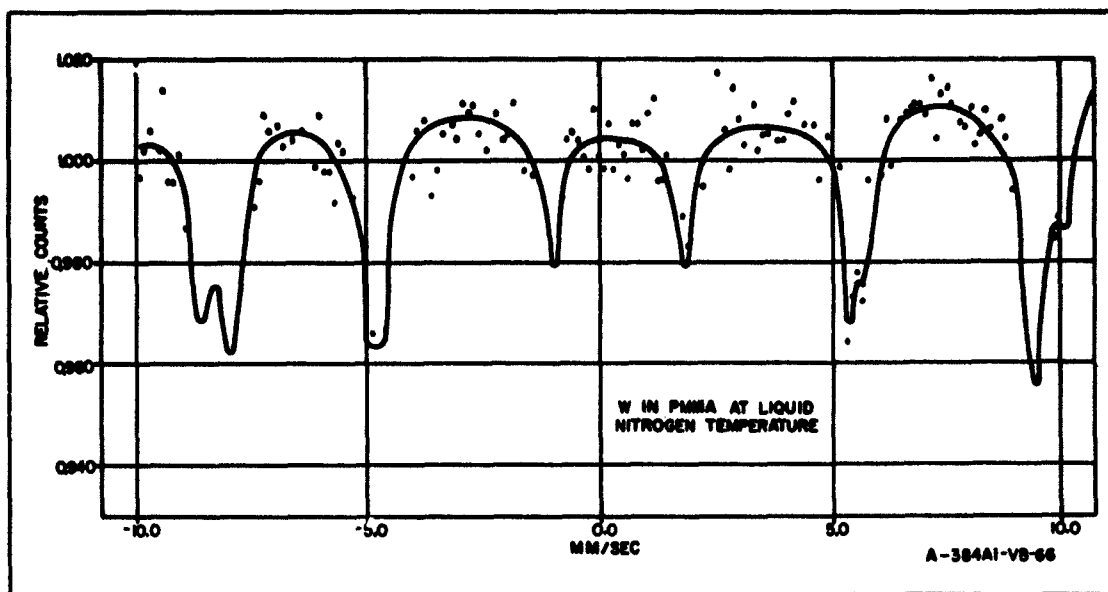


Figure 77. Plot of Mössbauer Spectra, Run 509

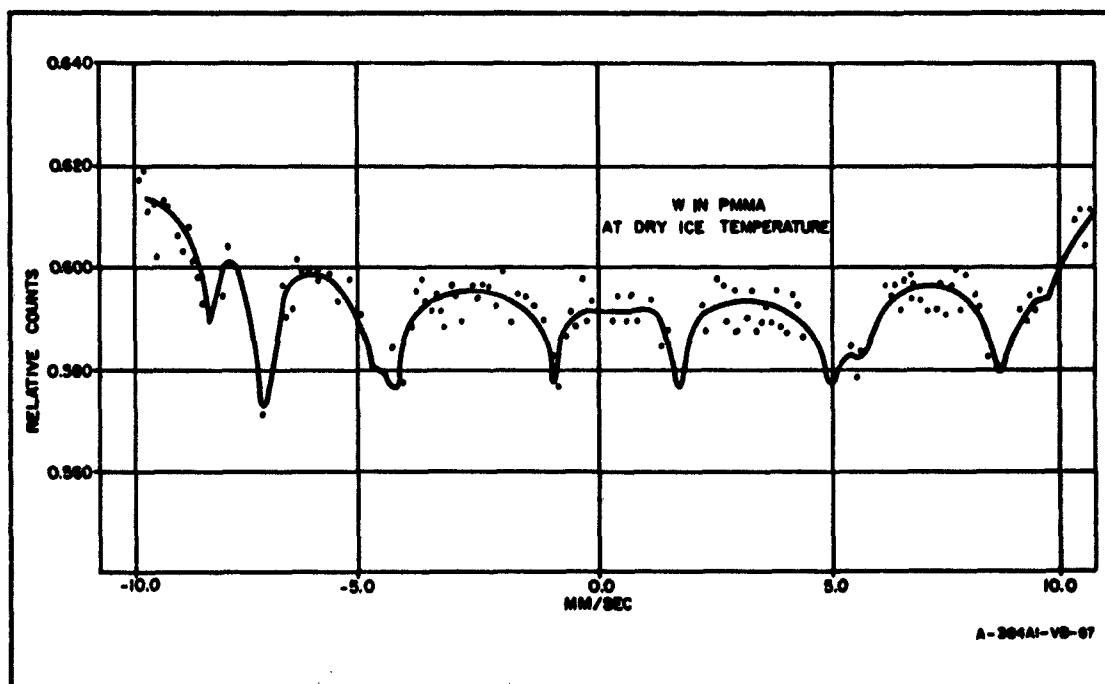


Figure 78. Plot of Mössbauer Spectra, Run 515

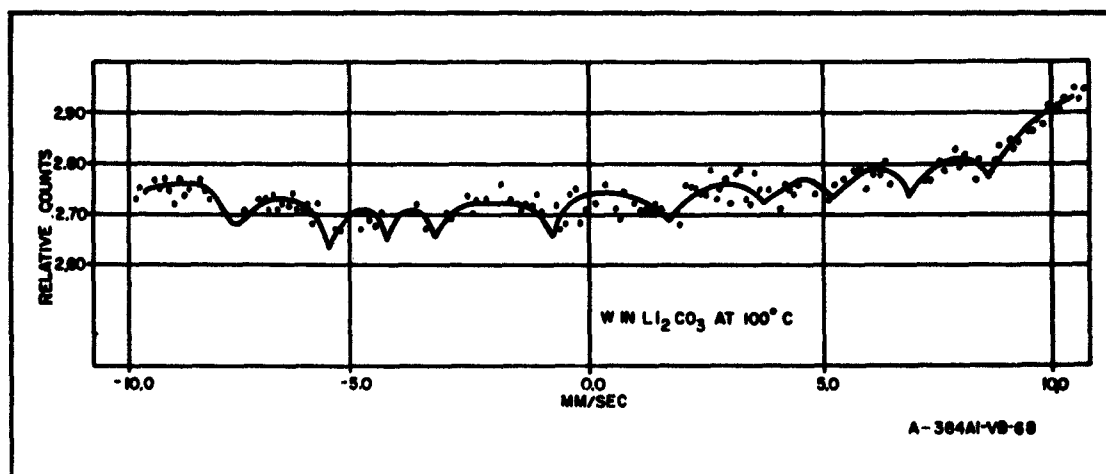


Figure 79. Plot of Mössbauer Spectra, Run 518



#### 4.19.3 Discussion of Results

##### 4.19.3.1 Interpretation of the Spectra of the Hexagonal Ferrites

The compound  $\text{BaO} \cdot 6\text{Fe}_2\text{O}_3$  will be used for purposes of discussion assuming that the Westinghouse samples are qualitatively the same. Before referring to the chemical structure the following general features revealed by the spectra can be listed.

- a. There are two major sets of iron atoms, which we will refer to as (a) and (b), set (a) exhibiting a larger hyperfine field than (b).
- b. These sets share a common magnetic axis as revealed by the equal attenuation in the oriented absorbers of lines 2 and 5 of each set.
- c. Set (b) is slightly more populous than set (a). However, quantitative comparison of peak heights (or areas) is not justified by the data.
- d. Set (b) showed a consistently larger quadrupole interaction  $\epsilon$  than (a), indicating an environment with a greater electric field gradient.
- e. Both sets exhibited center shifts which were typical of ferric ions such as in  $\text{Fe}_2\text{O}_3$ . The apparent slightly larger values for (b) are not necessarily significant because when lines 3 and 4 were not resolvable into two sets the difference in center shifts merely reflects the difference in  $\epsilon$ 's.
- f. Hyperfine fields were roughly of the same magnitudes as reported in previous work on iron oxides and garnets (references 9 and 10).

The limitations of the Mössbauer method must not be forgotten when considering the above features. Very small minority populations may have been ignored because of their low intensity relative to the deviations incurred through counting statistics and electronic errors. Furthermore, although "pure" lines were drawn on the graphs, it is quite likely that each of the two sets is indeed an average of more than one crystallographically distinguishable set of ions (of which indeed there are five altogether).

The above features (a through f) can be seen by examining table 10 and the illustrative spectra in figures 71 through 78. For all the Westinghouse samples at room temperature (20 runs excluding runs 506 and 528),  $\text{Hf(a)} = 502 \pm 10$  (standard deviation) and  $\text{Hf(b)} = 415 \pm 10$  (standard deviation).

For all the indox samples (seven runs excluding numbers 418, 502, 507, and the irradiated samples)  $Hf(a) = 515 \pm 7$  (standard deviation) and  $Hf(b) = 423 \pm 5$  (standard deviation).

The diminution of lines 2 and 5 in an oriented sample is illustrated in figure 72. This orientation effect occurs to about the same extent in the magnetized oriented samples as illustrated in figure 74, the effect of magnetization being merely to make unidirectional the already parallel domain fields.

The relative populations are illustrated well in figure 73 which is an unusually good run with respect to scatter. The height of peak 2a is unexpectedly high but this is attributable to its proximity to 1b.

Average values for the  $\epsilon$ 's taken from table 10 considering all runs on hexagonal ferrites (total of 38 runs) are  $\epsilon_a = 0.084$  (average deviation  $\pm 0.039$ ) and  $\epsilon_b = 0.196$  (average deviation  $\pm 0.040$ ) and in every run but two  $\epsilon_b > \epsilon_a$ .

Similarly the center shift for (a) was 0.410 (average deviation  $\pm 0.055$ ) with respect to stainless steel and for (b) was 0.485 ( $\pm 0.063$  average deviation). Comparable values from the literature (references 7 and 10) are  $0.5 \pm 0.05$  for  $Fe_2O_3$ ;  $0.35 \pm 0.1$  for nickel ferrite,  $0.45 \pm 0.10$  for the octahedral ferric ions in  $Fe_3O_4$ ;  $0.35 \pm 0.10$  and  $0.55 \pm 0.10$  for the two sites in YIG; and  $0.5 \pm 0.1$  and  $0.6 \pm 0.1$  for DYIG (dysprosium yttrium iron garnet). In contrast, the center shift of the ferrous ion hyperfine field in  $Fe_3O_4$  (below the order-disorder transition) was  $1.15 \pm 0.15$ .

Next the Mössbauer pattern must be reconciled with the detailed crystal structure. The compound  $BaO \cdot 6Fe_2O_3$  has the magnetoplumbite structure for which the spin assignments have been discussed by Smit and Wijn (reference 19). The structure is made up of alternate blocks  $SRS^*R^*$  comprising two formula units, S referring to the "spinel block," R to the "hexagonal block," and the asterisk denoting a 180-degree rotation. For purposes of counting and assigning ions, one formula unit (i. e., 12 iron ions) is sufficient. These are distributed as shown in table 12. This assignment of spins and the assumption of 5 Bohr magnetons per ion yields the measured saturation magnetization at very low temperatures.

TABLE 12  
CONFIGURATION AND SPIN DIRECTION OF IRON IONS  
IN THE MAGNETOPLUMBITE STRUCTURE

Number of Ions	Designation*	Coordination to Oxygen	Spin Direction	Block Location
1	2a	Octahedral	(up)	S
1	2b	Five-fold		R
2	4f <sub>1</sub>	Tetrahedral	(down)	S
2	4f <sub>2</sub>	Octahedral		R
6	12k	Octahedral		borderline

\* Notation of Bertaut, et al., (reference 20).

The assignment of these ions to the two sets observed in the Mössbauer spectrum is not clear cut. A first guess could be that all the octahedral ions belong to one set, but that would imply at least a 9:3 population ratio which is inconsistent with the observed spectra. \* Another thought is that perhaps all the upward directed spins belong to one set and the downward spins to the other. In this case, the population ratio of 8 to 4 is a little more credible but is still more lopsided than suggested by the relative intensities of the Mössbauer sets. Another objection is that it would be logical to expect the "2a" ion to display the same hyperfine field as its companions in the S block, the "4f<sub>1</sub>" ions, (i. e., join the downward rather than upward set) because in Fe<sub>3</sub>O<sub>4</sub> (at low temperatures) this is the case.

At any rate it is reasonable to expect that the six identical "12k" ions belong to the same set. This must be the more populous (b) set, since the

---

\* It is assumed that the peak heights for the two sets accurately reflect the corresponding populations. This would not be so if the two sets had different *f* values (*f* = resonant fraction), a situation which is conceivable for different lattice sites. However, the percent effect for both sets is qualitatively as high at room temperature as it is at very low temperatures. This very slight temperature dependence of the *f*'s must mean that they are both close enough to unity so that our initial assumption is valid.

"12k's" already constitute half the possible Mössbauer ions. Additional reasons for assigning the "12k" ions to set (b) arise from their unusual environment, being located symmetrically with respect to the barium ion and along the interblock border. The dissymmetry in this environment would account for the larger value of  $\epsilon$  exhibited by the (b) set. Furthermore this environment may also be responsible for the rather sensitive temperature dependence (see below) of Hf of this set. In  $\text{Fe}_3\text{O}_4$ , Hf of the truly octahedral FeIII ions (analogous to our "2a's") changed very little between room temperature and liquid nitrogen (reference 7).

Accordingly, tentatively identified is set (a) as the "4f<sub>1</sub>'s, " "4f<sub>2</sub>'s, " and "2a's, " a total of five ions; and set (b) as the six "12k's. " Temporarily it is questioned as to whether the "2b" belongs to either set.

#### 4.19.3.2 Variation of Hf's With Temperature

In principle, a knowledge of the variation of hyperfine fields with temperature plus the saturation magnetization curve should help one decide on the identities of the sets.

From the data in table 10 the curves of figure 79 are drawn showing how the two fields in the Westinghouse ferrite vary with temperature. (The two low points at 195°K are both from run 511.) In drawing the curves, the portions below 80°K were extrapolated rather freely. It was tempting to draw Hf(b) as shown by the dotted curve which is a linear extrapolation of the data and also intercepts 0°K at about the same value as Hf(a). Since the magnetization per ion is known to be the same for all 12 ions at 0°K, we would expect the Hf's to be the same if the proportionality factor were the same for both sets. However, the dotted curve is used to construct the saturation magnetization ( $\sigma$ ) curve (as described below) it is not possible using any combination of ions for each set to duplicate the flat characteristic of  $\sigma$  near 0°K. (See figure 80.) This is only possible if the Hf curves are parallel. Accordingly, in the absence of any lower temperature data, both curves were drawn flat as shown. This also implies that the proportionality

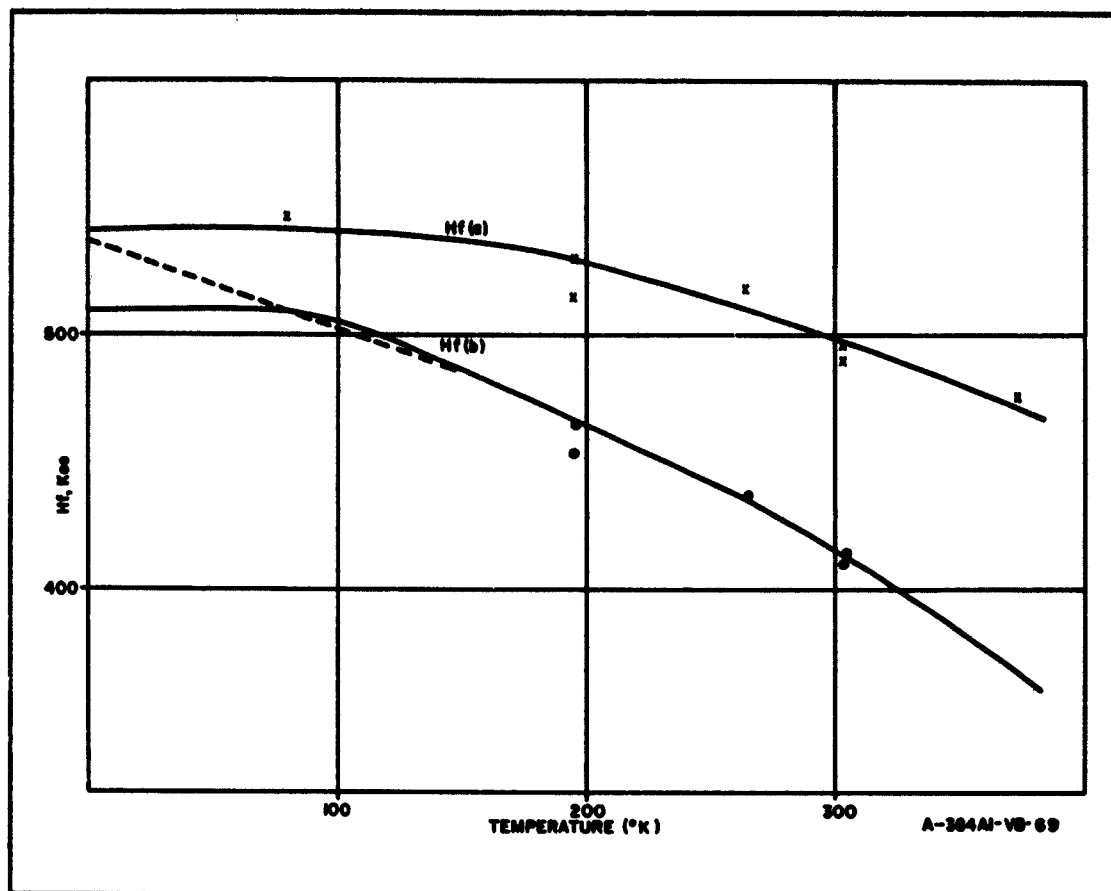


Figure 80. Variation of Hf With Temperature, Westinghouse Hexagonal Ferrite

factor is not the same for the two fields. Bauminger, et al., (reference 6) came to this same conclusion regarding the garnets. An extension of the data to lower temperatures is still required to prove this point.

A curve of saturation magnetization for  $\text{BaO} \cdot 6\text{Fe}_2\text{O}_3$  is given by Smit and Wijn (reference 19) (their figure 38.2), and it is expected that a similar curve for the Westinghouse material would be nearly identical. This curve is reproduced as the solid line in figure 81.

Using the curves of figure 79 one can now calculate  $\sigma$  values (normalized to the 0°K value) for comparison to figure 81, based on the various probable assignments of ions to sets as follows:

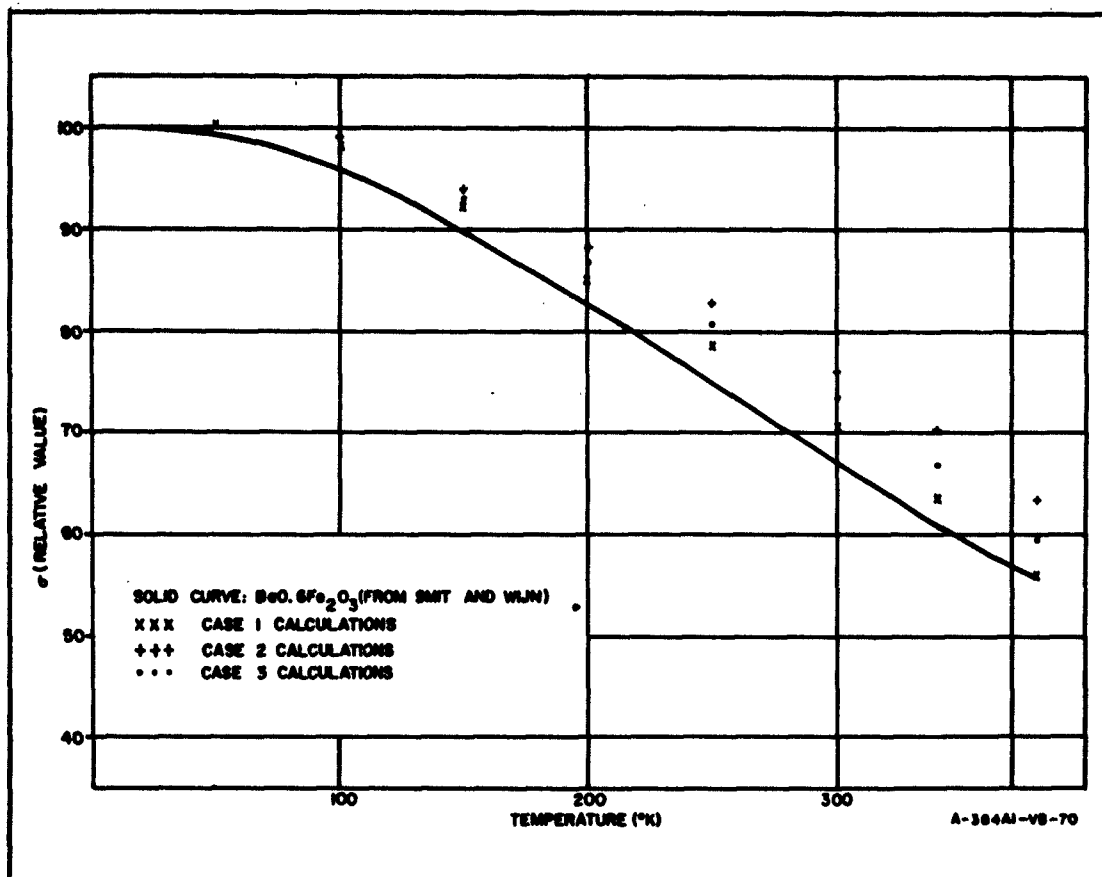


Figure 81. Variation of Saturation Magnetization With Temperature

Case 1: Assume set (b) comprises all the upward spins and set (a) all the downward spins. Then  $\sigma \approx 8Hf(b) - 4Hf(a) \left( \frac{509}{542} \right)$  where the ratio of Hf's at 0°K has been inserted to account for the difference in proportionality factors for (a) and (b). The results are shown by x's on figure 81.

Case 2: Assume set (b) comprises the six spin-up "12k" ions and set (a) all the spin-down ions plus the spin-up "2a" ion as concluded in the previous section. Whether or not the "2b" ion contributes to the observed Mössbauer sets, it does contribute to the magnetization and has some temperature characteristic which we can only guess at. If this temperature characteristic is very different than (a) or (b) the case cannot be treated but the calculation

can be continued on the assumption that either it follows set (a) or it follows set (b). Consider as Case 2 the assumption that it follows (a); whereupon  $\sigma \approx 6Hf(b) - 4Hf(a) \left( \frac{509}{542} \right) + 2Hf(a) \left( \frac{509}{542} \right)$ . The results are shown by +'s in figure 81.

Case 3: This is like Case 2 except that the second assumption is made, i. e., that the magnetization of the "2b" ion varies as  $Hf(b)$ . In this case  $\sigma \approx 7Hf(b) - 4Hf(a) \left( \frac{509}{542} \right) + Hf(a) \left( \frac{509}{542} \right)$ . The results of all between those of Cases 1 and 2 are shown by solid dots on figure 81.

According to figure 81, Case 1 provides the best match. (The discrepancy near 0°K is not serious in view of the arbitrary drawing of figure 79. It is more significant that the x's follow the trend of the solid line.) Furthermore the assignment of any up-spin ion to set (a), (which reduces the contribution of  $Hf(a)$  to the calculation) can only make the case worse.

From the above attempts to match the  $\sigma$  curve, we should change our earlier assumption and conclude that set (a) contains only the four down-spin ions. The fact that set (b) does not appear by comparison to contain eight ions at room temperature could be due to a very large temperature effect for one or two of these eight, most likely the "2b" ion. It is significant that at low temperatures the relative intensity of the (b) lines is much greater (see figures 76 and 77) than at room temperature. If indeed there were one ion in the majority set whose magnetization were fast approaching zero around room temperature, this would explain the noticeable inflection in the  $\sigma$  curve in this region. Also there were suggestions in some runs (see notes in table 10 and figure 71) of an absorption at -2.4, +0.1, and +2.9 which may have been due to an ion with a very small  $Hf$ . If the possibility of a majority set ion is admitted with a very large temperature effect, then the calculations of figure 81 are no longer conclusive in deciding whether the "2a" ion belongs to set (a) or (b).

In summary, regarding the ion assignments, the following situation has been attained. For the most part, set (b) comprises the six "12k" ions and set (a) the four down-spin ions. If in attempting to balance the populations,

the two remaining ions are assigned to (a) or one ion to each, as sharp a drop is not expected in  $\sigma$  versus temperature as is observed. On the other hand, it may be that the sharp drop in  $\sigma$  is the result of one ion (let us say "2b") which appears with set (b) at low temperatures and then drops rapidly in magnetization. This suggestion helps balance the populations at room temperature. Also admission of this suggestion means that it is no longer needed to exclude the "2a" ion from set (a) on the basis of the temperature data.

The above difficulties could be resolved by obtaining more precise Mössbauer spectra from which could be obtained either (or both) more accurate values for the relative populations or more definite evidence for another ion set and its Hf versus temperature.

#### 4.19.3.3 Spectra of YIG

The spectra of the garnets resemble roughly those of the hexagonal ferrites. Bauminger et al. (reference 10) obtained similar spectra and assigned to the ion set with the large Hf the octahedral ions and to the set with the smaller Hf, but greater intensity, the tetrahedral ions which are  $3/2$  as numerous as the octahedral ions. Bauminger et al. used the term "d" set rather than the Westinghouse "b" set and found a temperature dependence for both Hf's similar to the Westinghouse Hexagonal ferrite results, except that the difference between (a) and (b) in the garnet at liquid nitrogen was much greater than in the ferrites.

For the center shifts, Bauminger found  $0.55 \pm 0.10$  for the (a) set and  $0.35 \pm 0.10$  for the (b) set which agrees with the Westinghouse run 527. Westinghouse found also in agreement that (a) is consistently shifted more than (b), except for the early run 403. Bauminger speculated that the smaller shift, which is correctly interpreted as an indication of covalency, might be correlated to the smaller Hf, but Westinghouse results on the hexagonal ferrites are contrary to this.

Bauminger's work indicated little or no quadrupole interaction; Westinghouse's average values for  $e$  were 0.060 for (a) and  $\sim 0.001$  for (b). Wertheim (reference 8) points out that considering the various angles of the



symmetry axis of the electric field gradient tensor there are no less than seven nonequivalent sites. Wertheim studied YIG as a single crystal in a magnetic field arranged in such a direction as to reduce the number of equivalent sites to three, and under these circumstances, found appreciable values for  $\epsilon$ , indicating that in the powder studies the quadrupole interaction has been averaged out.

The Westinghouse average values for Hf were  $489 \pm 12$  for (a) and  $400 \pm 4$  for (b) compared to Bauminger's values of  $485 \pm 15$  and  $390 \pm 10$  respectively, and Wertheim's values of  $474 \pm 7$  and  $392 \pm 5$  respectively. This agreement with Wertheim's work seems to indicate that proper values for Hf are obtainable from the powder study, despite the averaging of several strictly nonequivalent sites into one Mössbauer set.

#### 4.19.3.4 Comparison of Westinghouse and Indox Materials

The data accumulated in this study also made it possible to seek out differences in chemical structure between the two hexagonal ferrites which contained different divalent ions. Both hyperfine fields, as pointed out earlier, were slightly larger in Indox although the probable ranges overlapped. These differences, both in the same direction, would not reflect on the net magnetization, which is indeed not significantly different. If real, the differences may reflect a lesser temperature effect in Indox, or possibly just a difference in proportionality factor between  $\sigma$  (ion) and Hf.

No systematic differences in  $\epsilon$ 's between the two ferrites were evident. However, the probable ranges for  $\epsilon$  were large and obscured small differences. The same can be said for the center shifts. It is conceivable that the change in divalent ion might have affected the  $\epsilon$  and center shift of the "b" set particularly because of the arrangement of the "12k" ions around the divalent ion.

Both Indox and Westinghouse materials displayed qualitatively similar orientation effects.

#### 4.19.3.5 Radiation Effects

The spectra of the irradiated samples, on visual inspection, very closely resembled those of the unirradiated samples. Figures 74 and 75 provide a comparison for an oriented (and, incidentally, magnetized) sample, and figures 71 and 73 a similar comparison for a nonoriented sample. Both figures 73 and 75 are for the high radiation dose. In seeking evidence for radiation changes, the following visual features should be observed.

In oriented samples, any increase in the intensities of lines 2 and 5 could be interpreted as a rotation of the axis of easy magnetization. In these samples also, the growth of new lines could be readily observed in the "empty" regions of the spectrum. New lines would imply the formation of new "kinds" of iron. Any reduction to ferrous ion would result in peaks at about 0 and 3.00 mm/sec if paramagnetic, or in a six line pattern if ferromagnetic, almost 1 mm/sec to the right of the ferrite patterns.

If changes occurred which were too small to cause new visible patterns they might by mixing with the proper pattern cause apparent changes in the parameters. One may list the difference in parameters before and after irradiation for the 12 absorbers from run 521 to 532. The results are: for Hf(a) a decrease of  $6 \pm 6$  and Hf(b) a decrease of  $7 \pm 9$ . These cannot be considered significant and may be due in part to a slight drift in scale calibration between the start and the end of the work. When compared to runs 510 and 517, which were made about the same time, these high radiations runs averaged very nearly the same Hf's. The increase in average center shift after irradiation was -0.01 for (a) and 0.06 for (b). The decrease in average  $\epsilon$  was 0.032 for (a) and 0.005 for (b). These changes are clearly not significant, especially if one recalls that the velocity scale was 0.10 mm/sec per channel. The data for the irradiated garnet was included in the above since its behavior was the same as the ferrites.

This lack of change in the Mössbauer spectra upon irradiation substantiates the results of the magnetic measurements of the irradiated samples, indicating that there were no significant changes in the composition or chemical structure of the materials.

#### 4.19.4 Significance

The Mössbauer effect is recognized to be one of the most sensitive types of experiments for investigation of the details of the internal structure of materials. It is applicable only to those materials possessing atoms with suitable nuclear moment. To study the failure mechanisms that high energy radiation may introduce into solid state materials, this effect has been used on ferrites of two types, at temperatures from liquid nitrogen to 100°C, and at radiation doses from zero to  $10^{11}$  rads. The result from the Mössbauer studies confirms magnetic measurements that the total irradiation used produces little measurable change in the composition or structure of the materials studied. The results have accomplished the preliminary requirement; namely, of essentially identifying the ion assignments and structure in the ferrites used. Following this, they have shown that (1) any change in the electrical properties of the ferrite type studies which may be observed following high energy electron irradiation up to  $10^{11}$  rads must be caused by other than gross structural changes in the material, (2) further experimental work should be undertaken with more precise spectra and better resolution to seek additional effects such as whether an ion with a small Hf exists at room temperature before or after irradiation, and (3) heavy particle irradiation measurements (e.g., proton bombardment) should be made to enhance the gross structural damage which can occur to the ferrite structure.

#### 4.20 HIGH ENERGY RADIATION INDUCED FAILURE IN THE SOLID STATE: ELECTRON DAMAGE TO CAPACITANCE AND PARTICLE DETECTION CAPABILITY OF SI DIODES

Multiple measurements were made on five pairs of charged-particle-counting Si diodes of various resistivities, both p-type and n-type, as a function of irradiation with 2 Mev electrons. To identify and study the failure mechanisms, the most sensitive property available was studied; namely, the capacitance of the diode. It is known that the capacitance is not only sensitive to radiation but its change with radiation does not agree with existing solid state theory.

In an "abrupt" p-n junction the capacitance varies with bias voltage as  $C \approx \sqrt{n/(V + V_b)}$ , where  $n$  is the concentration of free charge carriers and  $V_b$  the barrier potential. Although  $n$  is known to decrease during neutron and charged particle bombardment, recent fast neutron damage experiments have shown the capacitance of Si diodes to increase during irradiation.

The diode capacitances were measured as functions of bias voltage, by two independent methods, at intervals during the irradiation. The n-type base diodes failed mechanically after a dosage of less than  $4 \times 10^{14}$  electrons/cm<sup>2</sup>. The 10,000 ohm-cm p-type diodes increased about 130 percent in capacitance after exposure to  $4 \times 10^{14}$  electrons/cm<sup>2</sup>. No change was observed in the lower resistivity diodes during this period. Subsequent irradiation to  $7 \times 10^{16}$  electrons/cm<sup>2</sup> produced little change in the magnitude of capacitance in any of the diodes. The relation between capacitance and applied bias did change, the exponent in the relationship  $C \propto (V + V_b)^{-n}$  decreasing from the initial value of 0.5 to about 0.33. Some annealing occurred at room temperature following the bombardment. Changes in counting characteristics are also discussed.

##### 4.20.1 Purpose and Significance

Nuclear radiations are becoming more important as an environmental factor in military and space electronics. Damaging radiation effects have consequently become an integral part of the study of failure of electronic

systems. Of all the components and parts used in electronic systems, diodes and transistors are among the most vulnerable to radiation damage. In Si, the effects of irradiation with various types of nuclear particles (and gamma rays) have been extensively studied, and rather well verified theoretical models are available to describe the operation of diodes and bipolar transistors and to predict their behavior in radiation fields. This useful theoretical structure, however, disagrees greatly with the observed behavior in one area; the change in junction capacitance with exposure to radiation. Change in junction capacitance affects the operation of both diodes and transistors, and is particularly serious in the high resistivity surface junction diodes now finding increasing use as charged particle energy spectrometers.

This report describes a study of the effects of 2 Mev electron irradiation on Si p-n junction particle detectors having several different values of base material resistivity. The study had two purposes: (1) to determine the rate of change of junction capacitance with electron dosage, as an initial step toward understanding the mechanism of capacitance change, and (2) to measure the effects of electron dosage on the operation of Si p-n junction particle detectors.

The intention of the full program of studying radiation-induced capacitance changes is to explain the variation of capacitance with radiation dosage in terms of the otherwise fairly satisfactory theoretical models of radiation damage in simple Si devices. Extension of these theoretical models to include the presently anomalous capacitance changes should make possible the prediction of radiation effects on Si diodes, transistors, and many other types of Si solid state components. To do this will require an understanding of the nature of the defects introduced by radiation of various types and the detailed mechanisms by which they affect junction capacitance. The work reported here was an initial step in this program; the study of capacitance changes as functions of one parameter, the resistivity of the junction base

material, induced by exposure to one type of damaging radiation. These changes were studied in a particular type of diode, the abrupt surface junction diodes used for detection and energy measurement of charged particles and other radiations. This type of junction was appropriate for the study of capacitance changes because the capacitance of an abrupt junction is described by a particularly simple model. Also, the previous instances of anomalous radiation induced capacitance changes were observed in similar devices.

A second motivation for the present study was the need for more knowledge of charged particle damage to Si surface junction particle detectors. These detectors are increasingly used to study energetic charged particle fluxes in space. The rather large incidence of damaging particles in the Van Allen and solar flare radiations can be expected to cause significant permanent damage to Si particle detectors in some space missions. Since energetic electrons are a major constituent of these radiations, the direct observation of the effects of electron irradiation on counting properties was thought to be highly pertinent. Because the particle detecting junctions were of the type most appropriate for the capacitance studies, it was possible to pursue both investigations simultaneously.

#### 4.20.2 Scientific Background to the Measurements

##### 4.20.2.1 Bulk Radiation Effects

In many semiconductor devices, the device characteristics can be interpreted in terms of eight bulk parameters - the concentrations of electrons and holes, the lifetime of excess carriers, the drift mobilities, and the diffusion constants. The important effect of bombardment by energetic charged particles or fast neutrons is to displace atoms from their normal lattice sites, thus creating vacancy-interstitial pairs (Frenkel defects). These defects act as trapping centers to decrease the excess majority carrier concentration, as recombination centers to decrease the minority carrier lifetime, and as scattering centers to reduce the carrier mobilities.

Considerable quantitative knowledge of the rates of decrease of these bulk parameters in Si due to bombardment with various particles has been obtained by Wertheim (references 21, 22, and 23) and by many others (reference 24). The operation of Si abrupt junction diodes is described rather accurately in terms of the above parameters, in the absence of radiation damage, by the Sah-Shockley extension (reference 25) of the Shockley-Read theory (reference 26). Easley (reference 27) and others (reference 28) have shown that the effects of irradiation on the current gain of bipolar transistors can be accurately interpreted in terms of the known rates of change of the bulk parameters. In contrast, recent fast neutron damage experiments on Si junctions, (references 15 and 16) have shown serious departures from the expected behavior of capacitance.

#### 4.20.2.2 Capacitance of Abrupt Junctions

The theory describes the capacitance ( $C$ ) of an abrupt p-n junction in terms of the majority carrier concentration in the base material ( $n$ ) and the applied reverse bias voltage ( $V$ ) as

$$C = Kn^{1/2} (V + V_b)^{-1/2} \quad (77)$$

where  $K$  is a constant and  $V_b$  is the "built-in" barrier voltage (usually about 0.55 volt for high purity Si). If  $C$  is given in pf ( $1 \text{ pf} = 10^{-12} \text{ farad}$ ),  $V$  and  $V_b$  in volts, and  $n$  in  $\text{cm}^{-3}$ , then the constant  $K$  equals  $10^6 A(K_e/8\pi)^{1/2}$ , where  $K$  is the dielectric constant of Si (11.8),  $A$  is the junction area in  $\text{cm}^2$ , and  $e$  is the electronic charge ( $1.6 \times 10^{-19} \text{ coulombs}$ ). Equation 28 has been found to hold for a wide variety of abrupt junctions, including the shallow diffused and surface barrier junctions used for particle detection, in the absence of radiation damage. The term abrupt applies to a junction in which the region over which the net carrier concentration changes from  $p$  to  $n$  is narrow compared to the width of the high field region. The use of equation 28 also implies that the net concentration of acceptor or donor sites in the base region is very small compared to the net concentration in the region of opposite type. Under these conditions, the high field region extends entirely

into the base region, and the origin of equation 28 can be interpreted quite simply. If p-type and n-type Si are brought into perfect contact, a diffusion of electrons and holes across the boundary begins and must continue to equilibrium; i. e., until enough charge has been exchanged to produce an electric field just sufficient to oppose the transfer of further charge. This creates a region with a roughly constant electric field,  $E$ , from which all charge has been removed to the boundaries. If the width of this space charge region is  $d$ , the field, written in rationalized mks units, must be  $E = \sigma/\epsilon = dne/\epsilon$ . The resulting potential difference is  $(V + V_b) = Ed = d^2 ne/\epsilon$ . The capacitance is simply that of a parallel plate capacitor, where  $C = \epsilon A/d$ . Combining these two relations, we have  $C = A (\epsilon ne)^{1/2} (V + V_b)^{-1/2}$ . Rewriting this in the units of equation 28, we have  $C = 10^6 A (K_e/3.6\pi)^{1/2} n^{1/2} (V + V_b)^{-1/2}$ . The difference of about  $2^{1/2}$  in the constant is a consequence of the electric field being not quite constant.

The  $n$  in equation 28 is found to be identical to the excess majority carrier concentration (which we shall call  $n'$ ), which is determined by conductivity or Hall voltage measurements. Fast neutron irradiation and irradiation with most types of charged particles is known to reduce  $n$  at a roughly linear rate, and might consequently be expected to cause  $C$  to decrease. In one experiment at this laboratory (reference 28), the capacitance of a 5000 ohm-cm phosphorous diffused (p-type base) Si surface junction was seen to increase with fast neutron dosage at a roughly constant rate. From the forward voltage drop at the diode,  $n'$  was inferred to have decreased as expected. The author has also observed apparent increases in capacitance due to alpha particle bombardment. Similar increases in the capacitance of 5000 ohm-cm p-type junctions upon irradiation with reactor neutrons have been observed recently by Kramer (reference 30).

The core of the problem is clearly the exact identification of the two charge carrier populations  $n'$  and  $n$ . Conductivity measurements give the sum over all types of movable charge of the charge concentrations multiplied by their respective drift mobilities. Since only electrons and holes have



large mobilities, conductivity measurements indicate only electron and hole populations; i. e.,  $n'$  is the concentration of free electrons and holes. Capacitance, on the other hand, is affected by any charge that can be separated by the junction field, even though the separation takes place very slowly. Thus, the population  $n$  might also include charged defect sites with low mobilities, as well as electrons and holes from deep-lying defect sites which are normally un-ionized. Apparently such additional defect sites are not important in unirradiated Si, but become more prevalent with irradiation. Thus, the thorough examination of defect sites introduced by irradiation becomes a direct approach to the understanding of the anomalous capacitance changes. Many of the low-lying defect sites may be ionized or un-ionized, depending on the Fermi level in the Si. For this reason, a variation of the Fermi level, accomplished by studies of diodes of different base material resistivities, was selected as the first phase of investigation. Later studies will investigate the nature of the defect levels in bulk Si by the more direct methods customarily employed.

#### 4. 20. 2. 3 Counting Characteristics of Particle Detectors

The use of high resistivity Si surface p-n junctions for the measurement of charged particle (references 31 and 32) and neutron (reference 33) fluxes has expanded greatly in recent years. The mechanism of counting and energy measurement is thoroughly treated in the literature cited above. Briefly, as an energetic charged particle traverses the high field region of a Si junction, it ionizes a number of electron-hole (e-h) pairs, equal to  $E/p$ , where  $E$  is the energy lost by the particle in traversing the high field region, in electron volts (ev), and  $p$  is the average energy required for ionization, 3.5 ev in Si. The e-h pairs are separated by the junction field, and collected at the contacts in a time usually of the order of  $10^{-8}$  second. This charge can be treated in several ways to provide a pulse output which is accurately proportional to the energy lost by the energetic particle. If the minority carrier lifetime is not long compared to the collection time, some of the pulse energy will be lost due to recombination. Detectors are normally operated under

relatively high applied reverse bias voltages in order to widen the high field region and to reduce the junction capacitance. Parameters important to the proper operation of such detectors are junction capacitance, reverse leakage current, noise level, thickness of dead layer, and charge collection efficiency. The term dead layer represents the thin, heavily doped surface region in which the carrier lifetime and the field strength are so low that no charge can be collected. Consequently, a particular type of particle will lose a characteristic amount of energy in entering the detector which is not included in the output signal. The charge collection efficiency is the fraction of charge which is collected from the high field region before undergoing recombination. In good Si detectors, it closely approaches unity.

The available information on radiation damage to the counting properties of Si particle detectors is rather scanty. The studies by Westinghouse and by Kramer of fast neutron damage effects in 5000 ohm-cm detectors have shown increases in diode capacitances, leakage currents, and pulse rise times to ensue at integrated fluxes of about  $10^{12}$  nvt. Kramer also observed pronounced degradations of pulse height resolution. Klingensmith (reference 34) observed that the response of Au-Si surface barrier (n-type base) detectors to monoenergetic  $\alpha$  particles began to deteriorate after exposure to roughly  $10^{12}$  nvt fission neutrons. He observed a broad secondary peak in the lower portion of the pulse height distribution which contained progressively more counts until it eventually replaced the original peak. Other workers have found rather erratic changes of capacitance and pulse height resolution in Au-Si surface barrier detectors (reference 35).

#### 4. 20. 3 Irradiation and Measurement

##### 4. 20. 3. 1 General Description of Experiment

Ten detectors were simultaneously irradiated with 2 Mev electrons at flux rates varying from  $5 \times 10^{10}$  to  $5 \times 10^{11}$  electrons/cm<sup>2</sup>-sec. The detectors were mounted in a linear array within a sealed target chamber, (figure 82), which contained pure He gas maintained at a pressure five to nine mm of Hg greater than ambient. The electron beam was magnetically swept along the



**Figure 82. View of Target Box Following Irradiation,  
Showing Swollen Surface Barrier Detectors**

detector array 100 times per second, entering the target chamber through a 5-mil Dural window. The maximum detector temperature was monitored by mounting an eleventh detector, equipped with a thermocouple, at the position of maximum average beam intensity. This detector was physically identical to the neighboring units mounted in high flux positions. The highest temperature recorded was 42°C.

Integrated electron flux density was determined in two ways: (1) The flux pattern was mapped with a chemical dosimeter (du Pont MCS-300 light blue cellophane), (reference 34), and the total beam current was collected and integrated. The relative flux densities obtained from the cellophane measurements were normalized by reference to the integrated beam current. Since no suppression potentials were used, and the geometry was not simple, the current measurements were probably between zero and 40 percent low because of electron backscatter. (2) The cellophane measurements were interpreted directly in terms of the energy absorbed per unit volume (Rad), to an accuracy of about 20 percent, then converted to electron dosage with

an overall uncertainty of perhaps 40 percent. The two methods of normalization agreed well within the expected error limits. Relative dosages between different detectors were uncertain to about 15 percent.

The irradiation was interrupted at intervals and measurements taken in situ. The characteristics measured were:

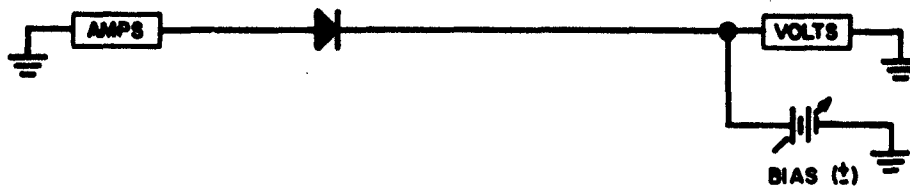
- a. Variation of capacitance with applied bias voltage, by division of known voltage pulses between a reference capacitor and the unknown capacitance.
- b. Variation of  $\alpha$ -particle pulse heights with bias voltage, observed with a charge sensitive amplification system (CSA). The alpha particles were derived from a thin film of U-234, electroplated on Pt foil.
- c. Variation of  $\alpha$  pulse heights with bias voltage, observed with a voltage sensitive amplification system (VSA).
- d. Current-voltage (I-V) characteristics.

The CSA measurements indicated the charge collection efficiencies as functions of bias voltage. With the amount of charge collected from incident monoenergetic  $\alpha$  particles ( $Q$ ) known, the VSA measurements provided independent estimates of the detector capacitances ( $C$ ), because the voltage pulse generated must be proportional to  $Q/(C + C_g)$ , (where  $C_g$  represents the total shunt capacitance of the circuit). Overall pulse height resolutions were also determined from the CSA measurements. The effects of angular separation of the U-234 sources and the detectors, and the lengths of the  $\alpha$  particle paths through the He gas, represented a considerable portion of the observed resolution width in some cases. Pulse rise and decay times were observed in all cases in order to estimate their influence on the observed pulse heights.

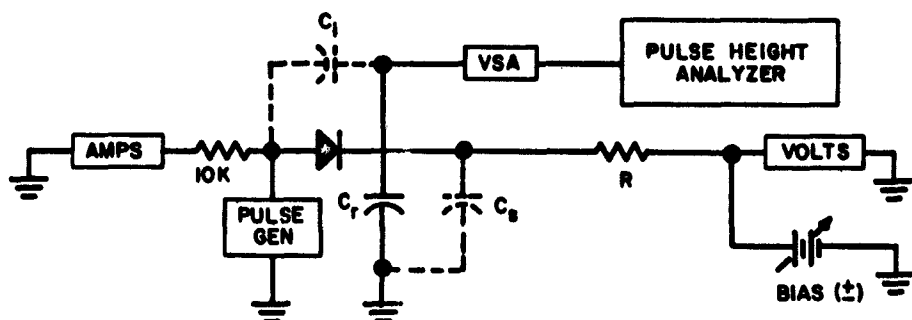
#### 4.20.3.2 Measurement Circuits

Figure 83 is a simplified sketch of the measurement circuits intended to show the separate functions clearly. The equipment actually used consisted of the single complicated circuit shown in figure 84. Except for the readout instruments, pulse generators, and pulse amplifiers, the circuitry of

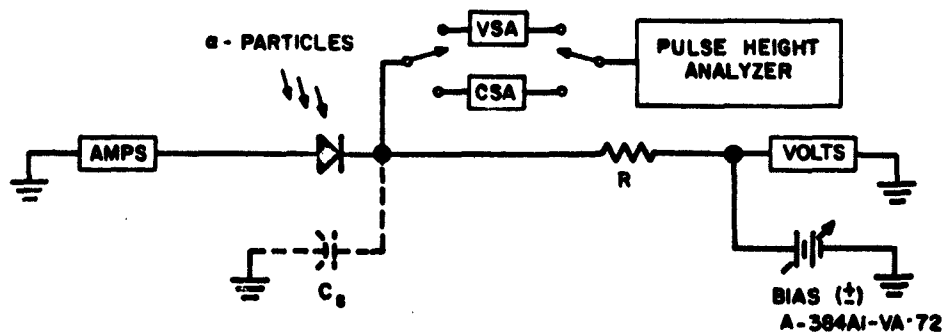
### A. CURRENT-VOLTAGE CHARACTERISTICS



### B. CAPACITANCE BY VOLTAGE PULSE DIVISION



### C. ALPHA PULSE MEASUREMENTS



A-384AI-VA-72

Figure 83. Simplified Sketch of Measurement Circuitry.  
DC Blocking Capacitors, Calibration Inputs,  
and Switching Details Are Omitted.

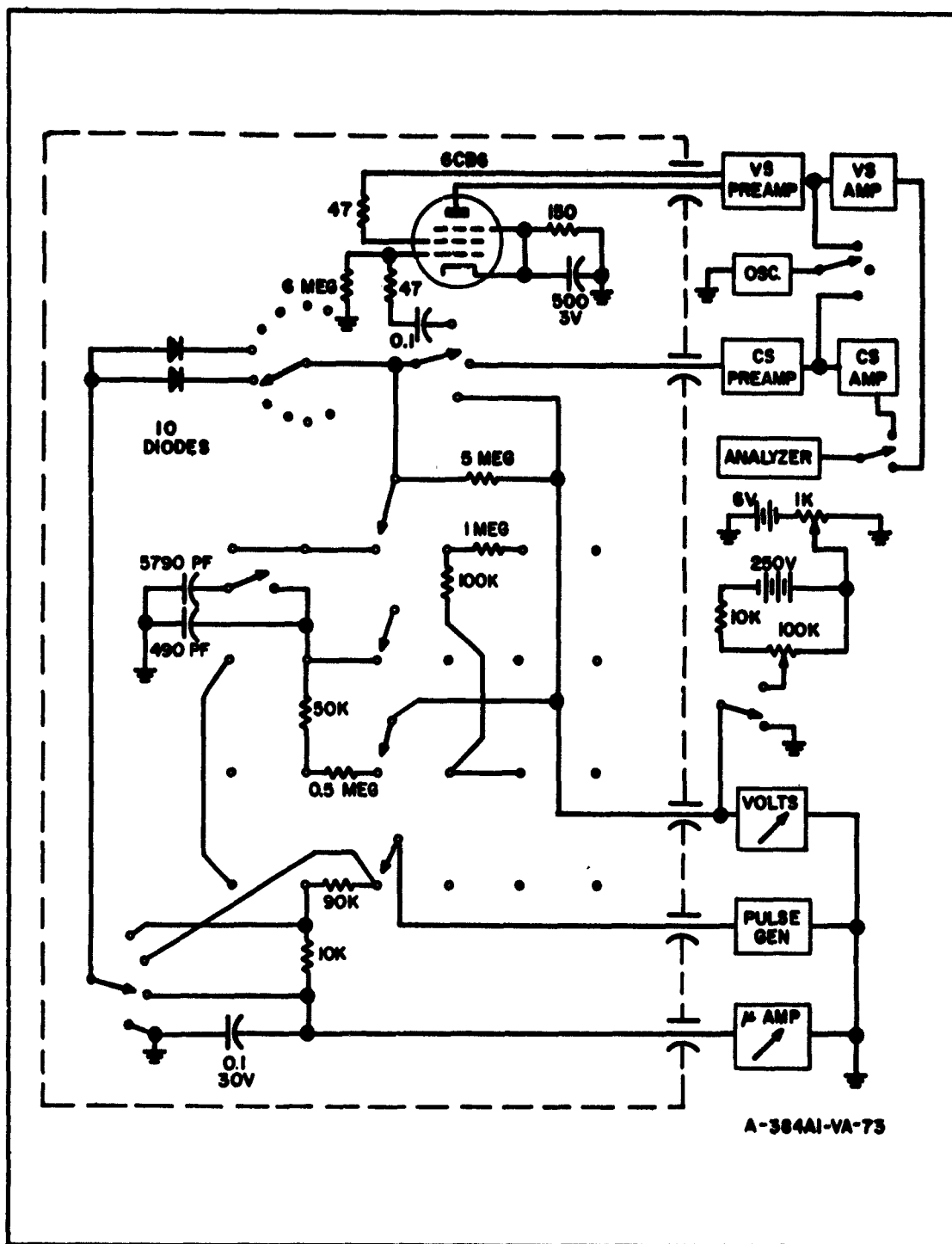


Figure 84. Measurement Circuitry Included in Target Chamber (Dashed Outline)

figure 84 was contained in a chassis box which was positioned in the electron beam of the Van de Graaff and served as a mount for the sample diodes. Combination of the circuitry in the target box, and the careful wide-spaced construction of the circuitry, made possible the relatively low shunt capacitances (referred to below as  $C_s$  and  $C_i$ ) required for accurate pulse measurements. The input stage of the VS preamplifier was also built into the box in order to minimize the input capacitance. Ten detectors were mounted in a linear array on the top surface of the box, at intervals of about 1 cm. The electron beam was swept along this line, providing a nonuniform beam intensity (by a factor of two) which was mapped to define the flux intensity at each detector position. The intensity variation over the area of any particular detector was negligible. The top surface of the box consisted of a 3/8-inch thick Al plate on which the samples were mounted, with a 5-mil Dural foil about 1/2 inch above the samples. He gas was fed into this top space at slightly greater than atmospheric pressure, leaked past the Al plate into the circuitry compartment, and was removed at the bottom while still at about 5 mm of Hg above atmospheric pressure. The Al plate also served to protect the circuitry from the electron beam. Individual U-234  $\alpha$ -particle sources were mounted above each detector at such an angle that they did not shadow the detectors from the electron beam. The detectors were slightly tilted so that the  $\alpha$ -particles were perpendicularly incident on the average, thus minimizing the spread in energy loss in the He gas and the detector dead layers. Source and detector geometries were carefully measured.

Referring again to figure 83, the VSA shown was used for both pulse division and  $\alpha$ -pulse measurements. The complete amplification system had a rise time of 1  $\mu$ sec and a decay, supplied by RC clipping, with a 13- $\mu$ sec time constant. However, since the preamplifier output was unclipped, and rose in less than 0.2  $\mu$ sec, a true representation of the pulse rise and decay times was obtained at the oscilloscope (not shown in figure 83). In both measurements (a and c above), the observed pulse voltage initially increased with a rise time characteristic of the detector, the bias voltage, and  $C_s$ .

In nearly all cases (exceptions are discussed under "results"), this rise time was short ( $< 0.5 \mu\text{sec}$ ) compared to the  $13 \mu\text{sec}$  clipping time, and the maximum pulse height was well represented at the pulse height analyzer. The total shunt capacitance ( $C_s$ ) was measured for each detector position, and ranged from 20 pf to 23 pf. In the pulse division measurements, the relevant shunt capacitance was the interlead capacitance ( $C_i$ ). This was in the range  $6.0 \pm 0.3 \text{ pf}$  for all detector positions. Several alternate values of bias isolation resistance ( $R$ ), ranging from 50 kohms to 5 megohms were available to compensate for the changes in detector resistance resulting from irradiation. Two values of the reference capacitance ( $C_r$ ), 490 pf and 5790 pf, were supplied in order to accommodate the full range of detector capacitances.

The CSA was used in two ways: To measure resolution the double RC clipping at about  $1.5 \mu\text{sec}$ , provided in the preamplifier, was used. This provided the minimum noise level, but underestimated some charge pulse heights because of long detector rise times. To measure the amount of charge collected, the pulse shaping was removed from both the preamplifier and amplifier, resulting in system decay times on the order of  $50 \mu\text{sec}$ . All CS measurements were normalized to the charge pulse generator contained in the ORTEC charge-sensitive amplifier. The charge pulse generator was calibrated from the pre-irradiation  $\alpha$ -pulse heights and the known  $\alpha$ -particle energy, taking into account the energy losses in the source ( $< 10 \text{ Kev}$ ), in the He gas ( $\sim 230 \text{ Kev}$ ), and in the detector dead layers ( $\sim 20 \text{ Kev}$  for the surface barrier detectors,  $\sim 300 \text{ Kev}$  for the diffused junction detectors).

The voltage pulse division method, illustrated by circuit B in figure 83, provided capacitance measurements of greater precision than could be obtained with either the  $\alpha$ -particle pulse height methods or with the several types of impedance bridges which were tried. A quick rising ( $< 0.1 \mu\text{sec}$ ), slow falling ( $> 150 \mu\text{sec}$ ) 60 cps voltage pulse of magnitude  $S_0$  is applied by the pulse generator. This is followed by an immediate rise of the voltage at the amplifier input ( $S$ ) to the value  $S = S_0 C_i / (C_i + C_r + C_s)$ , where  $C_s$  is the capacitance to ground of all wiring directly connected to the preamplifier



input (including the input capacitance of the preamplifier), and  $C_i$  is the interlead capacitance between all wiring directly connected to the pulse generator (the d-c ground for the detector diode) and the wiring connected to the VSA input. The initial rise is followed by a further rise to the value

$$S = S_0 (C + C_i) / (C + C_i + C_r + C_s), \quad (78)$$

during a period given approximately by the rise time of the detector. The total rise time is usually less than  $0.5 \mu\text{sec}$ .  $S$  then falls with a time constant that is roughly the shortest among the three decay times represented by the pulse generator ( $t > 150 \mu\text{sec}$ ), the d-c isolation resistor ( $t \sim R (C_r + C_s)$ ), and the leakage path through the detector ( $t \sim R_d (C_r + C_s)$ ), where  $R_d$  is the inverse resistance of the detector at this applied bias voltage. If this overall decay time and the VSA decay time are both long compared to the detector rise time, equation 78 above will give exactly the maximum pulse height at the amplifier input. This pulse height, times the gain of the VSA, is analyzed and stored in the pulse height analyzer. At intervals, the pulse generator is connected directly to the amplifier input, and the generator output times the VSA gain is stored in the pulse height analyzer. By matching these two outputs at the pulse height analyzer, we treat the amplification system and pulse height analyzer as a null detector and thus measure  $S$  directly. The ratio  $S/S_0$  depends only on the linearity of the attenuating potentiometer on the pulse generator. Since  $C_i$ ,  $C_r$ , and  $C_s$  are all known, the detector capacitance  $C$  is readily calculated from equation 78. This procedure is repeated for each detector at a number of bias voltages during each measurement cycle.

The conditions on signal rise and decay time which apply to equation 78 are roughly the inverse of the maximum and minimum frequencies between which an accurate a-c bridge measurement could be made. The pulse division measurement has the advantage that the maximum pulse corresponds automatically to the optimum frequency for an a-c bridge measurement. Also, the pulse division method is empirically more precise than those

bridge systems the use of which was attempted. Figure 85 shows a comparison of bridge and pulse division methods. An RCA detector of the type of samples 1a and 1b (see below) was measured by both methods, and the resulting capacitances are shown in figure 85 as functions of bias voltage. The observed absolute values are shown to agree quite well, but the scatter in the values obtained by bridge measurement is considerably greater. The slight break in the trend of pulse division value corresponds to a substitution for the voltmeter used to measure bias voltages. The two voltmeters were apparently not well intercalibrated.

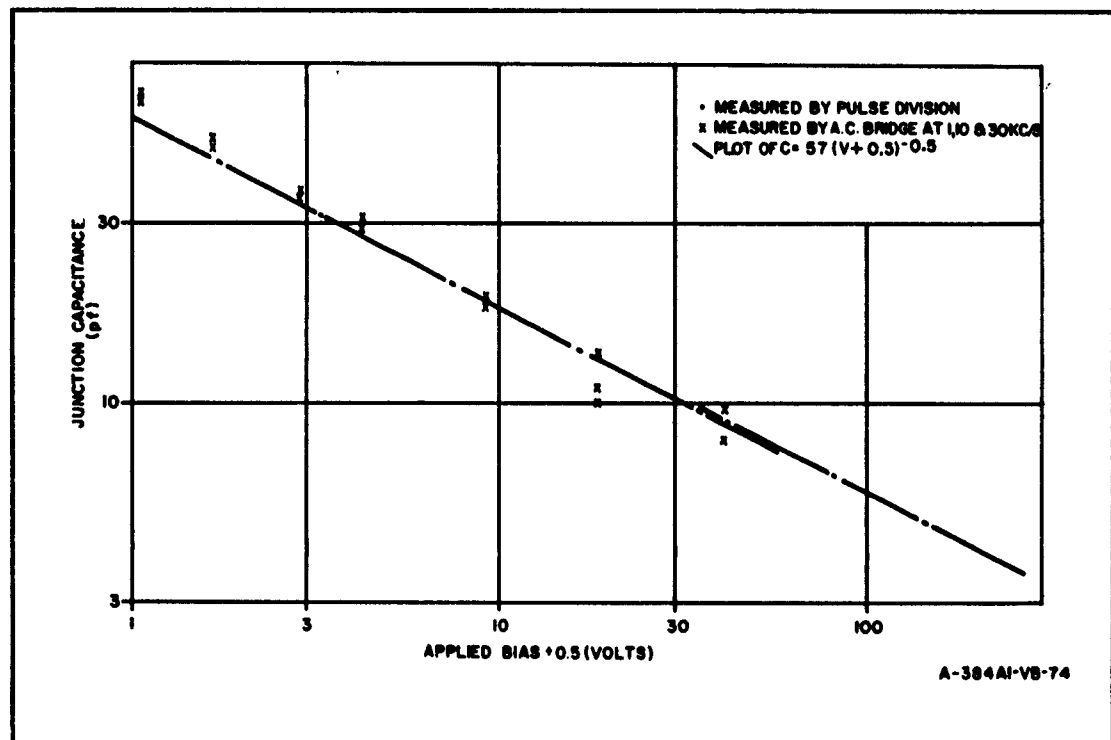


Figure 85. Capacitance vs Bias of Abrupt Junction Si Diode, by Two Methods (Break in Plotted Line Corresponds to the Substitution of One Voltmeter for Another)

A more complete analysis of the pulse division measurements, including the effect of various time constants, is given in paragraph 4.20.6. An equation is derived which may be used, with some labor, to calculate

corrections. Such corrections were estimated for several cases, and found to be minor in most cases.

The measurements of I-V characteristics were quite straightforward, the usual corrections being made for voltage drops and shunt current paths.

#### 4. 20. 3. 3 Sample Detectors

Five pairs of detectors differing in initial base material resistivity were studied. They were:

- a. 1a, 1b RCA (of Canada) type A-4-250-2.0; resistivity nominally 10,000 ohm-cm p-type.
- b. 2a, 2b RCA (of Canada) type A-3-250-2.0; resistivity nominally 1000 ohm-cm p-type.
- c. 3a, 3b RCA (of Canada) type C-2-25-2.0; resistivity nominally 100 ohm-cm p-type.
- d. 4a, 4b ORTEC type 20A-20; resistivity nominally 300 ohm-cm n-type.
- e. 5a, 5b ORTEC type 16B-20; resistivity nominally 3000 ohm-cm n-type.

Each pair of detectors was intended to be identical, and, in fact, the observed characteristics and radiation induced changes were essentially equal for each pair. An eleventh detector (RCA type A-4-250-2.0) was employed in a prior check irradiation, then used as the temperature monitor mentioned previously. The ORTEC detectors had square areas 4 mm on a side. They were Au-Si surface barrier detectors with Au contact layers of 50 to 100  $\mu\text{g}/\text{cm}^2$ , and initial resolutions (full width at half maximum for 5 Mev  $\alpha$ -particles) on the order of 25 Kev. The RCA detectors were p-n junctions with a nominal phosphorus diffusion depth of 2 microns, leading to a "dead layer" of about 300 Kev for 5 Mev  $\alpha$ -particles. The active areas of types A and C are circular, about 5 and 20  $\text{mm}^2$  respectively; the total diode areas are somewhat larger, respectively 14 and 37  $\text{mm}^2$ . The actual resistivities, as indicated by these junction areas and the observed pre-irradiation values of capacitance were quite close to the nominal values, except for detectors 3.

The respective values of resistivity were; 10,000 and 10,100 ohm-cm for detectors 1, 810 and 670 ohm-cm for detectors 2, 130 and 140 ohm-cm for detectors 3, 380 and 400 ohm-cm for detectors 4, and 3500 and 2900 ohm-cm for detectors 5.

#### 4.20.4 Results

##### 4.20.4.1 Surface Barrier Detectors

These samples failed almost immediately because of an unfortunate sensitivity of the supporting structure to electron damage. Consequently, no information was obtained concerning electron irradiation effects on the surface barrier itself. After the first irradiation (an integrated dosage of less than  $4 \times 10^{14}$  electrons/cm<sup>2</sup>), one of the detectors showed no electrical contact and the other three had ceased to operate normally, generating poor quality  $\alpha$ -pulses of nearly full amplitude but opposite polarity. This peculiar counting mechanism is unexplained. At the conclusion of the experiment, the target chamber was opened and the surface barrier detectors were inspected. In these devices, the Au-Si junction is held in a disk of potting compound, which is normally flat. This potting compound now had almost the texture of foamed silica, and had swollen until the former upper surface of the disk formed a hemisphere which had raised the Au-Si disk above its original position sufficiently to destroy the normal electrical contact. A photograph of these detectors, taken just after the irradiation, was shown in figure 82. The top has been removed from the target box and the four swollen detectors can be seen to the right. The degree of swelling is seen to be greater toward the center of the target box, where the beam was more intense.

##### 4.20.4.2 Change in Capacitance of Diffused Junctions

Initially, the capacitance of all 10 detectors varied with bias voltage in the expected way,  $C = B (V + V_b)^{-0.5}$ , where  $V_b$  is taken as 0.55,  $C$  is in pf/cm<sup>2</sup>, and  $B$  is a constant equal to  $Kn^{1/2}/A$  in equation 77. The only exception is that the 100 ohm-cm detectors were best described by an exponent of -0.46 rather than -0.5. For the 1000 ohm-cm and 10,000 ohm-cm

detectors, the two independent measures of capacitance (pulse division and  $\alpha$ -pulse height) were in satisfactory agreement throughout irradiation to a total integrated dosage of about  $2 \times 10^{16}$  electrons/cm<sup>2</sup>. During this period, the  $\alpha$ -pulse measurements on the 100 ohm-cm detectors tended to give capacitance values between 10 and 30 percent lower than those measured by pulse division. From this time until the end of irradiation, capacitance was measured only by the pulse division method. Postirradiation measurement of capacitance via  $\alpha$  pulse heights proved to be quite erratic because of the greatly increased leakage currents and noise levels. The pulse division measurements appeared reliable, although correction for the errors introduced by long rise times and high leakage currents, by means of the relation derived in paragraph 4.20.6, is not yet complete. In particular, the post-irradiation values for the 1000 ohm-cm detectors may require some modification.

Two effects of electron irradiation on detector capacitance were observed: (1) a proportional increase in capacitance at all bias voltages, and (2) a steady increase in the capacitance at high bias relative to the low bias values. The variation of capacitance with bias voltage was at all times adequately described by an equation of the form  $C = B (V + 0.55)^{-m}$ . In these terms, the proportional increase in capacitance is described by increasing the constant B, and the bias-dependent behavior corresponds to a decrease in the exponent m. The former effect (increase in B) occurred only in the 10,000 ohm-cm detectors at the earliest stage of the irradiation. The steady decrease in m was seen in all cases proceeding more rapidly in the higher resistivity detectors. If log C is plotted against log (V + 0.55), this latter effect is seen as a steady rotation with electron dosage of a straight line fitting the observed data. This is illustrated in figure 86, where the capacitance of detector 2A is shown as a function of bias voltage for several levels of electron dosage. The dots indicate pulse division measurements and the open circles indicate values computed from  $\alpha$  pulse heights. The capacitance values in figure 86 at successive electron dosages are increased

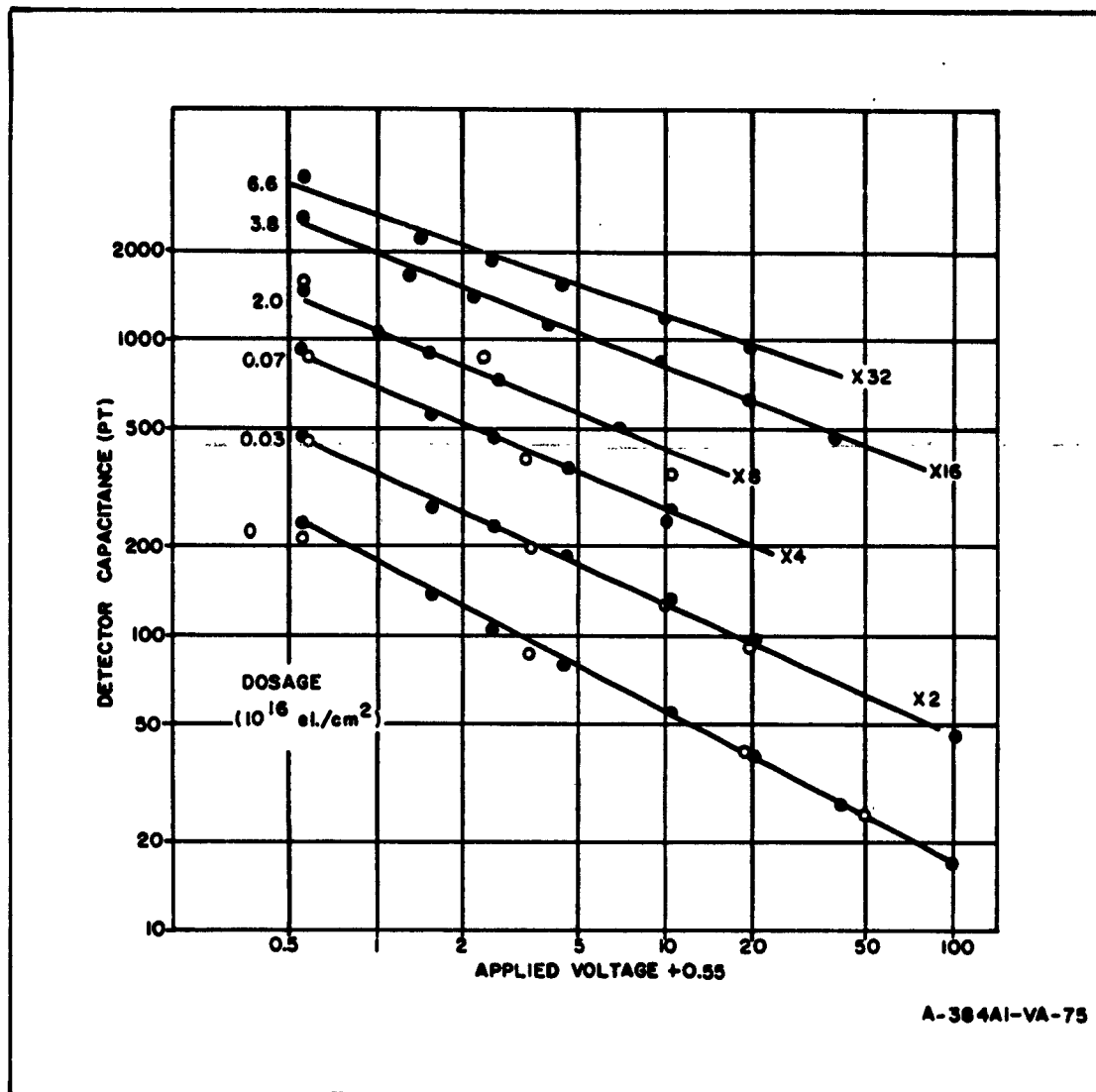


Figure 86. Dependence of Capacitance on Applied Bias at Several Dosages for Detector 2A. The Dots Indicate Pulse Division Measurements; the Open Circles Represent  $\alpha$ -Particle Data. Each Successive Curve Is Shown Displaced Upward by a Factor of 2.

by factors of two to make them legible. The observed capacitance data for all of the detectors is tabulated as values of B and m. Tables 13, 14, and 16 represent, respectively, the 10,000 ohm-cm detectors, the 1000 ohm-cm detectors, and the 100 ohm-cm detectors. The last few entries in table 14,

TABLE 13

CHANGE IN CAPACITANCE VERSUS BIAS VOLTAGE RELATIONSHIP  
 OF 10,000 OHM-CM DETECTORS WITH ELECTRON DOSAGE. B  
 AND m ARE CONSTANTS OF THE EQUATION  
 $C = B (V + 0.55)^{-m}$ , WHERE V IS THE  
 APPLIED BIAS IN VOLTS. (VALUES  
 GIVEN IN PARENTHESIS ARE LESS  
 RELIABLE.)

Sample	Total Electron Dosage ( $10^{16}/\text{cm}^2$ )	Time Since Irradiation (days)	B ( $\text{pf}/\text{cm}^2$ )	-m
1a	0		348	0.50
	0.028		745	0.47
	0.12		775	0.45
	0.35		775	0.41
	1.0		675	0.35
	1.7		655	0.32
	3.2		635	0.27
	5.6	0	570	0.27
	5.6	2	725	0.32
	5.6	15	615	0.27
	5.6	24	635	0.29
	0		323	0.48
	0.025		725	0.45
	0.051		(800)	(0.39)
1b	0.31		(850)	(0.42)
	0.94		585	0.31
	1.5		610	0.28
	2.9		660	0.29
	4.9	0	610	0.23
	4.9	2	860	0.34
	4.9	15	640	0.29
	4.9	24	650	0.23

TABLE 14  
CHANGE IN CAPACITANCE VERSUS BIAS VOLTAGE RELATIONSHIP  
OF 1000 OHM-CM DETECTORS WITH ELECTRON DOSAGE. B  
AND m ARE CONSTANTS OF THE EQUATION  
 $C = B (V + 0.55)^{-m}$ , WHERE V IS THE  
APPLIED BIAS IN VOLTS. (VALUES  
GIVEN IN PARENTHESIS ARE LESS  
RELIABLE.)

Sample	Total Electron Dosage ( $10^{16}/\text{cm}^2$ )	Time Since Irradiation (days)	B ( $\text{pf}/\text{cm}^2$ )	-m
2a	0		1200	0.50
	0.034		1250	0.44
	0.068		1200	0.41
	0.14		1150	0.39
	0.42		980	0.40
	1.2		910	0.40
	2.0		940	0.42
	3.8		840	0.38
	6.6	0	570	0.33
	6.6	2	880	0.40
	6.6	15	990	0.42
	6.6	24	990	0.41
2b	0		1330	0.49
	0.032		1350	0.45
	0.12		1230	0.43
	0.39		1140	0.41
	1.1		900	0.40
	1.9		(870)	(0.39)
	3.6		930	0.38
	6.2	0	690	0.36
	6.2	2	1070	0.44
	6.2	15	930	0.42
	6.2	24	1210	0.41



TABLE 15

CHANGE IN CAPACITANCE VERSUS BIAS VOLTAGE RELATIONSHIP  
OF 100 OHM-CM DETECTORS WITH ELECTRON DOSAGE. B AND  
m ARE CONSTANTS OF THE EQUATION  $C = B (V + 0.55)^{-m}$ ,  
WHERE V IS THE APPLIED BIAS IN VOLTS.

Sample	Total Electron Dosage ( $10^{16}/\text{cm}^2$ )	Time Since Irradiation (days)	B (pf/cm <sup>2</sup> )	-m
3a	0		3000	0.47
	0.038		3000	0.46
	0.076		2900	0.47
	0.15		2900	0.45
	0.50		2950	0.45
	1.4		2700	0.41
	2.3		2900	0.39
	4.3		2950	0.36
	7.4	0	2900	0.33
	7.4	2	3000	0.35
	7.4	15	2950	0.35
	7.4	24	2900	0.33
	7.4	25	2850	0.32
3b	0		2800	0.45
	0.036		3050	0.48
	0.15		2900	0.45
	0.45		2750	0.43
	1.3		2700	0.42
	2.2		2700	0.38
	4.1		2800	0.35
	7.1	0	2850	0.33
	7.1	2	2850	0.33
	7.1	15	2700	0.33
	7.1	24	2850	0.33
	7.1	25	2880	0.33

taken after irradiation, show some evidence of annealing at room temperature. However, since measurements of the capacitance of these 1000 ohm-cm units were very difficult at this point due to excessive leakage currents, these last entries must be regarded with suspicion. No significant degree of annealing is evidenced in tables 13 and 15.

Although the interpretation of these results is difficult without some sophisticated study of the defect sites involved, several striking features can be noticed:

a. No general decrease in capacitance is observed upon exposure to electron dosages sufficient to reduce greatly the conductivity in the base material. This might suggest that the shallow trapping centers introduced into the high field region do not remain filled.

b. The capacitance per unit area of the 10,000 ohm-cm detectors increased quite rapidly, more than doubling during exposure to  $3 \times 10^{-14}$  electrons/cm<sup>2</sup>, then remained relatively stable. Comparison to the constancy of capacitance values in the 100-ohm-cm and 100 ohm-cm detectors during the same irradiation period suggests either that the 10,000 ohm-cm samples had some peculiar material property not accounted for, or that some deep lying defect levels are involved which react in a sensitive manner to the slight changes in Fermi level corresponding to the different doping levels. If the latter is true, more extensive study of the capacitance changes induced by electron irradiation might provide a sensitive method for studying such low-lying defects. Similar study of the effect of resistivity on capacitance changes induced by other damaging radiations might also be rewarding.

The increase in capacitance of the 10,000 ohm-cm samples is notably reminiscent of the increases due to fast neutron irradiation of 5000 ohm-cm phosphorus diffused detectors. However, since the defect sites introduced by the two irradiations are known to differ, it would be surprising if the mechanisms were similar. In this connection, irradiation of lower resistivity detectors with fast neutrons would be particularly interesting.

A possible alternate explanation for bombardment induced increases in capacitance is that charged defect centers might themselves have sufficient mobility to be separated, and consequently the capacitance. Baruch (reference 35) has shown that electron-induced charged defects in Ge p-n junctions can be swept from the high field region by application of moderate reverse biases. If this were also possible in Si, it might account for increases in capacitance during irradiation. However, the absence of the effect in the lower resistivity detectors would be difficult to explain.

#### 4.20.4.3 Changes in Counting Characteristics of Diffused Junctions

The most rapid, and most apparent, effect of electron irradiation was to increase the inverse leakage currents and the amplitude of noise generated by the detectors. Charge collection efficiencies and pulse height resolutions changed more slowly, remaining at useful levels throughout the irradiation. The maximum inverse voltages which could be applied without causing excessive noise generation showed no consistent correlation with electron dosage, but were lower than the pre-irradiation values at all stages of the irradiation.

The effects of electron dosage on some counting characteristics are summarized in table 16. The values observed for the two detectors of a pair with a given nominal resistivity agreed relatively well in all cases. Table 16 shows the observed values for one unit of each pair. The leakage currents of the 10,000 and 1000 ohm-cm detectors are seen to increase erratically by several orders of magnitude. This large scatter results partly from a persistent ionization effect; both forward and reverse currents were unusually high immediately after an irradiation period, and decreased slowly for many hours after the electron beam was extinguished. Thus, their magnitude depended on the measurement schedule. The particularly large leakage currents of the 1000 ohm-cm detector made measurement of pulse heights extremely difficult toward the end of irradiation. These detectors were rendered essentially useless for particle detection.

TABLE 16  
CHANGE IN SOME COUNTING CHARACTERISTICS WITH ELECTRON DOSAGE

Resistivity (ohm-cm)	Electron Dosage ( $10^{16}/\text{cm}^2$ )	Days Since Irradiation	Leakage Current ( $\mu\text{amperes}$ )	Resolution (Kev)	Charge Collected (Mev)		
					V-0	V-3	V-20
10,000	0		0.06	100	3.5	3.9	4.07
	0.028		0.13	100	3.6	3.95	4.07
	0.057		0.16	110	3.44	3.92	4.05
	0.12		0.20		3.2	3.9	4.1
	0.35		0.34		2.5	3.75	4.1
	1.0		1.4		1.25	3.36	3.84
	1.7		10.5	120	0.82	3.25	3.65*
	3.2		3.6	170			
	5.6	0	2.7				
	5.6	2	11.5				
	5.6	15	12.5	225		2.66	3.5
	5.6	25	12.5	250		2.17	3.1
	0		0.05	85	3.86	4.04	4.16
	0.034		0.05	73	3.75	4.00	4.15
	0.068		0.07	130	3.67	3.94	4.04*
1000	0.14		0.14	120	3.5	3.92	4.0*
	0.42		0.25	120			
	1.2		20	300	1.47	2.6	3.75
	2.0		60	410	0.83	3.35	3.6*
	3.8		20	550			
	6.6	0	7.8				
	6.6	2	40				
	6.6	15	81				
	6.6	25	80	800		2.65	3.4*
	6.6					2.2	2.85*

\* Leakage current, resolution, and the starred values of charge collection were measured at 10 volts bias. Resolution is given as full width at half maximum.

TABLE 16 (Continued)

Resistivity (ohm-cm)	Electron Dosage ( $10^{16}/\text{cm}^2$ )	Days Since Irradiation	Leakage Current ( $\mu\text{amperes}$ )	Resolution (Kev)	Charge Collected (Mev)		
					V-0	V-3	V-20
100	0		0.28	97	3.34	3.82	4.09
	0.038		0.28	83	3.3	3.87	4.14
	0.076		0.33	100	3.16	3.8	4.05
	0.15		0.40	90	3.14	3.8	4.05
	0.50		0.39	94	2.97	3.8	4.1
	1.4		0.88	95	2.6	3.6	4.0
	2.3		1.66	97	2.34	3.5	4.0
	4.3		2.3	270			
	7.4	0	2.6				
	7.4	2	6.9				
	7.4	15	4.3	227	1.6	3.0	3.85
	7.4	25	4.1	230		2.6	3.45

The high frequency noise levels increased with leakage current, eventually becoming intolerable in the 1000 ohm-cm detectors. In the other samples, the noise background was confined to the lower portion of the pulse height spectra, corresponding to no more than 1 Mev. The nature of the noise voltage distribution was nonrandom, consisting of relatively small numbers of noise pulses of appreciable size, corresponding to as much as 1 Mev (in equivalent  $\alpha$  pulse height) in some cases. Because of the nonrandom distribution, the noise did not affect pulse height resolution in the usual manner. With random noise distributions, a given noise level produces a roughly equal spread in the resolution of the observed pulse height spectrum from monoenergetic particles. After irradiation, however, relatively large noise pulses were observed with enough frequency that the lower portions of the  $\alpha$  pulse height spectra showed large background counting rates, yet the spreads in observed  $\alpha$ -particle energies were much smaller. This can be understood in view of the infrequent occurrence of large noise pulses. When an  $\alpha$ -particle is detected, it is quite unlikely that a large noise pulse will be present at the same time.

The estimation of noise was qualitative at best. Noise was observed on a free running oscilloscope. With random noise distributions, a semiquantitative measure may be taken in this way. With the nonrandom distributions actually present, no meaningful measure of noise magnitude can be reported from the oscilloscope observations.

Pulse rise times were observed in both the VSA and CSA systems, with a lower limit in observable rise time of 0.2  $\mu$ sec. In the VSA,  $\alpha$ -pulse rise times remained below 0.2 for the 100 ohm-cm detectors during the entire irradiation. The 10,000 ohm-cm detectors also were fast at moderate bias levels, but rise times as long as 0.5  $\mu$ sec were seen with no applied bias. With the CSA, rise times of 1 to 3  $\mu$ sec were observed in both 10,000 and 1000 ohm-cm detectors toward the end of the irradiation. Unfortunately, the measurements of rise time were inaccurate, and it was not possible to determine whether the lengthened rise times were consistent with electron-induced changes in conductivity.

No noticeable annealing of the electron damage effects on counting characteristics was observed. In fact, a slight tendency for the counting characteristics to depreciate was observed upon aging at room temperature following irradiation.

The observed resolution widths at a 10-volt bias (expressed as full widths at half maximum, in Kev) are greatly broadened by two effects. First, the U-234 sources employed give two principal  $\alpha$ -particle energies, 4.77 and 4.71 Mev. If these two energies cannot be resolved, a wider combined peak is observed. Second, a 4.8-Mev  $\alpha$ -particle perpendicularly incident on the detector surface loses about 230 Kev in the He atmosphere, and about 300 Kev in the detector dead layers. The variation in this energy loss due to different angles of incidence is the order of 50 Kev. Because of the rather large uncertainty in estimating the latter effect, no correction to the observed resolution widths was made. The resolution of the 10,000 ohm-cm and 100 ohm-cm detectors was never observed to exceed about 5 percent, a value still adequate for many applications. The resolution widths observed toward the end of irradiation are not appreciably affected by the two effects mentioned above, because the several contributions to spread in observed energy combine roughly in quadrature. Consequently, spreads of 50 and 70 Kev represent a very minor contribution to those observed widths which exceeded 200 Kev.

Observed charge collection efficiencies are also given in table 16 for several bias voltages. The magnitude of pulse observed is given in Mev, for an incident  $\alpha$ -particle of  $4.76 - 0.23 - 0.30 = 4.23$  Mev. The fraction of ion pairs collected is equal to the ratio of the observed value to 4.23 Mev. The collection efficiency is seen to decrease considerably at low bias voltages, indicating a considerable decrease in minority carrier lifetimes due to electron damage. However, when the field strength is increased by application of a 20-volt bias, the collection efficiencies are seen to have decreased by less than 30 percent and 20 percent, respectively, in the 10,000 ohm-cm and 100 ohm-cm detectors.

On the whole, the detectors studied were more resistant to electron damage than had been expected. The rapid increases in leakage current and noise generation would prevent their use in high resolution applications after integrated fluxes of the order of  $10^{15}$  electrons/cm<sup>2</sup>. However, the charge collection mechanism appeared to operate reasonably well, at moderate bias voltages, following electron dosages as high as  $5 \times 10^{16}$ /cm<sup>2</sup>. In certain applications where resolution of a few percent is acceptable and noise in the lower portion of the energy spectrum can be tolerated, the use of low resistivity detectors to integrated fluxes of  $5 \times 10^{16}$  electrons/cm<sup>2</sup> or greater may be possible. One would hesitate, however, to apply these results to detectors from other sources, or from the same source at a different time. The major damage effect was to change the leakage current, and leakage current is notoriously sensitive to details of manufacture and material quality.

#### 4.20.5 Summary of Radiation Mechanism Investigation and Significance

It is known that high energy radiation affects semiconductor materials by both an immediate transient, and a slowly developing and more long-lasting effect. A number of investigations have been made of both of these, the usual interpretation being that the transient effect is a change in the number of carriers present, and the long-lasting effect is primarily the displacement of atoms in the lattice. Little effect is observed from nuclear transmutation.

The effects mentioned above are gross, rough effects. While they may conceptually be satisfying, the overall description is qualitative, and adds little to the understanding of radiation-induced failures or of how to guard against such failures. To begin to understand and guard against high energy radiation caused component failures, a much more detailed understanding of processes is necessary, and since the existing theory meets one of its stringent tests when applied to the capacitance of a diode, this capacitance was chosen for investigation. The investigation showed that for high resistivity ( $10^4$  ohm-cm) Si base material, the capacitance increased at all bias voltages as radiation progressed, and for lower resistivity materials, it stayed nearly constant; in all cases, however, the high bias capacitance increased faster



than the low bias capacitance. Leakage current increases, high frequency noise levels increase, and little annealing appears to take place. Quantitative values have been obtained which can now be dealt with theoretically; also the data indicate the presence of certain low-lying defect energy levels which may be related to the changes observed. Additional study and analysis is desirable for exact elucidation of the processes, but sufficient information has been obtained so that any theory may be rigorously tested, and the techniques and procedures necessary to minimize damage can be worked out.

## 5. REFERENCES

1. Skinner, S.M., The Thermodynamic Equilibrium of Electrical Charges on a Surface or at an Interface. (Office of Ordnance Research, Conference on Chemistry of Solid Surfaces, 26-27 March 1958.)
2. Shockley, W., "Electrons and Holes in Semiconductors," (D. Van Nostrand Co., New York, 1954).  
Shockley, W., M. Sparks, G.K. Teal, Phys. Rev. **83**, (1951), 151.
3. Spitzer, L., Jr., "Physics of Fully Ionized Gases," Interscience, New York, (1957).
4. Harnwell, G.P., Principles of Electricity and Electromagnetism, McGraw-Hill, (1949), 67.
5. Transistor Teachers Summer School, BTL, Phys. Rev., **98**, (1952), 1368.
6. Hippel, A.V., Molecular Science and Molecular Engineering, (Technology Press, John Wiley & Sons, New York, 1959).
7. Bauminger, R., et al.; Phys. Rev. **122**, (1961), 1447.
8. Wertheim, G.K., J. Appl. Phys. **32**, (1961), 1108.
9. Alff, C., and G.K. Wertheim, Phys. Rev., **122**, (1961), 1414.
10. Bauminger, R., et al.; Phys. Rev., **122**, (1961), 743.
11. Taimuty, S.I., and J.S. Mills, Conference Paper CP 62-1076, AIEE Meeting, Denver, (17-22 June 1962).
12. Moss, R.W., C.F. Kooi, and M.E. Baldwin, Conference Paper CP 60-1015, AIEE Meeting, San Diego, (August 1960).
13. Sakiotis, N.G., E.I. Salkovitz, A.I. Schindler, NRL-5321 (June 1959).
14. Gordon, D.I., R.S. Sery, and R.H. Lundsten, ONR-5, I, Symposium at Philadelphia, 17-19 March 1959), 253-292.
15. NOLTR 61-45 (May 1961).
16. Westinghouse Report ME #5942-3500-A.

17. For general reviews see
  - a. Wertheim, G.K., Nucleonics, (January 1961), also ref. 2.
  - b. DeBenedetti, S., Sci. American 202, (1960), 72.
  - c. Frauenfelder, Hans, The Mössbauer Effect, (W.J. Benjamin, Inc., New York, 1962).
18. Marshall, W., and J.P. Schiffer, "Debye Waller Factor in Mössbauer Effect," AERE Communication, (April 1960).
19. Smit, J., and H.P.J. Wijn, Ferrites, John Wiley & Sons, N.Y. (1959).
20. Bertaut, E.F., et al.; J. de Phys. et La Radium 20, (1959), 404.
21. Wertheim, G.K., "Energy Levels in Electron-Bombarded Silicon," Phys. Rev., 105, No. 6, (15 March 1957), 1730-1735.
22. Wertheim, G.K., "Electron-Bombardment Damage in Silicon," Phys. Rev., 110, No. 6, (15 June 1958), 1272-1279.
23. Wertheim, G.K., "Neutron-Bombardment Damage in Silicon," Phys. Rev., 111, No. 6, (15 September 1958), 1500-1505.
24. An excellent bibliography of these studies is given in "Space Radiation and Its Effects on Materials," REIC Memo No. 21, (30 June 1961).
25. Sah, C.T., R.N. Noyce, and W. Shockley, Proc. IRE, 45, (1957), 1228.
26. Shockley, W., and W.T. Read, Phys. Rev., 87, (1952), 835.
27. Easley, J.W., Third Semi-Annual Radiation Effects Symposium, 4, (1958).
28. Gordon, F., Third Semi-Annual Radiation Effects Symposium, 4, (1958).
29. Babcock, R.V., IRE Trans. on Nuclear Science, NS-8, No. 1, (1961), 98.
30. Kramer, G., Radiation Physics Laboratory, Hughes Research Laboratory, Final Report of DASA contract DA-146-16-XZ-016 (July 1962).
31. An extensive bibliography on this subject has been compiled: Blankenship, J.L., "Bibliography on Semiconductor Nuclear Radiation Detectors," Office of Technical Information Extension, USAEC, Report No. TID-2907, (6 December 1960, unpublished).
32. More recent work in this field has been published in the IRE Trans. on Nuclear Science, NS-7, NS-8, and NS-9.
33. Babcock, R.V., et al., "Coated Semiconductor Is Tiny Neutron Detector," Nucleonics 17, No. 4, (1959).
34. Henley, E.J., Nucleonics 12, No. 9, (September 1954), 62.
35. Baruch, P., J.A.P., 32, No. 4, (April 1961), 653.

36. Study of Failure Mechanisms, Quarterly Report No. 1, RADC-TDR-61-325, Rome Air Development Center, (December 1961).
37. Study of Failure Mechanisms, Quarterly Report No. 2, RADC-TDR-62-160, Rome Air Development Center, (June 1962).
38. Study of Failure Mechanisms, Quarterly Report No. 3, RADC-TDR-62-407, Rome Air Development Center, (October 1962).

APPENDIX I

EQUATIONS OF MOTION FOR THE FLEXURE TEST  
APPARATUS

The flexure testing apparatus may be represented, with respect to its dynamic functions, as shown in figure I-1 where

$a$  = distance from the drive rod pivot point to the upper end of the sample (in.).

$b$  = sample length (in.). (This includes only the free sample length, and not the end sections which are clamped or potted for support.)

$R$  = radius (in.) of the circle described by the secondary eccentric drive arm as it revolves about the axis of the primary drive or motor shaft.

$L$  = distance (in.) from the drive rod pivot point to a horizontal reference line normal to, and intersecting, the motor shaft axis.

$x$  = horizontal displacement (in.) of the bottom end of the sample at any time,  $T$ .

$\theta = \omega t$  = angular displacement of  $R$  from the horizontal reference at any time  $T$ .

$\alpha$  = angle between the drive rod and vertical at any time  $T$ .

$\omega$  = angular velocity (rad/sec).

$c, d, e, f$ , are self-explanatory.

The right side of the sketch illustrates the position of the drive rod at some arbitrary time, showing the same displacement,  $x$ , for two positions (1) and (2) of the eccentric drive arm. The left hand portion illustrates the position of the drive arm, (3), and the drive rod for maximum sample displacement,  $x_{\max}$ .



272

The operation of the device can be described as follows: From the sketch:

$$\tan \alpha = d/L = (d - c)/e$$

where

$$c = (R^2 - e^2)^{1/2} \quad (1)$$

$$e = R \sin \theta$$

substituting:

$$d/L = [d - R \cos \theta] / R \sin \theta \quad (2)$$

so that

$$\tan \alpha = R \cos \theta / (L - R \sin \theta); \quad (3)$$

but

$$\tan \alpha = x/f$$

and

$$f = a + (b^2 - x^2)^{1/2} \quad (4)$$

so that  $x$  as a function of  $\theta$  is the solution to the quadratic:

$$(1 + \omega^2) x^2 - (2 a \omega) x + (a^2 \omega^2 - b^2 \omega^2) = 0 \quad (5)$$

where

$$\omega = \tan \alpha = R \cos \theta / (L - R \sin \theta).$$

The solution is

$$x = \frac{a + b \left[ 1 + \omega^2 \left( 1 - \frac{a^2}{b^2} \right) \right]^{1/2}}{\omega + (1/\omega)} \quad (6)$$

The derivative

$$\frac{dx}{d\theta} \propto (a^2 \omega^2 - b^2) (R - L \sin \theta) \quad (7)$$

Therefore, maxima may be obtained at values of  $\theta$  satisfying

$$\theta = \sin^{-1} (R/L) \quad (8)$$

or

$$\theta = \sin^{-1} (gL/R) \pm \cos^{-1} g, \quad (9)$$

where

$$g^2 = b^2 / (a^2 + b^2).$$

The second of these is primarily a condition on  $a$ , and the first is a condition on  $\theta$ . Considering the three ranges of  $R/L$

- a.  $R/L < g$
- b.  $g < R/L < 1$
- c.  $R/L > 1$

it is evident that in the first range, equation 8 is valid. This is the design relationship chosen in the present apparatus. In the third range, equation 9 is valid, and in the center one, both are valid. When equation 9 is valid, it may be seen that a point exists for which  $dx/d\theta$  becomes infinite, so that this contingency and any related complications with respect to an S-shaped flexure are eliminated by the choice made.

With the design parameters used, the quantity in brackets in equation 6 is always nearly equal to one, so that

$$x = \frac{a + b}{\frac{L - R \sin \theta}{R \cos \theta} + \frac{R \cos \theta}{L - R \sin \theta}} \quad (10)$$



This relation is plotted (figure I-2) for one full cycle, using two values of  $R$  and the following values for other constants:  $a = 1.03$ ,  $b = 1$ , and  $L = 8.5$ . As seen from the plot, the above relation gives a cyclic variation in  $x$  with time, the maximum values of  $x$  being offset from zero by an angular amount  $\theta = \sin^{-1}(R/L)$ , and the values of  $\theta$  where  $x = 0$  not being offset. The offset of the maximum in the present apparatus is  $\omega t =$  approximately 7 degrees.

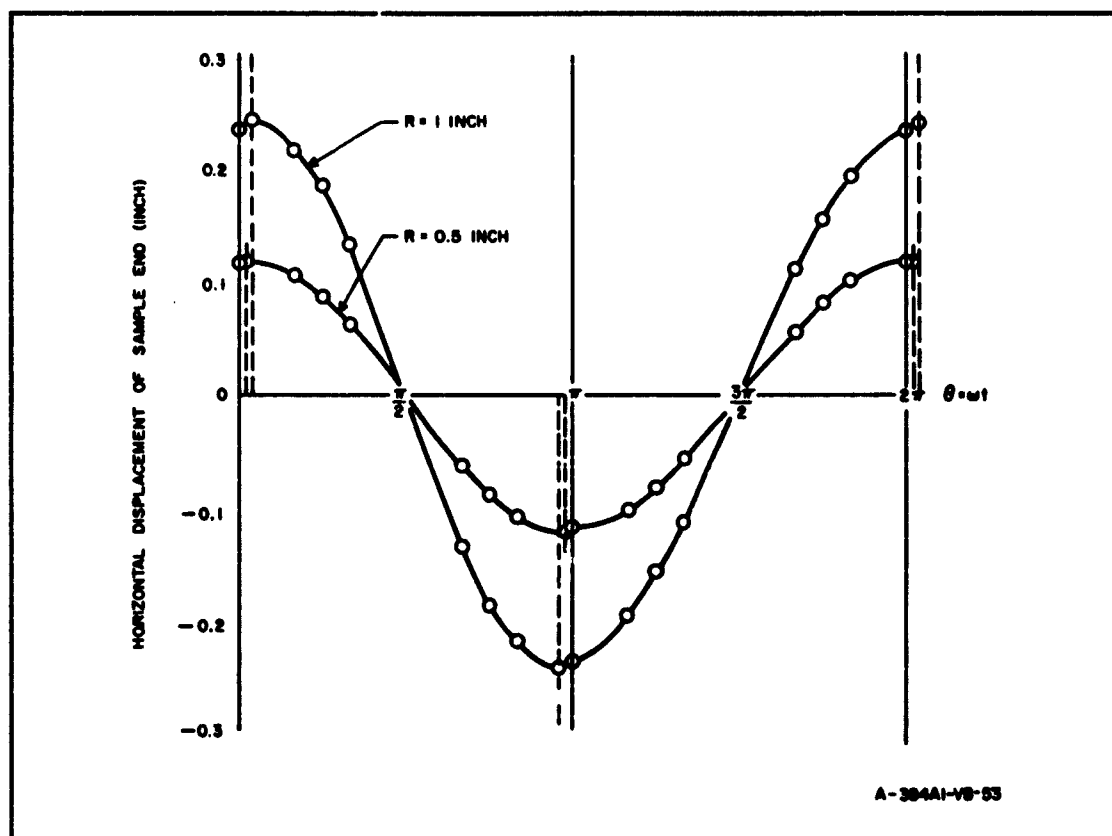


Figure I-2. Displacement Time Curves for Repetitive Flexure Apparatus

## APPENDIX II

### ESTIMATION OF ERROR IN CAPACITANCE MEASUREMENTS

In the calculation of junction capacitance from pulse division measurements, two possible causes of error were ignored. The first is competition between the detector rise time and the decay time of the amplification system, which prevents the output signal from rising to its ideal maximum value. The second error arises because the resistance of the reverse biased junction in series with the bias isolation resistor forms a voltage divider between the amplifier input and the bias supply, which is a-c ground. This resistive voltage divider, which is in parallel with the reactive voltage divider formed by the detector and reference capacitances, can seriously affect the measured voltage. The combined magnitude of both errors will be determined by deriving the magnitude of the output signal as a function of time for the unidealized network, which includes shunt resistances and time responses. The maximum value of this signal,  $S_o(t)_{\max}$ , is the quantity measured by the pulse height analyzer. For convenience, compute  $S_i(t)_{\max}$ , which has the time variation of  $S_o(t)_{\max}$ , but whose amplitude is referred to the amplifier input, and compare this with the ideal value given by equation 29 of the text.

Consider the network shown in figure II-1, which represents the a-c circuit of the pulse division measurements.  $R_d$  and  $C$  are the inverse resistance and the capacitance of the detector junction.  $R$ , the bias isolation resistor, goes directly to a-c ground because of the large cable capacitance between it and the slidewire of the 100 kilohm potentiometer which serves as a source of bias voltage. The contact resistance of the detector,  $r$ , is assumed to have a value such that  $rC$  equals the observed rise time of the detector. The load capacitance  $C_l$  is the sum of the reference capacitance

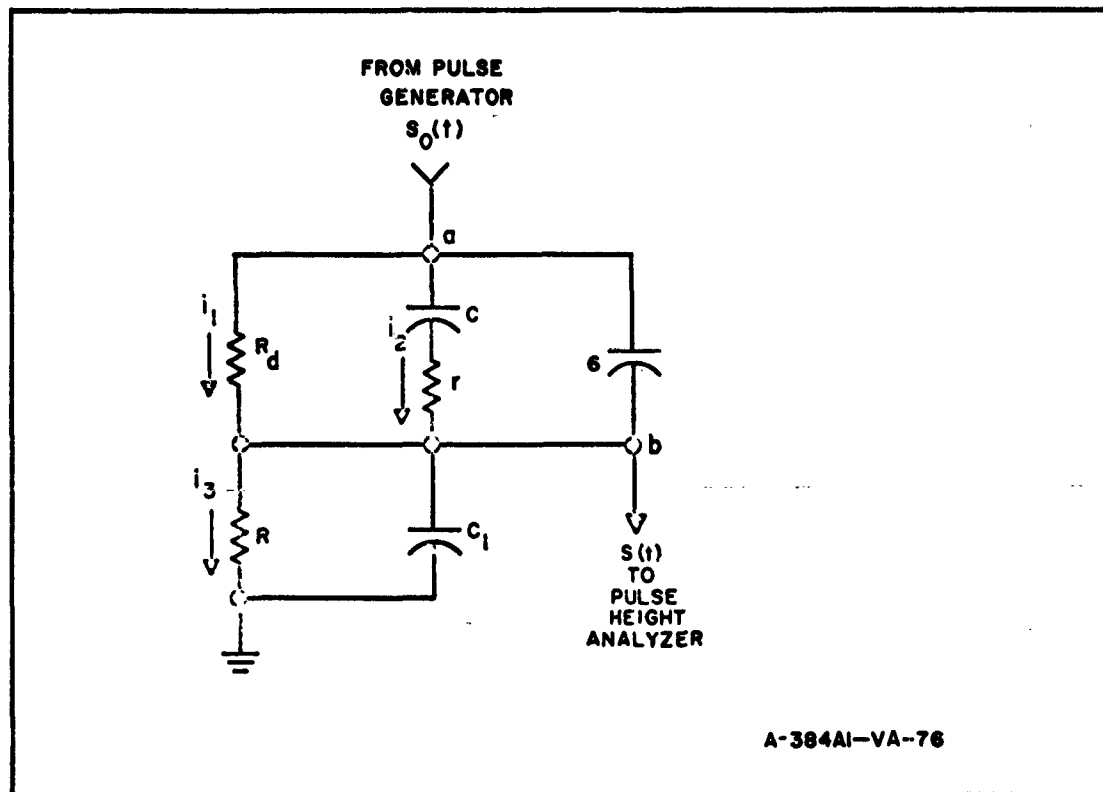


Figure II-1. AC Circuit for Pulse Division Measurements

( $C_r$  in the text) and the shunt capacitance to ground ( $C_g$  in text). The 6 pf capacitor represents the interlead capacitance ( $C_i$  in text). A step change of 1 volt is applied at point a, and we wish to calculate  $S(t)$ , the resulting voltage profile at point b.

From simple circuit theory, the rate of rise of the voltage at B, times the total capacitance  $C_1 + 6$ , is equal to the sum of the incoming currents;\*

$$\begin{aligned} (C_1 + 6)S' &= i_1 - i_3 + i_2 \\ &= \frac{(1 - S)}{R_d} - \frac{S}{R} + \frac{(1 - V_c - S)}{r}, \end{aligned} \quad (\text{II-1})$$

\* Throughout the discussion, primes denote differentiation with respect to time.

where  $V_c$  is the voltage drop across the p-n junction of the detector. If equation II-1 is now differentiated with respect to  $t$ ,  $V_c'$ , can be replaced by  $i_2/C$ , and equation II-1 is transformed to:

$$(C_1 + 6)S'' + \left[ \frac{1}{R_d} + \frac{1}{R} + \frac{1}{r} + \frac{C_1 + 6}{rC} \right] S' + \frac{1}{rC} \left[ \frac{1}{R_d} + \frac{1}{R} \right] S = \frac{1}{RrC}. \quad (\text{II-2})$$

A solution to the differential equation II-2 is:

$$S(t) = Ae^{-k^+ t} + Be^{-k^- t} + D,$$

where

$$K^\pm = \frac{f \pm f^2 - 4(C_1 + 6)(R + R_d)/rCRR_d^{1/2}}{2(C_1 + 6)},$$

and

$$f = \frac{R + R_d}{RR_d} + \frac{C_1 + C + 6}{rC}. \quad (\text{II-3})$$

The condition that the equilibrium value of  $S(t)$  is determined by the resistive voltage divider; i. e.,  $S(\infty) = R/(R + R_d)$ , implies that  $D = R/(R + R_d)$ . The initial value of  $S(t)$  is determined solely by the capacitive voltage divider; i. e.,  $S(0) = 6/(C_1 + 6)$ , implying that  $A + B + D = 6/(C_1 + 6)$ . If  $R$  and  $R_d$  are very large  $k^-$  must equal zero and the equilibrium value of  $S(t)$  is determined by the complete capacitive voltage divider  $(C + 6)/(C_1 + C + 6)$ . Consequently,  $B + D = (C + 6)/(C_1 + C + 6)$ . The last two conditions, together with the known value of  $D$ , determine the constants  $A$  and  $B$ , and one can write a full solution:

$$S(t) = \left[ \frac{6}{C_1 + 6} - \frac{C + 6}{C_1 + C + 6} \right] e^{-k^+ t} + \left[ \frac{C + 6}{C_1 + C + 6} - \frac{R}{R + R_d} \right] e^{-k^- t} + \frac{R}{R + R_d} \quad (\text{II-4})$$

The frequency response of the amplification system employed is adequately described by an exponential rise with a time constant of  $1/\alpha = 1 \mu\text{sec}$  and an exponential decay with a time constant of  $1/\beta = 12.5 \mu\text{sec}$ . Imposing these conditions, the time variation of the output signal may be determined.

The gain of the system is taken as one, so that the resulting function,  $S_i(t)$ , has its amplitude referred to the amplifier input, and may be compared to equation 29 of the text. For simplicity, the amplifier response will be represented by a low pass filter at the first stage of the amplifier, in series with a high pass filter at the output.

The signal following the low pass filter is given by the integral:

$$S_1(t) = S(0) (1 - e^{-at}) + \int_{\tau=0}^t S'(\tau) (1 - e^{-a(t-\tau)}) d\tau, \quad (\text{II-5})$$

where  $S(0) = 6/(C_1 + 6)$ , and  $S'(t)$  is obtained by differentiating equation II-4. Performing the indicated integration and collecting the exponential terms of like argument gives immediately:

$$S_1(t) = \frac{R}{(R + R_d)} - \frac{aA}{(k^+ - a)} e^{-k^+ t} - \frac{aB}{(k^- - a)} e^{-k^- t} + g e^{-at},$$

where

$$g = \frac{Ak^+}{(k^+ - a)} + \frac{Bk^-}{(k^- - a)} - \frac{6}{(C_1 + 6)} \quad (\text{II-6})$$

Similarly, the signal passed by the output filter is found from the integral:

$$S_i(t) = S_1(0) e^{-\beta t} + \int_{\tau=0}^t S_1'(\tau) e^{-\beta(t-\tau)} d\tau, \quad (\text{II-7})$$

where  $S_1(0)$  is zero, and  $S_1'(t)$  is found by differentiating equation II-6. Performing the indicated integration, and simplifying, gives:

$$\begin{aligned} \frac{S_i(t)}{a} = & \frac{Ak^+ (e^{-\beta t} - e^{-k^+ t})}{(k^+ - a)(k^+ - \beta)} \\ & + \frac{Bk^- (e^{-\beta t} - e^{-k^- t})}{(k^- - a)(k^- - \beta)} \\ & + \frac{g(e^{-\beta t} - e^{-at})}{(\beta - a)} \end{aligned} \quad (\text{II-8})$$

This expression can in principal be differentiated and  $S_i'(t)$  equated to zero to find the time  $t_{\max}$  at which  $S_i(t)$  is maximum, and its maximum value. However, because an explicit solution for  $t_{\max}$  is quite difficult to find, it is simpler to calculate  $S_i(t)$  for a particular set of parameters and determine the maximum value  $S_i(t_{\max})$  by inspection. Remembering that equation 34 in the text describes the measurement of a ratio of two output voltages,  $S/S_o$ , one must still find the maximum value of the output response when the step function is applied directly to the amplifier input,  $S_{oi}(t)_{\max}$ . The ratio  $S_i(t_{\max})/S_{oi}(t)_{\max}$  can then be compared directly to  $S/S_o$  to determine the error due to the two effects under discussion.

The signal  $S_o(t)$  applied at point a was a step function of 1 volt amplitude. The effect of the amplifier time response can be determined by integrating  $S_o(t)$  in the same manner that  $S(t)$  was integrated in equation II-5 and equation II-7 above. This gives directly:

$$S_{oi}(t) = (e^{-\beta t} - e^{-\alpha t}) \alpha / (\alpha - \beta) \quad (\text{II-9})$$

Differentiating equation II-9 and equating  $S'_{oi}(t)$  to zero gives an explicit solution for the time when  $S_{oi}(t)$  reaches its maximum value,  $t_m$ , which may be substituted into equation II-9 to give:

$$S_{oi}(t)_{\max} = (e^{-\beta t_m} - e^{-\alpha t_m}) \alpha / (\alpha - \beta), \text{ where } t_m = \log(\alpha/\beta) / (\alpha - \beta) \quad (\text{II-10})$$

Evaluating equation II-10 for this particular amplification system, with  $\alpha = 1$  and  $\beta = 0.08^*$ , we find  $t_m = 2.75 \mu\text{sec}$  and  $S_{oi}(t)_{\max} = 0.803$  volt.

The error has been evaluated for an applied bias of 10 volts for the most serious case encountered in the experiment, the postirradiation measurement of the 1000 ohm-cm detectors, where  $(C_1 + 6) = 500$  pf,  $R = 0.05$  megohms and  $rC \sim 0.5 \mu\text{sec}$ . At 10 volts bias  $R_d = 10/i$  megohms, and  $C \approx 55$  pf. With these choices of parameters, the percentage error introduced by calculating C from equation 28 in the text is found to be:

\* For quantitative evaluation, a consistent system of units is adopted in which time is measured in  $\mu\text{sec}$ , resistance in megohms, capacitance in pf ( $10^{-12}$  farad), current in  $\mu\text{a}$ , and voltage in volts.

Leakage current, $i(\mu\text{a})$	125	100	50	20	0
Percent error if $C = 50 \text{ pf}$	?	+40	+11	-2	-9
Percent error if $C = 100 \text{ pf}$	+16	+12	+1		-8

The question mark appears for  $C = 50 \text{ pf}$ ,  $i = 125 \mu\text{a}$  because under these conditions no peak voltage exists. The output signal rises continuously to the limiting value determined by the resistive voltage divider;  $S_o R / (R + R_d)$ . The overestimates of  $C$  at high current are due to the resistive divider, and the underestimates at low current are due to the  $0.5\text{-}\mu\text{sec}$  rise time in the detector.

Since the values of leakage current observed during postirradiation measurement of the  $1000 \text{ ohm-cm}$  detectors varied from  $10$  to  $80 \mu\text{a}$ , one sees that the error in these measurements due to the effects under discussion was appreciable. However, in all other measurements of capacitance by the pulse division method, these errors can probably be neglected.

# DISTRIBUTION LIST

	<u>No. of Copies</u>
**RADC (RASGP, ATTN: J. Schramp) Griffiss Air Force Base, New York	1
*RADC (RAAPT) Griffiss Air Force Base, New York	1
*RADC (RAALD) Griffiss Air Force Base, New York	1
*GEEIA (ROZMCAT) Griffiss Air Force Base, New York	1
*RADC (RAIS, ATTN: Mr. Malloy) Griffiss Air Force Base, New York	1
*US Army Electronics R&D Laboratories Liaison Officer RADC Griffiss Air Force Base, New York	1
*AUL (3T) Maxwell Air Force Base, Alabama	1
ASD (ASAPRD) Wright-Patterson Air Force Base, Ohio	1
Chief, Naval Research Laboratory ATTN: Code 2027 Washington 25, D.C.	1
Commanding Officer US Army Electronics R&D Laboratories ATTN: SELRA/SL-ADT Fort Monmouth, New Jersey	1
National Aeronautics & Space Administration Langley Research Center Langely Station Hampton, Virginia ATTN: Librarian	1

\* Mandatory.

\*\*Project Engineer will enter his office symbol and name in space provided.



# DISTRIBUTION LIST (Continued)

	<u>No. of Copies</u>
RTD (RTGS) Bolling Air Force Base Washington 25, D.C.	1
AFSC (SCSE) Andrews Air Force Base Washington 25, D.C.	1
Commanding General US Army Electronics Proving Ground ATTN: Technical Documents Library Fort Huachuca, Arizona	1
*ASTIA (TISIA-2) Arlington Hall Station Arlington 12, Virginia	Minimum of 10 copies
AFSC (SCFRE) Andrews Air Force Base Washington 25, D.C.	1
ESD (ESRL) L. G. Hanscom Field Bedford, Massachusetts	1
Commanding Officer & Director US Navy Electronics Laboratory (LIB) San Diego 52, California	1
ESD (ESGT) L. G. Hanscom Field Bedford, Massachusetts	2
ESD (ESRDE, Major James W. Van Horn) L. G. Hanscom Field Bedford, Massachusetts	1
ASD (ASRCTE, Mr. E. Miller) Wright-Patterson Air Force Base, Ohio	1
Westinghouse Electric Corporation Air Arm Division (Dr. John Dzimianski) Friendship International Airport P.O. Box 1897 Baltimore 3, Maryland	2

\*Ibid.

# DISTRIBUTION LIST (Continued)

	<u>No. of Copies</u>
Motorola, Incorporated Solid State Integrated Circuits Lab. ATTN: Mr. J.R. Black 8201 E. McDowell Road Scottsdale, Arizona	2
Hughes Aircraft Company Ground Systems Division ATTN: Mr. F.M. LaFleur Fullerton, California	2
Cleveland Clevite Corporation Electronic Research Division ATTN: Mr. Robert Gerson Cleveland, Ohio	2
Armour Research Foundation of Illinois Institute of Technology Technology Center ATTN: Dr. G.T. Jacobi Chicago 16, Illinois	2
Raytheon Comapny Research Division ATTN: Dr. P. Nutter Waltham 54, Massachusetts	2
General Telephone and Electric Bayside Laboratories ATTN: Dr. Thomas Polanyi Bayside, New York	2
Syracuse University ATTN: Dr. Glen Glasford Syracuse, New York	2
Clevite Corporation Shockley Transistor Division ATTN: Dr. Hans Queisser Stanford Industrial Park Palo Alto, California	2
Sprague Electric Company ATTN: Dr. Preston Robinson Director, Consultant N. Adams, Massachusetts	1

# DISTRIBUTION LIST (Continued)

	<u>No. of Copies</u>
Frank Brand Chief Microwave Quantum Electronics Branch SIGRA/SL-PFM Fort Monmouth, New Jersey	1
William Spurgeon Bendix Corporation Research Laboratory Division Southfield, Michigan	1
Autonetics Division North American ATTN: Dr. West 9150 E. Imperial Highway Downey, California	1
John G. Landers 307 The Great Road Bedford, Massachusetts	1
International Resistance Company ATTN: Jack Iskind Project Manager XTL Resistors 401 N. Broad Street Philadelphia, Pennsylvania	1
Avco, RAD ATTN: Mr. D. Earles 201 Lowell Street Wilmington, Massachusetts	1
Command Officer Diamond Ordnance Fuse Laboratories ATTN: Mr. Asaf A. Benderly Washington 25, D.C.	1
Corning Glass Works Electronic Components Division ATTN: Mr. Richard O'Brien Bradford, Pennsylvania	1
Fairchild Semiconductor Corporation ATTN: Mr. Jack Gorry 545 Whisman Road Mountainview, California	1

# DISTRIBUTION LIST (Continued)

	<u>No. of Copies</u>
General Electric Company Semiconductor Products Department ATTN: Mr. Conrad Zierat Electronics Park Syracuse, New York	1
Pacific Semiconductor, Incorporated ATTN: Mr. R.A. Campbell Culver City, California	1
Minneapolis Honeywell ATTN: Mr. J.M. Bedrick 1400 Soldiers Field Road Boston, Massachusetts	1
Battelle Memorial Institute ATTN: Mr. T. Shilladay Columbus, Ohio	1
Hughes Aircraft Company Semiconductor Division ATTN: Library P.O. Box 1278 Newport Beach, California	1
NASA Hq. ATTN: Mr. Fred Redler Washington, D.C.	1
General Telephone and Electronics Laboratories ATTN: Dr. Daniel George Bayside, New York	2
USASRDL (SIGRA/SL-PFS, Mr. N. Korolkoff) Evans Area Fort Monmouth, New Jersey	2
AGED Secretariat Working Group on Low Power Devices 346 Broadway New York 13, New York	3
Texas Instruments, Incorporated ATTN: Semiconductor Components Library P.O. Box 5012 Dallas 22, Texas	1

# **DISTRIBUTION LIST (Continued)**

	<u>No. of Copies</u>
Microwave Associates Incorporated ATTN: Dr. Arthur Uhlir, Jr. Burlington, Massachusetts	1
Motorola Incorporated Semiconductor Products Division ATTN: Dr. Steward S. Flaschen 5005 E. McDowell Road Phoenix, Arizona	2
General Electric Company Valley Forge Technology Center ATTN: Mr. T.G. Nicoforo P.O. Box 8555 Philadelphia 1, Pennsylvania	1
International Telephone and Telegraph Corporation Components Division ATTN: Mr. G.G. Perry P. O. Box 412 Clifton, New Jersey	1
Delco Radio ATTN: Mr. K. Doversberger Kokomo, Indiana	1
ARINC ATTN: Dr. H. Jervis 1700 K Street, N.W Washington, D.C.	1